

Chemical Evolution and Galaxy Formation

Dissertation

der Fakultät für Physik
der
Ludwig-Maximilians-Universität München

vorgelegt von

Daniel Thomas

aus München

München, den 5. Oktober 2000

1. Gutachter: Prof. Dr. Ralf Bender
2. Gutachter: Prof. Dr. Harald Lesch

Tag der mündlichen Prüfung: 18. Dezember 2000

Zusammenfassung

In die Entstehung und Entwicklung von Galaxien sind viele verschiedene Prozesse involviert, die auf äußerst komplexe Art gekoppelt sind. So muss man, um ein Szenario möglichst realistisch zu simulieren, sowohl die Dynamik von Sternen, Gas und Dunkler Materie, als auch Sternentstehung, die Wechselwirkung mit dem interstellaren Gas und chemische Anreicherung verschiedener Elemente berücksichtigen. Da diese Problemstellung unter einer zu großen Anzahl an unbekannten Parametern leidet, ist es effizienter, den dynamischen und chemischen Ansatz zu entkoppeln. Mit letzterem können dann Sternentstehungsgeschichten, Supernova-Raten, Ein- und Ausfallraten von Gas, die stellare Anfangsmassenfunktion, und Elementhäufigkeiten im interstellaren Gas, in den Sternen und im intergalaktischen bzw. intracuster Medium bestimmt werden. Das Ziel dieser Arbeit ist es, Galaxienentstehung unter dem Blickwinkel der chemischen Entwicklung mit Hilfe von theoretischen Modellen zu diskutieren.

Überblick

Während der primordialen Nukleosynthese in den ersten Minuten nach dem Urknall werden lediglich Wasserstoff, Helium und Spuren von Lithium synthetisiert. Sämtliche chemische Elemente, die schwerer als Helium sind, werden in Sternen produziert, und in stellaren Winden und Supernova-Explosionen in das interstellare Medium einer Galaxie geblasen, aus dem sich dann neue, chemisch angereicherte Sterngenerationen bilden können. Simulationen der chemischen Entwicklung von Galaxien versuchen, diesen Kreislauf der chemischen Anreicherung zu modellieren, um so wichtige Erkenntnisse über die Mechanismen und Zeitskalen der Entstehung von Sternpopulationen in Galaxien zu gewinnen. Über die Bestimmung von Elementverhältnissen kann chemische Entwicklung als eine Art ‘Uhr’ für Sternentstehung verwendet werden, da Eisen als Produkt von Typ Ia Supernovae deutlich verzögert relativ zu den sog. α -Elementen (O, Mg, Si, Ca, Ti) angereichert wird. Letztere werden in Supernovae vom Typ II gebildet, deren Vorläufer kurzlebige, massereiche Sterne sind. Beobachtungstechnisch zugänglich sind insbesondere die Elemente Mg und Fe.

Die Nukleosynthese der für die chemische Entwicklung von Galaxien sehr wichtigen α - und Eisengruppen-Elemente werden in dieser Arbeit daher ausführlich diskutiert. Anschließend wird die Anreicherungsgeschichte dieser Elemente im Halo und in der Scheibe der Milchstraße modelliert. Dieser Teil dient auch als Kalibration des numerischen Codes, da unsere Galaxis hinsichtlich der

Elementhäufigkeiten in Sternen und dem interstellaren Medium von Seiten der Beobachtung am detailliertesten untersucht werden kann.

Den Schwerpunkt der Arbeit bilden elliptische Galaxien. Es werden unterschiedliche Entstehungsszenarien diskutiert vom klassischen monolithischen Kollaps, über die Verschmelzung zweier Spiralgalaxien, bis hin zur Theorie der hierarchischen Galaxienentstehung.

Alter und Metallizitäten von elliptischen Galaxien, die dann von Modellen der Galaxienentstehung reproduziert werden müssen, werden mit Hilfe der sog. Populationssynthese aus den beobachteten Spektren abgeleitet. Eine genauere Untersuchung dieses Verfahrens und eine kritische Diskussion der in der Literatur abgeleiteten Alter von Galaxien sind Gegenstand eines eigenen Kapitels dieser Arbeit.

Die Rolle von (überwiegend elliptischen) Galaxien verschiedener Masse und Leuchtkraft bei der chemischen Anreicherung des intergalaktischen Medium durch galaktische Winde in Galaxienhaufen wird nachfolgend behandelt.

Für die in dieser Arbeit theoretisch behandelten hellen elliptischen Galaxien existiert eine umfangreiche Datenbasis in der Literatur. Zwergelliptische Galaxien, hingegen, sind aufgrund ihrer geringen Leuchtkräfte und insbesondere ihrer geringen Oberflächenhelligkeiten mit 4m-Klasse Teleskopen nur schwer beobachtbar, weshalb in diesem Fall sehr viel weniger Beobachtungsdaten vorliegen. Um diese Lücke zu füllen, werden in dieser Arbeit, zusätzlich zu den rein theoretischen Betrachtungen der vorangehenden Kapitel, beobachtete Spektren von Zwerggalaxien diskutiert und deren Alter, Metallizitäten und Elementverhältnisse bestimmt.

Einblick

Im folgenden werden die wichtigsten Ergebnisse der Arbeit zusammengefasst.

Stellare Nukleosynthese

Zur Analyse der Nukleosynthese in Typ II Supernovae werden die Ergebnisse der Simulationen von Woosley & Weaver (1995, WW95) und Thielemann, Nomoto & Hashimoto (1996, TNH96) verglichen. Während beide Arbeiten in den Berechnungen der totalen Metallizitäten Z gut übereinstimmen, sind im Falle der für die ‘chemische Uhr’ wichtigen Elemente Mg und Fe signifikante Diskrepanzen festzustellen. In einem $20 M_{\odot}$ -Stern produzieren TNH96 fünf mal mehr Mg als WW95, die hingegen für Sterne massereicher als $25 M_{\odot}$ eine deutlich höhere Fe-Produktion vorhersagen. Weiterhin werden die Elementhäufigkeiten in dem von einer Sternpopulation abgeworfenen Material für die beiden unterschiedlichen Nukleosynthese-Modelle berechnet. Mit TNH96 ergibt sich unter der Annahme einer Salpeter-Anfangsmassenfunktion (Salpeter 1955) ein Elementverhältnis von $[Mg/Fe] \equiv \log Mg/Fe - \log(Mg/Fe)_{\odot} = 0.26$, mit WW95 lediglich $[Mg/Fe] = 0.05$. Bereits aus diesem vorläufigen Ergebnis kann gefolgert werden, dass die von WW95 errechneten Mg/Fe Werte nicht ausreichen, die Elementverhältnisse weder im Halo unserer Galaxis noch in elliptischen Galaxien zu erklären.

Die Milchstraße

Mit Hilfe des Standard-Modells (Matteucci & Greggio 1986), das die Bildung der Scheibe unserer Galaxis anhand von zeitlich ausgedehntem Einfall primordialen Gases beschreibt, wird die chemische Entwicklung der Milchstraße simuliert. Unter Verwendung der TNH96-Modelle und der Salpeter-Anfangsmassenfunktion können sowohl die in Halo- als auch die in Scheibensternen beobachteten Häufigkeiten (einschließlich der Sonne) der Elemente H, O, Mg, Fe und Z, sowie Supernova-, Sternentstehungs-, Gaseinfallsraten reproduziert werden. Insbesondere wird mit der von Greggio & Renzini (1983) entwickelten analytischen Beschreibung der Supernova Ia-Rate der in Scheibensternen beobachtete steile Abfall von $[\text{Mg}/\text{Fe}]$ mit wachsendem $[\text{Fe}/\text{H}]$ von den Modellen korrekt beschrieben. Mit der WW95-Nukleosynthese lassen sich die Beobachtungsdaten, wie oben bereits vermutet, nicht zufriedenstellend gut reproduzieren.

Desweiteren wird eine leichte Modifikation der Gleichungen der chemischen Entwicklung vorgeschlagen, die es ermöglicht, eine Verzögerung in der Durchmischung des von den Sternen abgeworfenen Materials mit dem interstellaren Medium zu berücksichtigen. Das Modell mit Mischungszeitskalen von 10–100 Myr, führt zu einem nahezu konstanten, von der Metallizität unabhängigen α/Fe Verhältnis in den Halo-Sternen. Der steile Anstieg von $[\text{O}/\text{Fe}]$ mit abnehmendem $[\text{Fe}/\text{H}]$ zwischen $-3 \leq [\text{Fe}/\text{H}] \leq -0.3$, der kürzlich von Rebolo, Israelian, & García López (1999) gemessen wurde, impliziert dann, dass die Mischungszeitskalen geringer als 10^7 Jahre sein müssen.

Elliptische Galaxien

Zur Entstehung von elliptischen Galaxien werden zwei fundamental unterschiedliche Szenarien, nämlich der Kollaps einer einzelnen fragmentierenden Gaswolke und die Verschmelzung zweier Spiralgalaxien ähnlich unserer Milchstraße, betrachtet. Im Rahmen des ersteren Modells können die in elliptischen Galaxien beobachteten super-solaren Mg/Fe Verhältnisse ($[\text{Mg}/\text{Fe}] \approx 0.2$) auch unter Annahme einer Salpeter-Anfangsmassenfunktion reproduziert werden, solange die Sternentstehung innerhalb von 1 Gyr abgeschlossen ist. Das Modell der Verschmelzung zweier entwickelter Spiralgalaxien bei Rotverschiebung $z \approx 0.45$, hingegen, ergibt $[\text{Mg}/\text{Fe}] \lesssim 0.1$ und kann somit die beobachteten Mg/Fe Werte nicht erklären, selbst wenn ein durch die Verschmelzung verursachter kurzer Sternentstehungsausbruch einbezogen wird. Auch die Annahme einer abgeflachten Anfangsmassenfunktion kann das Problem nicht einfach lösen, da sich dann unrealistisch hohe Metallizitäten von über 3-fach solar ergeben.

Im einfachen Kollaps-Modell wird angenommen, dass angereichertes Gas von außen nach innen strömt um dort Sterne zu bilden, so dass das Mg/Fe Verhältnis bei kleinen Radien am geringsten ausfällt. Bei der Verschmelzung der Spiralen werden lediglich während des Sternentstehungsausbruchs im Zentrum — bei flacher Anfangsmassenfunktion — Mg/Fe überhäufige Sterne gebildet, womit sich ein genau umgekehrt gerichteter radialer Gradient in Mg/Fe vorhergesagt wird.

Hierarchische Galaxientstehung

Basierend auf der Theorie der Kalten Dunklen Materie, werden in den sog. hierarchischen Modellen der Galaxientstehung massereiche Objekte durch die sukzessive Verschmelzung kleinerer Einheiten gebildet. Die sich daraus ergebenden Sternentstehungsgeschichten werden hier in Hinblick auf die Erzeugung von Mg/Fe überhäufigen Sternpopulationen untersucht. Die von Kauffmann (1996) vorhergesagten mittleren, globalen Sternentstehungsraten führen zu $[\text{Mg}/\text{Fe}] \approx 0$ (solar) für Spiral- und zu $[\text{Mg}/\text{Fe}] \approx 0.04$ für elliptische Galaxien, wobei das errechnete, nahezu solare Mg/Fe-Verhältnis in elliptischen Galaxien deutlich unter dem beobachteten Wert ($[\text{Mg}/\text{Fe}] \approx 0.2-0.3$) liegt. Ein $[\text{Mg}/\text{Fe}] \approx 0.2$ erhält man nur, wenn ca. 30 Prozent der Sterne in einem kurzen, von der Verschmelzung zweier großer Galaxien initiierten Sternentstehungsausbruch unter der Annahme einer flachen ($x = 0.8$, wenn $x = 1.35$ der Salpeter-Funktion entspricht) stellaren Anfangsmassenfunktion gebildet werden. Dieses Modell hätte jedoch radiale Gradienten in Mg/Fe zur Folge, die in Beobachtungsdaten bisher nicht gefunden wurden. Weiterhin wird gezeigt, dass im Rahmen der hierarchischen Modelle — wiederum im Widerspruch zur Beobachtung — die leuchtkräftigsten und somit massereichsten Ellipsen die geringsten Mg/Fe-Werte aufweisen. Die Modelle implizieren außerdem, dass isolierte elliptische Galaxien im Feld, aufgrund ihrer zeitlich weiter ausgedehnten Sternentstehungsgeschichten, geringere Mg/Fe-Verhältnisse als ihre Gegenstücke in Galaxienhaufen haben. Die ‘Bulges’ von Spiralgalaxien weisen die höchsten Mg/Fe-Verhältnisse auf, da sie die ersten Sphäroide sind, die sich im Rahmen der hierarchischen Modelle bilden. Die Dichotomien Haufen-Feld und Galaxie-Bulge lassen sich hier nur schlecht quantifizieren, da die in elliptischen Galaxien beobachteten, absoluten Mg/Fe-Werte ja nicht reproduziert werden können.

Die Alter von elliptischen Galaxien

Üblicherweise werden die mittleren Alter von elliptischen Galaxien über die Balmer-Absorption ($\text{H}\beta$ Index) durch Vergleich von gemessenen Linienstärken mit Modellen für einfache stellare Populationen bestimmt. Je höher $\text{H}\beta$, desto geringer das Alter der Galaxie. In dieser Arbeit werden Populationssynthese Modelle, basierend auf den Modellen von Maraston (1998), vorgestellt, die aus einer 14 Gyr alten, metallreichen Haupt- und aus einer 15 Gyr alten, metallarmen Subkomponente (≤ 10 Prozent in Masse) bestehen. Für verschiedene Metallizitäten und relative Massen der Subkomponente, wird der Bereich $1.4 \lesssim \text{H}\beta \lesssim 2 \text{ \AA}$, $2 \lesssim \text{Fe}5335 \lesssim 3.5 \text{ \AA}$ und $3.5 \lesssim B-K \lesssim 4.5$ abgedeckt, der die gemessenen Linienstärken der meisten elliptischen Galaxien, insbesondere aller Haufenellipsen und aller massereichen Feldellipsen, einschließt. Die beobachtete Streuung der Balmerabsorption bis zu $\text{H}\beta \approx 2 \text{ \AA}$ kann folglich allein durch Metallizitäts-Effekte, ohne eine Variation im Alter erklärt werden. Im Hinblick auf das sog. G-Zwerg Problem in elliptischen Galaxien wird gezeigt, dass die hier vorgestellten Modelle trotz der metallarmen Subkomponente hervorragend mit den spektralen Energieverteilungen in einem Wellenlängenbereich von $1200 \leq \lambda \leq 6000 \text{ \AA}$, insbesondere mit dem Minimum

im mittleren UV ($\sim 2500 \text{ \AA}$), übereinstimmen.

Galaxienhaufen

Die nächsthöhere Skala, auf der chemische Entwicklung betrachtet werden kann sind Galaxienhaufen, deren intergalaktisches Medium durch galaktische Winde angereichert wird. Mit Hilfe der von Trentham (1998) gemessenen Galaxien-Leuchtkraftfunktion, die den gesamten Bereich an Leuchtkräften ($-10 \leq M_B \leq -22$) überspannt, wird der Beitrag von Galaxien verschiedener Leuchtkräfte zur chemischen Anreicherung des Intracuster Mediums (ICM) untersucht. Die gesamte beobachtete Masse an Eisen im ICM sämtlicher betrachteter Galaxienhaufen verschiedener Masse kann unter der Annahme einer Salpeter-Anfangsmassenfunktion reproduziert werden, insbesondere weil die Anreicherung von Eisen durch Typ Ia Supernovae (63 Prozent) berücksichtigt wird. Das theoretische Eisen-zu-Sternmasse Verhältnis von 0.002 ist in perfekter Übereinstimmung mit dem beobachteten Wert ($2.05 \pm 0.45 \cdot 10^{-3}$, Arnaud et al. 1992). Den größten Anteil zur Gesamtleuchtkraft und auch zur Elementanreicherung liefern Galaxien um L^* ($M^* \approx -20$), 16 Prozent des Eisens, hingegen, kommt von Zwerggalaxien mit $M_B > -18$. Die von einer Galaxienpopulation abgeworfene Gasmasse (56 Prozent von Zwerggalaxien) reicht nicht aus, die Beobachtungsdaten zu erklären, was bedeutet, dass ein signifikanter Anteil (50–66 Prozent) des Gases zwischen den Galaxien nicht am Prozess der Galaxienentstehung teilgenommen hat. Das von dem Modell vorhergesagte Mg/Fe Elementverhältnis $[\text{Mg}/\text{Fe}] = -0.12$ ist mit dem über *ASCA* ermittelten Wert ($[\text{Mg}/\text{Fe}] = -0.1$) konsistent.

Zwerggalaxien

Es werden hochauflösende ($\sigma \sim 40 \text{ km/s}$) Spektren von sechs Zwerg-Frühtypgalaxien im Wellenlängenbereich $4500\text{--}5500 \text{ \AA}$ präsentiert. Mit Ausnahme der dS0-Galaxie NGC7626 #15 ($\sigma \approx 80 \text{ km/s}$) haben alle Objekte äußerst geringe Geschwindigkeitsdispersionen am Rande der instrumentellen Auflösung. Die vier Zwergelliptischen Galaxien weisen keine signifikante Rotation auf. Alle sechs Objekte, einschließlich der dS0s NGC7626 #15 ($v_{\text{rot}} = 45 \text{ km/s}$, Anisotropieparameter $(v/\sigma)^* = 0.6$) und NGC7626 #13 ($v_{\text{rot}} \approx 16 \text{ km/s}$, Anisotropieparameter $(v/\sigma)^* \approx 0.75$), sind durch eine anisotrope Geschwindigkeitsverteilung charakterisiert. Das Sample zeigt eine Korrelation zwischen σ und Mg_2 -Index in Übereinstimmung mit dem Sample von Bender, Burstein, & Faber (1993). Die aus den Absorptions-Indizes $\text{H}\beta$, Mg_2 , $\text{Fe}5270$ und $\text{Fe}5335$ mit Hilfe von Populationssynthese Modellen abgeleiteten mittleren Alter weisen eine große Variation von 4 bis 14 Gyr auf, während die Metallizitäten zwischen $[Z/\text{H}] = -1.1$ und $[Z/\text{H}] = -0.4$ liegen. Die aus den $\langle \text{Fe} \rangle$ -Indizes ermittelten Metallizitäten sind um ca. 0.2 dex höher als die aus dem Mg_2 -Index abgeleiteten Werte, was auf leicht sub-solare Mg/Fe-Verhältnisse schließen lässt. Die hier abgeleiteten kinematischen Eigenschaften, die Alter, Metallizitäten und Element-Verhältnisse weisen deutlich auf eine Dichotomie zwischen Zwerggalaxien und den klassischen, massereichen Galaxien hin.

Ausblick

Die chemische Entwicklung ist ein wirkungsvolles Instrument um Szenarien der Galaxienentstehung und -entwicklung zu testen. Diese Arbeit zeigt, dass wir noch weit von einem umfassenden, konsistenten Bild der Entstehung von Galaxien entfernt sind.

Um chemische Entwicklung zuverlässiger modellieren zu können, ist es wichtig, sowohl die Simulationen der stellaren Nukleosynthese in massereichen Sternen, als auch das Szenario für Typ Ia Supernova-Explosionen weiter zu entwickeln. Auch unser Kenntnistand über die stellare Anfangsmassenfunktion, die entscheidend in die Interpretation von Elementverhältnissen eingeht, muss unbedingt sowohl von theoretischer als auch von beobachterischer Seite erweitert werden, mit dem Ziel die Anfangsmassenfunktion entkoppelt von der chemischen Entwicklung festlegen zu können. Ideal für die Kalibration der numerischen Codes der chemischen Entwicklung wäre die unabhängige Bestimmung der Sternentstehungsgeschichte in der Milchstraße.

Elliptische Galaxien, die für die Theorie der Galaxienentstehung eine wichtige Rolle spielen, geben uns weiterhin Rätsel auf, da ihre Kinematik einerseits deutliche Spuren von Verschmelzungsprozessen, ihre stellaren Populationen andererseits aber einen hohen Grad an Homogenität aufweisen. Verschmelzungen finden sicherlich statt, doch ist es unklar zu welchem Zeitpunkt, und auch in welchem Maße Prozesse wie Dissipation und insbesondere Sternentstehung beteiligt sind. Die Ergebnisse dieser Arbeit zeigen, dass eine elliptische Galaxie nicht so einfach aus der Verschmelzung zweier Spiralgalaxien gebildet werden kann, selbst wenn sich eine elliptische Form ergibt, und selbst wenn wir Verschmelzungsprozesse im lokalen Universum beobachten können. Die heutigen Modelle der hierarchischen Strukturentstehung sind zwar sehr vielversprechend, weil sie Galaxienentstehung in einem kosmologischen Zusammenhang begreifen, weisen aber insbesondere bei der Behandlung von Gas, Sternentstehung und der Bildung und Entwicklung von stellaren Populationen noch deutliche Defizite aus. Fundamentale Eigenschaften der elliptischen Galaxien, u.a. die hier diskutierten Mg/Fe-Verhältnisse, können nicht reproduziert werden. Die Vorhersage signifikanter Unterschiede zwischen Haufen- und Feldgalaxien wird in Zukunft anhand von großen, homogenen Datensätzen zu testen sein.

Aus der Analyse des diffusen Lichts elliptischer Galaxien lassen sich mit Hilfe von einfachen Populationssynthese-Modellen lediglich mittlere Alter und Metallizitäten ableiten. In komplexeren Modellen, hingegen, ist es schwierig, Alters- und Metallizitäts-Effekte zu trennen, wie in dieser Arbeit gezeigt wird. Spektren von Kugelsternhaufen in elliptischen Galaxien, hingegen, sind sehr viel einfacher und robuster zu interpretieren, und sind nun mit den neuen 8m-Klasse Teleskopen in großer Anzahl beobachtbar.

Galaxienhaufen sind hervorragende Laboratorien, um die chemische Entwicklung einer gesamten Galaxienpopulation selbstkonsistent zu behandeln, da in guter Näherung keine Elemente ‘verloren gehen’ können. Hier wird in Zukunft, wenn mit den neuen Röntgen-Satelliten bessere Daten über die Häufigkeiten verschiedener Elemente im intergalaktischen Gas vorliegen, und

auch die Analysemethoden robuster geworden sind, viel nicht nur über die Haufen selbst sondern auch über die Entstehung und Entwicklung von Galaxien zu lernen sein.

Eine bisher relativ wenig beachtete Galaxienklasse, die Zwerggalaxien bzw. Zwergellipsen, könnte einmal zur entscheidenden Herausforderung für Modelle der Galaxienentstehung werden. Da sie beobachtungstechnisch sehr viel weniger zugänglich sind, ist die existierende Datenbasis — auch wenn mit dieser Arbeit sechs weitere Objekte hinzugefügt werden — noch zu dürftig, um zwingende Randbedingungen an die Theorie der Galaxienentstehung stellen zu können.

Contents

1	Introduction	1
1.1	Outline	1
1.2	Fundamentals	2
1.2.1	Chemical evolution: the star formation clock	2
1.2.2	Stellar population synthesis	4
1.2.3	Galaxy formation	6
2	Stellar Yields and Chemical Evolution	11
2.1	The fundamentals of chemical evolution	11
2.1.1	The basic equations	11
2.1.2	The initial mass function	14
2.2	Stellar nucleosynthesis	14
2.2.1	Intermediate-mass stars and Type Ia supernovae	14
2.2.2	Type II supernovae	15
2.3	SSP-yields	22
2.4	Summary	24
3	The Milky Way	27
3.1	The model parameters	28
3.2	Observational constraints	28
3.2.1	Current infall rate and gas fraction	29
3.2.2	Abundance Distribution Function	30
3.2.3	Supernova rates	31
3.2.4	Age-Metallicity Relation	32
3.2.5	Element abundances	33
3.3	Delayed mixing	37
3.3.1	The two gas phases	37
3.3.2	Element abundances	37
3.4	Summary	39
4	Elliptical Galaxies	41
4.1	Merging Spirals vs. Clumpy Collapse	41
4.2	The model	43
4.2.1	Input ingredients for the chemical evolution	45
4.2.2	Average abundances	45
4.3	Results	46

4.3.1	Predictions from the closed box model	47
4.3.2	Central abundances in a Clumpy Collapse	48
4.3.3	Central abundances in Merging Spirals	52
4.3.4	Comparison Merging Spirals vs. Fast Clumpy Collapse . .	54
4.4	Discussion	56
4.4.1	Gradients inside the galaxy	56
4.4.2	Upper mass cutoff	57
4.4.3	How to interpret spectral indices?	57
4.5	Summary	58
5	Hierarchical Galaxy Formation	61
5.1	Average star formation histories	61
5.1.1	The model	61
5.1.2	Global populations	63
5.1.3	Burst populations in the elliptical	67
5.1.4	Global-to-burst population mixtures	68
5.1.5	Summary	73
5.2	Individual star formation histories	74
5.2.1	The model	74
5.2.2	Environment and morphology	75
5.2.3	Trends with luminosity	75
5.2.4	Bulges	77
5.2.5	Summary	80
5.3	Discussion	80
5.3.1	Universal or variable IMF?	80
5.3.2	Selective mass loss	81
5.3.3	Cluster vs. Field	81
5.3.4	Early star formation and late assembly?	81
6	The Ages of Elliptical Galaxies	83
6.1	Simple stellar population models	83
6.1.1	Spectral line indices	84
6.1.2	Spectral energy distributions	85
6.2	Results	87
6.2.1	Indices and colors	87
6.2.2	Constraints from the mid-UV	89
6.2.3	Models for $H\beta > 2 \text{ \AA}$	95
6.3	Discussion	95
6.3.1	Metallicity distributions in ellipticals	95
6.3.2	Evidence against recent star formation	96
6.4	Summary	97
7	Galaxy Clusters	99
7.1	Observational diagnostics	99
7.2	The luminosity function	100
7.3	The model	101
7.3.1	Chemical evolution	101

7.3.2	Metallicity-luminosity relation	102
7.3.3	Galaxy-cluster asymmetry	102
7.4	Results	105
7.4.1	Total iron mass	106
7.4.2	Total gas mass	106
7.4.3	Abundance ratios	108
7.4.4	Galaxy contributions	108
7.5	Summary	111
8	Dwarf Galaxies	113
8.1	The dwarf galaxy population	113
8.1.1	Basic properties	113
8.1.2	Open problems	114
8.2	Observations	115
8.2.1	The sample	115
8.2.2	Data reduction	118
8.2.3	Kinematics	118
8.2.4	Line indices	120
8.3	Results	121
8.3.1	Kinematics	126
8.3.2	Line indices	128
8.4	Discussion	139
8.5	Summary	140
9	Outlook	143

List of Figures

2.1	SNII ejecta of total mass and hydrogen	17
2.2	SNII ejecta of oxygen and total metallicity	19
2.3	SNII ejecta of magnesium and iron	21
2.4	Mg/Fe in SNII ejecta	23
2.5	Mg/Fe ratio in SSPs	24
3.1	Abundance distribution function	30
3.2	Supernova rates	32
3.3	Age-metallicity relation	33
3.4	$[\alpha/\text{Fe}]$ vs. $[\text{Fe}/\text{H}]$	34
3.5	$[\text{Mg}/\text{Fe}]$ vs. $[\text{Fe}/\text{H}]$ for delayed mixing	39
4.1	Star formation histories	44
4.2	$[\text{Mg}/\text{Fe}]$ for WW95	47
4.3	$[\text{Mg}/\text{Fe}]$ for TNH96	49
4.4	Central abundances for the clumpy collapse model	50
4.5	Central abundances in merging spirals	54
5.1	Global $[\text{Mg}/\text{Fe}]$ and $[\text{Fe}/\text{H}]$ in ellipticals	64
5.2	Global $[\text{Mg}/\text{Fe}]$ and $[\text{Fe}/\text{H}]$ in spirals	65
5.3	$[\text{Mg}/\text{Fe}]$ with flat IMF during the burst	69
5.4	Contours of constant $[\text{Mg}/\text{Fe}]$	70
5.5	Contours of constant $[\text{Fe}/\text{H}]$	71
5.6	Distribution of global $[\text{Mg}/\text{Fe}]$ ratios as function of environment .	76
5.7	$[\text{Mg}/\text{Fe}]$ vs. V -magnitude in ellipticals	77
5.8	Distribution of $[\text{Mg}/\text{Fe}]$ ratios in bulges as function of environment	78
5.9	$[\text{Mg}/\text{Fe}]$ in bulge vs. bulge+disk	79
6.1	Calibration of the SSP models on galactic globular clusters . . .	84
6.2	Calibration of the synthetic SEDs in the UV	86
6.3	$\text{H}\beta$ vs. Fe5335 and $B-K$	88
6.4	$\text{H}\beta$ vs. $\text{Mg } b$	89
6.5	Spectral energy distributions as a function of wavelength	94
7.1	Galaxy luminosity function in clusters	101
7.2	Metallicities and iron abundance vs. transformed gas fraction . .	103
7.3	Mg/Fe vs transformed gas fraction	104
7.4	Cluster iron and gas masses vs. luminosity	107

7.5	Contributions to enrichment of Mg and Fe	110
8.1	Spectra of the dwarf galaxy sample	117
8.2	Comparison FCQ with Monte Carlo simulations	119
8.3	Index calibration for run Oct94	122
8.4	Index calibration for run Aug95	123
8.5	Index calibration for run Mar98a	124
8.6	Index calibration for run Mar98b	125
8.7	Kinematics of NGC 7626#13 and NGC 7626#15	127
8.8	Kinematics of NGC 1052#1 and VCC 608	129
8.9	Kinematics of VCC 1087 and VCC 1308	130
8.10	Mg- σ relation	133
8.11	H β as a function of Mg ₂ and $\langle\text{Fe}\rangle$	134
8.12	[Z/H] vs. M_B	136
8.13	Mg ₂ -Fe plane	138
8.14	Relation age-[Mg/Fe]	139

List of Tables

2.1	Type Ia Supernova Ejecta	14
2.2	Supernova II Nucleosynthesis Models	16
2.3	He-Yields	18
2.4	SNII Yields	20
2.5	Observation vs. Model	22
3.1	Parameter Constraints	29
3.2	Solar Element Abundances	36
3.3	Delayed Mixing	38
4.1	Different Gas Fractions	51
4.2	Spiral Merger	53
4.3	Results	55
5.1	Global-Burst Mixtures	72
5.2	Radial Gradients	73
6.1	Model Parameters	91
6.2	Flux Contributions	92
6.3	Results	93
7.1	Fractional Contributions	109
7.2	Relative Contributions	111
8.1	Dwarf Galaxy Sample	116
8.2	Index Definitions	121
8.3	Kinematical Results	131
8.4	Line Indices within $r_e/2$	132
8.5	Ages and Metallicities	135

Chapter 1

Introduction

Understanding the formation and evolution of galaxies is difficult because it involves many different processes that are coupled in a complex way. In order to simulate a scenario properly, one has to consider the dynamics of stars, gas and dark matter as well as star formation, the interaction with the interstellar medium (ISM), and chemical enrichment (e.g., Hensler & Burkert 1990). Since this problem includes many unknown parameters, it is more effective to decouple the dynamical and the chemical approach, the latter constraining star formation histories, supernova rates, in- and outflow of gas, and element abundances in the interstellar medium (ISM), in the stars, and in the intergalactic or intracluster medium (ICM).

The aim of this work is to discuss galaxy formation by means of theoretical simulations of chemical evolution for different formation scenarios. The main focus is set on elliptical galaxies, because these objects play a key role in distinguishing fundamentally different formation scenarios as described in Section 1.2.3.

1.1 Outline

The thesis is organized as follows.

In Chapter 2, the principal ideas, the main input parameters, and the basic set of integro-differential equations of chemical evolution models are illustrated (Section 2.1). The numerical methods adopted and the chemical evolution code developed to solve these equations is described in Thomas (1997). An important ingredient to the simulations are the stellar ejecta, the so-called stellar yields, that are discussed in Section 2.2. The content of this chapter is published in Thomas, Greggio, & Bender (1998).

In Chapter 3, the application of the code on the chemical evolution of the Milky Way is presented, with the purpose to calibrate the code by using standard prescriptions from the literature (Section 3.2). In particular, the impact of different supernova nucleosynthesis prescriptions and stellar yields from Type II supernovae on chemical evolution models are discussed. In Section 3.3 a refinement of the standard model is proposed, in which the assumption of instantaneous mixing of the stellar ejecta in the ISM is relaxed. The content of this

chapter is published in Thomas, Greggio, & Bender (1998).

Elliptical galaxies are the subject of the Chapters 4, 5, and 6. In the former, the chemical evolution of two fundamentally different formation scenarios, namely a ‘*fast clumpy collapse*’ and the ‘*merger of two spirals*’, are simulated and compared to observational constraints focusing on the enhancement of α -elements (see Section 1.2.2). The content of this chapter is published in Thomas, Greggio, & Bender (1999).

Current models of hierarchical galaxy formation, that are based on Cold Dark Matter theory (see Section 1.2.3), are considered in Chapter 5. It is investigated, if such models are capable to reproduce the abundance ratios observed in ellipticals, which require the stellar populations in these galaxies to have formed on rather short timescales. The content of this chapter is published in Thomas (1999a), Thomas & Kauffmann (1999), and Thomas (2001).

The subsequent Chapter 6 focuses on the derivation of galaxy ages from integrated spectra. A two-component population synthesis model is presented, that reproduces all observed spectral features of ellipticals without invoking a spread in age. The content of this chapter is published in Maraston & Thomas (2000).

Chapter 7 then deals with chemical evolution on the next larger scale, namely galaxy clusters, whose intergalactic medium or intracluster medium (ICM) is chemically enriched by galactic winds. For a given galaxy luminosity function which is typical for clusters, the contributions from galaxies of different luminosities spanning the whole range from giant to dwarf galaxies to the ICM enrichment are theoretically explored. The content of this chapter is partly published in Thomas (1999b).

Intermediate-mass and dwarf galaxies, that turn out to play a non-negligible role in the chemical evolution of galaxy clusters, are the subject of the last chapter. In contrast to the purely theoretical studies of the previous chapters, Chapter 8 presents observational data of dwarf early-type galaxies, with the aim to determine their ages, metallicities, and abundance ratios.

1.2 Fundamentals

In this section I briefly describe some basic concepts of the present work.

1) Simulations of *chemical evolution* are the main tool which is used in Chapters 3, 4, 5, and 7 to set constraints on the formation mechanisms of the stellar populations in galaxies and galaxy clusters. 2) *Population synthesis* is the major diagnostic instrument to analyze colors and spectra of galaxies, and most observational constraints discussed here are derived by means of population synthesis models. 3) Finally, current models of *galaxy formation* are briefly illustrated.

1.2.1 Chemical evolution: the star formation clock

During primordial nucleosynthesis in the first few minutes after the Big Bang, only the elements hydrogen and helium, and trace amounts of lithium are synthesized. As there are no stable elements of mass 5 or 8, and the temperatures

and densities in the early universe are not adequate to bridge this barrier, further nucleosynthesis by combining hydrogen and helium does not take place. Elements heavier than helium, that altogether establish the so-called metallicity Z , are only produced in stars. In the cores of low- and intermediate mass stars ($m \lesssim 8 M_\odot$), the temperatures and densities are sufficient only to synthesize lighter elements like carbon and nitrogen. Heavier elements (i.e. oxygen, magnesium, iron...), instead, are mainly produced in massive stars with $m > 8 M_\odot$.

In order to enter the cycle of chemical evolution in a galaxy, the elements *newly* produced in the stars have to be ejected into the ISM. *Stellar winds* consist of the elements out which the star has formed plus some of the lighter newly produced elements like carbon, nitrogen, and small amounts of oxygen that have been dredged up to the surface. The chemical enrichment of heavy elements (i.e. oxygen, magnesium, iron...) happens through *supernova explosions*, in which both old and new heavy elements are ejected. The consequence from supernovae being the only contributor of heavy elements is twofold, as there are essentially two different types of supernovae.

1. Type II supernovae (SNII) are the final evolutionary stages of short-lived (~ 10 Myr), massive ($m \gtrsim 8 M_\odot$) stars. The envelope around the iron core¹, containing the elements that have been produced in hydrostatic nuclear burning before the explosion, is ejected. Additionally, nucleosynthesis takes place during the explosion, in which particularly iron and heavier elements are produced. SNII dominate the enrichment of the so-called α -elements (i.e. O, Mg, Si, Ca, Ti) and of total metallicity Z .
2. Type Ia supernovae (SNIa) are produced in close binary systems consisting of long-lived (~ 0.1 – 1 Gyr), intermediate ($1 \leq m \leq 8 M_\odot$) and low-mass ($m \leq 1 M_\odot$) stars. The most favorable model for SNIa is a single-degenerate binary system, in which mass flow from the secondary filling the Roche lobe on the degenerate white dwarf primary star causes an explosion and probably the complete disruption of the system (Hansen & Wheeler 1969; Whelan & Iben 1973). SNIa contribute a substantial fraction to the enrichment of *iron*.

Item (1) implies that the initial mass function (IMF) plays an important role in chemical evolution. The more massive stars relative to the number of low-mass stars are born in one stellar generation, the more metals per mass of a stellar generation are produced. From Item (1) it can be further concluded that the neglect of finite stellar lifetimes (the *instantaneous recycling approximation*, see Chapter 2, Section 2.1) is a viable approximation to describe the enrichment of total metallicity Z and of those elements that are predominantly produced in SNII for $t \gg 10$ Myr.

Due to Item (2), the enrichment of iron, instead, crucially depends on the rate of SNIa, and is therefore delayed with respect to the enrichment of α -elements by ~ 0.1 – 1 Gyr. Because of this effect, α/Fe ratios in the stars of

¹The iron core is the stellar remnant of the explosion and forms a neutron star or a black hole.

a galaxy carry information on the timescale of chemical enrichment and thus provide a clock with which the formation times of the stellar populations in that galaxy can be measured. Note, however, that the α/Fe ratio also depends on the shape of the IMF, as more α -elements are produced with an IMF containing more massive stars. The application of the α/Fe -clock is further complicated by uncertainties in SNII nucleosynthesis and by our poor knowledge on SNIa rates. These issues are discussed in the Chapters 2 and 3 in more detail. The α/Fe ratio is the central observational constraint considered in this work.

Element abundances are build up successively from stellar generation to stellar generation in the cycle of chemical evolution. Note that the element abundances of a star are measured in its atmosphere, reflecting essentially the abundances of the ISM at the time when the star was born. More details and the basic equations of chemical evolution are discussed in Chapter 2 (Section 2.1). It should be emphasized, that the mean metallicity of an object does not depend on star formation timescales but mainly on the fraction of gas converted into stars. The more efficient star formation is, the higher is the mean metallicity.

The abundance X_{El} of the element El is usually given logarithmically and normalized to the solar value with the following notation.

$$[\text{El}] = \log X_{\text{El}} - \log X_{\text{El},\odot} \quad (1.1)$$

Solar abundances are adopted from Anders & Grevesse (1989), meteoritic values.

1.2.2 Stellar population synthesis

As individual stars in galaxies outside the Local Group cannot be resolved, studies of their stellar populations are restricted to the observation of either the diffuse, integrated light or — with the new 8m-class telescopes — the globular clusters hosted by these galaxies. In order to derive ages and metallicities, the observed colors and spectra are then interpreted by means of population synthesis models. These so-called SSP models predict observational quantities like colors and spectra of Simple Stellar Populations (SSP) — populations of single age and metallicity — as functions of age and metallicity. Such models are constructed as follows.

SSP models

A simple stellar population of age t and metallicity Z is described by an *isochrone*, that specifies the stellar parameters bolometric luminosity L , effective temperature T and surface gravity g of the individual stellar masses m . The isochrone is computed from the theoretical stellar evolutionary tracks of the single masses. The spectro-photometric integrated properties of the SSP (spectrum, colors, mass-to-light ratios) are obtained by summing up the contributions to the flux from all masses. The flux as a function of wavelength λ emitted from each mass is given by stellar atmosphere libraries (e.g., Kurucz 1979), for the parameters T , g , and Z . The weight of each stellar mass is determined by the adopted IMF.

In the isochrone synthesis method (e.g., Charlot & Bruzual 1991), the integration along the isochrone extends to post-main sequence evolutionary phases up to the end of the isochrone, typically the early asymptotic giant branch. The accuracy of this method, however, suffers from very small steps in mass at late evolutionary phases leading to possible numerical instabilities. An alternative approach is based on the fuel consumption theorem (Renzini & Buzzoni 1986), in which — following the conservation of energy — the bolometric luminosity of each post-main sequence evolutionary stage is derived from the amount of nuclear fuel (i.e. mass of hydrogen and/or helium) burned in that stage. The fuel consumption theorem is applied in the population synthesis models of Buzzoni (1989) and Maraston (1998). The latter are the basis for the composite population models presented in Chapter 6.

The best SSPs in nature are globular cluster systems, on which model SSPs should always be calibrated. At super-solar metallicities, which is the relevant range for elliptical galaxies, this calibration is not possible, however, as even the most metal-rich Galactic globular clusters have sub-solar metallicities.

Spectral line indices

In order to allow for a universal interpretation of galaxy spectra, Burstein et al. (1984) introduced a set of spectral absorption line indices in the optical, which is known as the Lick system. These indices are defined as the ratio of the flux in the line to the flux in the continuum adjacent to the line, which essentially gives a measure for the strength of the absorption. The most commonly used indices are the Balmer line index $H\beta$, and the metallic indices Mg_2 , Mgb , $Fe5270$, and $Fe5335$. For further details on the exact definitions of these indices, see Chapter 8, Section 8.2.4.

In principle, line indices of a theoretical SSP can be calculated from the corresponding theoretical spectrum. However, the resolution of the flux libraries mentioned above is too low ($\Delta\lambda = 20 \text{ \AA}$) to match the index definitions within the Lick system ($\Delta\lambda \approx 8 \text{ \AA}$). The Lick indices for SSPs are therefore computed by inserting in the above integration the so-called *fitting functions* (Gorgas et al. 1993; Worthey et al. 1994) weighted with the continuum flux at the wavelength of the line feature. These fitting functions give index values as functions of the stellar parameters T , g , and Z . They are purely empirical, and are obtained by fitting the index features of Milky Way stars in the 3-dim. parameter space (T, g, Z) . A discussion on uncertainties and their impact on SSP models is given in Maraston, Greggio, & Thomas (2001). A major drawback is that the stellar data base in the solar neighborhood becomes scarce at super-solar metallicities. Therefore the fitting functions are best defined around solar metallicity, while the values at higher Z are essentially extrapolated. This has to be kept in mind when interpreting elliptical galaxies, that presumably have metallicities up to $3 Z_\odot$. This problem cannot be easily circumvented, because — as mentioned above — a careful calibration of SSP models at such high metallicities is hampered by the lack of metal-rich globular clusters in our Galaxy.

The age-metallicity degeneracy

An isochrone responds to changes in age and metallicity in the same way, such that both increasing the age and increasing the metallicity of a stellar system results in lower temperatures and hence redder colors (Tinsley 1972; Faber 1972; O’Connell 1976). This effect complicates the interpretation of galaxy spectra and colors.

Because — at higher metallicities — Balmer lines are predominantly age sensitive, the combination of Balmer lines with metallic indices can be used to break the age-metallicity degeneracy (González 1993; Worthey 1994). At low metallicities, however, also the Balmer absorption exhibits a dependence on metallicity, so that this concept collapses. This issue is discussed in Chapter 6.

The enhancement of α -elements in elliptical galaxies

Modeling the metallic line indices of elliptical galaxies, it turns out that — for a fixed Fe-index — the observed Mg-index (Mg_2 , $\text{Mg } b$) is stronger than what is predicted by the SSP models (Peletier 1989; Gorgas, Efsthathiou, & Aragón Salamaça 1990; Faber, Worthey, & González 1992; Worthey, Faber, & González 1992; Davies, Sadler, & Peletier 1993; Carollo & Danziger 1994; Fisher, Franx, & Illingworth 1995; Kuntschner & Davies 1998; Mehlert et al. 2000). As the latter are computed with fitting functions based on essentially solar abundance ratios, this effect is attributed to an enhancement of Mg/Fe and α /Fe with respect to the solar ratio. While this interpretation is likely to be qualitatively correct, a quantitative derivation of Mg/Fe ratios in ellipticals is not an easy task, because the translation of index variations into element abundances is not straightforward (see Chapter 4, Section 4.4). The responses of Lick indices to element abundance variations are theoretically computed by Tripicco & Bell (1995) for a 5 Gyr-old isochrone of solar metallicity. Using these so-called *response functions*, Trager et al. (2000a) confirm the previous estimates that the Mg/Fe ratios of the stellar populations in elliptical galaxies are on average a factor of 1.5–2 higher than the solar value ($0.2 \lesssim [\text{Mg}/\text{Fe}] \lesssim 0.3$). Magnesium is usually considered to be representative for all α -elements. The implication of α -enhancement for the formation and evolution of elliptical galaxies is discussed in Chapter 4.

It is interesting to mention that the stars of the Galactic bulge with metallicities around solar show an enhancement of α -elements that is comparable with the one found in elliptical galaxies (McWilliam & Rich 1994). This result indicates that bulges and elliptical galaxies may have formed in the same way.

1.2.3 Galaxy formation

The aim of this work is to set constraints on galaxy formation by means of chemical evolution simulations, focusing on the ability of the different scenarios to produce α -enhanced stellar populations. In Chapter 4, the *single collapse* model is confronted with the *merger of two spirals*, while Chapter 5 discusses the chemical evolution of galaxies in the framework of *hierarchical clustering*.

Single collapse

In the classical view, galaxies form in a *monolithic collapse* of a single gas cloud (Eggen, Lynden-Bell, & Sandage 1962; Larson 1974). The resulting shape from this collapse depends on the rotation of the system and on the role of gas, that is losing energy due to dissipational processes which leads to the formation of a disk. A spheroidal system forms, if star formation takes place on short timescales at the beginning, so that the dynamics of the collapse are dominated by dissipationless, only gravitationally interacting stars. As the virialization timescales of 2-body relaxations are by far too large, the system is assumed to virialize through violent relaxation (Lynden-Bell 1967). Metallicity gradients in elliptical galaxies can be understood in this picture, if flows towards the center of chemically enriched gas are taken into account (Larson 1974).

The consideration of a single, homogeneous gas cloud is certainly an oversimplification, and it was already proposed by Larson (1976) that it may be more realistic to assume a fractalization of the cloud in sub-clumps with sizes from globular clusters to small galaxies. These sub-clumps then merge to form the larger system. Such a ‘clumpy collapse’ model additionally solves a major drawback of the simple monolithic collapse, which predicts metallicity gradients that are too steep (Davies, Sadler, & Peletier 1993). Moreover, the merging of the subunits during the collapse reconciles the classical picture with the observational finding that at least 50 percent of all elliptical galaxies show kinematical signatures of merging (Bender 1996).

As illustrated in Chapter 4 (Section 4.1), the tightness of the color-magnitude relation and of the Fundamental Plane relations of elliptical galaxies indicate that their stellar populations must have formed at redshifts $z \gtrsim 2$ with subsequent passive evolution. These fundamental observational constraints on the stellar populations of elliptical galaxies can be easily reproduced in the framework of the classical clumpy collapse model. The color-magnitude relation implies that galaxy metallicities increase with galaxy mass (Kodama & Arimoto 1997), which can be reproduced with the so-called wind model (Larson 1974; Arimoto & Yoshii 1987; Matteucci & Tornambè 1987): The higher potential well of more massive objects prevents gas to escape, so that a larger fraction of the gas is turned into stars leading to higher metallicities.

Spiral merger

N -body simulations first performed by Toomre & Toomre (1972) show that an alternative path to form elliptically shaped objects is the merger of two spiral galaxies of similar size. Metallicity gradients can be produced in this picture, if the merger event is accompanied by star formation plus a flow of chemically enriched gas towards the center. Indeed, Barnes & Hernquist (1996) find in their simulations, that the gas participating the merger is drifting to the center of the new object. However, it is unlikely that the spiral merger can also explain the stellar population properties of ellipticals, because local spirals are younger than local ellipticals.

Hierarchical clustering

The main disadvantage of the two scenarios illustrated above is that they do not consider galaxy formation in a cosmological framework. Models of hierarchical galaxy formation, instead, are based on the fundamental cosmological principle that the origin of structures are primordial density fluctuations, that grow with the expansion of the universe. In a Cold Dark Matter cosmology, fluctuations on small scales grow faster, and merge later to larger structures. The major breakthrough of this theory was when numerical simulations of gravitational clustering succeeded at reproducing large-scale structure (e.g., Frenk 1991).

Merger trees Due to computational limitations, it is not possible to resolve the formation and evolution of the galaxy population in such simulations. Hence, based on the Press-Schechter theory (Press & Schechter 1974; Bond et al. 1991; Bower 1991), White & Rees (1978) and White & Frenk (1991) developed a *semi-analytical model* to describe the abundance of dark matter halos hosting galaxies as a function of redshift. A similar approach, but using the statistical properties of the peaks of the initial linear density field instead of Press-Schechter theory to construct models for halo formation and merging, was pursued by Lacey & Silk (1991) and Lacey et al. (1993). Based on the model of White & Frenk (1991), Kauffmann & White (1993) initiated the use of Monte Carlo simulations, to generate the merging histories of present-day dark matter halos (the so-called ‘merger trees’). Finally, Kauffmann, White, & Guiderdoni (1993) and Cole et al. (1994) set the link to galaxy formation assuming that a galaxy forms from gas which cools and turns into stars at the center of a halo until that halo merges with a more massive object.

Star formation The gas temperature is derived from the circular velocity of the halo using the equations of hydrostatic equilibrium. The cooling time of the gas is defined as the ratio of the thermal energy density to the cooling rate per unit volume, the latter being determined by the cooling functions depending on the temperature and the metallicity of the gas (Sutherland & Dopita 1993). The description of star formation essentially follows the classical Schmidt-law (Schmidt 1963), assuming that the star formation rate is proportional to the total mass of cold gas, with the star formation efficiency being a free parameter. Note that this prescription may be an oversimplification, as star formation seems to depend rather on local surface densities than on the total gas mass (Kennicutt 1989). Due to kinetic energy ejecta from supernovae, the cold gas is reheated to the virial temperature of the halo. As the efficiency of this process is highly uncertain, the fraction of energy used to reheat the cold gas, the so-called *feedback*, is also treated as a free parameter. The recipe for the metal enrichment included in the models of Kauffmann & Charlot (1998a) is similar to the process of reheating. A metallicity yield is adopted, that specifies the amount of metals ejected through supernovae per stellar generation into the hot gas phase. Instantaneous recycling is assumed. The enrichment of individual elements, in particular the delayed enrichment of iron from Type Ia supernovae, is not considered in hierarchical models so far.

Evolution of galaxies Following the merging paths according to the methods mentioned above, halos merge and form halos of larger mass (Kauffmann, White, & Guiderdoni 1993). It is important to emphasize that the galaxies belonging to each halo do not necessarily merge. The galaxy of the largest predecessor becomes the central galaxy, while the others become satellite galaxies within the newly formed large dark matter halo. All the gas that has not already cooled is assumed to be shock-heated to the virial temperature of the new halo, and to cool on to the *central* galaxy. Infall of cold gas on to the satellites is disrupted, and star formation within them continues only until their existing cold gas reservoirs are exhausted. Note that within this model, all galaxies in a galaxy cluster, being characterized by one single, large dark matter halo, are satellites except the central object. As a consequence, cluster galaxies are predicted to terminate star formation much earlier than their counterparts in the field.

As illustrated in Kauffmann, White, & Guiderdoni (1993), merging of galaxies happens only due to accretion of satellites by the central galaxy in a dark matter halo. The model does not allow for mergers between the satellites themselves. The exact mechanism of this process is very uncertain, and is modeled by calculating the dynamical friction timescale for each companion following the description in Binney & Tremaine (1987). The resulting galaxy merger rate is further manipulated by multiplying the merger probability with a free parameter, that is typically assumed to be larger than unity. As a consequence, mergers between galaxies are much less frequent than those of their parent halos (Cole et al. 1994).

In the beginning, galaxies form out of gas and have therefore disk-like morphologies. A spheroidal object is produced by mergers of equally sized disk galaxies (e.g., Barnes 1988). As the exact conditions under which the merger yields an elliptically shaped object are not known, a free parameter is introduced. If the ratio of the mass of the accreted satellite to the mass of the central galaxy exceeds the value of that parameter (typically 0.1–0.2), a spheroidal is assumed to form. In this so-called ‘major merger’, all the cold gas is assumed to turn into stars in an instantaneous burst (Kauffmann 1996; Baugh, Cole, & Frenk 1996). The further fate of the resulting spheroid is two-fold. If it becomes the central galaxy in a new dark matter halo, it will accrete cold gas, will establish a disk component, and will thus turn into the bulge of a spiral galaxy. Otherwise it is called an elliptical galaxy.

Observational constraints The hierarchical models predict galaxy numbers, circular velocities, and — by means of population synthesis models — luminosities and colors. They can be compared to a number of observational constraints like B and K luminosity functions, galaxy colors, the Tully-Fisher relation, faint galaxy number counts, redshift distributions etc. Some basic properties like luminosity functions and redshift distributions are rather well matched (Cole et al. 1994; Kauffmann & Charlot 1998b), while the Tully-Fisher relation of spiral galaxies still causes problems, in the sense that the circular velocities at a given luminosity are predicted too large (Cole et al.

2000).

Also the stellar population properties of elliptical galaxies remain a challenge for the semi-analytic models. In a bottom-up scenario, larger objects form naturally later and are therefore bluer, if metallicity effects are neglected. The observed color-magnitude relation in which more luminous ellipticals, instead, are redder (Bower, Lucey, & Ellis 1992) can be obtained, if metal enrichment is taken into account, such that the larger objects have higher metallicities (Kauffmann & Charlot 1998a). Based on the classical wind-model mentioned above, this mass-metallicity relation is achieved, because larger galaxies have more massive progenitors. The correct slope, however, can only be accomplished under the assumption of strong feedback at the expense of other successes of the model, e.g., disk sizes (Cole et al. 2000). Moreover, the observed small scatter about the relation is not reproduced by the models (Cole et al. 2000). As these failures are most likely due to the large diversity in star formation histories and due to the on average rather extended star formation timescales predicted, Bender (1996) questioned whether the observed α/Fe ratios in ellipticals are compatible with hierarchical models. However, semi-analytic models are not able to consider this important observational constraint, because the enrichment of individual elements is not taken into account. This issue is addressed quantitatively in this work (Chapter 5), in which the star formation rates predicted by the models from Kauffmann (1996) and G. Kauffmann (1999, private communication) are incorporated in simulations of chemical evolution.

Chapter 2

Stellar Yields and Chemical Evolution

Chemical evolution is a powerful tool to set constraints on galaxy formation. Typical input parameters of chemical evolution models are: the shape and slope x of the initial mass function (IMF), the star formation rate, the in- and outflow of gas, and the fraction of close binary systems producing Type Ia supernovae. In this chapter, after briefly introducing the basic equations of chemical evolution, an additional source of uncertainties, namely SNII nucleosynthesis and the so-called stellar yields are discussed. For this purpose, the following recently published SNII nucleosynthesis calculations are compared focusing on the production of the elements O, Mg and Fe: (1) Woosley & Weaver (1995), hereafter WW95; (2) Thielemann, Nomoto, & Hashimoto (1996) and Nomoto et al. (1997)¹, hereafter TNH96. The content of this chapter is published in Thomas, Greggio, & Bender (1998).

2.1 The fundamentals of chemical evolution

2.1.1 The basic equations

Non-primordial elements develop in the cycle of birth and death of stars. Stars form out of the interstellar medium (ISM), process elements, and eject them during the late stages of their evolution via stellar winds, superwinds (the envelope ejection at the end of the thermally pulsing AGB) yielding planetary nebulae (PN), or supernovae (SNIa and SNII), depending on their initial mass m . The formation of stars and the re-ejection of processed gas in galaxies can be described by the following phenomenological equations (Tinsley 1980; Pagel 1997):

$$dM_{\text{tot}}/dt = f \quad (2.1)$$

$$dM_s/dt = \psi - E \quad (2.2)$$

$$dM_g/dt = -\psi + E + f \quad (2.3)$$

¹In Nomoto et al. (1997), the results of Thielemann, Nomoto, & Hashimoto (1996) are extended by the initial masses 40 and 70 M_{\odot} .

The total baryonic mass $M_{\text{tot}} = M_s + M_g$ only depends on the infall or outflow f of primordial or enriched gas. The total stellar mass M_s *increases* according to the star formation rate ψ , and *decreases* due to re-ejection E of gas. The total gaseous mass M_g behaves exactly contrary to M_s with the additional component of in-falling or out-flowing gas f .

The ejection rate E is obtained by integrating the ejected mass fraction $(1 - w_m)$, folded with the star formation rate and the normalized IMF ϕ , from the turnoff mass m_t to the maximum stellar mass m_{max} . The quantity w_m denotes the mass fraction of the remnant.

$$E(t) = \int_{m_t}^{m_{\text{max}}} (1 - w_m) \psi(t - \tau_m) \phi(m) dm \quad (2.4)$$

The quantity τ_m is the stellar lifetime of a star with mass m . In the *instantaneous recycling approximation*, τ_m is assumed to be negligible compared to the evolutionary time t . This approximation is relaxed in numerical simulations as well as in the present evolution code. The instantaneous recycling approximation must not be confused with the instantaneous *mixing* approximation which is assumed in most chemical evolution models (Matteucci & Greggio 1986; Timmes, Woosley, & Weaver 1995; Tsujimoto et al. 1995; Pagel & Tautvaisiene 1995). In Chapter 3, I also relax the instantaneous mixing approximation (Section 3.3), by considering a delay in the mixing of the stellar ejecta.

Parallel to Equation 2.3, the mass production of the element i in the ISM ($X_i M_g$) is:

$$d(X_i M_g)/dt = -X_i \psi + E_i + X_{i,f} f \quad (2.5)$$

Here, X_i is the abundance of element i in the ISM, $X_{i,f}$ is the abundance of element i in the in-falling or out-flowing gas. The element ejection rate E_i is obtained by integrating the ejected mass fraction Q_{im} (including both the initial abundance and the newly produced material) of the element i , again folded with the star formation rate and IMF over the appropriate mass range, equivalent to Equation 2.4:

$$E_i(t) = \int_{m_t}^{m_{\text{max}}} Q_{im} \psi(t - \tau_m) \phi(m) dm \quad (2.6)$$

Equations 2.3 and 2.5 can be combined to describe the evolution of the abundance X_i of element i in the ISM.

$$M_g dX_i/dt = E_i - X_i E + (X_{i,f} - X_i) f \quad (2.7)$$

The key value in this equation is the so-called *stellar yield* Q_{im} , which is the crucial ingredient in the element ejection rate E_i . In the following, stellar winds during the evolution of the star are neglected, and it is assumed that the stars enrich the ISM only when they die. Depending on their initial mass, they either experience a SNII explosion ($m > 8 M_\odot$) or become a white dwarf blowing off their envelopes ($m < 8 M_\odot$). Elements heavier than oxygen are mainly processed in supernovae. A substantial fraction of iron is produced in

SN Ia. Adopting the description of supernova rates from Greggio & Renzini (1983), the element ejection rate integrated over the total mass range can be described with the following equation (Matteucci & Greggio 1986):

$$\begin{aligned}
E_i(t) = & \int_{16}^{m_{\max}} Q_{im}^{\text{SNII}} \psi(t - \tau_m) \phi(m) dm \\
& + (1 - A) \int_8^{16} Q_{im}^{\text{SNII}} \psi(t - \tau_m) \phi(m) dm \\
& + (1 - A) \int_3^8 Q_{im}^{\text{PN}} \psi(t - \tau_m) \phi(m) dm \\
& + A \int_3^{16} \phi(m) dm \int_{\mu_{\inf}}^{0.5} 24\mu^2 Q_{im}^{\text{SN Ia}} \psi(t - \tau_{\mu m}) d\mu \\
& + \int_{m_t}^3 Q_{im}^{\text{PN}} \psi(t - \tau_m) \phi(m) dm
\end{aligned} \tag{2.8}$$

The enrichment from stars in the mass range $3-16 M_{\odot}$ is split into the contribution from SNII (Q^{SNII}) plus planetary nebulae (Q^{PN}), due to single stars, and SN Ia ($Q^{\text{SN Ia}}$), assumed to be the end-product of close binary evolution. The quantity μ is the ratio between the mass of the secondary and the total mass m of the system. The maximum fraction of the secondary is 0.5 by definition, while the minimum mass μ_{\inf} is dependent on the turnoff as defined in the following equation (Greggio & Renzini 1983):

$$\mu_{\inf} \equiv \text{MAX} [m_t/m, (m - 8)/m] \tag{2.9}$$

The distribution of the secondary component $f(\mu) \sim \mu^2$, folded with the yield (independent of the mass of the system) and the star formation rate, has then to be integrated over the appropriate mass range. The clock of the SN Ia explosion is given by the lifetime of the secondary, $\tau_{\mu m}$, whose mass can be as low as $0.8 M_{\odot}$ (Greggio & Renzini 1983). Thus, the enrichment due to SN Ia is substantially delayed with respect to SNII. The number of SN Ia per stellar population depends on the fraction A of close binaries, which is a free parameter in chemical evolution. Greggio & Renzini (1983) calibrate A on the ratio between the current SNII and SN Ia rates in the Galaxy.

It should be noticed that Equation 2.8 is not completely self consistent, as m refers to the mass of single and binary stars. However, as long as the parameter A is small (as in this case), SN Ia events can be regarded as a small perturbation. Hence, Equation 2.8 is an acceptable approximation, and it allows to describe the delayed release of iron from SN Ia.

The rates of SNII and SN Ia can be described by the following equations:

$$R_{\text{II}} = \int_{16}^{m_{\max}} \psi(t - \tau_m) \frac{\phi(m)}{m} dm + (1 - A) \int_8^{16} \psi(t - \tau_m) \frac{\phi(m)}{m} dm \tag{2.10}$$

$$R_{\text{Ia}} = A \int_3^{16} \frac{\phi(m)}{m} dm \int_{\mu_{\inf}}^{0.5} 24\mu^2 \psi(t - \tau_{\mu m}) d\mu \tag{2.11}$$

2.1.2 The initial mass function

The IMF is a declining function of mass, usually described by the following power law: $\phi \sim m^{-x}$. The IMF is usually normalized to $1 M_{\odot}$. The slope $x = 1.35$ corresponds to the Salpeter-value (Salpeter 1955).

$$\int_{m_{\min}}^{m_{\max}} \phi(m) dm = C \cdot \int_{m_{\min}}^{m_{\max}} m^{-x} dm = 1 \quad (2.12)$$

To avoid uncertain extrapolations of the stellar yields to the high mass end, $m_{\max} = 40 M_{\odot}$ is adopted in the following, which is the maximum mass for which WW95-models are computed. TNH96 additionally provide the yields for a $70 M_{\odot}$ star. For the comparison between the two sets of models, however, m_{\max} is fixed to $40 M_{\odot}$. The effect of adopting $m_{\max} = 70 M_{\odot}$ is discussed in Section 2.2.2. The lowest stellar mass is assumed to be $m_{\min} = 0.1 M_{\odot}$.

2.2 Stellar nucleosynthesis

2.2.1 Intermediate-mass stars and Type Ia supernovae

The chemical composition in the stellar ejecta of intermediate-mass stars ($1 \leq m \leq 8 M_{\odot}$) is taken from Renzini & Voli (1981). These stars predominantly eject H, He, C, N and small amounts of O, hence do not significantly contribute to the enrichment of elements heavier than O.

TABLE 2.1
TYPE IA SUPERNOVA EJECTA

Element	Ejecta	Element	Ejecta	Element	Ejecta
^{12}C	3.2e-2	^{28}Si	1.6e-1	^{56}Fe	6.1e-1
^{16}O	1.4e-1	^{32}S	8.2e-2	^{57}Fe	1.1e-2
^{20}Ne	1.1e-2	^{36}Ar	2.2e-2	^{58}Ni	6.1e-2
^{24}Mg	2.3e-2	^{40}Ca	4.1e-2	^{60}Ni	1.1e-2

NOTE.—The most abundant elements ejected in a Type Ia supernova according to Nomoto, Thielemann, & Yokoi (1984, their W7 model, values in M_{\odot}). White dwarfs in close binary systems are assumed to be the progenitors of SNIa. The ejecta of SNIa are clearly dominated by ^{56}Fe .

SNIa are assumed to occur in close binary systems (Whelan & Iben 1973). In this model, the explosion is caused by a carbon-deflagration of the degenerate white dwarf that accretes material from the evolved secondary filling the Roche lobe (Hansen & Wheeler 1969; Nomoto 1980a; Nomoto 1980b; Weaver & Woosley 1980; Nomoto 1981). The nucleosynthesis calculations of Nomoto,

Thielemann, & Yokoi (1984) assuming the classical W7-model are adopted. As shown in Table 2.1, SNIa produce significantly more iron than oxygen or magnesium, ^{56}Fe is clearly dominating the ejecta.

2.2.2 Type II supernovae

As mentioned before, two sets of SNII nucleosynthesis calculations, namely WW95 and TNH96, are compared. In the following, I outline the major differences summarized in Table 2.2.

While WW95 calculate the complete pre-supernova evolution (Weaver & Woosley 1995), the simulations by TNH96 start with the evolution of He-cores of mass m_α , adopting the relation between the initial stellar mass m and m_α from Sugimoto & Nomoto (1980). The $^{12}\text{C}(\alpha, \gamma)^{16}\text{O}$ -rate is lower by 26 per cent in WW95 than in TNH96, which increases the production of carbon and C-burning products including O and Mg in WW95. However, the Schwarzschild criterion for convection, adopted by TNH96, leads to larger convective shells than the Ledoux criterion (WW95), which enhances the production of C in TNH96. Thus, these two effect counter balance each other.

It should be emphasized that the iron, that is produced in hydrostatic Si-burning during the pre-supernova evolution, is not ejected but forms the remnant of the supernova. All the iron in the ejecta is exclusively produced during the explosion through the decay of ^{56}Ni to ^{56}Fe . Thus, the Fe-SNII yield mainly depends on the simulation of the explosion. The explosion energies are essentially the same in both sets of models ($1.2 \cdot 10^{51}$ erg in WW95 and $1.0 \cdot 10^{51}$ erg in TNH96). In their model B, WW95 enhance the explosion energies for masses $m \geq 30 M_\odot$ by a factor ~ 1.5 , in model C additionally for masses $m \geq 35 M_\odot$ by a factor ~ 2 . TNH96 generally enhance the explosion energies for $m \geq 25 M_\odot$ by a factor of 1.5, so that their models correspond best to model B of WW95. The simulation of the explosion mechanism, instead, is significantly different in WW95 and TNH96. While the former aim to model the explosion itself by situating a piston at the Y_e discontinuity, TNH96 simply deposit the energy and assume the star to explode. Therefore, TNH96 cannot address issues like mass fallback and black hole formation, that may be important for massive stars (WW95). The nucleosynthesis in WW95 is caused by the energy transport of neutrinos, which is not considered in TNH96.

WW95 provide a finer grid of stellar masses, while TNH96 additionally calculate the yield of a $70 M_\odot$ star (Nomoto et al. 1997). TNH96 only consider solar initial metallicity. WW95, instead, discuss the initial metallicities $Z_{\text{in}} = 0, 10^{-4}, 0.01, 0.1, 1 Z_\odot$.

In the following, the yields of H, He, O, Mg, Fe and the total ejected metallicity Z_{ej} as functions of the initial stellar masses m (M_\odot) are discussed. In Figs 2.1 (total mass and H), 2.2 (O and metallicity), and 2.3 (Mg and Fe) the ejected masses (M_\odot) of these elements are plotted versus the stellar initial masses m (M_\odot). The solid (Z_\odot), dashed ($0.1 Z_\odot$), dash-dotted ($0.01 Z_\odot$), dot-dashed ($10^{-4} Z_\odot$), and dotted ($Z = 0$) lines are the yields of WW95. The diamonds are the yields of TNH96 (Z_\odot). As TNH96 only evolve He-cores, the total ejected mass of an element is given by the yields calculated in TNH96 plus

TABLE 2.2
SUPERNOVA II NUCLEOSYNTHESIS MODELS

	WW95	TNH96
stellar evolution	entire stars	helium cores
$^{12}\text{C}(\alpha, \gamma)^{16}\text{O}$	$1.7 \times$ Caughlan & Fowler (1988), 74 per cent of TNH96	Caughlan et al. (1985)
convection	Ledoux criterion, modification for semi-convection	Schwarzschild criterion, convective shells have greater extend
explosion energy	1.2×10^{51} erg (model A) model B: $E_B \approx 1.5 \times E_A$ for $m \geq 30 M_\odot$ model C: $E_C \approx 2 \times E_A$ for $m \geq 35 M_\odot$	1.0×10^{51} erg $E = 1.5 \times 10^{51}$ erg for $m \geq 25 M_\odot$
explosion mechanism	piston situated at the Y_e discontinuity	deposition of energy
neutrinos	nucleosynthesis caused by the flood of neutrinos	neutrino process <i>not</i> included
mass grid	11, 12, 13, 15, 18, 19, 20, 22, 25, 30, 35, 40 M_\odot	13, 15, 18, 20, 25, 40, 70 M_\odot
initial metallicity	grid of 5 different Z_m	only solar Z_m

NOTE.—The main differences in the SNI nucleosynthesis prescriptions of WW95 and TNH96. Models B and C in WW95 assume enhanced explosion energies in high mass stars by a factor of 1.5 and 2, respectively. TNH96 do not specify different models, but also enhance the explosion energy in high mass stars by a factor of 1.5. Differences in stellar evolution ($^{12}\text{C}(\alpha, \gamma)^{16}\text{O}$ -rate, convection theory) mainly affect the nucleosynthesis of intermediate elements lighter than iron. The yield of iron itself is highly dependent on the explosion.

the original element abundance in the envelope $m - m_\alpha$.

Total mass and hydrogen

The left panels in Fig. 2.1 show the total ejected masses. Model A (WW95) suffers from the fallback of envelope material in the high mass range, an effect less pronounced in model B and virtually absent in model C. Except for the (most uncertain) case $Z = 0$, the dependence on metallicity is negligible. The ejected masses in the WW95 and TNH96 models are very similar.

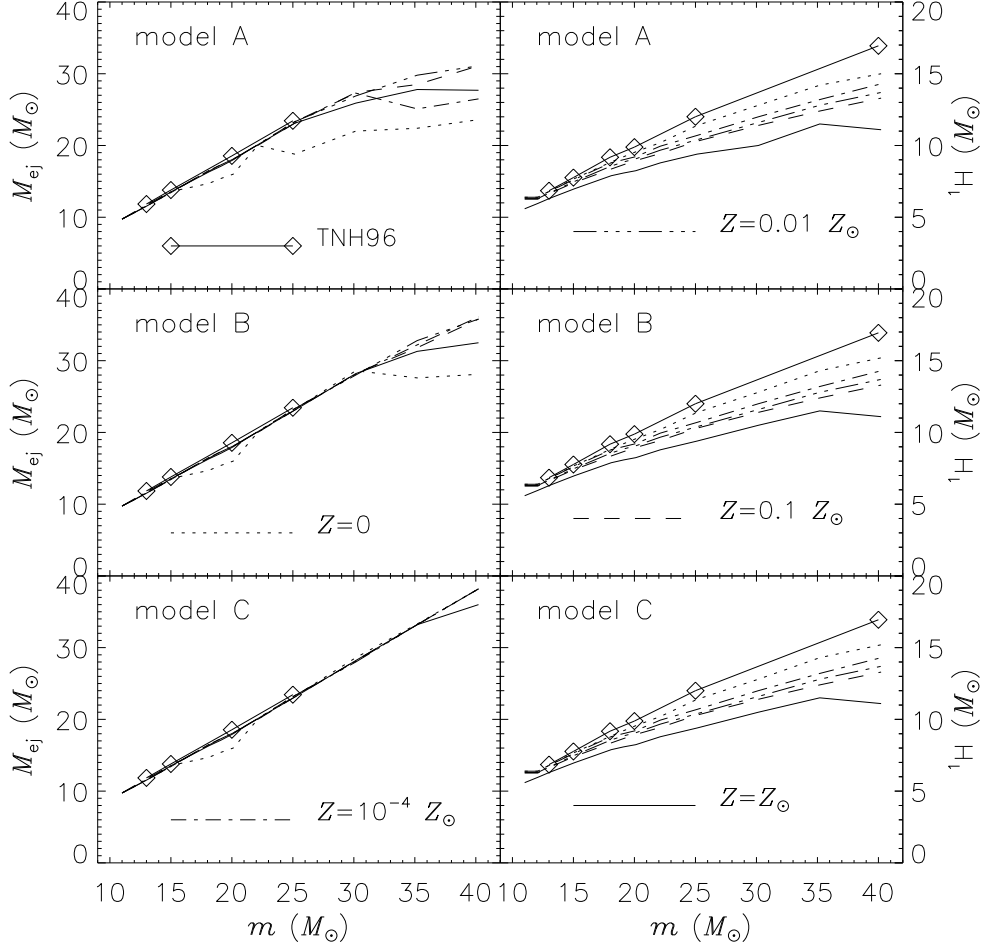


Figure 2.1: Total ejected mass (left panel) and hydrogen yield (right panel) of SNI as a function of the initial stellar mass (M_\odot). In each panel, one of the different linestyles is defined, indicating the five different initial metallicities assumed in WW95. The diamonds refer to the results of TNH96 (Z_\odot). The middle and bottom panels show the results for enhanced explosion energies in high mass stars in the calculations of WW95 (see Table 2.2). The yields include both initial and newly synthesized material.

TABLE 2.3
HE-YIELDS

	13 M_{\odot}	15 M_{\odot}	20 M_{\odot}	25 M_{\odot}
WW95	4.51	5.24	6.72	8.64
TNH96	4.13	4.86	5.95	6.63

NOTE.—SNII ${}^4\text{He}$ yields according to WW95 (Z_{\odot} , model B) and TNH96. The numbers are given in M_{\odot} . Since Nomoto et al. (1997) do not give He-yields, only $m \leq 25 M_{\odot}$ are considered.

The H-yield (right panels), instead, is clearly dependent on the initial metallicity of the star, especially at the high mass end. The H-yield of TNH96 is significantly larger, particularly for masses $m \gtrsim 20 M_{\odot}$. However, as the higher H-yield in TNH96 corresponds to a lower He-yield (Table 2.3), the resulting Z-yields of TNH96 and WW95 are consistent (see Fig. 2.2). These differences are due to the different m_{α} - m relations at He-ignition, and due to the fact that TNH96 neglect H-shell burning. For example, the m_{α} of a 25 M_{\odot} star is 9.21 M_{\odot} in the WW95 models, which is 1.21 M_{\odot} larger than what is adopted by TNH96 for the same initial mass. The resulting He-yield of WW95 is 2 M_{\odot} larger than in TNH96, because of the additional He-production in the H-burning shell. A fair comparison between the predictions of the two sets of models should therefore be performed at constant m_{α} . This is not possible, because the m_{α} -values in WW95 for masses other than 25 M_{\odot} are not available.

Oxygen and metallicity

Fig. 2.2 compares the yields of oxygen (left panel) and the total metallicity Z (right panel). Notice that Z is clearly dominated by oxygen. Both yields depend only weakly on the initial metallicity except for the $Z_{\text{in}} = 0$ case. TNH96 is in good agreement with WW95 for $m \leq 25 M_{\odot}$. At larger masses, the WW95 simulations predict the fallback of envelope material onto the remnant, so that TNH96 agrees only with their model C. The enhanced production of oxygen in TNH96 is most likely due to the higher ${}^{12}\text{C}(\alpha, \gamma){}^{16}\text{O}$ -rate. At the lower mass range ($m \leq 20 M_{\odot}$), WW95-yields tend to be slightly larger for the same metallicity (Z_{\odot}), possibly because of the larger m_{α} . It can be concluded that the uncertainty in the O-yields from SNII is small.

Magnesium and iron

The Mg-yield of TNH96 (Fig. 2.3, left panel) is larger by about a factor of 3–5 in the mass range 18–25 M_{\odot} . The reasons for this significant discrepancy are explored in the following.

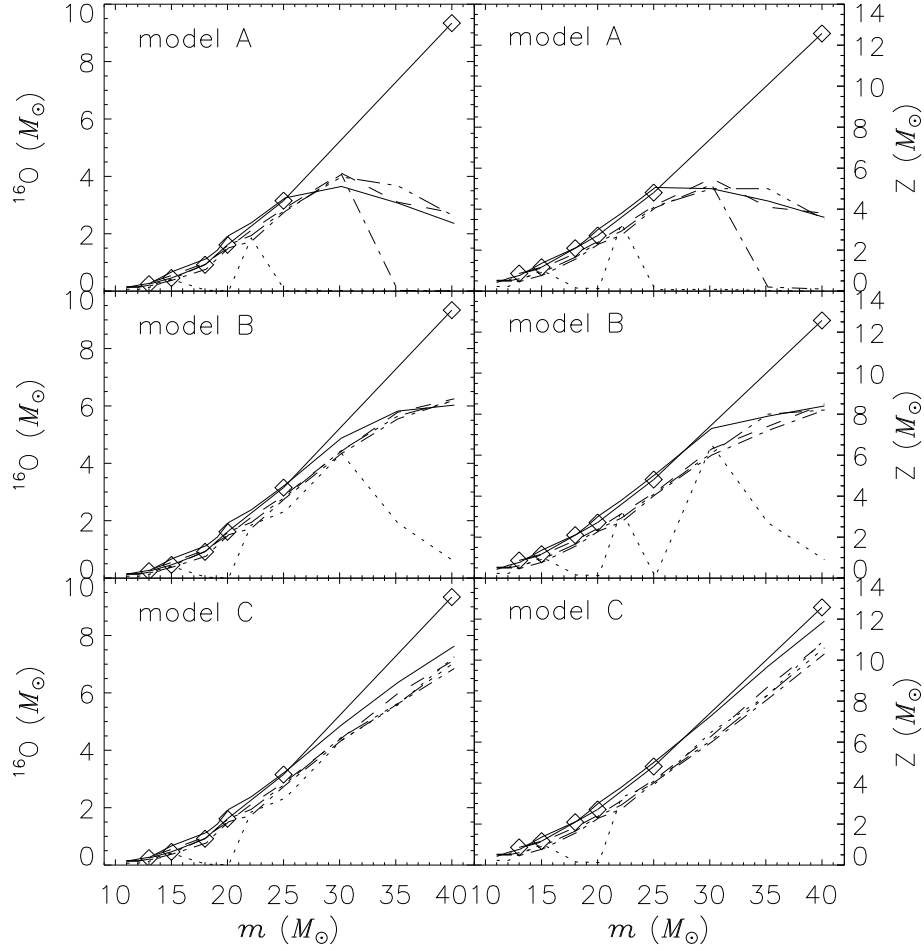
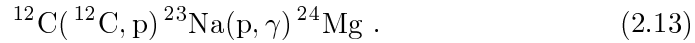


Figure 2.2: Oxygen yield (left panel) and ejected metallicity (right panel) of SNI as a functions of initial stellar mass (M_{\odot}). The different linestyles and symbols are explained in Fig. 2.1. The yields include initial and newly synthesized material. The oxygen yield of the $70 M_{\odot}$ star of TNH96 is $22 M_{\odot}$.

The dominant fraction of ^{24}Mg is produced during hydrostatic C-burning in the following reaction (Arnett & Thielemann 1985):



Hence, the Mg abundance is linked to carbon and the other C-burning products, i.e. Ne and Na. The yields of these elements plus the O-yield are listed in Table 2.4.

The C-yields of WW95 are systematically higher for all stellar masses, because of the larger He-cores and the lower $^{12}\text{C}(\alpha, \gamma)^{16}\text{O}$ -rate (carbon is a He-burning product). However, WW95-yields of the C-burning products ^{20}Ne , ^{23}Na , and ^{24}Mg are higher only at lower masses $m \leq 20 M_{\odot}$. For the 20 and $25 M_{\odot}$ stars, instead, this pattern is reversed, with the effect being strongest

TABLE 2.4
SNI YIELDS

	$13 M_{\odot}$	$15 M_{\odot}$	$18 M_{\odot}$	$20 M_{\odot}$	$25 M_{\odot}$	$40 M_{\odot}$
^{12}C	WW95	1.14(−1)	1.61(−1)	2.48(−1)	2.13(−1)	3.22(−1)
	TNH96	3.21(−2)	1.16(−1)	2.04(−1)	1.56(−1)	2.00(−1)
^{16}O	WW95	2.72(−1)	6.80(−1)	1.13	1.94	3.25
	TNH96	2.44(−1)	4.60(−1)	9.17(−1)	1.61	3.15
^{20}Ne	WW95	4.46(−2)	1.11(−1)	2.77(−1)	1.05(−1)	3.94(−1)
	TNH96	3.82(−2)	3.86(−2)	1.82(−1)	2.52(−1)	6.22(−1)
^{23}Na	WW95	1.08(−3)	3.42(−3)	9.99(−3)	1.53(−3)	1.08(−2)
	TNH96	1.05(−3)	5.20(−4)	7.68(−3)	1.62(−3)	1.87(−2)
^{24}Mg	WW95	1.64(−2)	2.67(−2)	5.52(−2)	3.13(−2)	1.06(−1)
	TNH96	1.42(−2)	3.73(−2)	4.29(−2)	1.54(−1)	1.68(−1)

NOTE.—SNI yields of the elements C, O, and the main C-burning products; comparison of WW95 (Z_{\odot} , model B) and TNH96. The numbers are given in units of M_{\odot} . The TNH96 numbers consist of the given yield from He-core evolution plus the initial abundance (solar) of the envelope (see text).

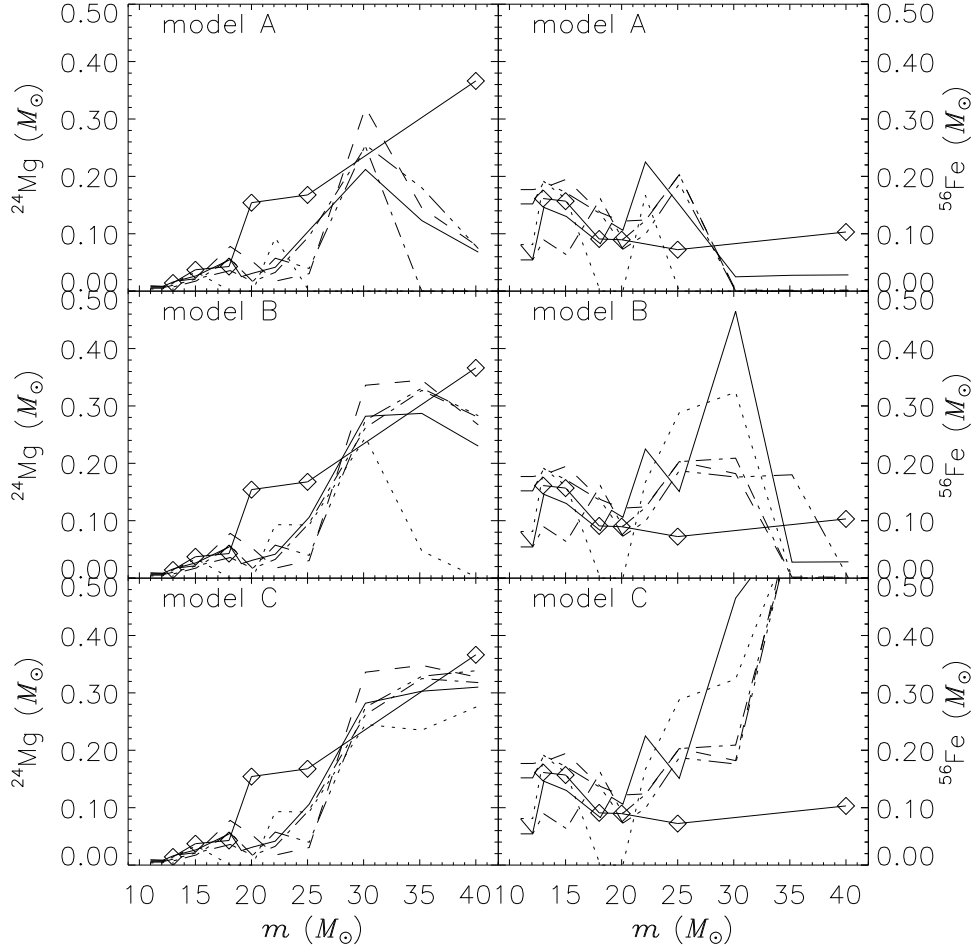


Figure 2.3: Magnesium yield (left panel) and iron yield (right panel) of SNII as a function of initial stellar mass (M_{\odot}). The middle and bottom panels show the results for enhanced explosion energy in high-mass stars in WW95. The yields include initial and newly synthesized material. The Mg and Fe-yields of the $70 M_{\odot}$ star according to TNH96 are $0.8 M_{\odot}$ and $0.1 M_{\odot}$, respectively.

for the Mg-yield at $25 M_{\odot}$. WW95 argue that the larger extent of the convective shells in the TNH96-models (Schwarzschild criterion) is responsible for this behavior. Note that the rather high Mg abundances observed in metal-poor stars in the Milky Way require high Mg-yields (see Chapter 3), which could be interpreted as an argument in favor of the Schwarzschild criterion for convection theory. The higher O-yields of WW95 result from the larger He-cores.

Due to re-implosion, the Mg-yields of WW95 saturate or even decline with increasing mass above $40 M_{\odot}$. It should be emphasized that this fallback effect is not present in the TNH96 yields, because they only model the nucleosynthesis during the explosion, but not the explosion itself.

The Fe-yield decreases with increasing mass for $m \leq 20 M_{\odot}$ (Fig. 2.3). As

TABLE 2.5
OBSERVATION VS. MODEL

m_* (M_\odot)	observation	WW95 (Z_\odot)	TNH96
14 ± 1	0.100 ± 0.02	$0.133 - 0.115$	$0.153 - 0.130$
20	0.075 ± 0.01	0.088	0.074

NOTE.—Observed ^{56}Ni (M_\odot) ejected in the SNII events SN1993J ($14 M_\odot$; Arnett et al. 1989) and SN1987A ($20 M_\odot$; Baron, Hauschildt, & Young 1995; Nomoto, Iwamoto, & Suzuki 1995) compared to the theoretical results by WW95 and TNH96. Both nucleosynthesis prescriptions are consistent with the observations.

shown in Table 2.5, both sets of models reproduce the observed ^{56}Ni ejected in the supernovae SN1993J ($14 M_\odot$; Baron, Hauschildt, & Young 1995; Nomoto, Iwamoto, & Suzuki 1995) and SN1987A ($20 M_\odot$; Arnett et al. 1989). At masses $m \geq 25 M_\odot$, instead, WW95 produce significantly more iron, particularly in model C. The Fe-yield seems to be highly uncertain.

The Mg/Fe ratio

In Fig. 2.4, the abundance ratios $[\text{Mg}/\text{Fe}]$ produced in WW95 (Z_\odot , broken lines) and TNH96 (solid line) are plotted as a function of initial stellar mass. The upper x-axis denotes the lifetime τ_m of the star with mass m (Schaller et al. 1992). TNH96 produce supersolar Mg/Fe ratios ($[\text{Mg}/\text{Fe}] > 0.5$) in stars with masses $m \geq 20 M_\odot$, WW95 (model B) only in stars with $m \geq 30 M_\odot$.

2.3 SSP-yields

In order to estimate the impact of the above uncertainties on chemical evolution, the SSP-yields Q_{SSP} of one simple stellar population as a function of the turnoff mass m_t for the elements Mg and Fe are calculated.

$$Q_{\text{SSP}}(m_t) = \int_{m_t}^{m_{\text{max}}} Q_{\text{Mg,Fe}} \phi(m) dm \quad (2.14)$$

Equation 2.14 is equivalent to the Equations 2.6 and 2.8 setting $\psi(t) = 1$. TNH96-yields are extrapolated to $11 M_\odot$, the contributions from stars with mass $8 - 11 M_\odot$ are neglected (see WW95). The enrichment from both Type II SNe and Type Ia SNe is taken into account. The fraction of close binary systems A (see Equation 2.8) is adopted from Chapter 3 (Section 3.2.3), in which $A = 0.035$ is calibrated on the supernova rates and the Fe abundances in the solar neighborhood. The upper mass cutoff is $m_{\text{max}} = 40 M_\odot$.

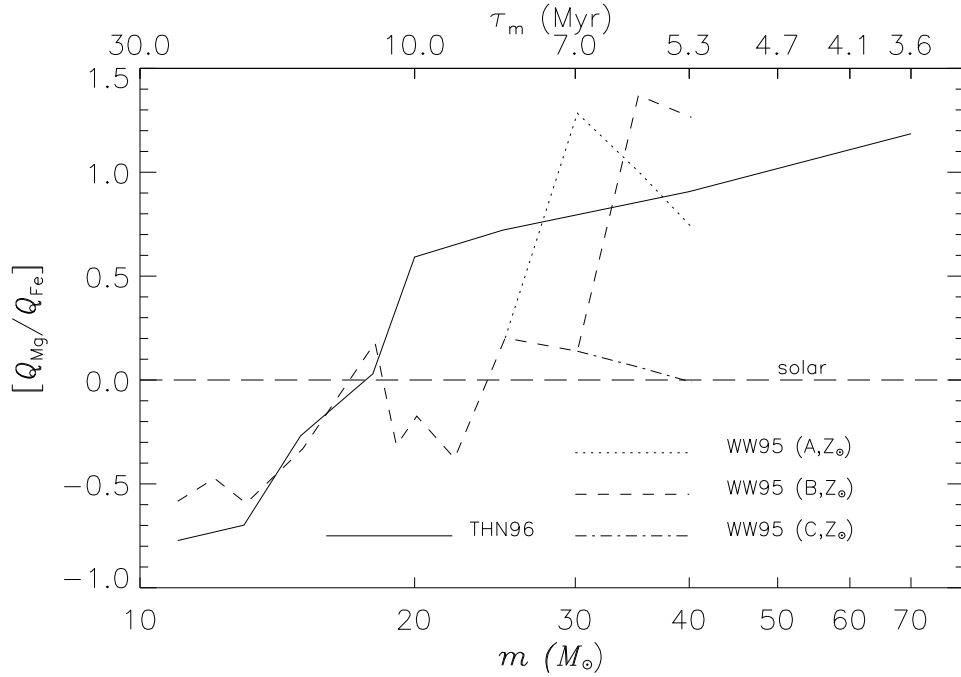


Figure 2.4: Abundance ratio $[\text{Mg}/\text{Fe}] = \log(\text{Mg}/\text{Fe}) - \log(\text{Mg}/\text{Fe})_{\odot}$ in the ejecta of SNII as a function of initial stellar mass. The WW95-models of solar initial metallicity are considered. The upper x-axis denotes the lifetime τ_m of the star with mass m (Schaller et al. 1992).

In Fig. 2.5, the SSP-yield $[\text{Mg}/\text{Fe}]$ is plotted as a function of the turnoff mass. The corresponding stellar lifetimes (Schaller et al. 1992) are given by the upper x-axis. The IMF slopes $x = 1.7$ (dotted lines), $x = 1.35$ (Salpeter, solid lines), $x = 1.0$ (dashed lines), and $x = 0.7$ (dash-dotted lines) are considered.

As long as the turnoff mass m_t is above the lowest limit for Type II supernovae ($m = 11 M_{\odot}$, $t = 24$ Myr), the Mg/Fe in the ejecta decreases with decreasing m_t , because smaller masses produce less Mg and more Fe (Fig. 2.3). Once the turnoff is below $11 M_{\odot}$, no further Mg and Fe are produced. Mg/Fe stays constant until SNIa start to eject new iron ($m_t \lesssim 5 M_{\odot}$ and $t \lesssim 0.1$ Gyr).

The Mg/Fe-ratios in WW95 nucleosynthesis are too low compared to the ones observed in the halo stars of the Milky Way ($[\text{Mg}/\text{Fe}] \approx 0.3$, see Chapter 3). Even taking only SNII into account, the $[\text{Mg}/\text{Fe}]$ of one SSP with Salpeter IMF is only $[\text{Mg}/\text{Fe}] = 0.05$ for WW95 (model B). In the extreme case of a flat IMF ($x = 0.7$), still the $[\text{Mg}/\text{Fe}]$ by WW95 remains too low (~ 0.1). The yields by TNH96, instead, provide a good match of the observations, with $[\text{Mg}/\text{Fe}] = 0.26$ for the Salpeter IMF, and $[\text{Mg}/\text{Fe}] = 0.36$ for the flat IMF.

Assuming the upper mass cutoff to be $m_{\text{max}} = 70 M_{\odot}$ instead of $40 M_{\odot}$, the $[\text{Mg}/\text{Fe}]$ in the SNII ejecta of one SSP with Salpeter IMF increases by 0.18 dex to 0.44, if TNH96 nucleosynthesis is adopted. This significant increase is due to the high Mg/Fe ratios in the ejecta of massive stars given by TNH96

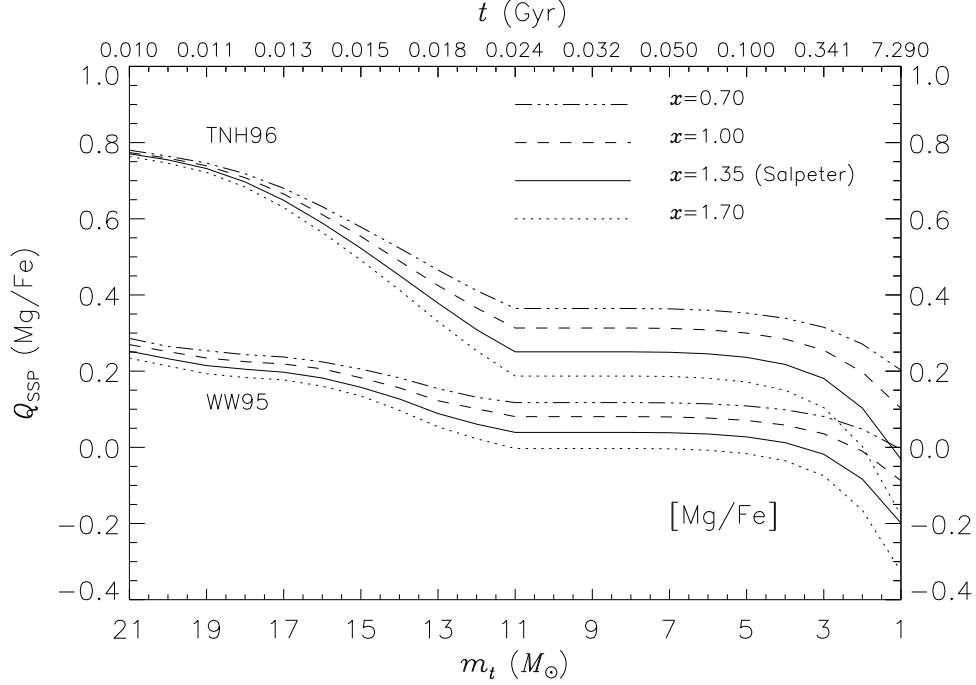


Figure 2.5: Abundance ratio Mg/Fe in the ejecta of one stellar population as a function of the turnoff mass m_t . The upper x-axis gives the lifetimes (in Gyr) of the masses. Q_{SSP} is defined in Equation 2.14. The upper mass cutoff is $m_{\text{max}} = 40 M_{\odot}$. The enrichment from both Type II SNe and Type Ia SNe is taken into account. The fraction $A = 0.035$ of binaries exploding as SNIa is determined in the chemical evolution model for the solar neighborhood in section 3.2.3. The linestyles refer to different IMF slopes x .

(Fig. 2.4). The same exercise for WW95 (model B), extrapolating the yields to $70 M_{\odot}$, raises $[\text{Mg}/\text{Fe}]$ by only 0.07 dex to $[\text{Mg}/\text{Fe}] = 0.12$. Note that the extrapolation leads to very low Mg/Fe-yields of massive stars, because of the fallback of envelope material (Fig. 2.3). It should be emphasized that TNH96 assume that all the synthesized Mg is ejected, so that it is not clear if the very high Mg/Fe yields predicted for massive stars are real. This issue remains a major source of uncertainty and certainly requires further investigations.

2.4 Summary

After briefly illustrating the main principles of chemical evolution, the two different nucleosynthesis calculations for Type II supernovae by WW95 and TNH96 are compared. The impact of uncertainties like the treatment of convection, the adopted $^{12}\text{C}(\alpha, \gamma)^{16}\text{O}$ -rate, and the prescription the explosion impact on the resulting stellar yields of the elements H, He, O, Mg, and Fe is discussed.

It turns out that the yields of oxygen and total metallicity are consistently predicted by WW95 and TNH96 over the whole mass range of SNI. Major

discrepancies, instead, are found in the Mg-yields for masses $18 \leq m \leq 25 M_{\odot}$. For a $20 M_{\odot}$ star, the Mg-yield of TNH96 is ~ 5 times higher than the Mg-yield of WW95. The Fe-yield is mainly uncertain in the upper mass range, while WW95 and TNH96 agree well at lower masses ($13 M_{\odot} \leq m \leq 20 M_{\odot}$) that are well constrained by the observed light curves of the Type II supernovae SN1987A and SN1991J. For high mass stars with $m \geq 25 M_{\odot}$, instead, WW95 models give significantly higher Fe-yields than TNH96. The [Mg/Fe] ratios in the ejecta of a simple stellar population with Salpeter IMF are 0.05 and 0.26 for WW95 and TNH96, respectively.

Chapter 3

The Milky Way

In the classical numerical models describing the chemical evolution of the solar neighborhood, the disk is assumed to form by accretion of primordial gas (e.g., Matteucci & Greggio 1986; Timmes, Woosley, & Weaver 1995; Pagel & Tautvaisiene 1995; Tsujimoto et al. 1995; Yoshii, Tsujimoto, & Nomoto 1996; Chiappini, Matteucci, & Gratton 1997; Portinari, Chiosi, & Bressan 1998). In such models the old, metal-poor halo stars, and the young, metal-rich disk stars are considered to belong to the same evolutionary sequence. This approach seems very rough, as halo stars and disk stars have very different angular momentum distributions (Wyse & Gilmore 1992; Ibata & Gilmore 1995). Furthermore, Nissen & Schuster (1997) and Gilmore & Wyse (1998) show that metal-rich ($[\text{Fe}/\text{H}] \approx -1$) halo stars have lower Mg/Fe than thick-disk stars of the same metallicity, which points towards two decoupled evolutionary paths of halo and disk. Analyzing high-quality spectra of F- and G-type stars in the halo and the disk, Fuhrmann (1998) even finds a dichotomy between the stellar populations of the thin and the thick disk. These results certainly require more detailed and more sophisticated models taking the different evolutionary paths of the various components as well as dynamical constraints into account.

Still, the classical simple-minded models are very successful at reproducing the main observational features of the solar neighborhood, in particular — if the delayed Type Ia supernovae enrichment is included — the evolution of α/Fe as a function of Fe/H (Matteucci & Greggio 1986). The aim of this chapter is to *calibrate* the present chemical evolution code on the solar neighborhood, and to analyze the impact of the different nucleosynthesis prescriptions discussed in Chapter 2. The content of this chapter is published in Thomas, Greggio, & Bender (1998).

3.1 The model parameters

The accretion timescale

The disk is assumed to form due to accretion of primordial gas. The infall rate $f(t)$ is (Timmes, Woosley, & Weaver 1995):

$$f(t) = [M_{\text{tot}}(t_{\text{now}}) - M_{\text{tot}}(t_0)] \times \frac{\exp(-t/\tau_{\text{disk}})}{\tau_{\text{disk}}[1 - \exp(-t_{\text{now}}/\tau_{\text{disk}})]} , \quad (3.1)$$

with $M_{\text{tot}}(t_{\text{now}} = 15 \text{ Gyr})$ and $M_{\text{tot}}(t_0 = 0 \text{ Gyr})$ being the surface densities ($M_{\odot} \text{pc}^{-2}$) of the total mass (stars+gas) today and at the beginning of the disk formation, respectively. The parameter τ_{disk} is the timescale of accretion.

The star formation efficiency

The star formation rate ψ is assumed to depend on the gas density of the interstellar medium (ISM) (Schmidt 1959; Schmidt 1963). The efficiency ν (Gyr^{-1}) of star formation and the so-called Schmidt-exponent k are free parameters.

$$\psi(t) = \nu M_{\text{tot}} \left[\frac{M_g(t)}{M_{\text{tot}}(t)} \right]^k \quad (3.2)$$

Type Ia supernova

The description of the SNIa rate is adopted from Greggio & Renzini (1983). The fraction A of close binary systems (see Chapter 2, Equations 2.10 and 2.11) is a free parameter, that has to be calibrated on the current supernova rates and on the Fe abundance in our Galaxy.

Type II supernova

As shown in the previous chapter, the yields of SNII are affected by many uncertainties. Hence, they are treated as a parameter in the sense that both nucleosynthesis prescriptions discussed in Chapter 2 (WW95 and TNH96) are considered.

Initial mass function

The IMF is a crucial parameter in chemical evolution. In the case of the solar neighborhood, it should not deviate much from the observationally determined Salpeter-shape (Salpeter 1955).

3.2 Observational constraints

The above parameters are constrained by different observational features. These are: the gas infall rate and the current gas fraction (Section 3.2.1), the abundance distribution function (ADF, Section 3.2.2), the current supernova rates (Section 3.2.3), the age-metallicity relation (AMR, Section 3.2.4), and the element abundances in the stars (Section 3.2.5). The parameters are adjusted

to provide the best possible simultaneous fit to these observational constraints. These and the values adopted for each parameter are summarized in Table 3.1.

TABLE 3.1
PARAMETER CONSTRAINTS

Parameter	Observational Constraint	Adopted
Accretion timescale τ_{disk}	Current infall rate ADF	4 Gyr
Star formation efficiency ν	Current gas fraction	1.3 Gyr^{-1}
Schmidt exponent k	ADF	2
Close binary fraction A	$N_{\text{SNII}}/N_{\text{SNIa}}$ AMR	0.035
Stellar yields	Element abundances	TNH96
IMF slope x	Element abundances	1.36

NOTE.—The parameters are chosen to match simultaneously the observational constraints: ADF, AMR, supernova rates, element abundances, current infall rate, and current fraction of gaseous mass. The second column shows the main observational constraints on the respective parameter. The third column gives the final adopted values.

First, the calculations are performed using the stellar yields of TNH96. Then additional computations are made under the same conditions but using WW95 nucleosynthesis. The present age of the Galaxy is assumed to be $t_{\text{now}} = 15 \text{ Gyr}$, the age of the Sun is 4.5 Gyr. Stellar lifetimes are taken from Schaller et al. (1992).

3.2.1 Current infall rate and gas fraction

The current infall rate is estimated from observations of high velocity HI clouds to be $0.2 - 1.0 M_{\odot} \text{pc}^{-2} \text{Gyr}^{-1}$ (Bothun 1985; Magain 1989; Muller, Oort, & Raimond 1963; Oort 1970; Tosi 1988; Wakker 1991; Wakker & Schwarz 1991; Wakker & van Woerden 1991). With the present-day surface density being $M_{\text{tot}}(t_0) \approx 77 M_{\odot} \text{pc}^{-2}$ (Kuijken & Gilmore 1989a; Kuijken & Gilmore 1989b; Kuijken & Gilmore 1989c; Statler 1989; Gould 1990; Kuijken & Gilmore 1991), the accretion timescale in Equation 3.1 is then $\tau_{\text{disk}} \approx 3 - 5.5 \text{ Gyr}$. A further confinement of τ_{disk} by means of the abundance distribution function (ADF) is discussed in the next section. The current fraction of gas $M_g/M_{\text{tot}}(t_{\text{now}})$ is 0.10 ± 0.03 (Rana & Basu 1992), which is well reproduced with a star formation efficiency of $\nu = 1.3 \text{ Gyr}^{-1}$ (see also Table 3.2, p. 36).

3.2.2 Abundance Distribution Function

The differential ADF is the number of stars that are born per unit metallicity as a function of metallicity. Pagel & Patchett (1975) derived this relation for a sample of 132 G-dwarfs in the solar vicinity (~ 25 pc). The most important feature of the ADF is the paucity of extremely metal-poor stars. The so-called *Simple Model*, assuming a closed box for the chemical evolution, predicts too many metal-poor stars (van den Bergh 1962; Schmidt 1963; Tinsley 1980), which is known as the G-dwarf problem. Possible solutions are the consideration of pre-enrichment (Truran & Cameron 1971) or infall of primordial gas (Larson 1972). In the former case, it is assumed that the first stellar generations do not form out of primordial, but previously enriched gas. But also the latter option leads to the formation of less metal-poor stars for the following reason: The gas surface density is assumed to be very low in the beginning, so that

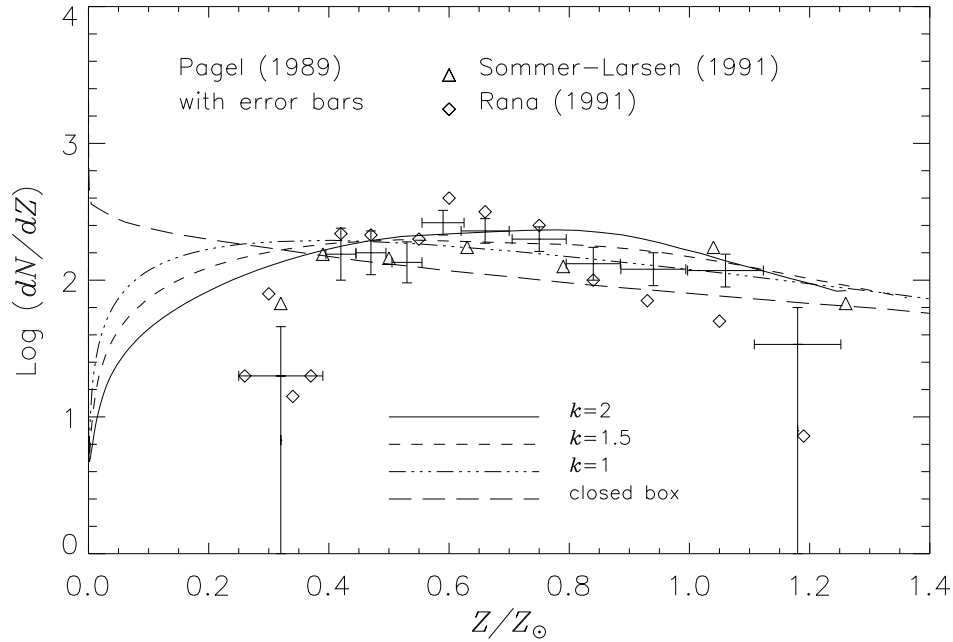


Figure 3.1: The abundance distribution function (ADF) giving the number of stars that are born per unit metallicity $\log(dN/dZ)$ as a function of metallicity. The observational data points with error bars refer to the reanalysis of the Pagel & Patchett (1975) data by Pagel (1989), taking the metallicity-excess calibration of Cameron (1985) into account. Additional re-interpretations of the data set by Rana (1991) and Sommer-Larsen (1991) include corrections for the increase of the velocity dispersion with time and the correction for the vertical height distribution of dwarfs. The solid, dashed, and dash-dotted lines are models with the Schmidt-exponents $k = 2, 1.5, 1$, respectively. The accretion timescale is $\tau_{\text{disk}} = 4$ Gyr. The long-dashed line shows the calculated ADF for a closed box model without infall.

the first stellar generations very efficiently enrich the ISM. As a consequence, high metallicities are built up very quickly, and only a small number of very metal-poor stars form. Subsequent infall of (primordial) gas then leads to higher gas densities and the formation of subsequent, metal-rich stellar populations. As the infall of primordial gas additionally dilutes the ISM abundances, the metallicity at which the largest number of stars form is higher the more the infall is delayed. In the present model, this delay is controlled by the timescale τ_{disk} of accretion of primordial gas (see Equation 3.1).

The shape of the resulting theoretical ADF therefore mainly depends on the accretion timescale τ_{disk} and the exponent k of the Schmidt-law (Matteucci & François 1989). In Fig. 3.1 the ADF is plotted for different choices of the parameter k and $\tau_{\text{disk}} = 4$ Gyr. Fig. 3.1 shows that the inclusion of infall solves the G-dwarf problem in the sense that the extremely high amount of metal-poor stars ($Z < 0.2 Z_{\odot}$) predicted by the closed-box model (long-dashed line) is significantly decreased. The general shape of the ADF with a peak at intermediate metallicities ($Z \approx 0.6 Z_{\odot}$) is reproduced by the model. The smaller the exponent k is, the more stars of high and low metallicity are formed. Since the ADF predicted by the model is already too flat, $k = 2$ is the best choice.

A better fit to the ADF-data requires an improvement of the adopted model, which exceeds the scope of this work. In general, as the model predicts a too large number of both metal-poor ($Z < 0.3 Z_{\odot}$) and metal-rich ($Z \gtrsim 1.2 Z_{\odot}$) stars, a different description of the infall-term may be necessary. In addition, the consideration of pre-enrichment of the infalling gas would further reduce the number of low metallicity stars.

3.2.3 Supernova rates

In Fig. 3.2, the predicted rates of SNIa (solid line) and SNII (dashed line) are plotted versus time t . The dotted line is the star formation rate ψ . Note that only the supernova rates *today* are constrained observationally. The predicted today's surface density $N_{\text{SNII}} \approx 0.01 \text{ pc}^{-2} \text{ Gyr}^{-1}$ is a factor 2 lower than the observational estimate of Tammann (1982), that is based on historical data. However, because of the small size of that sample, this value is very uncertain. It is likely that the historical data significantly overestimate the absolute number of SNII (van den Bergh & Tammann 1991), so that the calculated SNII rate is still consistent with Tammann (1982).

Also the relative frequency of SNII and SNIa is not well determined observationally. Van den Bergh & Tammann (1991) find $N_{\text{SNII}}/N_{\text{SNIa}} \approx 2.7$ for Sab–Sb galaxies and $N_{\text{SNII}}/N_{\text{SNIa}} \approx 8$ for Sc–Scd galaxies. Assuming that our Galaxy has a Hubble type between Sb and Sc (van den Bergh & Tammann 1991), the predicted relative frequency of $N_{\text{SNII}}/N_{\text{SNIa}} \approx 5$ is in agreement with the above numbers for $A = 0.035$.

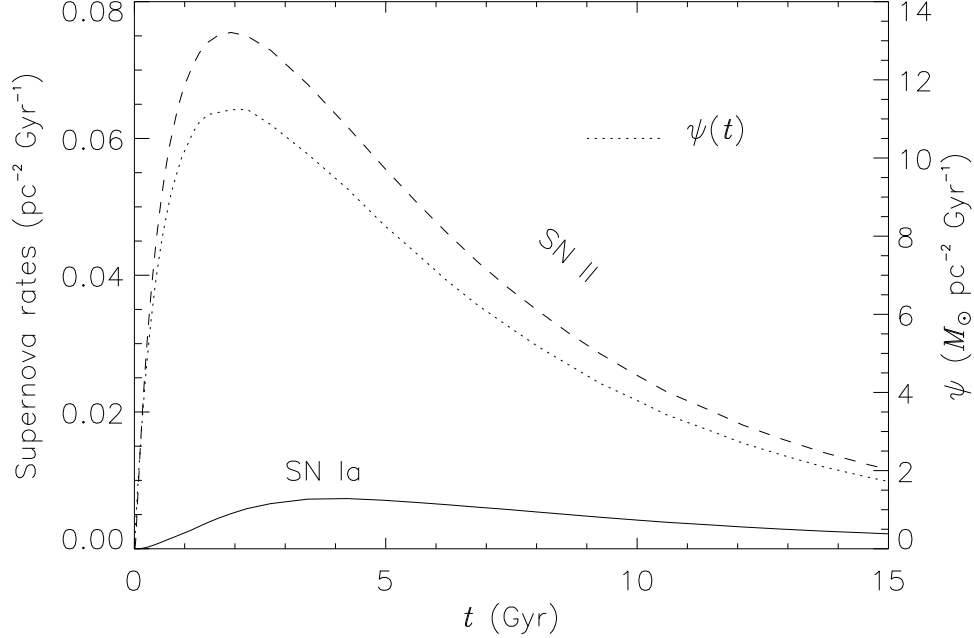


Figure 3.2: Supernova rates as a function of time t . The solid and the dashed lines are the predicted SNIa and SNII rates, respectively. The dotted line is the star formation rate ψ (scale at the right y-axis).

3.2.4 Age-Metallicity Relation

Metal-rich stars in the solar neighborhood tend to be younger than the more metal-poor ones, which is the so-called age-metallicity relation (AMR). Since the element abundances in the ISM at time t are locked in stars of age $(t_{\text{now}} - t)$, the AMR reflects the evolution of $[\text{Fe}/\text{H}]$ in the ISM as a function of time.

In Fig. 3.3, $[\text{Fe}/\text{H}]$ is plotted versus the evolutionary time $t = t_{\text{now}} - \text{age}$ for the data of Twarog (1980) (diamonds), Carlberg et al. (1985) (triangles), Meusinger, Reimann, & Stecklum (1991) (squares), and Edvardsson et al. (1993) (crosses). The solid and the dashed lines are the model predictions using TNH96 and WW95 (model B) nucleosynthesis, respectively. The dotted line is the predicted star formation rate ψ .

In the first few Gyrs, the metallicity rapidly increases with increasing ψ to $[\text{Fe}/\text{H}] \sim -0.5$. After the maximum in the star formation rate at 2 Gyr, the further increase in $[\text{Fe}/\text{H}]$ becomes more shallow, reaching solar metallicity at $t \approx 10$ Gyr. This pattern is very well reproduced by the models. WW95 nucleosynthesis (dashed line) leads to higher $[\text{Fe}/\text{H}]$ than TNH96 by ~ 0.1 dex, owing to the larger Fe-yields of WW95 (Chapter 2). The models without SNIa enrichment (lower curves) clearly fail to reproduce the observed iron abundances. This effect is less pronounced for the WW95-models, again because of the larger SNII-Fe-yields. In this case, 50 per cent of the solar Fe abundance comes from SNIa, while TNH96 require a 60 per cent contribution. The predicted total

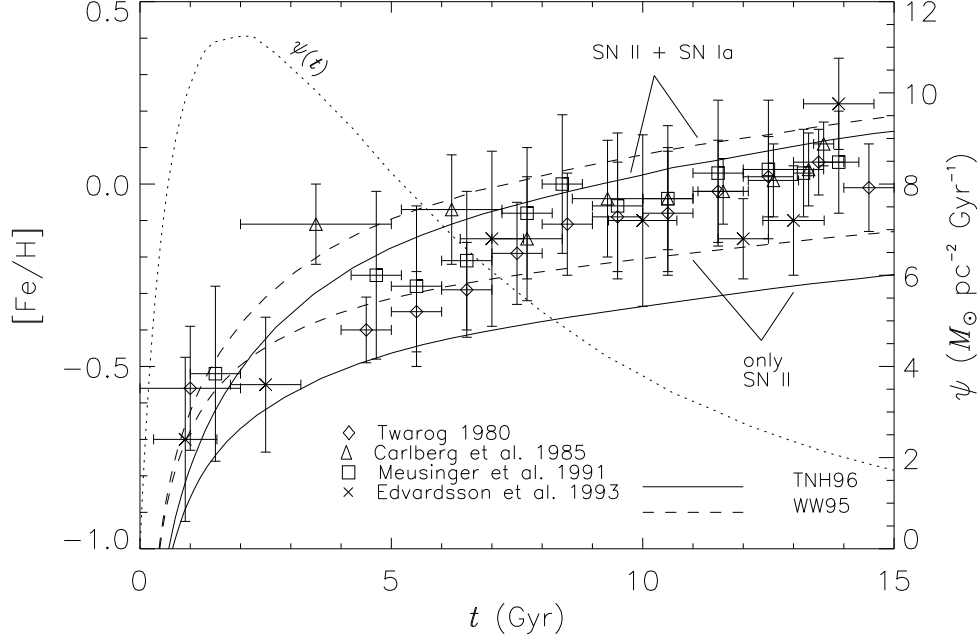


Figure 3.3: $[\text{Fe}/\text{H}]$ as a function of the evolutionary time $t = t_{\text{now}} - \text{age}$. Twarog (1980) (diamonds) determined age and metallicity for two samples of 1007 and 2742 local disk stars, respectively. Carlberg et al. (1985) (triangles) and Meusinger, Reimann, & Stecklum (1991) (squares) reanalysed these data using new isochrones from Vandenberg (1985). Edvardsson et al. (1993) (crosses) derived abundances for 189 F and G disk dwarfs. The error bars are determined from the spread of several stars of given age and metallicity. The solid and the dashed lines are the model predictions using TNH96 and WW95 (model B) nucleosynthesis, respectively. The lower curves show the result without the enrichment from SNIa. The dotted line is the predicted star formation rate ($M_{\odot} \text{pc}^{-2} \text{Gyr}^{-1}$, scale on the right y-axis).

iron abundance crucially depends on the fraction of close binary systems (here $A = 0.035$). A lower value would be still consistent with the observed AMR, but is in conflict with the relative frequencies of Type II and Type Ia supernovae discussed in the previous section.

3.2.5 Element abundances

$[\text{O}/\text{Fe}]$ vs. $[\text{Fe}/\text{H}]$

In the top panel of Fig. 3.4, the abundance ratios $[\text{O}/\text{Fe}]$ of metal-poor halo stars and metal-rich ($[\text{Fe}/\text{H}] \geq -1$) disk stars are plotted versus their metallicities $[\text{Fe}/\text{H}]$. The data are from Gratton & Ortolani (1986, diamonds), Bessell, Sutherland, & Ruan (1991, squares), Nissen et al. (1994, crosses), and Edvardsson et al. (1993, star-symbols). The scatter of O/Fe in the halo stars is very

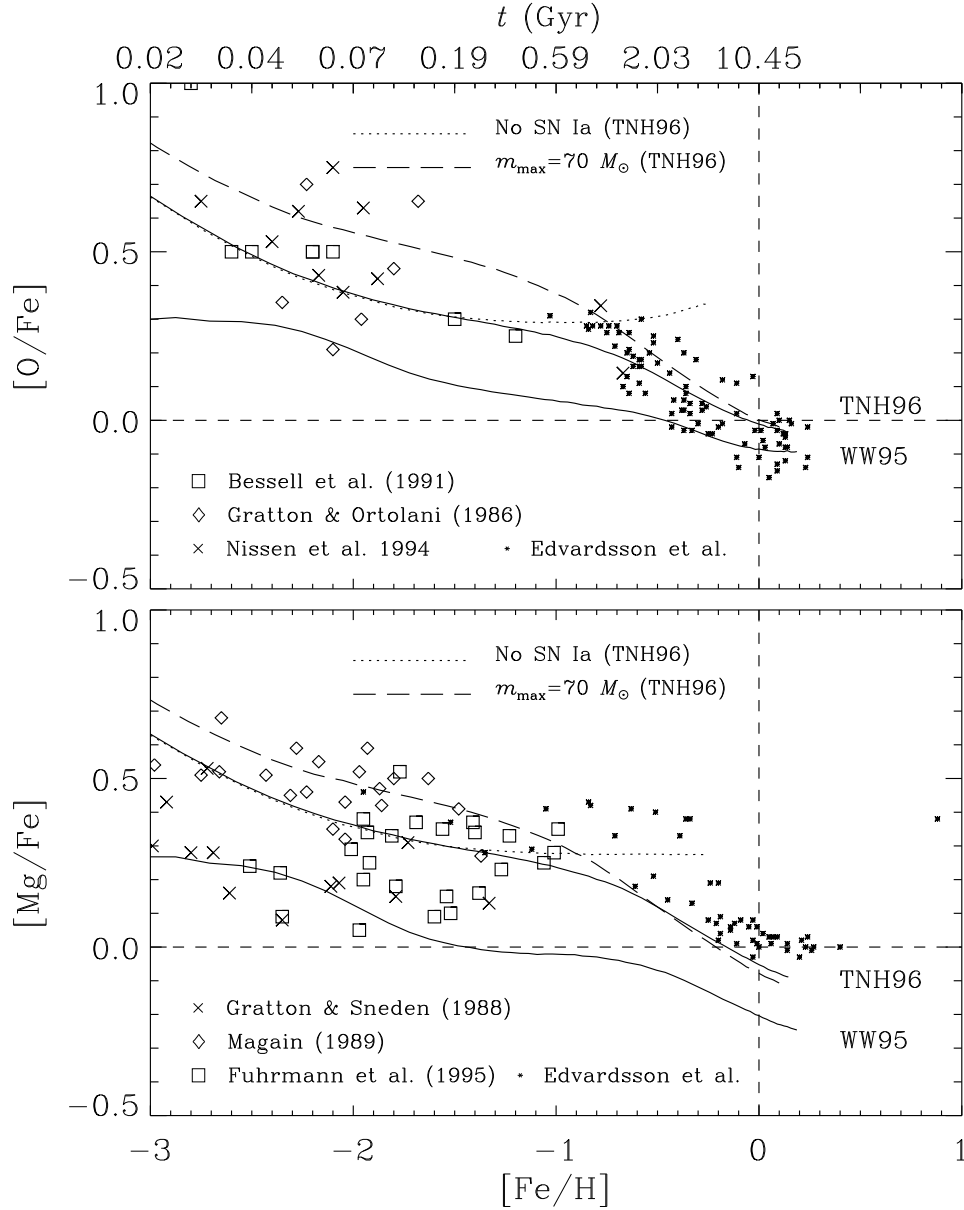


Figure 3.4: *Top panel:* $[\text{O}/\text{Fe}]$ as a function of $[\text{Fe}/\text{H}]$. The data are from Gratton & Ortolani (1986, diamonds), Bessell, Sutherland, & Ruan (1991, squares), Nissen et al. (1994, crosses), and Edvardsson et al. (1993, stars). *Bottom panel:* $[\text{Mg}/\text{Fe}]$ as a function of $[\text{Fe}/\text{H}]$. The data are from Gratton & Sneden (1988, crosses), Magain (1989, diamonds), Fuhrmann, Axer, & Gehren (1995, squares), and Edvardsson et al. (1993, star-symbols). The two solid lines show the models using TNH96 (upper curve) and WW95 (model B), respectively. The dotted lines are the results without SNIa. The dashed lines are simulations with TNH96 for $m_{\text{max}} = 70 M_{\odot}$ and $A = 0.06$. The upper x-axis gives t from the AMR for the TNH96 model (solid line).

large, and may be partly due to inhomogeneous mixing processes (Tsujimoto, Shigeyama, & Yoshii 1999), partly due to observational errors. A mean value of $0.6 \geq [\text{O}/\text{Fe}] \geq 0.3$ in the metallicity range $-3 \leq [\text{Fe}/\text{H}] \leq -1$ seems a reasonable estimate. The $[\text{O}/\text{Fe}]$ ratios in the disk stars are better constrained (Edvardsson et al. 1993).

The most important feature in Fig. 3.4 is the change of slope in the decrease of O/Fe with increasing Fe/H at $[\text{Fe}/\text{H}] \approx -1$ from $\Delta[\text{O}/\text{Fe}]/\Delta[\text{Fe}/\text{H}] \approx -0.15$ to $\Delta[\text{O}/\text{Fe}]/\Delta[\text{Fe}/\text{H}] \approx -0.3$, which comes from the fact that the decrease of O/Fe with increasing Fe/H has different origins at low and at high metallicities. At very early times $t < 30$ Myr and low $[\text{Fe}/\text{H}]$, when the turnoff mass is $m_t > 10 M_\odot$, the α/Fe (i.e. O/Fe or Mg/Fe) ejected from a simple stellar population through SNII still decreases with decreasing m_t as illustrated in Chapter 2 (Section 2.3). The decrease at times later than ~ 1 Gyr can only be understood with the additional delayed Fe-enrichment, most likely from SNIa. This pattern is well reproduced with the present model (TNH96, upper solid line). If, instead, the contribution from SNIa is neglected (dotted line), $[\text{O}/\text{Fe}]$ remains super-solar for all metallicities, and even increases with increasing metallicity due to the additional O-enrichment from intermediate-mass stars (Renzini & Voli 1981).

The dashed line shows that with the larger mass cutoff $m_{\text{max}} = 70 M_\odot$, higher O/Fe ratios in the metal-poor stars are obtained. In this model, the close binary fraction is increased to $A = 0.06$, in order to produce solar O/Fe at $[\text{Fe}/\text{H}] = 0$.

The model using WW95 (model B, lower solid line) fails to reproduce the O/Fe ratios observed, because of the high Fe-yields in WW95 (see Chapter 2).

$[\text{Mg}/\text{Fe}]$ vs. $[\text{Fe}/\text{H}]$

In the bottom panel of Fig. 3.4, the abundance ratios $[\text{Mg}/\text{Fe}]$ are plotted versus $[\text{Fe}/\text{H}]$. The data are from Gratton & Sneden (1988, crosses), Magain (1989, diamonds), Fuhrmann, Axer, & Gehren (1995, squares), and Edvardsson et al. (1993, star-symbols). Similarly to O/Fe , the scatter of Mg/Fe in the halo stars is very large most likely due to observational errors. The large scatter of Mg/Fe in the disk stars of the Edvardsson et al. (1993) data, and the rather high Mg/Fe in the most metal-rich stars are very likely observational artifacts. Note that in the Edvardsson et al. (1993) data $[\text{Mg}/\text{Fe}]$ is systematically higher than $[\text{O}/\text{Fe}]$ by ~ 0.2 dex. Indeed, Fuhrmann (1998, 2000) analyzed high-quality spectra of stars from the Edvardsson et al. (1993) sample and finds both a lower scatter and lower Mg/Fe ratios.

Adopting TNH96, the predicted $[\text{Mg}/\text{Fe}]$ is very similar to $[\text{O}/\text{Fe}]$, the average Mg/Fe ratios of the halo stars are again well reproduced (upper solid line). The $[\text{Mg}/\text{Fe}]$ of the disk stars are not matched, mainly because of the ~ 0.2 dex higher $[\text{Mg}/\text{Fe}]$ in the Edvardsson et al. (1993) data as discussed above. The $[\text{Mg}/\text{Fe}]$ predicted by the model is lower than the predicted $[\text{O}/\text{Fe}]$ by 0.05 dex, because of the additional contribution to the O-enrichment from intermediate-mass stars. As the model is normalized such that solar O abundance is reproduced, the predicted solar Mg abundance is slightly too low. As

there is no contributor to the enrichment of Mg besides SNII, the model without SNIa saturates to the SNII-SSP-yield (see Section 2.3) at high metallicities (dotted line).

Note that the models with WW95-yields lead to lower $[\text{Mg}/\text{Fe}]$ than $[\text{O}/\text{Fe}]$, which reinforces the conclusion of the previous chapter, that WW95 underestimate the Mg-yield of SNII.

Fuhrmann (1998) shows that — for metallicities $-1 \lesssim [\text{Fe}/\text{H}] \lesssim -0.5$ — stars of similar metallicity but with significantly different $[\text{Mg}/\text{Fe}]$ ratios belong to two different components of the Galaxy, namely the *thick* (high Mg/Fe) and the *thin* disk (low Mg/Fe). This implies that the stellar populations in the thick disk have formed decoupled from the thin disk and on much shorter timescales. This scenario is consistent with the results shown in Fig. 3.4, as the stars with the highest α/Fe ratios are reproduced by the models, in which the Fe-enrichment from SNIa is ‘switched off’ (dotted lines).

Solar element abundances

The predicted solar element abundances, which are the abundances in the ISM at $t = 10.45$ Gyr, are given in Table 3.2. Using TNH96, the solar O abundance is slightly overestimated by 3 per cent, while the solar Mg abundance is underestimated by 7 per cent. This inconsistency between O and Mg implies that either SNII produce more Mg or additionally intermediate-mass stars have to eject small amounts of Mg (see also Timmes, Woosley, & Weaver 1995). The solar Mg abundance with WW95 is too low mainly because of the low SNII-yield.

TABLE 3.2
SOLAR ELEMENT ABUNDANCES

	TNH96	WW95	Observation
$M_g/M_{\text{tot}}(t_{\text{now}})$	0.13	0.13	0.10 ± 0.03
$f(t_{\text{now}})$	0.46	0.46	$0.2 - 1.0$
Solar Z	$1.96(-2)$	$1.86(-2)$	$1.88(-2)$
Solar ^1H	$6.96(-1)$	$6.89(-1)$	$7.06(-1)$
Solar ^{16}O	$9.92(-3)$	$9.36(-3)$	$9.59(-3)$
Solar ^{24}Mg	$4.80(-4)$	$3.68(-4)$	$5.15(-4)$
Solar ^{56}Fe	$1.26(-3)$	$1.41(-3)$	$1.17(-3)$

NOTE.—The observed solar abundances are taken from Anders & Grevesse (1989), meteoritic values.

3.3 Delayed mixing

In the above simulations it is assumed that the stellar ejecta mix instantaneously with the ISM. The validity of this assumption depends on the timescale of the mixing process. Malinie et al. (1993) claim that due to chemical inhomogeneities in the disk, re-mixing and star formation may be delayed by 10^{8-9} yr. In this section, the delayed mixing is included in the models, and the impact on the results for different mixing timescales is discussed.

3.3.1 The two gas phases

Two different phases of the gas component are considered: the *active* and the *inactive* phase. The *inactive* gas consists of the enriched stellar ejecta. Since this component is hot and not homogeneously distributed, stars cannot form out of this phase. The *active* phase, instead, is assumed to be cool and well mixed, hence, star formation is possible only in the *active* gas phase. It is assumed that the *inactive* phase converts to the *active* star forming phase on a certain timescale, which includes both the *cooling* and the *mixing* process. The timescale is treated as a free parameter in the simulations.

For this purpose, the Equations 2.3 and 2.7 presented in Section 2.1 are changed in the following way:

$$dM_g^{\text{inactive}}/dt = E - \frac{1}{\tau_{\text{mix}}} M_g^{\text{inactive}} \quad (3.3)$$

$$dM_g^{\text{active}}/dt = -\psi + f + \frac{1}{\tau_{\text{mix}}} M_g^{\text{inactive}} \quad (3.4)$$

To keep the equations as simple as possible, the mass flow between the two gas phases is assumed to be proportional to the total amount of *inactive* gas divided by the mixing timescale. The abundance in the *active* and the abundance in the *inactive* gas phases will be different.

$$M_g^{\text{inactive}} dX_i^{\text{inactive}}/dt = E_i - X_i^{\text{inactive}} E \quad (3.5)$$

$$M_g^{\text{active}} dX_i^{\text{active}}/dt = (X_i^{\text{inactive}} - X_i^{\text{active}}) \frac{1}{\tau_{\text{mix}}} M_g^{\text{inactive}} + (X_{i,f} - X_i^{\text{active}}) f \quad (3.6)$$

The star formation rate described by the Schmidt-law is dependent only on the density of the *active* gas:

$$\psi = \nu M_{\text{tot}} \left[\frac{M_g^{\text{active}}}{M_{\text{tot}}} \right]^k \quad (3.7)$$

The infalling material is assumed to mix instantaneously with the *active* gas.

3.3.2 Element abundances

Table 3.3 gives the element abundances in both gas phases at $t = 10.45$ Gyr for the mixing timescales 0.01, 0.1, and 1 Gyr. The solar abundances are

TABLE 3.3
DELAYED MIXING

τ_{mix}	0.01 Gyr	0.1 Gyr	1 Gyr
$M_g^{\text{active}}/M_{\text{tot}}(t_{\text{now}})$	1.30(−1)	1.30(−1)	1.35(−1)
$M_g^{\text{inactive}}/M_{\text{tot}}(t_{\text{now}})$	6.55(−5)	6.70(−4)	8.38(−3)
Z^{active}	1.88(−2)	1.91(−2)	2.08(−2)
Z^{inactive}	5.70(−2)	5.73(−2)	5.85(−2)
H^{active}	6.98(−1)	6.97(−1)	6.92(−1)
H^{inactive}	5.70(−1)	5.70(−1)	5.67(−1)
O^{active}	9.43(−3)	9.58(−3)	1.05(−2)
O^{inactive}	2.86(−2)	2.88(−2)	2.96(−2)
Mg^{active}	4.57(−4)	4.64(−4)	5.17(−4)
Mg^{inactive}	1.34(−3)	1.35(−3)	1.41(−3)
Fe^{active}	1.23(−3)	1.25(−3)	1.32(−3)
Fe^{inactive}	3.93(−3)	3.93(−3)	3.87(−3)

NOTE.—Abundances in the two different gas phases for various mixing timescales. Stellar yields are taken from TNH96. The gas fractions give the fractions of *active* and *inactive* gas to the total mass at $t = 15$ Gyr. The abundances in the *inactive* gas are systematically higher.

reproduced in the *active* gas phase, while the abundances in the *inactive* gas (except H) are systematically higher.

Fig. 3.5 shows models (TNH96 yields) for the mixing timescales $\tau_{\text{mix}} = 0$ (solid line), 0.01 (dash-dotted line), 0.1 (short-dashed line), and 1 Gyr (dotted line) in the $[Mg/Fe]$ - $[Fe/H]$ diagram. Predominantly the very early chemical evolution is affected by the delay in the mixing. The larger τ_{mix} is, the lower are the Mg/Fe ratios in stars with metallicities $[Fe/H] < -2$. The models predict that the slope $\Delta[Mg/Fe]/\Delta[Fe/H]$ decreases from ≈ -0.2 to ≈ 0 with increasing mixing timescale in the range $\tau_{\text{mix}} = 0 - 1$ Gyr. The scatter in the data is too large, however, to distinguish between these cases.

Rebolo, Israelian, & García López (1999) derived the oxygen abundances in a sample of 23 metal-poor ($-3.0 \leq [Fe/H] \leq -0.3$) disk-stars, and find that the $[O/Fe]$ ratio is steeply increasing from 0.6–1.0 for $[Fe/H]$ decreasing from -1.5 to -3 . These data are in good agreement with the model predictions (TNH96, $m_{\text{max}} = 70 M_{\odot}$) in Fig. 3.4 (dashed line) in which instantaneous mixing is assumed. This result implies mixing timescales $\tau_{\text{mix}} \ll 10^8$ yr.

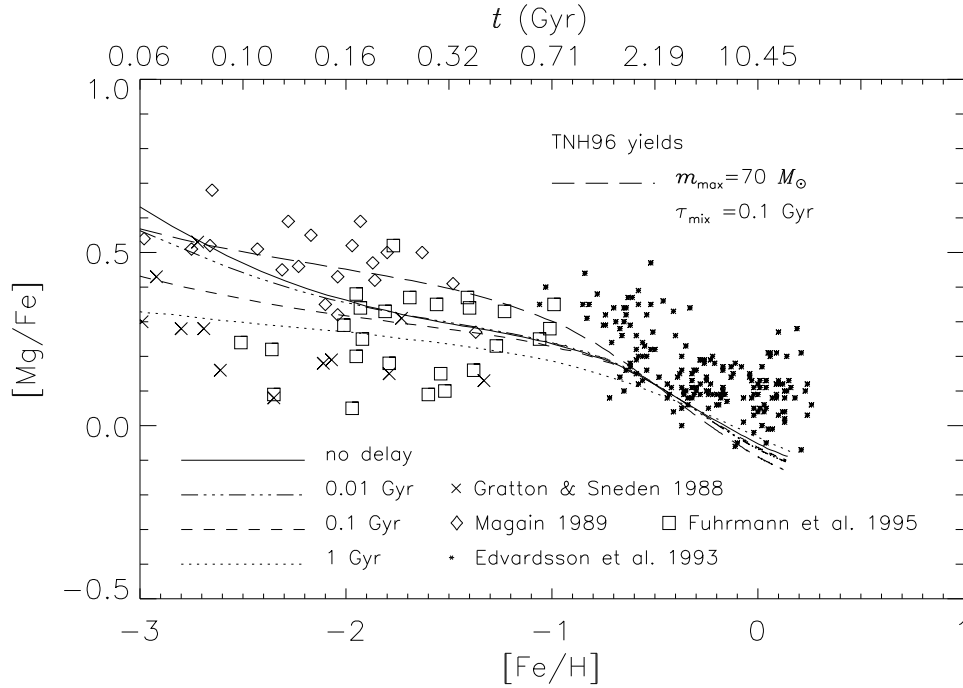


Figure 3.5: $[\text{Mg}/\text{Fe}]$ as a function of $[\text{Fe}/\text{H}]$. For a detailed description see caption of Fig. 3.4. Models for the mixing timescales $\tau_{\text{mix}} = 0, 0.01, 0.1, 1$ Gyr are shown as solid, dash-dotted, short-dashed, and dotted lines, respectively. The long-dashed line is the model with $\tau_{\text{mix}} = 0.1$ Gyr and $m_{\text{max}} = 70 M_{\odot}$. TNH96-yields are adopted in all models. The timescale on the upper x-axis refers to $\tau_{\text{mix}} = 0.1$ Gyr.

3.4 Summary

The main purpose of this chapter is the calibration of the chemical evolution code on observational features of the solar neighborhood. Applying the standard infall-model, the current infall rate and gas fraction, the abundance distribution function, the present-day rates of SNII and SNIa, the age-metallicity relation, and the abundance ratios $[\text{O}/\text{Fe}]$ and $[\text{Mg}/\text{Fe}]$ as function of $[\text{Fe}/\text{H}]$ are well reproduced with TNH96 nucleosynthesis. As already discussed in Chapter 2, WW95 nucleosynthesis, instead, predicts too low O/Fe and particularly too low Mg/Fe ratios to explain the abundance ratios in the metal-poor halo stars. The steep decline of $[\text{O}/\text{Fe}]$ and $[\text{Mg}/\text{Fe}]$ with increasing $[\text{Fe}/\text{H}]$ in the metal-rich disk stars ($[\text{Fe}/\text{H}] \geq -1$) are matched with the delayed Fe-enrichment from SNIa following the prescription of Greggio & Renzini (1983) and assuming a close binary fraction of $A = 0.035$.

In addition to this, the relaxation of the instantaneous *mixing* approximation for the chemical evolution in the solar neighborhood is explored. For this purpose, the basic equations of chemical evolution have been modified by separating the gaseous component into an active and an inactive phase, such that the stellar ejecta enter the inactive phase, while stars form out of the active gas

component. The two components are assumed to mix on timescales from 10^7 to 10^9 yr. A delay in the mixing between 0.1 and 1 Gyr lowers the $[\alpha/\text{Fe}]$ in the most metal-poor halo stars considerably, so that $[\alpha/\text{Fe}]$ stays constant for the metallicities $-3 \leq [\text{Fe}/\text{H}] \leq -1$. The steep rise of $[\text{O}/\text{Fe}]$ with decreasing $[\text{Fe}/\text{H}]$ between $-3 \leq [\text{Fe}/\text{H}] \leq -0.3$ recently found by Rebolo, Israelian, & García López (1999) implies then that mixing timescales must be of the order 10^7 yr and below.

Chapter 4

Elliptical Galaxies

As illustrated in Chapter 1, the stellar populations of luminous elliptical galaxies have super-solar α/Fe ratios. Possible explanations for this enhancement of α -elements are (e.g. Faber, Worthey, & González 1992): (1) short star formation timescales, (2) an initial mass function (IMF) that is biased towards massive stars, (3) selective mass loss, such that SNIa products are lost more efficiently, (4) a smaller fraction of close binaries, that are the origin of Type Ia supernovae. Option (3) seems unpalatable, as there is no physical mechanism known that leads preferentially to the loss of SNIa products. Also option (4) is an ad hoc assumption without real justification. Nova rates and LMXB populations observed in early-type galaxies indicate that such galaxies do not contain less binary stars than later types (Davies 1996). Options (1) and (2) have been investigated numerically by several authors (e.g., Matteucci 1994; Tantalo et al. 1996; Vazdekis et al. 1997; Gibson & Matteucci 1997; Chiosi et al. 1998) in the framework of single collapse models. These works tend to favor the flat IMF option for elliptical galaxies.

In this chapter, options (1) and (2) are explored for different formation scenarios for ellipticals in the framework of hierarchical galaxy formation, namely a fast clumpy collapse and the merger of two spiral galaxies. The content of this chapter is published in Thomas, Greggio, & Bender (1999).

4.1 Merging Spirals vs. Clumpy Collapse

There are several indications that merging must play an important role in galaxy formation. Approximately 50 per cent of luminous ellipticals host kinematically decoupled cores (Bender 1990a; Bender 1996). In some cases, the stellar populations in these cores show markedly different properties in the spectral indices (Bender & Surma 1992; Davies, Sadler, & Peletier 1993). As shown by Greggio (1997), the strong Mg- and Fe-indices measured in the centers of ellipticals indicate a substantial degree of pre-enrichment in the gas which is converted into stars in the inner parts of these galaxies. Although not exclusively, this can be accomplished in a merging formation scenario, provided that gas dissipation plays an important role.

In merging scenarios, the kinematical and the stellar population properties

are determined by the ratio of star formation to merging timescales (Bender & Surma 1992; Bender, Burstein, & Faber 1992). In this framework one can envisage two extreme cases for the formation of ellipticals, mainly distinguished by the overall formation timescale of the object:

Fast Clumpy Collapse On rather short timescales (~ 1 Gyr), massive objects are built up by merging of smaller entities. Star formation occurs within these entities as they merge. The different dissipative properties of the newly formed stars and the gas produce a chemical segregation, such that the enriched material flows to the center (Bender & Surma 1992; Greggio 1997). On a larger scale, however, the whole system participates in a general collapse, merging and star formation occurring within the same (short) timescale. Notice that, from a chemical evolution point of view, this formation mode can also be considered as a refinement of the classical monolithic collapse (Eggen, Lynden-Bell, & Sandage 1962; Larson 1974).

Merging Spirals The merging event is assumed to occur when the merging entities have converted a considerable fraction of their gas into stars. For example, two spirals similar to the Milky Way merge to form an elliptical galaxy (Farouki & Shapiro 1982; Negroponte & White 1983; Gerhard 1983; Barnes 1988; Hernquist 1993). Most of the stars in the merging entities have formed in a continuous and long lasting (~ 10 Gyr) star formation process, leading to approximately solar abundances in the interstellar medium (ISM). At merging, the (enriched) residual gas flows down to the center (Hernquist & Barnes 1991; Barnes & Hernquist 1996) where it experiences a violent star formation episode on a short timescale. The global star formation history, however, lasts ~ 10 Gyr or more. Such mergers occur in nature (IRAS galaxies, e.g., Soifer & et al. 1984; Joseph & Wright 1985; Sanders et al. 1988; Melnick & Mirabel 1990), but it is not clear, if the end-product can be considered a ‘normal’ elliptical galaxy.

Semi-analytic models of galaxy formation in the framework of the CDM theory for structure formation (Kauffmann, White, & Guiderdoni 1993; Lacey et al. 1993; Cole et al. 1994) provide a continuum between these two extremes, with a distribution of timescales for the formation of ellipticals which depends on specific assumptions in the modeling. There are several arguments constraining short formation timescales and old formation ages of elliptical galaxies, hence pointing towards the *fast clumpy collapse* model. They are mainly based on the tightness of Fundamental Plane relations, i.e. the relation between stellar populations and σ (Dressler et al. 1987; Djorgovski & Davis 1987) and the small scatter in M/L ratios perpendicular to the Fundamental Plane (Renzini & Ciotti 1993). Also the color evolution (Aragón Salamanca et al. 1993), and the evolution of the Mg- σ relation with redshift (Bender, Ziegler, & Bruzual 1996; Ziegler & Bender 1997) push the star formation ages of *cluster* ellipticals to high redshift ($z \gtrsim 2$). Hierarchical models predict ellipticals in the field and in clusters to be intrinsically different (Kauffmann, Charlot, & White 1996), in

the sense that cluster galaxies form earlier and on shorter timescales (Kauffmann & Charlot 1998a). In the framework of hierarchical clustering, the merger of evolved spirals is a plausible scenario for the formation of a field elliptical. It should be emphasized, however, that the α -enhancement does not seem to depend on environmental densities (Jørgensen, Franx, & Kjaergaard 1995; Beuing, Bender, & Mendes de Oliveira 2000). Also, the Mg- σ relation measured in many clusters is remarkably independent of cluster properties (Colless et al. 1999). Moreover, slope and zero-point of the Mg- σ relation of field ellipticals do not differ significantly from the ones derived from cluster galaxies (Bernardi et al. 1998).

4.2 The model

The basic observational constraints on the modeling, aimed at describing the central stellar populations of bright ellipticals, are (see Chapter 1 and references therein):

1. High (super-solar) total metallicities Z .
2. Enhancement of α -elements of the order $[\alpha/\text{Fe}] \sim 0.2\text{--}0.4$ dex.

The first requirement comes from the observed nuclear Mg₂ index and points towards either higher metallicity yields (e.g., shallow IMF) in the central regions or to a scenario of *enriched* inflow (Edmunds 1990; Edmunds 1992; Greggio 1997). The latter implies that the stellar populations in the nuclear regions of ellipticals are characterized by a metallicity distribution with a minimum metallicity $Z_{\text{min}} > 0$ and a maximum metallicity Z_{max} , i.e. they are composite stellar populations (CSP). The second requirement, instead, comes from both Mg and Fe indices, thus in principle the two constraints might refer to different components of the CSP. However, since the Mg and Fe indices are measured in the same spectral range, the component of the CSP dominating the Mg₂ index also dominates the Fe index. Hence, requirements (1) and (2) must be met simultaneously from the stellar population dominating the visual light.

The first constraint is accomplished with a high degree of chemical processing, hence a large fractional amount of gas has to be turned into stellar mass. This can be achieved on both short (like in galactic bulges) or long (as in galactic disks) timescales. The second item points towards relatively short timescales. Note that both constraints are generally more easily met when a flatter IMF is assumed.

The *fast clumpy collapse* and the *merging spirals* modes differ mainly in their timescales of the pre-enrichment processes. These are mimicked by assuming different initial conditions for the chemical processing of the gas which forms the CSP in the central parts of the galaxy. In the *fast clumpy collapse* the process of formation is so fast that the galaxy can be viewed as a single body. Its chemical evolution can be described as a closed box with only radial segregation of different stellar populations. The initial abundance for the star formation process is assumed to be primordial. In the *merging spirals* model, instead, the gas which is turned into stars at the merging event has been enriched in the

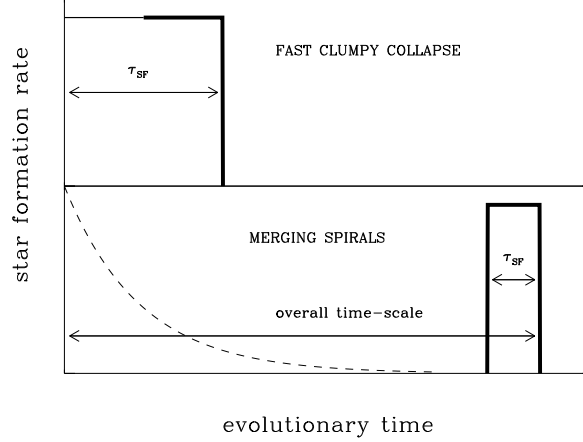


Figure 4.1: A sketch of the star formation histories assumed for the *fast clumpy collapse* (top panel) and the *merging spirals* (bottom panel) schemes. The arrows indicate the duration of the star formation episode in the modeling (τ_{SF}). The thick solid lines indicate the star formation episode yielding the stellar populations which end up in the central parts of the modeled galaxy. The dashed line (bottom panel only) sketches the star formation history of the parent spirals before the merger.

extended evolution history of the parent spirals leading to approximately solar abundances. The two different star formation histories are sketched in Fig. 4.1. The duration of the active star formation process will be referred to as the star formation timescale τ_{SF} (arrows in the figure). In the case of the *merging spirals* model (bottom panel) the overall formation timescale for the final elliptical is much longer than τ_{SF} . The phase of chemical enrichment in the parent spirals *before* the merger is indicated by the dashed line. The chemical outcome of this phase is reflected in the initial abundances assumed for the gas participating the merger (see Table 4.2). The thick lines in Fig. 4.1 indicate the metal-rich stellar populations that are assumed to form the nucleus of the elliptical.

In the simulations, star formation is assumed to proceed until the gas is completely used up, yielding the maximum metallicity, which is appropriate for the most massive ellipticals. This is consistent with the wind models of Arimoto & Yoshii (1987) and Matteucci & Tornambè (1987), in which the mass fraction of the galactic wind of the most massive object is lower than 0.01 for Salpeter IMF.

One further distinction between the two extreme cases for elliptical galaxy formation concerns the contribution of SNIa to the Fe-enrichment. In the merger of the two spirals, the contribution from those SNIa whose progenitors were born in the parent spirals (dashed line in Fig. 4.1) and explode during the merging are neglected. In other words, it is assumed that the products of these SNIa do not efficiently mix down to the central part where the merger induced star burst occurs. This corresponds to maximizing the [Mg/Fe] overabundance

achieved in the nuclear CSP.

4.2.1 Input ingredients for the chemical evolution

A constant star formation rate is adopted in the computations, since in both models the star formation episode generating the high Z stars has to be short to accomplish significant $[\text{Mg}/\text{Fe}]$ overabundances.

The chemical evolution is calculated by solving the usual set of differential equations as described in Chapter 2.

Enrichment from intermediate-mass stars (Renzini & Voli 1981), high-mass stars (WW95, TNH96) and SNIa occurring in close binary systems (Nomoto, Thielemann, & Yokoi 1984) are taken into account. The fraction A of close binaries is calibrated on a simultaneous fit of the age-metallicity relation in the solar neighborhood and the ratio $N_{\text{SNII}}/N_{\text{SNIa}} \approx 5$ typically observed in Sbc galaxies (van den Bergh & Tammann 1991), leading to $A = 0.035$ (Chapter 3). The IMF is assumed as the usual single slope power-law normalized by mass, the slope $x = 1.35$ referring to the Salpeter-value (Salpeter 1955). The upper and lower mass cutoffs are $40 M_{\odot}$ and $0.1 M_{\odot}$, respectively. The effect of adopting a different contribution from SNIa, different mass cutoffs, and an IMF deviating from the single power law (e.g., Scalo 1986) will be discussed in addition. The timescale τ_{SF} , and the IMF slope x represent the main parameters in the calculations.

4.2.2 Average abundances

The model output are abundances. For a comparison to the observed properties, that are obtained from spectral features in the optical band, V -luminosity weighted, mean stellar abundances have to be computed. Note that the real abundances averaged by mass are larger, since at constant age metal-poor stars are brighter (e.g., Greggio 1997).

The mass-averaged abundance of element i in a CSP of age t_g , including living stars and remnants, is given by the following equation:

$$\langle X_i \rangle_*(t_g) = \frac{\int_{t_0}^{t_1} X_i(t) \psi(t) m_*^{\text{SSP}}(t_g - t) dt}{\int_{t_0}^{t_1} \psi(t) m_*^{\text{SSP}}(t_g - t) dt}, \quad (4.1)$$

where t_0 and t_1 are the epochs of start and end of the active star formation process, respectively. The quantity $m_*^{\text{SSP}}(t_g - t)$ is the fraction of mass in stars (living and remnants) that, being born at time t , are present at time t_g . SSP means *Simple Stellar Population* of single age and metallicity.

$$m_*^{\text{SSP}}(t_g - t) = \int_{m_{\min}}^{m_{\text{to}}(t_g - t)} \phi(m) dm + \int_{m_{\text{to}}(t_g - t)}^{m_{\max}} w_m \phi(m) dm \quad (4.2)$$

In Equation 4.2 m_{to} is the turnoff mass at time t_g of the SSP of age $(t_g - t)$ born at time t ; m_{\min} and m_{\max} are the lower and upper mass cutoffs of the IMF, respectively, and w_m is the remnant mass of a star of initial mass m . The values

of w_m as a function of mass are taken from the nucleosynthesis prescriptions. The IMF $\phi(m)$ is normalized to 1. Thus the product $\psi(t) \cdot m_*^{\text{SSP}}(t_g - t)$ gives the mass-contribution at the time t_g from a stellar population born at time t , when the abundance in the ISM was $X_i(t)$.

The V -light-averaged abundances are weighted with the luminosities in the visual band:

$$\langle X_i \rangle_V(t_g) = \frac{\int_{t_0}^{t_1} X_i(t) \psi(t) L_V^{\text{SSP}}(t_g - t) dt}{\int_{t_0}^{t_1} \psi(t) L_V^{\text{SSP}}(t_g - t) dt} \quad (4.3)$$

$L_V^{\text{SSP}}(t_g - t)$ is the luminosity of an SSP with age $(t_g - t)$, and is given by standard SSP models as a function of age and metallicity. The models from Worthey (1994) are adopted. The spread in age and metallicity of the CSP are $[t_0, t_1]$ and $[Z_{\min}(t_0), Z_{\max}(t_1)]$, respectively.

The averaged abundance ratio is obtained by taking the ratio of the averaged abundances. For the sake of clarity, the following notation is used:

$$\langle [X_i/X_j] \rangle \equiv [\langle X_i \rangle / \langle X_j \rangle] \quad (4.4)$$

where the square brackets denote the usual normalization to the solar abundances, for which meteoritic abundances (Anders & Grevesse 1989) are used.

In agreement with estimates by Edmunds (1992), the mass-averaged metallicities turn out systematically higher than the V -light-averaged metallicities by 0.1 dex.

4.3 Results

In the following, the average abundances 15 Gyr after star formation started are discussed. Note that the results are insensitive to the exact age, as the passive evolution of stellar populations is most rapid in the first Gyr (Edmunds 1992).

Since most of the data in the literature concern Mg- and Fe-indices, the main focus is on the abundance ratio Mg/Fe. Mg can be considered as a representative for α -elements. Indeed, the ratios [Mg/Fe] and [O/Fe] do not differ significantly in the TNH96 models as shown in the Chapters 2 and 3. The V -luminosity averaged quantities are discussed, as both the Mg₂ and the Fe-indices (Fe5270, Fe5335) fall in this spectral range.

First, the average abundances of a closed box model are considered, which is a good description of the *global* properties of an elliptical galaxy formed in the *fast clumpy collapse* mode (Section 4.3.1). Second, the abundances of the high metallicity components of the closed box model are discussed, describing the properties of the *nuclear regions* of an elliptical galaxy formed in a *fast clumpy collapse* mode (Section 4.3.2). Third, the *merging spirals* model is examined (Section 4.3.3). Finally, the two formation scenarios are compared in Section 4.3.4. The results are summarized in Table 4.3 (p. 55).

4.3.1 Predictions from the closed box model

As mentioned above, an $[\text{Mg}/\text{Fe}]$ overabundance can be accomplished either with short star formation timescales or with a flat IMF. This $\tau_{\text{SF}}-x$ degeneracy is explored quantitatively for both SNII nucleosynthesis prescriptions, WW95 and TNH96. In case of WW95 the results from model B are adopted which assumes an enhancement of the explosion energy in high mass stars by a factor 1.5 and therefore compares best to the TNH96 models. Note that model B produces the highest Mg/Fe ratio among the WW95 calculations (see Chapter 2).

WW95 yields

Fig. 4.2 shows the averaged α -enhancement as a function of the star formation timescale τ_{SF} and IMF slope x with WW95-yields. The parameter range for τ_{SF} and x are chosen such that the resulting abundance ratios cover the range indicated by the data ($0.2 - 0.4$ dex). As discussed in Chapter 2, when WW95 are used, the $[\text{Mg}/\text{Fe}]$ ratio in the SNII ejecta from one SSP is only slightly above solar. It follows that extremely short τ_{SF} are required to obtain values significantly above solar. In fact, Fig. 4.2 shows that $\tau_{\text{SF}} \sim 10^7$ yr is necessary, independent of the IMF slope. These results are presumably not compatible with timescales for cooling and mixing of the stellar ejecta.

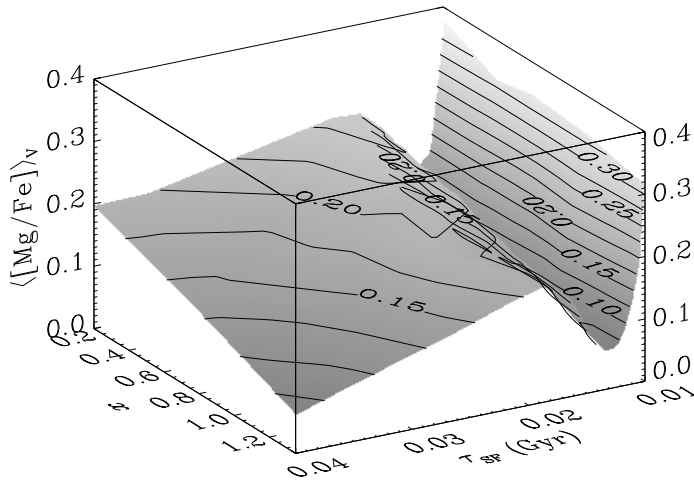


Figure 4.2: Average $[\text{Mg}/\text{Fe}]$ overabundance in the stars weighted by V -band luminosity as a function of the star formation timescale τ_{SF} and IMF slope x (by mass). SNII nucleosynthesis is adopted from WW95. The contour lines mark levels of constant $\langle [\text{Mg}/\text{Fe}] \rangle$. No segregation of metal-rich populations is considered, therefore the results are interpreted as *global* properties of the galaxy. The timescales required for a significant α -enhancement are unphysically short ($\sim 10^7$ yr).

The minimum in $\langle [\text{Mg}/\text{Fe}] \rangle$ at $\tau_{\text{SF}} = 11 - 17$ Myr is a consequence of the metallicity dependence of the WW95 yields, in which the highest $[\text{Mg}/\text{Fe}]$ ratios are achieved for the lowest ($10^{-4} Z_{\odot}$) and the highest ($1 Z_{\odot}$) initial metallicity

(see Thomas, Greggio, & Bender 1998). Thus, the calculated Mg/Fe reaches a minimum, if stellar populations of intermediate Z dominate the enrichment.

It should be noticed that the model for the SNIa rate adopted in the computations does not influence this result. The Fe contribution from these objects starts to play a role only at ages larger than 10^8 yr. Lower Fe yields from SNII would lead to larger $\langle \text{Mg/Fe} \rangle$ for a given τ_{SF} . However, most of the Fe comes from stars of mass $\lesssim 20 M_{\odot}$, whose yields are in good agreement with observations (see Chapter 2).

TNH96 yields

The results for TNH96 nucleosynthesis are presented in Fig. 4.3. In this case, $\tau_{\text{SF}} \approx 1$ Gyr leads to $[\text{Mg/Fe}] \approx 0.2$, provided that the IMF is not steeper than Salpeter. It is important to emphasize that the higher Mg yields in TNH96 essentially stem from a higher contribution by stars in the mass range 18–25 M_{\odot} that are not severely affected by fallback (Chapter 2). The results are more clearly illustrated in the 2-dimensional panels of Fig. 4.3, in which contours of constant $\langle [\text{Mg/Fe}] \rangle$, $\langle [\text{Fe/H}] \rangle$, and $\langle [Z] \rangle$ are plotted in the $\tau_{\text{SF}}-x$ -plane.

The average Z and $[\text{Fe/H}]$ are only little sensitive to τ_{SF} , because a closed box model assuming complete gas consumption is assumed, in which the metallicity reaches the maximum possible value given by the stellar yields. Z therefore only depends on the IMF slope, for a given stellar nucleosynthesis prescription. The contours are not totally flat because of the relaxation of the instantaneous recycling approximation which allows for a delay in the enrichment. As a substantial fraction of Fe comes from SNIa, the time dependence is larger for $\langle [\text{Fe/H}] \rangle$. The plots also show that the iron abundances are lower than the actual total metallicity by roughly 0.1 – 0.2 dex. Hence, for star formation timescales $\tau_{\text{SF}} \lesssim 1$ Gyr, $[\text{Fe/H}]$ does not trace total metallicity $[Z]$.

In Fig. 4.3, solar $[\text{Fe/H}]$ is achieved with x in the range 1.2 – 0.9. For these values of the IMF slope an $[\text{Mg/Fe}]$ overabundance of 0.25 is obtained with τ_{SF} in the range 0.8 to 2.6 Gyr. For Salpeter IMF ($x = 1.35$), shorter timescales $\tau_{\text{SF}} \approx 0.1 - 1$ Gyr are required to obtain $0.2 \lesssim \langle [\text{Mg/Fe}] \rangle \lesssim 0.3$. The average iron abundance and metallicity, however, are low in the Salpeter-case: $\langle [\text{Fe/H}] \rangle \approx -0.4$ and $\langle [Z] \rangle \approx -0.2$ for $\tau_{\text{SF}} \approx 1$ Gyr. Note that the average metallicities predicted here are meant to describe the global properties of elliptical galaxies. The accomplishment of solar and super-solar metallicities in the central parts is discussed in the following sections. In the following, only TNH96 nucleosynthesis will be considered.

4.3.2 Central abundances in a Clumpy Collapse

In the *clumpy collapse* model, the stellar populations in the center are the high-metallicity tail of the closed box distribution. As Mg/Fe decreases with increasing metallicity, the larger the minimum metallicity (Z_{min}) is, the lower is the average Mg/Fe ratio.

This is demonstrated quantitatively in Fig. 4.4, showing the predicted Mg/Fe and Fe/H for a family of closed box models with Salpeter ($x = 1.35$) IMF (left

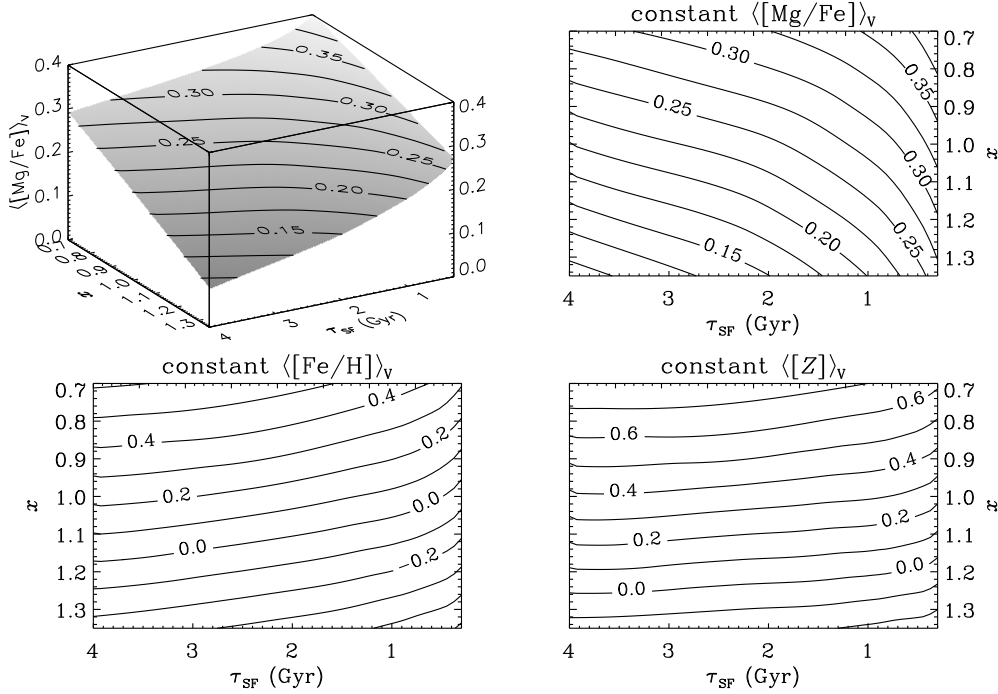


Figure 4.3: *Top-left panel:* The same as Fig. 4.2, however with TNH96 nucleosynthesis. *Top-right panel:* A projection of the contours indicating constant $\langle [\text{Mg}/\text{Fe}] \rangle_v$ onto the $\tau_{\text{SF}}\text{-}x$ -plane. *Bottom panels:* Contours of constant iron abundance (left panel) and total metallicity (right panel) are plotted as functions of τ_{SF} and x . The contours are dependent on τ_{SF} because finite stellar lifetimes are taken into account. This effect is larger for iron due to the substantial contribution from SNIa to the Fe-enrichment. Generally, the total metallicity is larger than the iron abundance by 0.1 – 0.2 dex. The *global* values of both $[\text{Fe}/\text{H}]$ and $[Z]$ turn out to be *sub-solar* (–0.4 and –0.2 dex, respectively), if an $[\text{Mg}/\text{Fe}]$ overabundance is accomplished with Salpeter IMF ($x = 1.35$).

panel) and flat ($x = 0.7$) IMF (right panel), as functions of τ_{SF} . The dotted and dashed lines bracket the possible solutions, showing respectively the results for $Z_{\text{min}} = 0$ (no segregation of the high Z populations) and $Z_{\text{min}} = Z_{\text{max}}$, which is the highest Z attained by the closed box model ($Z_{\text{max}} \sim 3 Z_{\odot}$, $17 Z_{\odot}$ for $x = 1.35$ and $x = 0.7$, respectively). Adopting Salpeter IMF and $\tau_{\text{SF}} \lesssim 1$ Gyr an $\langle [\text{Mg}/\text{Fe}] \rangle \gtrsim 0.2$ dex is obtained for every choice of Z_{min} . The amount of iron locked in stars, instead, is much more sensitive to the segregation of the populations. In the case of $\tau_{\text{SF}} = 1$ Gyr cutting the low-metallicity tail at $0.5 Z_{\odot}$, $\langle [\text{Fe}/\text{H}] \rangle$ increases from –0.44 to –0.15 dex. Assuming Salpeter IMF and a star formation episode lasting 1 Gyr, this model yields super-solar total metallicity ($\langle [Z] \rangle = 0.18$ dex), solar iron abundance ($\langle [\text{Fe}/\text{H}] \rangle = 0.01$), and a significant $[\text{Mg}/\text{Fe}]$ overabundance ($\langle [\text{Mg}/\text{Fe}] \rangle = 0.17$).

It can be concluded that the Salpeter IMF slope is compatible with the observations provided that τ_{SF} is not larger than ~ 1 Gyr.

A flatter IMF slope obviously relaxes the constraint on τ_{SF} . The case $x = 0.7$

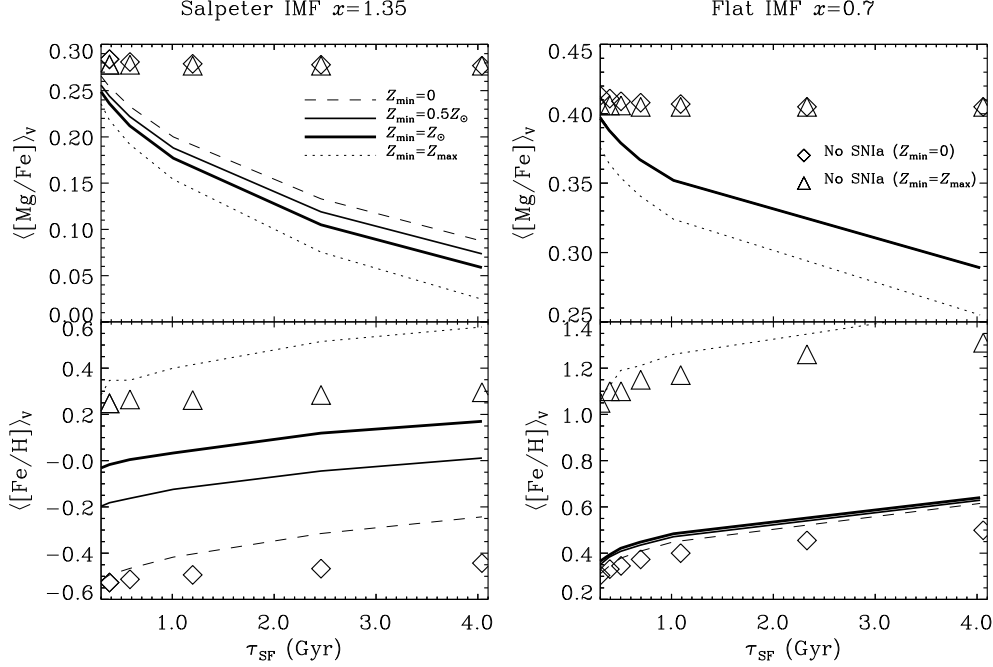


Figure 4.4: Average stellar $[\text{Mg}/\text{Fe}]$ ratio (top panels) and iron abundance (bottom panels) in the *fast clumpy collapse* model as a function of the star formation timescale τ_{SF} for Salpeter IMF ($x = 1.35$, left panel) and flat IMF ($x = 0.7$, right panel). TNH96 SNIi yields are adopted. The various line-styles denote different minimum metallicities Z_{min} of the central stellar population. The symbols represent models without SNIa for $Z_{\text{min}} = 0$ (diamonds) and $Z_{\text{min}} = Z_{\text{max}}$ (triangles).

is shown in the right panels of Fig. 4.4. In this case $\tau_{\text{SF}} \sim 4$ Gyr still yields $[\text{Mg}/\text{Fe}] = 0.29$, independent of Z_{min} . However, this flat slope leads also to very large iron abundances $[\text{Fe}/\text{H}] > 0.4$, in clear contradiction to observations. Moreover such models produce unphysically large $Z_{\text{max}} \approx 17 Z_{\odot}$. There are no known examples of stars with such high metallicities in any environment.

This ‘overproduction’ of metals can be reduced by transforming a smaller fraction of gas f_{trans} into stars. Table 4.1 gives the results for various f_{trans} , and fixed $\tau_{\text{SF}} = 1$ Gyr, $x = 0.7$, $Z_{\text{min}} = 0$. For this slope, not more than 70 per cent of the gas should be converted into stars, in order to obtain the observed $\langle [\text{Fe}/\text{H}] \rangle \lesssim 0.2$. The remaining ~ 30 per cent would then have to be ejected to the intergalactic or intracluster medium, as elliptical galaxies are devoid of interstellar matter.

Scalo-like IMF

An IMF which flattens at $m \lesssim 0.5 M_{\odot}$ (Scalo 1986; Kroupa, Tout, & Gilmore 1993; Gould, Bahcall, & Flynn 1997) pushes more mass to massive stars, and thus increases the efficiency of the chemical evolution processing. To investigate

TABLE 4.1
DIFFERENT GAS FRACTIONS

f_{trans}	$\langle [\text{Mg}/\text{Fe}] \rangle$	$\langle [\text{Fe}/\text{H}] \rangle$	$\langle [Z] \rangle$	Z_{max}/Z_{\odot}
1.0	0.35	0.45	0.70	16.9
0.9	0.35	0.36	0.62	12.0
0.8	0.36	0.29	0.56	9.9
0.7	0.36	0.19	0.48	7.9
0.6	0.36	0.12	0.41	6.6
0.5	0.36	0.00	0.30	5.0

NOTE.—Mean stellar abundances (V -luminosity weighted) for the *fast clumpy collapse* model with $\tau_{\text{SF}} = 1$ Gyr, $x = 0.7$ and $Z_{\text{min}} = 0$, TNH96 yields. The fraction of gaseous mass transformed into stars is varied from $f_{\text{trans}} = 1.0$ (complete exhaustion) to $f_{\text{trans}} = 0.5$. Column (5) gives the metallicities of the most metal-rich stars.

this effect, additional simulations are performed using the estimate by Gould, Bahcall, & Flynn (1997) of the flat IMF at the low-mass end:

$$\begin{aligned} m < 0.6 M_{\odot} &\rightarrow \phi \sim m^{0.44} \\ 0.6 M_{\odot} \leq m \leq 1 M_{\odot} &\rightarrow \phi \sim m^{-1.21} \end{aligned}$$

Salpeter slope above $1 M_{\odot}$ is assumed. Compared to the single-slope Salpeter-case, the averaged iron abundance increases to $\langle [\text{Fe}/\text{H}] \rangle \approx -0.14$ dex, whereas the Mg/Fe ratio is not affected. Cutting the metal-rich part of the CSP at $Z_{\text{min}} = 1 Z_{\odot}$ leads to significantly super-solar iron abundances ($\langle [\text{Fe}/\text{H}] \rangle \approx 0.18$ dex) and high total metallicities ($\langle [Z] \rangle \approx 0.34$ dex).

If instead a steeper IMF $x = 1.7$ above $1 M_{\odot}$ is adopted (Scalo 1986), the iron abundance decreases to $\langle [\text{Fe}/\text{H}] \rangle = -0.48$, and the Mg/Fe is reduced to $\langle [\text{Mg}/\text{Fe}] \rangle = 0.1$ dex. The Scalo-slope $x = 1.7$ at the high-mass end thus requires τ_{SF} of the order 10^8 yr in order to produce $\langle [\text{Mg}/\text{Fe}] \rangle = 0.2$ dex.

The SNIa rate

The timescales constrained above are crucially dependent on the adopted description for the SNIa rate. In the present models (Greggio & Renzini 1983), each stellar generation gives rise to the first SNIa event after 30 Myr from its birth, and 50 per cent of the explosions occur within the first 0.5 Gyr, which can be considered as the characteristic time-scale $\tau_{\text{Fe,Ia}}$ for the Fe-enrichment from Type Ia supernovae. The amplitude of the SNIa rate has been calibrated on the chemical evolution of the solar neighborhood (Chapter 3). The above models predict a current SNIa rate in elliptical galaxies of $R_{\text{Ia}} \approx 0.05 - 0.1$

SNU¹, depending on the IMF slope and τ_{SF} . This result is consistent with observational estimates $R_{\text{Ia}} = 0.14 \pm 0.1$ SNU (Cappellaro 1996, and references therein).

A substantially longer $\tau_{\text{Fe,Ia}}$ would imply τ_{SF} to be systematically larger than derived above. Note, however, that current supernova models predict values of $\tau_{\text{Fe,Ia}}$ not significantly longer than ~ 1 Gyr (Greggio 1996). Still, it is instructive to evaluate the impact of suppressing completely the Fe-contribution from SNIa, which allows to explore also the hypothesis of selective mass loss (see p. 41). The results obtained by omitting SNIa contributions are shown in Fig. 4.4 as open symbols. The diamonds refer to $Z_{\text{min}} = 0$, the triangles to $Z_{\text{min}} = Z_{\text{max}}$. Note that from the stellar abundance ratios alone, it is not possible to distinguish the options *selective mass loss* and *lower SNIa rate*, if galaxies are not closed boxes. In galaxy clusters, instead, the ICM abundance in combination with the stellar abundances can be used to distinguish between the two options, assuming that clusters are closed boxes and giant ellipticals dominate the ICM enrichment. Indeed, the very large amount of iron found in the ICM (Renzini et al. 1993) and the solar Mg/Fe ratios in the ICM (Mushotzky et al. 1996; Ishimaru & Arimoto 1997) makes unlikely the complete depression of SNIa iron production in ellipticals (see also Chapter 7).

Without the Fe-enrichment from SNIa the $\langle [\text{Mg}/\text{Fe}] \rangle$ saturates at the maximum SNII-SSP value 0.28 dex (Salpeter) and 0.4 dex ($x = 0.7$), independent of the lower Z cut and of τ_{SF} . The $\langle [\text{Fe}/\text{H}] \rangle$ is shifted to lower values by roughly 0.2 dex. The total metallicity (not shown in the figure), instead, is lowered only by 0.01 dex due to the small influence of SNIa on the total metallicity for the short star formation timescales considered here. Both Mg/Fe and Fe/H become independent of τ_{SF} , because there is no delayed iron enrichment from SNIa. This computation trivially shows that without the SNIa contribution, the α -elements overabundance does not constrain τ_{SF} , but the SSP-yields and the IMF slope. Adopting different models for the SNIa progenitors with longer $\tau_{\text{Fe,Ia}}$, and/or assuming that a fraction of the Fe ejected by SNIa is not incorporated in the ISM (e.g., selective mass loss) would lead to intermediate results.

4.3.3 Central abundances in Merging Spirals

Alternatively to the *fast clumpy collapse*, the merger of two identical spiral galaxies is discussed in this section. Two possible merger-redshifts are considered, $z_{\text{merger}} = 2.5$ and $z_{\text{merger}} = 0.45$, corresponding to lookback times 12 and 5 Gyr for $\Omega_m \approx 0.3$, $\Omega_m + \Omega_\Lambda = 1$, $H_0 = 65$ km/s/Mpc. The age of the universe is ~ 15 Gyr, so that the ages of the spirals at the time of merging are 3 Gyr for $z_{\text{merger}} = 2.5$, and 10 Gyr for $z_{\text{merger}} = 0.45$.

The element abundances of the population that forms in the merger-induced star formation burst are discussed. From a chemical point of view, the main difference with respect to the *fast clumpy collapse* case are the initial abundances, because the ISM of the parent spirals, out of which the burst population forms,

¹1SNU = $1\text{SNe} \times (10^{10} L_\odot)^{-1} \times (100 \text{ yr})^{-1}$. The luminosities are taken from Worthey (1994).

is obviously pre-enriched. These ISM element abundances and the gas fractions in the spirals at the time of the merger are adopted from the solar neighborhood-model of Chapter 3, for the ages 3 and 10 Gyr. The metallicities Z_{in} in the ISM of the parent spirals at these ages are half-solar and solar, respectively. The gas fractions are 50 and 20 per cent, respectively. The corresponding abundance ratios are $[\text{Fe}/\text{H}]_{\text{in}} = -0.39$ and 0.0, and $[\text{Mg}/\text{Fe}]_{\text{in}} = 0.08$ and 0.0 (see Table 4.2). Note that the higher z_{merger} is, the lower is $[\text{Fe}/\text{H}]_{\text{in}}$ and the higher is $[\text{Mg}/\text{Fe}]_{\text{in}}$.

TABLE 4.2
SPIRAL MERGER

z_{merger}	Age	Gas	Z_{in}	$[\text{Fe}/\text{H}]_{\text{in}}$	$[\text{Mg}/\text{Fe}]_{\text{in}}$
2.50	3 Gyr	50 %	0.5 Z_{\odot}	-0.39	0.08
0.45	10 Gyr	20 %	1.0 Z_{\odot}	0.00	0.00

NOTE.— The merger is assumed to occur at the redshift z_{merger} given in Column (1). The age of the spirals at z_{merger} is given in Column (2). The abundances are adopted from Chapter 3. The adopted cosmology is $\Omega_m \approx 0.3$, $\Omega_m + \Omega_{\Lambda} = 1$, $H_0 = 65$ km/s/Mpc.

In the following, τ_{SF} indicates the star formation timescale of the merger-induced burst. Note that the *overall* star formation timescale of the final object is much longer, as it includes both the burst and the preceding evolution of the parent spirals (see Fig. 4.1). The populations formed during the merger by construction have the minimum metallicities $Z_{\text{min}} = Z_{\text{in}} = 0.5$ and $1 Z_{\odot}$. They are assumed to represent the populations in the galaxy center.

The results of the calculations for the different parameters considered are shown in Fig. 4.5, in which the predicted $\langle[\text{Mg}/\text{Fe}]\rangle$ (top panels) and $\langle[\text{Fe}/\text{H}]\rangle$ (bottom panels) in the burst population are plotted as functions of τ_{SF} for Salpeter ($x = 1.35$) IMF (left panel) and flat ($x = 0.7$) IMF (right panel). The thick and thin solid lines are the models with $Z_{\text{min}} = Z_{\text{in}} = 1 Z_{\odot}$ and $Z_{\text{min}} = Z_{\text{in}} = 0.5 Z_{\odot}$, respectively. The calculations without SNIa are denoted by the symbols (diamonds: $Z_{\text{in}} = 1 Z_{\odot}$ and triangles: $Z_{\text{in}} = 0.5 Z_{\odot}$).

For a Salpeter IMF, the burst population of the late merger at redshift $z_{\text{merger}} = 0.45$ (thick lines) has $\langle[\text{Mg}/\text{Fe}]\rangle \lesssim 0.1$ and super-solar metallicities ($\langle[\text{Fe}/\text{H}]\rangle \approx 0.14$, $\langle[Z]\rangle \approx 0.20$). The Mg/Fe is significantly below the observational estimates. The very early merger at redshift $z_{\text{merger}} = 2.5$ (thin lines), instead, yields $\langle[\text{Mg}/\text{Fe}]\rangle \approx 0.2$, but too low metallicities $\langle[\text{Fe}/\text{H}]\rangle \lesssim -0.1$ and $\langle[Z]\rangle \approx 0.06$. Thus both models fail to reproduce simultaneously high metallicity and high Mg/Fe.

The weak impact of neglecting SNIa (symbols) comes from the fact that in this model SNIa are excluded only during the short burst phase. The iron pro-

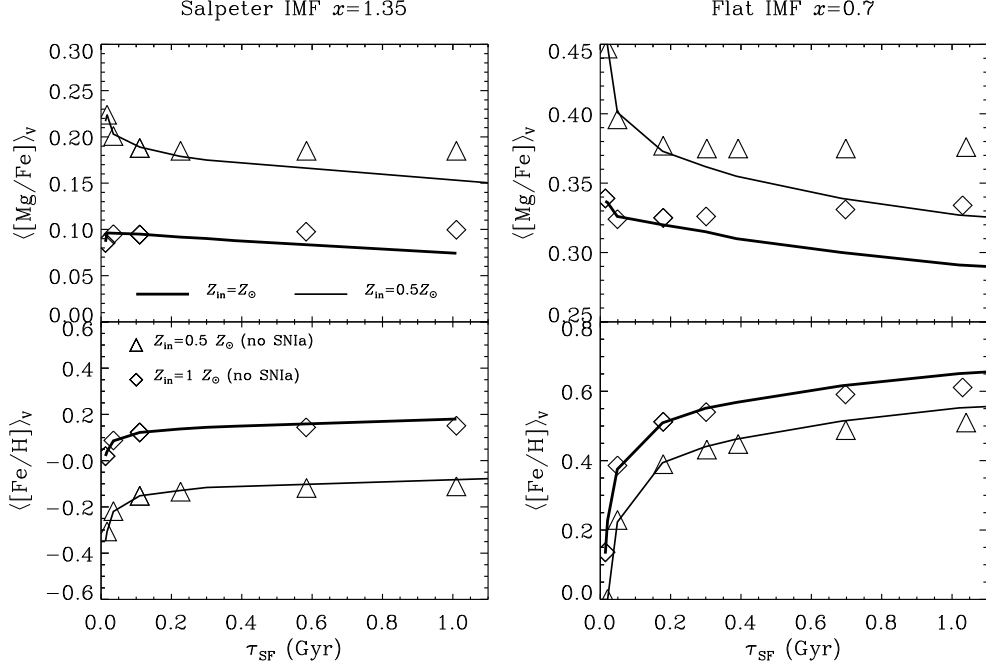


Figure 4.5: Average stellar $[Mg/Fe]$ (top panels) and iron abundance (bottom panels) in the *merging spirals* model as a function of the burst timescale, for Salpeter IMF (left panel) and flat IMF (right panel). TNH96 SNIi yields are adopted. The thick and thin solid lines are models with $Z_{min} = 1 Z_{\odot}$ and $Z_{min} = 0.5 Z_{\odot}$, respectively (see Table 4.2). The symbols represent models without SNIa during the burst for $Z_{min} = 0.5 Z_{\odot}$ (triangles) and $Z_{min} = 1 Z_{\odot}$ (diamonds).

vided by SNIa explosions during the evolution of the parent spirals is included by construction in the initial conditions.

Assuming a flatter IMF during the burst yields higher Mg/Fe, and high metallicities (Fig 4.5, right panels).

4.3.4 Comparison Merging Spirals vs. Fast Clumpy Collapse

The two formation scenarios considered here can be distinguished by the time-scale on which the pre-enrichment of the central stellar populations to solar-like abundances is accomplished. In the *merging spirals* scenario, the pre-enriched gas that forms the central burst population is not significantly α -enhanced, as the time-scale of the pre-enrichment extends to several Gyr. In the *fast clumpy collapse* scenario, instead, the pre-enriched gas forming the nucleus is enhanced in α -elements because of the preceding short ($\ll 1$ Gyr) star formation timescales.

In Table 4.3 the resulting abundance ratios for the star formation timescales $\tau_{SF} = 0.3, 1, 4$ Gyr, for the IMF slopes $x = 1.35, 1.0, 0.7$ and for the minimum (initial) metallicities $Z_{min} = 0, 0.5, 1 Z_{\odot}$ are summarized. The comparison of the

TABLE 4.3
RESULTS

FAST CLUMPY COLLAPSE							MERGING SPIRALS		
x	τ_{SF}	Z_{min}	CSP	[Mg/Fe]	[Fe/H]	[Z]	[Mg/Fe]	[Fe/H]	[Z]
(1)	(2)	(3)	(4)	(5)	(6)	(7)	(8)	(9)	(10)
1.35	0.3	0.0	1.0	0.27	−0.52	−0.27	—	—	—
		0.5	0.5	0.26	−0.20	0.03	0.18	−0.12	0.05
		1.0	0.2	0.25	−0.03	0.19	0.09	0.14	0.20
	1.0	0.0	1.0	0.20	−0.42	−0.22	—	—	—
		0.5	0.5	0.19	−0.12	0.06	0.15	−0.07	0.07
		1.0	0.3	0.18	0.03	0.20	0.07	0.18	0.23
	4.0	0.0	1.0	0.09	−0.24	−0.14	—	—	—
		0.5	0.6	0.07	−0.01	0.09	0.08	0.04	0.12
		1.0	0.3	0.06	0.17	0.22	0.04	0.23	0.29
	1.00	0.3	0.0	1.0	0.34	−0.05	0.24	—	—
		0.5	0.8	0.34	0.11	0.38	0.28	0.17	0.39
		1.0	0.7	0.33	0.20	0.47	0.21	0.34	0.48
1.00	1.0	0.0	1.0	0.28	0.07	0.31	—	—	—
		0.5	0.8	0.28	0.20	0.43	0.24	0.25	0.44
		1.0	0.7	0.28	0.29	0.50	0.19	0.41	0.53
	4.0	0.0	1.0	0.20	0.23	0.39	—	—	—
		0.5	0.8	0.20	0.34	0.48	0.18	0.38	0.50
		1.0	0.7	0.20	0.42	0.55	0.15	0.55	0.61
	0.70	0.3	0.0	1.0	0.40	0.31	0.62	—	—
		0.5	0.9	0.40	0.40	0.70	0.36	0.44	0.70
		1.0	0.8	0.40	0.45	0.74	0.32	0.55	0.75
	1.0	0.0	1.0	0.35	0.45	0.70	—	—	—
		0.5	0.9	0.35	0.52	0.76	0.33	0.55	0.76
		1.0	0.9	0.35	0.56	0.79	0.29	0.65	0.81
0.70	4.0	0.0	1.0	0.29	0.62	0.79	—	—	—
		0.5	0.9	0.29	0.67	0.83	0.27	0.70	0.84
		1.0	0.9	0.29	0.71	0.86	0.25	0.84	0.92

NOTE.— The average stellar abundances (V -luminosity weighted) in the *fast clumpy collapse* model (Columns 5 – 7) and the *merging spirals* scheme (Columns 8 – 10) for the following parameters: IMF slope x (Column 1), star formation timescale τ_{SF} (Column 2), and minimum metallicity Z_{min} (Column 3). TNH96 yields are adopted. Column 4 is the mass fraction of the segregated (central) composite stellar population for the *fast clumpy collapse*. In the *merging spirals* model, these fractions are 0.5 and 0.2 for $Z_{\text{min}} = 0.5 Z_{\odot}$ and $Z_{\text{min}} = 1 Z_{\odot}$, respectively (see Table 4.2).

fast clumpy collapse (Columns 5–7) with the *merging spirals* (Columns 8–10), shows that — for the same pre-enrichment (i.e. Z_{\min}) — the average metallicities $\langle[Z]\rangle$ of the central populations are approximately the same for the two scenarios, while the average Fe/H is larger and the average Mg/Fe is lower in the *merging spirals* model.

The total metallicities are the same, because in both cases closed box metallicity distributions covering the same metallicity ranges are considered, the maximum metallicity being determined only by the nucleosynthesis prescriptions and the IMF slope. The Fe abundances in the *merging spirals* model are higher, because all the Fe ejected by SNIa during the evolution of the parent spirals before the merger is incorporated in the gas undergoing the final burst of star formation in the center. For the same reason, the Mg/Fe is lower in the *merging spirals* than in the *fast clumpy collapse*. The differences in both $\langle[\text{Fe}/\text{H}]\rangle$ and $\langle[\text{Mg}/\text{Fe}]\rangle$ are larger when the larger minimum metallicity $Z_{\min} = 1 Z_{\odot}$ is considered. When τ_{SF} is sufficiently long (i.e. 4 Gyr) the two models converge to similar results for $\langle[\text{Fe}/\text{H}]\rangle$ and $\langle[\text{Mg}/\text{Fe}]\rangle$, since in this case also in the *clumpy collapse model* most of the Fe ejected by SNIa is incorporated in the high metallicity tail of the composite population.

The *clumpy collapse* scenario matches both high Mg/Fe and super-solar metallicities, for Salpeter IMF and star formation timescales up to 1 Gyr. The high average metallicities are accomplished by segregating the metal-rich populations (with a minimum metallicity around $1 Z_{\odot}$) in the central region from the rest of the galaxy. Super-solar iron abundance can be obtained when a flattening of the IMF at the *low-mass end* ($0.5 M_{\odot}$) and Salpeter slope for masses above $1 M_{\odot}$ are applied. Flatter IMFs (in particular at the high mass end) generally allow longer star formation timescales, for the same $\langle[\text{Mg}/\text{Fe}]\rangle$, and lead to larger average metallicities. The metal ‘overproduction’ can be avoided by assuming that only a fraction of the initial gas mass is converted into stars.

The *late merger* of two spiral galaxies at redshift $z_{\text{merger}} = 0.45$ does not reproduce the Mg/Fe observed in ellipticals. A flattening of the IMF during the merger induced star burst has to be assumed ($\langle[\text{Mg}/\text{Fe}]\rangle \approx 0.2$), which leads to unphysically high maximum metallicities in the center ($Z_{\max} = 17 Z_{\odot}$ for $x = 0.7$). These very high metallicities can be reduced to $Z_{\max} = 5 Z_{\odot}$ by assuming that only 50 per cent of the gas is transformed into stars (see Table 4.1). The residual 50 per cent are likely to remain in the center of the galaxy, as the deep potential well inhibits the gas from escaping. However, such large amounts of gas are not observed in ellipticals. The *early merger* at $z_{\text{merger}} = 2.5$ is instead successful at reproducing the observed Mg/Fe, but the resulting central metallicities are by far too low. Anyway, a merger at such high redshifts is hardly distinguishable from a fast clumpy collapse.

4.4 Discussion

4.4.1 Gradients inside the galaxy

In the *fast clumpy collapse* model, in order to accomplish large average metallicities in the core population, a cut in the Z distribution at Z_{\min} is assumed.

The central stellar populations have $Z > Z_{\min}$, so that the mean metallicity decreases with increasing radius. As the more metal-poor populations are also more α -enhanced, the *fast clumpy collapse* predicts the average Mg/Fe to increase towards the outer parts. The *spiral merger*, instead, yields the opposite gradient in Mg/Fe, if an Mg-enhanced population — with a flat IMF during the merger — forms in the central regions.

This trend of increasing Mg/Fe with increasing metallicity and decreasing radius — assuming a radially constant IMF slope — can only be achieved in a scenario in which the formation of the central, metal-rich population is evolutionary decoupled from the global, metal-poor population. This decoupling is the case for the *merging spirals* model, but not for the *fast clumpy collapse*. In principle, one could apply this same decoupling also to the *fast clumpy collapse* picture, assuming that the SNIa products of the low Z stellar generation do not mix efficiently with the collapsing gas, and are preferentially ejected in galactic winds. However, this looks rather artificial, because of the very short timescales over which the formation of the whole galaxy is accomplished.

The measurement of abundance gradients therefore offers the opportunity to understand if the outer and inner populations of a galaxy are evolutionary coupled, and probably to discriminate between the two formation scenarios. Therefore, it is very important to better understand how the line strengths map into real abundances (see also below), and to study the trend of Mg/Fe with radius in more detail. So far, the observations indicate that Mg/Fe is constant with radius inside the half-light radius (Worthey, Faber, & González 1992; Davies, Sadler, & Peletier 1993; Fisher, Franx, & Illingworth 1995; Mehlert et al. 2000).

4.4.2 Upper mass cutoff

Throughout the whole analysis, the upper mass cutoff was assumed to be $m_{\max} = 40 M_{\odot}$. As discussed in Chapter 3, $m_{\max} = 70 M_{\odot}$ (TNH96) leads to higher [Mg/Fe] by ~ 0.15 dex, and would therefore allow for larger star formation timescales. The Mg/Fe in the burst population of the spiral merger at $z_{\text{merger}} = 0.45$ — assuming Salpeter IMF — increases to $\langle [\text{Mg/Fe}] \rangle \approx 0.2$ if $m_{\max} = 70 M_{\odot}$. Note, however, that the contribution from stars more massive than $40 M_{\odot}$ is highly uncertain due to the fallback effect (WW95), and it is not clear if the TNH96-yields of a $70 M_{\odot}$ star are realistic. Moreover, it is possible that the most luminous elliptical galaxies are significantly more α -enhanced than assumed here (see discussion below), which could not be reproduced in the spiral merger even if $m_{\max} = 70 M_{\odot}$.

4.4.3 How to interpret spectral indices?

As illustrated in Chapter 1, spectral line indices measured in elliptical galaxies are interpreted by means of population synthesis models being based on the so-called fitting functions. It is a controversial issue in how far indices can be translated into element abundances (Greggio 1997; Tantalo, Chiosi, & Bressan 1998). The exact Mg/Fe ratios of elliptical galaxies are therefore not well

determined. While Worthey, Faber, & González (1992) initially estimated $0.2 \lesssim [\text{Mg}/\text{Fe}] \lesssim 0.3$, more quantitative studies find $0.3 \lesssim [\text{Mg}/\text{Fe}] \lesssim 0.7$ (Barbuy 1994; Weiss, Peletier, & Matteucci 1995; Greggio 1997). Trager et al. (2000a), instead, derive — based on the response function of Tripicco & Bell (1995) — $0.1 \lesssim [\text{Mg}/\text{Fe}] \lesssim 0.3$.

Moreover, there is the additional uncertainty due to the fitting functions, as discussed in Maraston, Greggio, & Thomas (2001). Worthey et al. (1994) give lower Fe-indices than Buzzoni, Gariboldi, & Mantegazza (1992) and Buzzoni, Mantegazza, & Gariboldi (1994), while the Mg_2 index is comparable. As a consequence, Mg/Fe ratios in elliptical galaxies are higher when derived with the Buzzoni, Gariboldi, & Mantegazza (1992) fitting functions. The studies mentioned above are all based on the Worthey et al. (1994) fitting functions, so that it is possible that luminous ellipticals actually exhibit $[\text{Mg}/\text{Fe}] > 0.3$.

4.5 Summary

Two extreme modes of elliptical galaxy formation have been considered, namely a *fast clumpy collapse* and *merging spirals*. The focus is on the reproduction of observed central features like metallicities and Mg/Fe ratios. In the *fast clumpy collapse* model $\langle [\text{Mg}/\text{Fe}] \rangle \approx 0.2$ dex is obtained with IMF slopes close to Salpeter, provided that the star formation timescale does not exceed 1 Gyr. The *merger of two spirals* at redshift $z_{\text{merger}} = 0.45$, instead, produces Mg/Fe ratios in agreement with the observed value only when a flat IMF for the burst population is assumed. This is due to the large Fe abundances in the ISM of the merging galaxies at the time of the merger. In general, the earlier the merging takes place, the easier it is to accomplish an Mg/Fe overabundance in the burst population. A basic conclusion is, that galaxy formation with star formation timescales exceeding a few Gyr *does not* provide [Mg/Fe] ratios consistent with observations, unless a significant deviation from a Salpeter-IMF is assumed.

The two formation models predict opposite trends for the Mg/Fe gradient within the galaxy: The *fast clumpy collapse* leads preferentially to larger overabundances in the outskirts, while the *merging spirals* model has approximately solar Mg/Fe in the outer stellar populations and super-solar Mg/Fe — if the IMF is flattened — in the center. Thus the behavior of Mg/Fe with radius can give important hints on the galaxy formation process.

Kauffmann (1996) proposed an intrinsic difference between the formation of cluster and field ellipticals, due to the high density environment favoring shorter galaxy formation (total) timescales. If field objects form in a merging event later than cluster objects, field ellipticals should exhibit lower Mg/Fe ratios. This issue is discussed in more detail in Chapter 5.

A major conclusion from this work is that present-day giant ellipticals cannot be the end-product of the merger of two spiral galaxies. Indeed, Maraston et al. (2000) find that the newly formed globular clusters in the merger remnant NGC 7252 are *not* significantly α -enhanced, in agreement with the predictions of the present model. The recent merger NGC 7252 resembles a ‘normal elliptical’ in terms of shape and light profile, while the stellar population properties,

i.e. age spread and abundance ratios, are very different from the ones observed in elliptical galaxies.

Chapter 5

Hierarchical Galaxy Formation

Models of hierarchical galaxy formation (e.g., Kauffmann, White, & Guiderdoni 1993; Cole et al. 1994; Somerville & Primack 1999) describe the formation of galaxies in the cosmological framework of cold dark matter theory. They are designed to match a number of observational features like the B and K luminosity functions, the Tully-Fisher relation, redshift distributions, and the slope and the scatter of the color-magnitude relation (see Chapter 1, Section 1.2.3). The constraint of α /Fe-enhanced stellar populations in elliptical galaxies, instead, is not considered, and the chemical enrichment of α - and Fe-group elements has not been included in hierarchical models so far. But it has been questioned by Bender (1996) whether hierarchical models are compatible with the observed super-solar Mg/Fe ratios, that require star formation timescales of the order $10^8 - 10^9$ yr (Chapter 4).

The aim of this chapter is to investigate this issue quantitatively. In Section 5.1, the average star formation histories of cluster elliptical and spiral galaxies are adopted from the models of Kauffmann (1996), and the resulting abundance ratios of Mg and Fe are explored. In Section 5.2 — in collaboration with G. Kauffmann — the star formation histories of individual galaxies are considered. The abundance ratios in the model galaxies as functions of environmental density, luminosity and disk-to-bulge ratios are discussed. The content of this chapter is published in Thomas (1999a), Thomas & Kauffmann (1999), and Thomas (2001).

5.1 Average star formation histories

5.1.1 The model

In the hierarchical clustering scheme, galaxies are subsequently built up starting from small disk-like objects. A spheroidal object forms when two disk galaxies of comparable mass merge, which is called a ‘major merger’. Before this event many ‘minor mergers’ between a central galaxy and its satellite systems happen. It is important to emphasize, that the bulk of stars, i.e. 70 – 90 per cent, form

in the progenitor disk-galaxies *before* the final ‘major merger’ that forms the elliptical galaxy. In the star burst ignited by the major merger, only up to 30 per cent of the total stellar mass of the elliptical is created. If gas is accreted subsequently, so that a disk component forms, the spheroidal becomes the bulge of a spiral galaxy. Otherwise it is called an elliptical galaxy (for more details see Chapter 1, Section 1.2.3).

In Kauffmann (1996), Monte Carlo simulations are performed, each corresponding to one individual (final) galaxy. The star formation history given in Kauffmann (1996) is an *average* about all these realizations. These average star formation histories of an elliptical and spiral galaxy, respectively, are adopted for the present analysis.

Star formation rates

The star formation history in Kauffmann (1996) is given by the age distribution of the stellar populations weighted in the V -band light. In other words, the fractional contributions L_V^{SP} from stellar populations to the total V -light as a function of their ages t are specified. Equation 5.1 shows how L_V^{SP} is connected to the star formation *rate* ψ :

$$L_V^{\text{SP}}(t_0, t_1) = \frac{\int_{t_0}^{t_1} \psi(t) L_V^{\text{SP}}(t) dt}{\int_0^{t_{\text{univ}}} \psi(t) L_V^{\text{SP}}(t) dt} . \quad (5.1)$$

The interval $[t_0, t_1]$ is the age bin of the population, t_{univ} is the assumed age of the universe, which is $t_{\text{univ}} \approx 13$ Gyr for the cosmology adopted in Kauffmann (1996) ($\Omega_m = 1, \Omega_\Lambda = 0, H_0 = 50$ km/s/Mpc). For the purposes of this work, the star formation rate ψ as a function of time is derived from the age distribution given by Kauffmann (1996) according to Equation 5.1. The V -light of a simple stellar population $L_V^{\text{SP}}(t)$ as a function of its age and metallicity is taken from Worthey (1994).

Chemical enrichment

The chemical evolution is calculated by solving the usual set of differential equations (see Chapter 2). The enrichment process of the elements hydrogen, magnesium, iron, and total metallicity is computed. The delayed enrichment by Type Ia supernovae (SNIa) is taken into account following the model by Greggio & Renzini (1983). The inclusion of SNIa is crucial for interpreting Mg/Fe ratios, since SNIa substantially contribute to the enrichment of iron. The chemical evolution code is calibrated on the chemical evolution in the solar neighborhood (Chapter 3). The ratio of SNIa to SNII is chosen such that observational constraints like supernova rates, the age-metallicity relation and the trend of Mg/Fe as a function of Fe/H in the solar neighborhood are reproduced. The SNII nucleosynthesis prescription is adopted from Thielemann, Nomoto, & Hashimoto (1996) and Nomoto et al. (1997), because the stellar yields of Woosley & Weaver (1995) are unable to account for the [Mg/Fe] ratios of metal-poor halo stars in the Milky Way (Chapter 3).

The IMF is truncated at $0.1 M_{\odot}$ and $40 M_{\odot}$. The slope above $1 M_{\odot}$ is treated as a parameter, below this threshold a flattening according to recent HST measurements (Gould, Bahcall, & Flynn 1997) is assumed. This flattening at the low-mass end does not significantly affect α/Fe ratios. It should be noted that stars more massive than $40 M_{\odot}$ are expected to play a minor role in the enrichment process, because of their small number and the fallback effect (Woosley & Weaver 1995). Moreover, the mean $[\text{Mg}/\text{Fe}]$ overabundance in the metal-poor halo stars of our Galaxy is well reproduced for an IMF with the above truncation and Salpeter slope $x = 1.35$ (Salpeter 1955), if Thielemann, Nomoto, & Hashimoto (1996) nucleosynthesis is adopted (Chapter 3).

The fraction of gas converted to stars is adjusted to reproduce the global metallicities observed in the respective galaxy type.

Finally, two simplifications of the present model should be mentioned:

1. A one-phase interstellar medium (ISM) is assumed. Kauffmann & Charlot (1998a), instead, distinguish between cold and hot gas allowing mass transfer between these two components. Since stars form out of cold gas, this process basically controls the feedback mechanism of star formation. The resulting effects on the star formation rate, however, are incorporated in the present analysis, because the star formation history is directly adopted from Kauffmann (1996). The influence on the abundance *ratio* of Mg and Fe is negligible, as long as these elements do not mix on significantly different timescales.
2. The final galaxy is treated as the whole single-unit from the beginning of its evolution, the economics of the individual progenitors are not followed separately as in Kauffmann (1996). Hence, the simulations do not directly include galactic mass loss taking place during disk galaxy evolution as well as mass transfer between the progenitor systems. The impact on the *global* properties of the *final* galaxy, however, is expected to be small. In particular, abundance *ratios* of non-primordial elements like Mg and Fe are not significantly affected by mass loss and gas transfer, unless one allows for selective mechanisms.

5.1.2 Global populations

Figs. 5.1 and 5.2 show the global average star formation histories from the models of Kauffmann (1996) of cluster elliptical and spiral galaxies, respectively. The lower x-axis denote ages (lookback time), the evolutionary direction of time therefore goes from the right to the left, so that the local universe is at age = 0. The corresponding redshifts for an $\Omega_m = 1$, $\Omega_{\Lambda} = 0$, $H_0 = 50 \text{ km/s/Mpc}$ cosmology are given by the upper x-axis. The solid histogram shows the quantity $L_V^{\text{SP}}(t_0, t_1)$ (left y-axis) as it is explained in Section 5.1.1. More than 70 per cent of the light in the V-band comes from stars that have formed in the first 3 Gyr at redshift $z \gtrsim 2$. The abundance ratios $[\text{Mg}/\text{Fe}]$ and $[\text{Fe}/\text{H}]$ of the ISM and of the stars, resulting from the chemical evolution model are shown in the top and bottom panels, respectively (scale on the right y-axis). The chemical

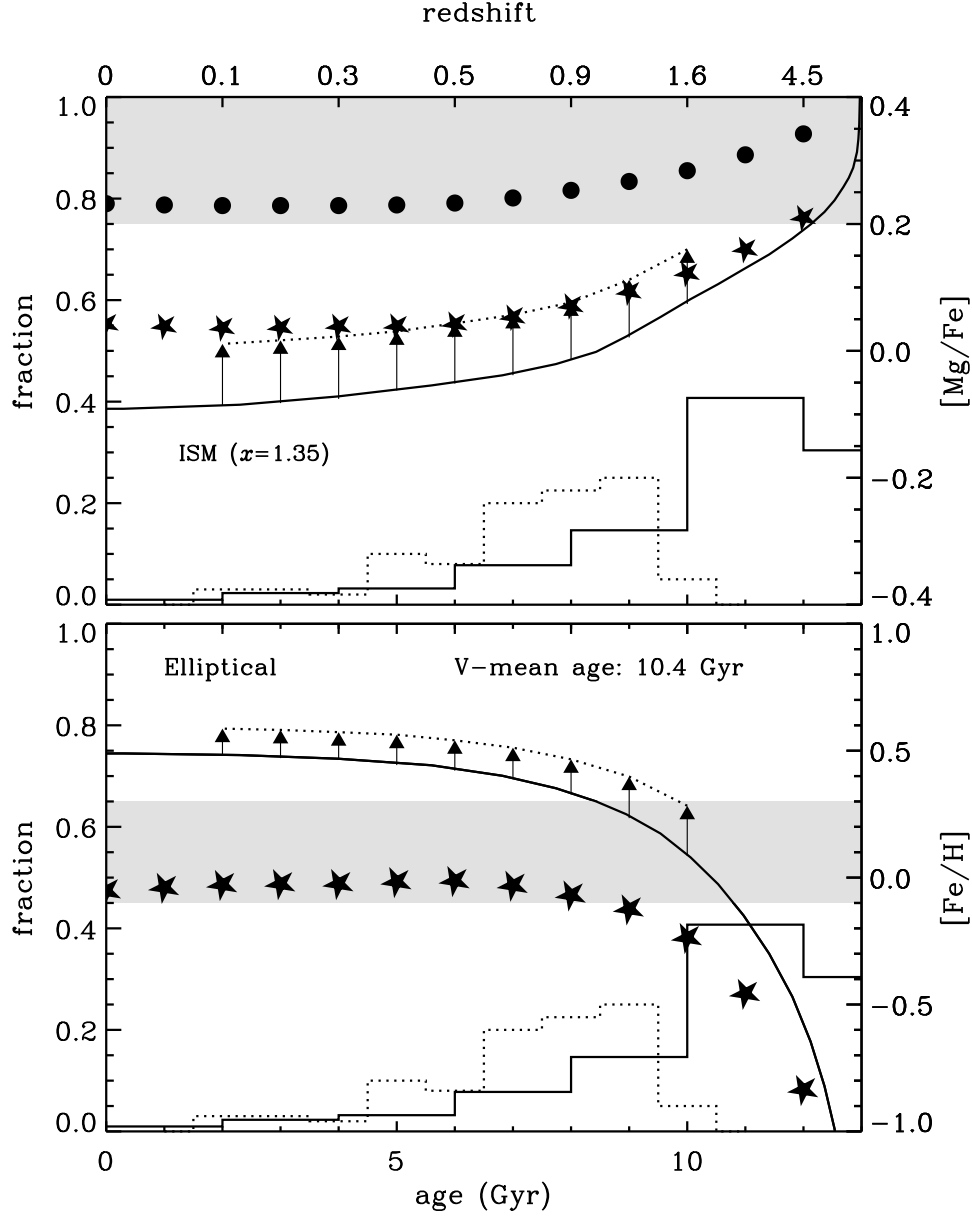


Figure 5.1: Star formation history and abundance ratios of the average cluster elliptical. The solid histogram is the fractional contribution to the total V-light from each stellar population as a function of age (lower x-axis) and birth-redshift (upper x-axis) from Kauffmann (1996; $\Omega_m = 1, \Omega_\Lambda = 0, H_0 = 50$ km/s/Mpc). The star-symbols and filled circles are the V-average [Mg/Fe] (top panel) and [Fe/H] (bottom panel) in the composite stellar population as function of redshift for Salpeter ($x = 1.35$) and flat ($x = 0.8$) IMF, respectively. The scale is on the right y-axis. The solid lines indicate the abundances in the interstellar medium ($x = 1.35$). The dotted histogram gives the fraction of ellipticals that experienced their last major merger at a given epoch. The arrows to the dotted lines at the various merger epochs give the abundance ratios of the newly created burst population formed in the last major merger. The shaded regions mark the observational constraints.

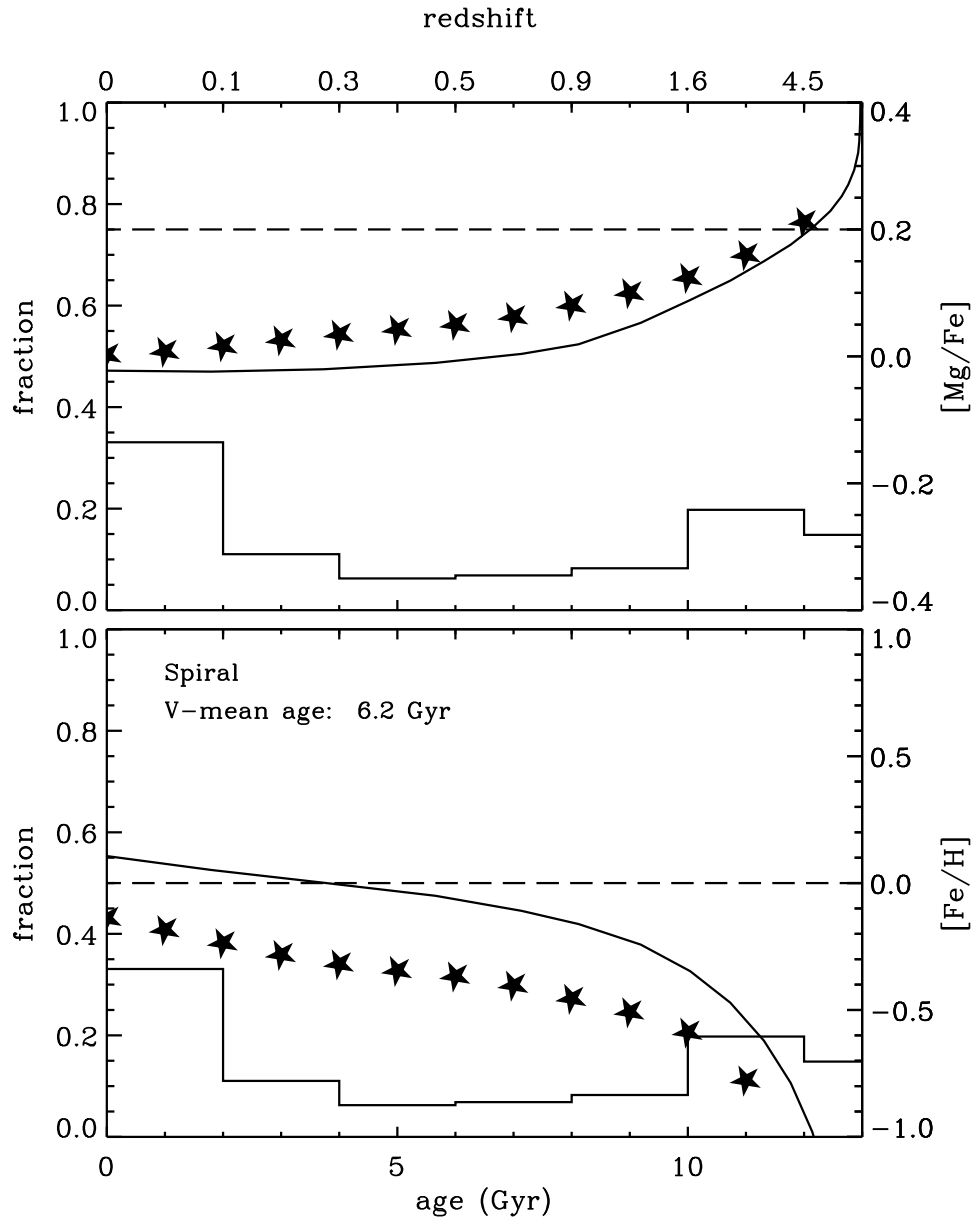


Figure 5.2: Star formation history and $[\text{Mg}/\text{Fe}]$ (top panel) and $[\text{Fe}/\text{H}]$ (bottom panel) of an average spiral. Axis and symbols see Fig. 5.1.

evolution of the ISM is denoted by the solid line, the filled star-symbols show the V -luminosity-weighted average abundance ratios of the composite stellar population of the galaxy as a function of age and redshift. The Salpeter-slope ($x = 1.35$) above $1 M_{\odot}$ is chosen. The effect of a flatter IMF ($x = 0.8$) on the Mg/Fe in the composite stellar populations of the elliptical is shown by the filled circles (Fig. 5.1, top panel).

Comparison elliptical vs. spiral

The star formation is much more extended towards lower redshift in the spiral than in the elliptical (solid histograms). The V -averaged ages of the spiral and the elliptical are 6.2 Gyr and 10.4 Gyr, respectively. In general, the mean abundances in the stellar populations differ from those in the ISM. The metallicity $[\text{Fe}/\text{H}]$ is always higher, and $[\text{Mg}/\text{Fe}]$ always lower in the ISM than in the V -average of the stars, because the stars archive the abundance patterns of early epochs. This effect is more prominent in the elliptical than in the spiral, because the star formation is skewed towards early times in the elliptical.

The gas fraction which is ejected from the galaxy is chosen such that the observationally constrained metallicity is reproduced. In the case of the elliptical it is assumed that the *global* stellar populations have solar metallicity at low redshifts (bottom panel), which requires the ejection of roughly 30 per cent of the (baryonic) mass of the galaxy during its evolution. In case of the spiral, 55 per cent of the gas is assumed to be ejected, in order to obtain solar metallicity in the ISM after 9 Gyr, which is supposed to represent a Milky Way-like spiral. As a consequence, the metallicities of the ISM and the stars are higher in the elliptical than in the spiral.

The Mg/Fe ratios, instead, depend mainly on the shape of the star formation rate as a function of time. Since there is no significant star formation at late times in the elliptical, the today's $N_{\text{SNII}}/N_{\text{SNIa}}$ is 20 times lower than in the spiral galaxy, which leads to a lower Mg/Fe in the present-day ISM of the elliptical by roughly 0.1 dex. The stars, instead, store the chemical abundances of the early epochs, so that the $\langle [\text{Mg}/\text{Fe}] \rangle$ is 0.04 dex higher in the elliptical galaxy than in the spiral, in accordance with the older mean age of the elliptical.

The Mg/Fe in the elliptical

Fig. 5.1 (top panel) demonstrates that with Salpeter IMF a super-solar mean $[\text{Mg}/\text{Fe}]$ ratio in the stars is only obtained at the very early stages of the evolution, namely in the first Gyr. The ongoing star formation drives $\langle [\text{Mg}/\text{Fe}] \rangle$ significantly below 0.2. Hence, the predicted mean Mg/Fe in the stellar populations of the elliptical at low redshift $\langle [\text{Mg}/\text{Fe}] \rangle = 0.04$ is well below the observationally derived value $0.2 \lesssim [\text{Mg}/\text{Fe}] \lesssim 0.4$, which is indicated by the shaded region in the top panel of Fig. 5.1 (see Chapter 1 and references therein).

One may argue that the average star formation history considered here does not apply to *bright* ellipticals in which the observed α -enhancement is most significant (Trager et al. 2000a). However, in the semi-analytic simulations brighter objects are on average younger (Kauffmann & Charlot 1998a),

and experience star formation histories that are even more skewed towards low redshift than the present example. They are therefore likely to exhibit even lower Mg/Fe ratios than calculated here, which is confirmed in a more detailed study presented in Section 5.2.

The star formation timescales that are required to obtain $[\text{Mg}/\text{Fe}] \approx 0.2$ for different IMF slopes are discussed in Chapter 4. The filled circles in the top panel of Fig. 5.1 demonstrate that a shallower IMF with $x = 0.8$ can reconcile the extended star formation history with the observed Mg/Fe (shaded region). However, particularly in the hierarchical picture in which the formation of different galaxy types can be traced back to the same (or similar) building blocks at early epochs, a flattening of the IMF restricted to elliptical galaxies does not provide a compelling solution.

From Fig. 5.1 one can also understand that only galaxy formation scenarios in which star formation *terminates* after 1 – 2 Gyr lead to $\langle [\text{Mg}/\text{Fe}] \rangle \gtrsim 0.2$ dex. The classical monolithic collapse provides such a star formation mode. In the hierarchical scheme, instead, (low) star formation at later stages seems unavoidable, which directly leads to lower Mg/Fe ratios in the stars that form out of the highly SNIa enriched ISM at lower redshift.

5.1.3 Burst populations in the elliptical

The star formation histories considered here apply to the *global* properties of the galaxy populations. However, in the picture of hierarchical clustering star bursts induced by mergers play an important role for the interpretation of (particularly central) abundance features. The star burst during the major merger forms 10 – 30 per cent of the final stellar mass, which is likely to dominate the galaxy core, as the gas is driven to the central regions of the merger remnant (Barnes & Hernquist 1996). In this section, the abundance patterns of the population that results from a 0.1 Gyr star burst triggered by the major merger forming the final elliptical are investigated.

Universal IMF

In Fig. 5.1, the dotted histogram gives the fraction of ellipticals that experienced their last major merger at a given epoch. In the star burst induced by such a major merger, the new stellar population forms out of the ISM the abundances of which are shown by the solid line in Fig. 5.1. Owing to the short duration of the star burst, the mean Mg/Fe ratios in the newly created stars are higher than the initial values in the ISM as indicated by the arrows and the dotted line. The slope of the IMF is assumed Salpeter also during the burst. It turns out that, due to the extremely low Mg/Fe ratios and the high metallicities in the ISM at the merger epoch, such star bursts are inappropriate to raise Mg/Fe up to a level consistent with observational values (shaded region). The resulting Mg/Fe does not differ from the mean average in the global stellar populations.

The metallicity $[\text{Fe}/\text{H}]$ increases to even higher values between 0.3 and 0.5 dex, depending on the burst epoch (bottom panel of Fig. 5.1). Under the assumption that the entire central population forms in the major burst the

model leads to radial metallicity gradients of $0.3 - 0.5$ dex from the inner to the outer parts of the galaxy, in contradiction to observational measurements of ~ 0.2 dex per decade (Davies, Sadler, & Peletier 1993; Kuntschner 1998). A mixture of $3/4 - 1/3$ between burst and global population in the galaxy nucleus is required to smooth the gradient down to the observed value.

The results shown in Fig. 5.1 unfold the principle dilemma in the hierarchical formation picture: the initial conditions in the ISM at the burst epoch, namely super-solar metallicity and sub-solar Mg/Fe, are highly unfavorable for producing α -enhanced populations. As shown in Chapter 4, this incapability of late merger events is independent of the burst timescale and SNIa rates during the burst. The most promising way out to reconcile an intermediate or late merger with α -enhancement is to assume a flattening of the IMF during the star burst.

Variable IMF

The arrows and dotted lines in Fig. 5.3 show the [Mg/Fe] (top panel) and the [Fe/H] (bottom panel) of the burst population if a shallow IMF ($x = 0.8$) *during the burst* is assumed. The chemical evolution of the global ISM is based on Salpeter IMF ($x = 1.35$) as before. It turns out that, with a significant flattening of the IMF, the major merger burst produces a metal-rich α -enhanced stellar population. As shown by the dotted histogram in Fig. 5.3, the bulk of ellipticals experience their major merger at lookback times of $7 - 9$ Gyr ($z \approx 0.7 - 1.5$) and therefore exhibit significant α -enhancement in the burst population.

These burst populations, however, will have metallicities exceeding the observed values, if all the residual gas is consumed during the major merger burst (Fig. 5.3, bottom panel). This issue is discussed in the following section in the context of the mixing of the global and the burst populations.

5.1.4 Global-to-burst population mixtures

If the abundance patterns, in particular the degree of α -enhancement, in global and burst populations are different, the global-to-burst mixture is a key ingredient in determining the final properties of the model galaxy. In the following, I discuss the resulting abundance ratios of the mixed population for different global-to-burst proportions and burst IMF slopes. The global population is always based on Salpeter IMF. If not otherwise specified, abundances always refer to the mixed stellar population, any variation of the IMF slope x_{burst} concerns only the burst population. The major merger is assumed to occur at $z = 1$, so that the burst population is 8 Gyr old throughout the following exercises. The fraction of stellar populations that are assumed to form during the major merger burst is f_{burst} .

Fig. 5.4 shows contours of constant [Mg/Fe] as a function of x_{burst} and the burst fraction f_{burst} . Contours that fit the observationally constrained α -enhancement ($[\alpha/\text{Fe}] \gtrsim 0.2$) are drawn with solid lines. The shaded area marks the range for f_{burst} , that is typically constrained in semi-analytic simulations ($0.1 \lesssim f_{\text{burst}} \lesssim 0.3$). The following conclusions can be drawn:

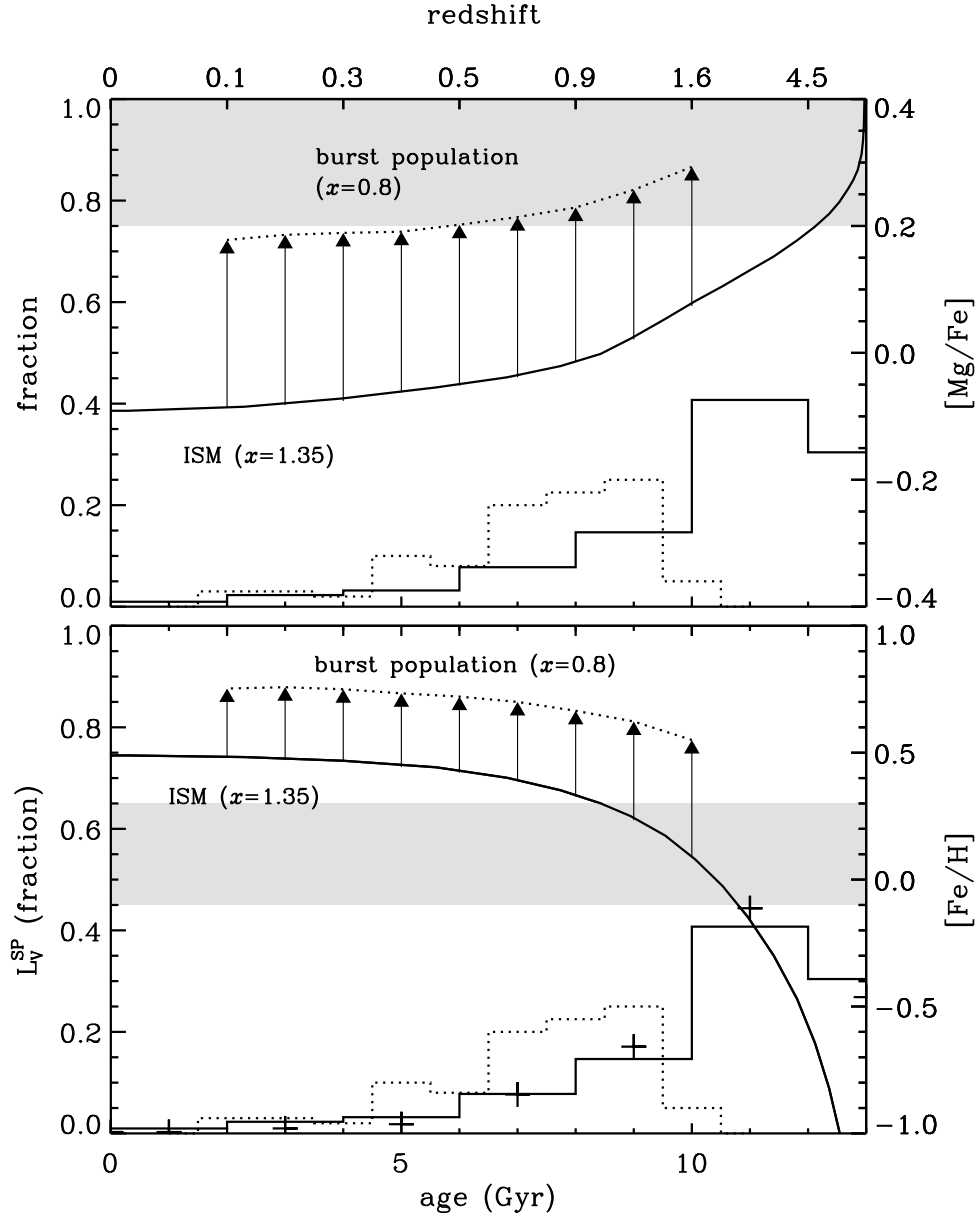


Figure 5.3: $[Mg/Fe]$ (top panel) and $[Fe/H]$ (bottom panel) in the average cluster elliptical with a flatter IMF during the burst. Axis and symbols are explained in Fig. 5.1. A flattening of the IMF ($x = 0.8$) during the major merger burst is assumed. For the evolution of the global interstellar medium (solid line), instead, Salpeter IMF ($x = 1.35$) is adopted.

1. The solid lines and the shaded area occupy two separate regions in the diagram. Hence, within the allowed range of f_{burst} , there is no IMF slope above $x_{\text{burst}} \approx 0$ for which a significantly Mg-enhanced mixed population can be produced.

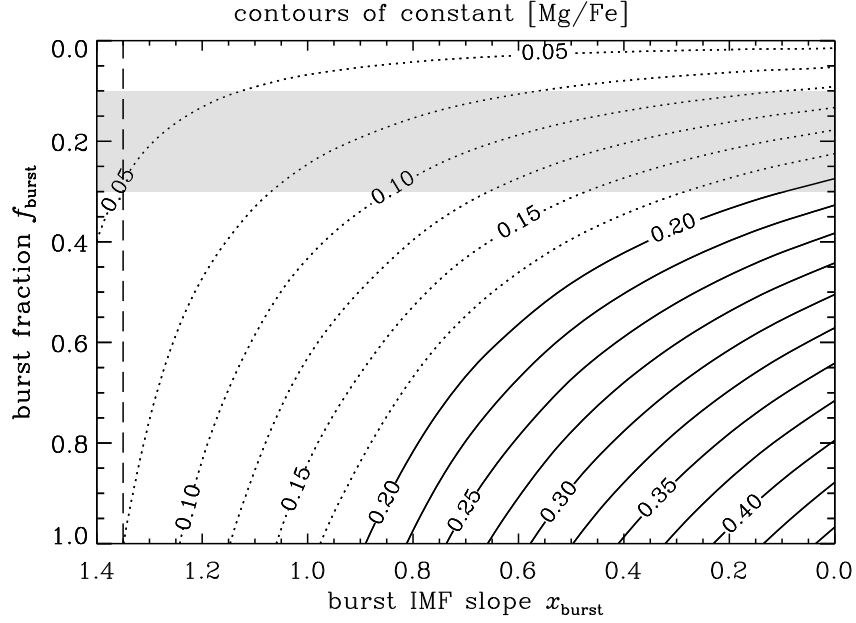


Figure 5.4: Contours of constant $[\text{Mg}/\text{Fe}]$ as a function of the burst fraction and the IMF slope assumed during the merger star burst. The $[\text{Mg}/\text{Fe}]$ values that fit the observations are drawn as solid lines. The shaded region denotes the burst fractions that are typically assumed for major mergers. The vertical dashed line indicates the Salpeter slope.

2. Assuming a universal Salpeter IMF, even the burst population alone does not exhibit super-solar $[\text{Mg}/\text{Fe}]$ ratios (case $f_{\text{burst}} = 1$).
3. The burst population reaches $[\text{Mg}/\text{Fe}] \gtrsim 0.2$ for $x_{\text{burst}} \lesssim 0.9$.

The major conclusion is that the star formation history from Kauffmann (1996) does not yield *globally* $[\text{Mg}/\text{Fe}]$ overabundant ellipticals, even if burst-like star formation at the major merger and a flattening of the burst IMF are taken into account. In other words, the percentage of the burst population (10–30 per cent) seems not large enough, in order to raise the $[\text{Mg}/\text{Fe}]$ *globally*. Note that the color-magnitude relation (Bower, Lucey, & Ellis 1992) and the redshift evolution of the Kormendy relation (Ziegler et al. 1999) constrain the burst strength to be even less than 10 per cent.

A flattening of the IMF generally increases the metallicity yield. The smaller x_{burst} , the more metal-rich the burst population becomes. Fig. 5.5 shows the contours of constant $[\text{Fe}/\text{H}]$ in the mixed stellar population as a function of x_{burst} and f_{burst} . The solid contours mark the metallicities that are compatible with determinations from observed central line indices, that suggest $0 \lesssim [\text{Fe}/\text{H}] \lesssim 0.5$ dex (Mehlert et al. 1998; Kuntschner & Davies 1998; Mehlert et al. 2000). Note that different population synthesis prescriptions, and uncertainties in the fitting functions can influence the metallicity determination by roughly 0.2 dex (Maraston, Greggio, & Thomas 2001). The filled contours

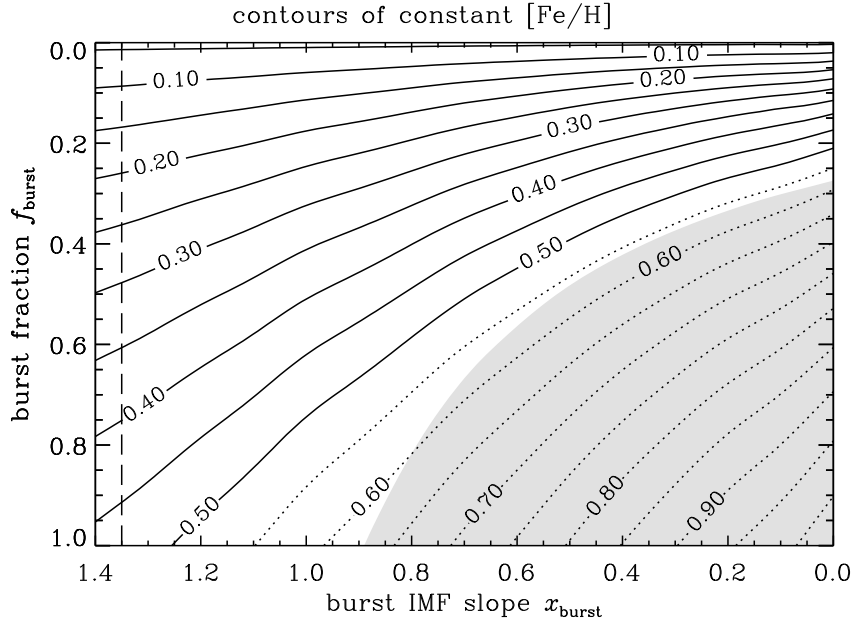


Figure 5.5: Contours of constant $[\text{Fe}/\text{H}]$ as a function of the burst fraction and the IMF slope that is assumed during the merger star burst. The $[\text{Fe}/\text{H}]$ values that fit the observations are drawn with solid lines. The shaded region denotes $f_{\text{burst}}-x_{\text{burst}}$ combinations that yield $[\text{Mg}/\text{Fe}] \gtrsim 0.2$ as shown in Fig. 5.4. The vertical dashed line indicates the Salpeter slope.

show the region of super-solar Mg/Fe ratios from Fig. 5.4. For these sets of x_{burst} and f_{burst} , the resulting metallicities are systematically too high (dotted contour lines). There is no combination of these parameters that matches the observed $[\text{Fe}/\text{H}]$ and Mg/Fe simultaneously.

In order to decrease the metallicity in the burst population, it has to be assumed that not all the available gas is transformed into stars during the major merger. Table 5.1 gives the ratios $[\text{Mg}/\text{Fe}]$ and $[\text{Fe}/\text{H}]$ for different global-burst mixtures, if the IMF slope is $x = 0.8$. $[\text{Fe}/\text{H}]'$ is the metallicity if the efficiency of the star burst is reduced from 99 to 50 per cent. In this way, the resulting metallicities for a dominant burst population can be reduced. It should be emphasized, however, that this additional condition seems contrived. In fact it is more realistic to consider complete gas exhaustion, because the star burst is assumed to take place in a deep potential well, from which the gas cannot escape.

As already mentioned, it is likely that the burst population does not mix homogeneously but dominates the central parts of the galaxy. Table 5.1 can then be interpreted in terms of increasing galaxy radius from bottom to top. Abundance gradients are then the result from different global-burst mixtures at different radii.

In order to explore abundance gradients, the following model is discussed, in which the galaxy is divided in three zones separated by the inner radius r_i

TABLE 5.1
GLOBAL-BURST MIXTURES

Global	Burst	[Mg/Fe]	[Fe/H]	[Fe/H]'
1.0	0.0	0.04	0.00	0.00
0.9	0.1	0.06	0.10	0.05
0.7	0.3	0.11	0.30	0.18
0.5	0.5	0.15	0.44	0.29
0.3	0.7	0.18	0.54	0.37
0.1	0.9	0.21	0.63	0.45
0.0	1.0	0.23	0.66	0.50

NOTE.—The average abundance ratios for different mixtures in V -light of the global (IMF slope $x = 1.35$) and burst ($x = 0.8$) populations. $[\text{Fe}/\text{H}]'$ denotes the metallicity if the efficiency of the star burst is reduced from 99 to 50 per cent. The burst epoch at 8 Gyr is chosen.

and the effective radius r_e . The resulting stellar abundance ratios in each zone for the respective different global-burst mixtures are shown in Table 5.2. Column 2 gives the V -light fraction of each zone, namely 5 per cent from the most inner part, and half of the light within the effective radius r_e . Altogether, the fractional contributions are chosen such that the burst population contributes 30 per cent to the total V -light of the galaxy. The star formation efficiency of the burst population is assumed to be 50 per cent, in order to avoid metallicities that exceed observational determinations (see above). In Table 5.2, the weight of the burst population is steadily decreasing towards the outer zones of the galaxy, which leads to gradients such that both Mg/Fe and Fe/H decrease with increasing radius.

The galaxy nucleus is most metal-rich and significantly α -enhanced, the gradients of both Mg/Fe and Fe/H within r_e , however, are rather shallow. Thus this model predicts the Mg/Fe overabundance not to decline remarkably out to r_e , in accordance with Worthey, Faber, & González (1992) and Davies, Sadler, & Peletier (1993). It is interesting to mention that the tendency of a slight decrease in α -enhancement is found in the Coma cluster sample analyzed by Mehlert et al. (2000). The gradient in metallicity as given in Table 5.2 is also consistent with the observational estimates by Davies, Sadler, & Peletier (1993) and Kuntschner (2000).

I recall here that these central metallicities and Mg/Fe ratios that are consistent with observational data are obtained only under the following assumptions:

1. The center predominantly consists of the burst population formed in the final major merger.

TABLE 5.2
RADIAL GRADIENTS

Zone	Light	Global	Burst	[Mg/Fe]	[Fe/H]'
$0 < r < r_i$	0.05	0.1	0.9	0.21	0.45
$r_i < r < r_e$	0.45	0.5	0.5	0.15	0.29
$r_e < r < \infty$	0.50	0.9	0.1	0.06	0.05

NOTE.—Abundance ratios in the three zones separated by r_i and r_e . Column (2) gives the fraction of the total light provided by the respective zone. Columns (3) and (4) give the global-burst mixtures within each zone. [Fe/H]' (Column 6) is explained in the caption of Table 5.1.

2. The burst population provides at least 30 per cent of the total V -light of the galaxy.
3. The IMF is significantly flattened ($x \lesssim 0.8$) *during the burst* with respect to the Salpeter value ($x = 1.35$).
4. The efficiency of star formation during the burst has to be reduced to roughly 50 per cent, in order to obtain shallow metallicity gradients within the galaxy.

The condition that 30 percent of the stars must have formed in a star burst (item 2), in which only 50 per cent of the gas into stars (item 4), implies that ~ 60 per cent of the galaxy mass at the epoch of the final major merger is gas.

Note furthermore that, except item (1), none of these necessary conditions is well justified.

5.1.5 Summary

In this section, average star formation histories predicted by current hierarchical clustering models are adopted to analyze their capability of producing the α -enhanced abundance ratios observed in elliptical galaxies. The V -luminosity weighted age distributions for the stellar populations of the model spiral and cluster elliptical galaxy are from Kauffmann (1996).

Owing to the constant level of star formation in spiral galaxies, their star formation history leads to roughly solar Mg/Fe ratios in the stars *and* in the ISM, in agreement with observations in the Milky Way. For elliptical galaxies, hierarchical models predict more star formation at high redshift and therefore significantly older mean ages. However, the present analysis shows, that their star formation histories are still too extended in order to accomplish a significant degree of global α -enhancement in the stars. The burst populations and their

proportions to the global populations turn out to play a crucial role in producing Mg/Fe overabundance in the framework of hierarchical galaxy formation. Star bursts ignited by the major merger forming the elliptical may be a possibility to produce metal-rich Mg/Fe overabundant populations, if: (1) the center is dominated by the burst population, (2) the fraction of the burst population is not below 30 per cent, (3) the IMF is flattened during the burst, and (4) the efficiency of star formation during the burst is low. None of these necessary conditions is well justified.

A direct consequence of the model is a small negative gradient in α -enhancement, i.e. α/Fe decreases with increasing radius. It should be emphasized again that the star formation histories discussed here are averages over many Monte Carlo realizations, individual galaxies are therefore not considered. This approach is sensible because the observational constraint has also to be interpreted as a mean α -enhancement about which the values measured for the single galaxies scatter. Still, it is of great interest to analyze the star formation histories of individual galaxies, to compare the theoretical scatter in α -enhancement with the observed one, and to explore the distribution of Mg/Fe values in both cluster and field galaxies of different morphological types and luminosities. This issue is the subject of the following section.

5.2 Individual star formation histories

In collaboration with G. Kauffmann, I explore the global abundance ratios of the individual objects generated via Monte Carlo realizations of the merging paths of dark matter halos. This allows a detailed discussion of the abundance ratios in galaxies of different morphological types, and of the predicted relations to various properties like environmental density, luminosity and disk-to-bulge ratios.

5.2.1 The model

The semi-analytic star formation histories from G. Kauffmann (1999, private communication) are incorporated into the chemical evolution code. They include both quiescent star formation in the disk galaxy progenitors as well as the starbursts triggered by the mergers. Note that the chemical evolution models assume that galaxies evolve as single-body, “closed-box” systems. This is not the case in the hierarchical models, in which supernova feedback effects are thought to be important in driving chemical evolution. Feedback effects could either drive the derived α/Fe ratios up or down, depending on the relative efficiencies with which the products of Type II and Type Ia supernovae are expelled. This will be explored in detail in future work. A universal Salpeter IMF slope $x = 1.35$ is assumed. In the following, $[\text{Mg}/\text{Fe}] \equiv \log(\text{Mg}/\text{Fe}) - \log(\text{Mg}/\text{Fe})_{\odot}$ is the global mean element ratio in the *stellar population* of an individual galaxy. Moreover, element ratios only at redshift zero are considered. The evolution of Mg/Fe with redshift for an average star formation history is discussed in Section 5.1. Results for a cold dark matter power spectrum with $\Omega = 1$, $H_0 = 50 \text{ km s}^{-1} \text{ Mpc}^{-1}$, and $\sigma_8 = 0.67$ are presented.

5.2.2 Environment and morphology

Fig. 5.6 shows the number distribution of Mg/Fe ratios among galaxies of different morphologies in environments of varying density. These distributions are computed by averaging over the galaxies in 15 halos with $V_c = 1000 \text{ km s}^{-1}$ (clusters), 50 halos with $V_c = 500 \text{ km s}^{-1}$ (groups), and 100 halos with $V_c = 300 \text{ km s}^{-1}$ (isolated galaxies).

The Mg/Fe values generally scatter between $0 \lesssim [\text{Mg/Fe}] \lesssim 0.17 \text{ dex}$, with a mean of 0.05–0.08 dex, significantly below the observed estimate. The spread in Mg/Fe results from the scatter in the star formation timescales in the models (Kauffmann 1996). Late-type galaxies experience more extended star formation histories. As a result, these objects have younger stellar populations and exhibit lower Mg/Fe ratios, in qualitative agreement with the observations. Although elliptical galaxies have the highest values of Mg/Fe among the various morphological types, they still do not match the observed α -enhancement. Only the oldest galaxies, which form most of their stars in the first 1–2 Gyr, reach Mg/Fe ratios close to the lower limit set by observations. Lenticular galaxies are predicted to be slightly less α -enhanced than ellipticals.

Galaxies in small halos form their stars over a more extended timescale than galaxies in clusters, where the supply of infalling gas is cut off as soon as the galaxy becomes the satellite of a central object in a larger dark matter halo. As a result, lower Mg/Fe values are found for isolated galaxies. In clusters, the formation is boosted at higher redshift and more galaxies form on short timescales. Bright, isolated ellipticals are thus predicted to have lower Mg/Fe values than their counterparts in clusters. Kauffmann & Charlot (1998a) find that the V -light weighted age difference between bright cluster and “field” ellipticals is $\sim 1 \text{ Gyr}$. This is in good agreement with the estimate by Bernardi et al. (1998), who find that variations in zero-point and slope of the Mg- σ relation of field and cluster ellipticals translate into an age difference of $1.2 \pm 0.35 \text{ Gyr}$. Their study did not include information from Fe-indices and they could not determine whether there were trends in α -enhancement from cluster to field. More work in this area would be very valuable.

5.2.3 Trends with luminosity

In Fig. 5.7, the Mg/Fe values of model ellipticals as a function of V -magnitude are plotted for cluster ellipticals (top panel) and group/isolated ellipticals (bottom panel). Faint ellipticals ($M_V > -20$) are predicted to exhibit a large scatter in Mg/Fe of 0–0.17 dex. Both the scatter and the median value decrease for brighter ellipticals because these objects form later and have younger mean stellar ages. This effect is even stronger in low-density environments.

The region in the diagram that is covered by the data of Trager et al. (2000a, 2000b) is shown as the shaded area. The Mg/Fe ratios predicted by the models for ellipticals of low luminosity with $M_V \gtrsim -19$ are observationally confirmed. However, the observed trend of increasing Mg/Fe with increasing luminosity for both cluster and field ellipticals is in clear contradiction with the hierarchical models. The Mg/Fe ratios predicted by hierarchical clustering for luminous

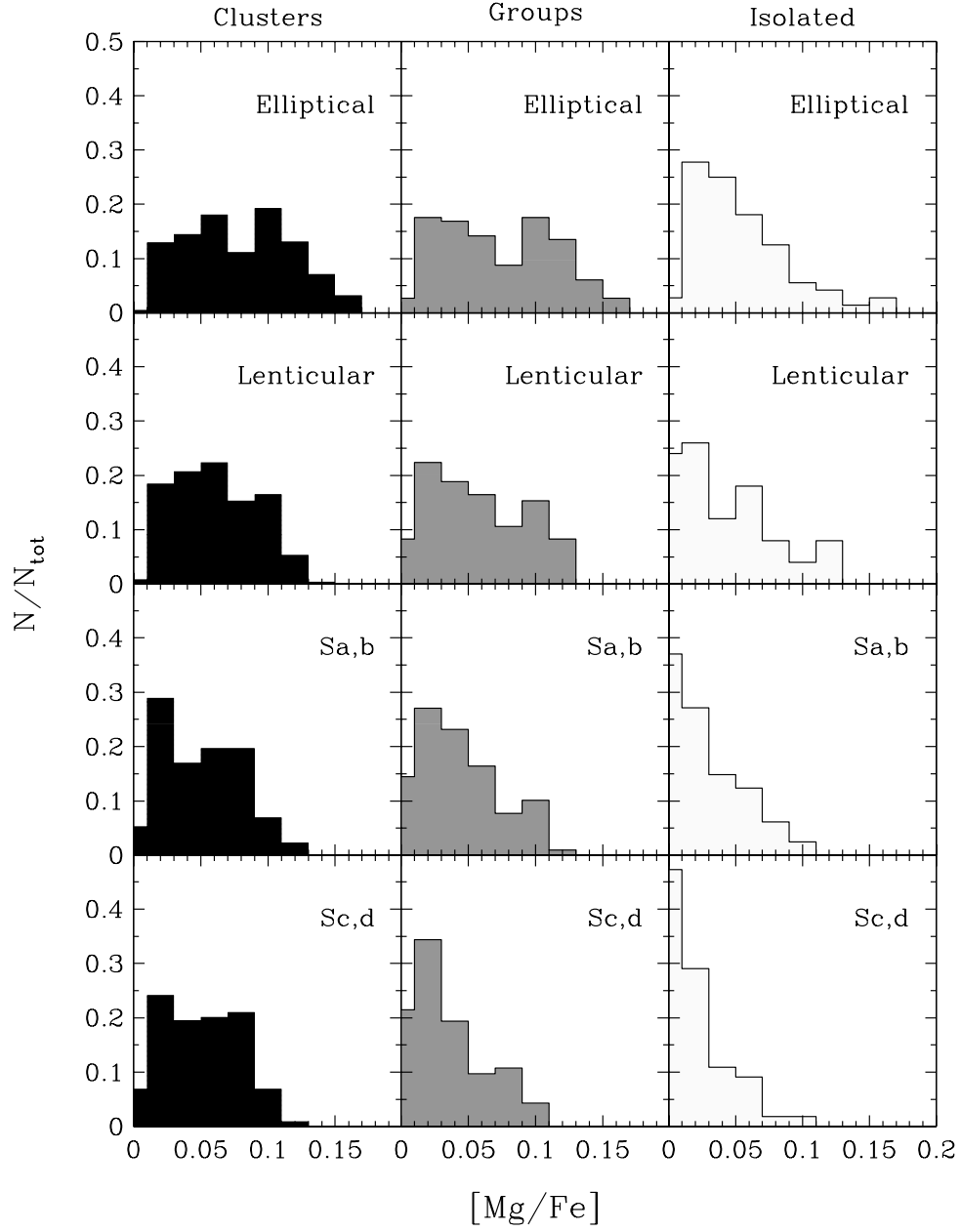


Figure 5.6: Number distribution of global $[\text{Mg}/\text{Fe}]$ ratios among galaxies of different morphologies in environments of varying density.

ellipticals are significantly below the observationally derived values. The reason is that in a hierarchical scheme *massive* objects naturally form later, hence on

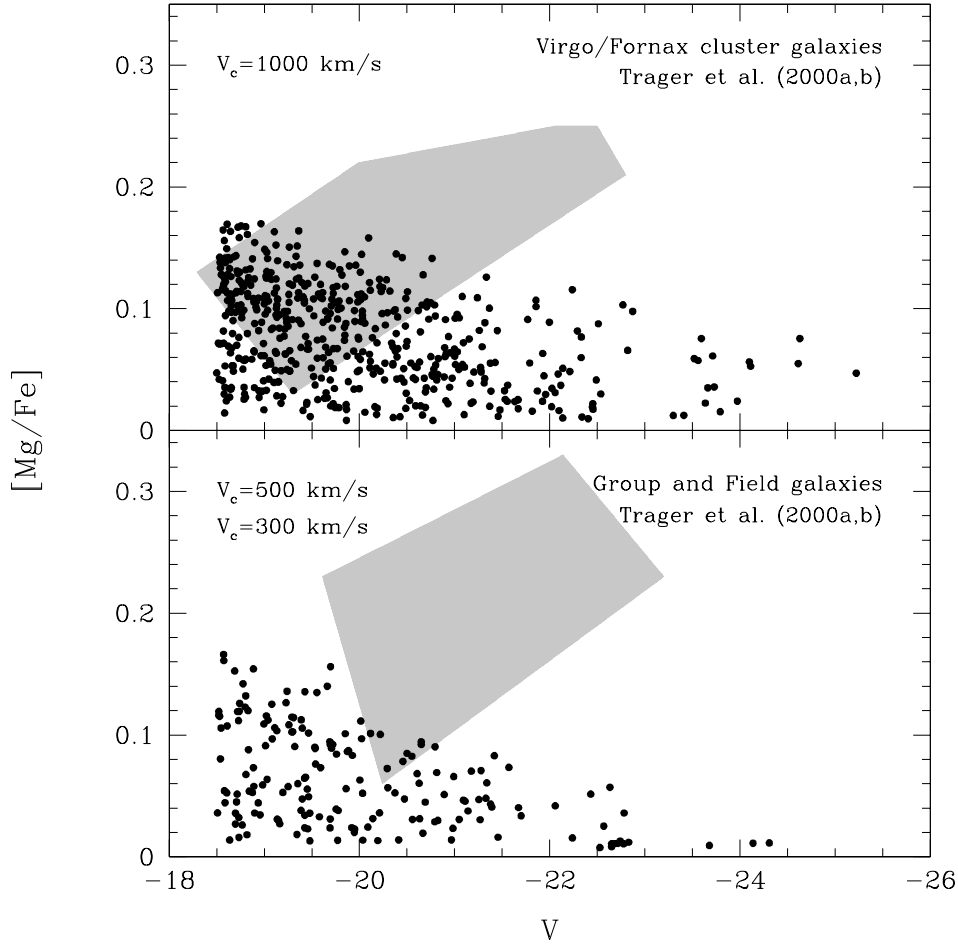


Figure 5.7: Global [Mg/Fe] in the model ellipticals (filled circles) as a function of absolute V -magnitude in a high-density (top panel) and low-density (bottom panel) environment. The data from González (1993) (field, group and Virgo cluster galaxies) and Kuntschner (2000) (Fornax cluster galaxies) analyzed by Trager et al. (2000a,b) are indicated by the shaded regions.

longer timescales, and therefore exhibit lower Mg/Fe. This is an important result, as it is independent of the uncertainties in stellar nucleosynthesis.

5.2.4 Bulges

Bulges are the first spheroids to form in major mergers at high redshift (Kauffmann 1996). Depending on the amount of gas accreted subsequently, these spheroids may become the bulges of spiral galaxies. The classification into morphological type is made according to disk-to-bulge ratios, so that also ellipticals have a minor disk component.

Fig. 5.8 shows the distribution of Mg/Fe among the *bulge components* of galaxies of different types in a variety of environments. The drop of the Mg/Fe

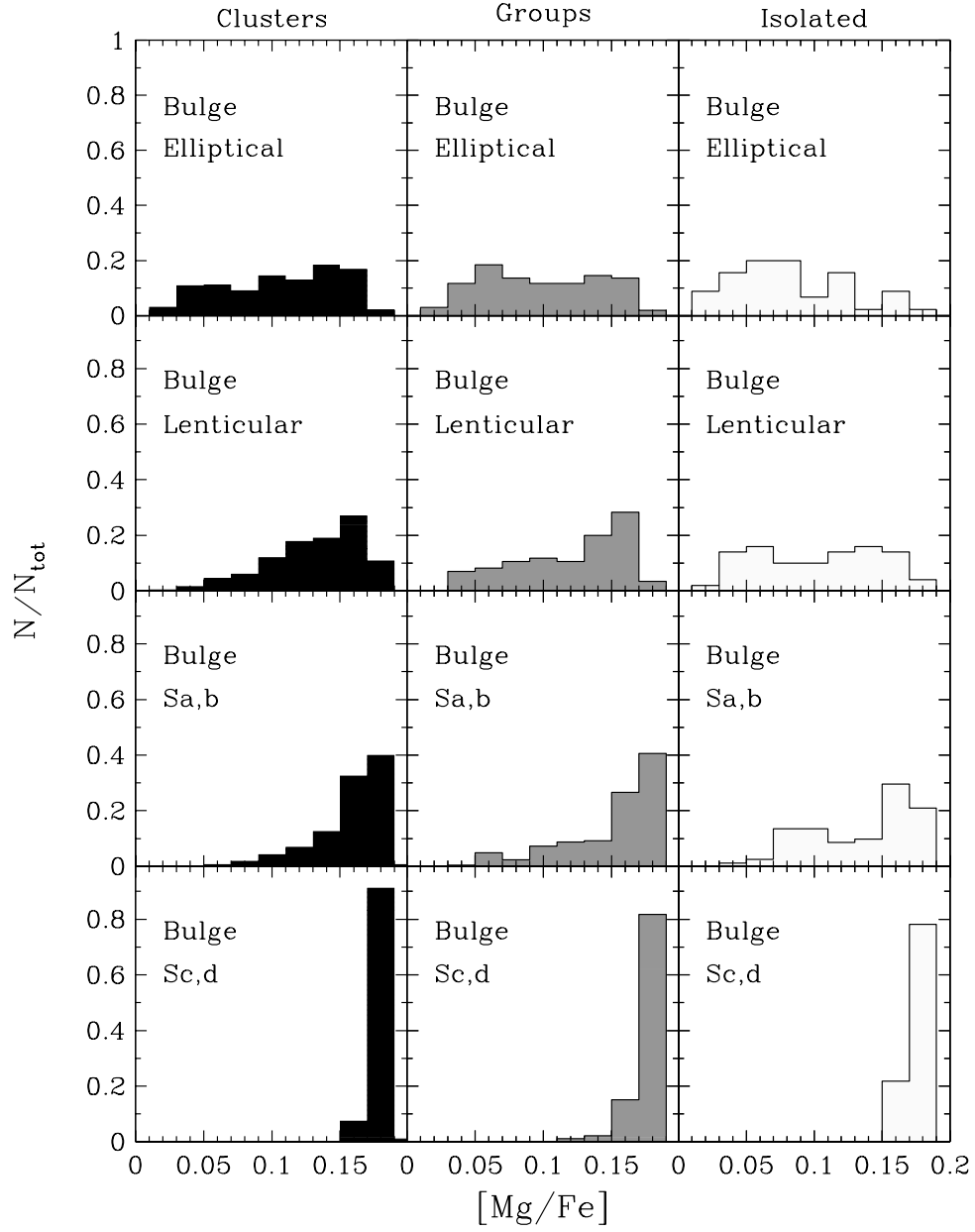


Figure 5.8: Number distribution of $[\text{Mg}/\text{Fe}]$ ratios among bulges in galaxies of different morphologies in environments of varying density.

ratio from high to low density environment is less pronounced in the bulge component. Another striking result is that the bulges of late-type galaxies are

more α -enhanced and exhibit a much smaller scatter in Mg/Fe than those of early-types. This result is expected in a scenario where the bulge forms first and the disk slowly accretes over a Hubble time. Indeed, the α -element enhancement in the bulge of our Galaxy ($[\alpha/\text{Fe}] \sim 0.4$ dex, McWilliam & Rich 1994) exceeds the values recently derived for ellipticals (Trager et al. 2000a). If the bulge forms out of the disk, one would not expect to see such an effect. It would be interesting to study Mg and Fe line indices in the bulges of galaxies of different morphological type in order to test some of these trends (Goudfrooij, Gorgas, & Jablonka 1999; Trager, Dalcanton, & Weiner 1999).

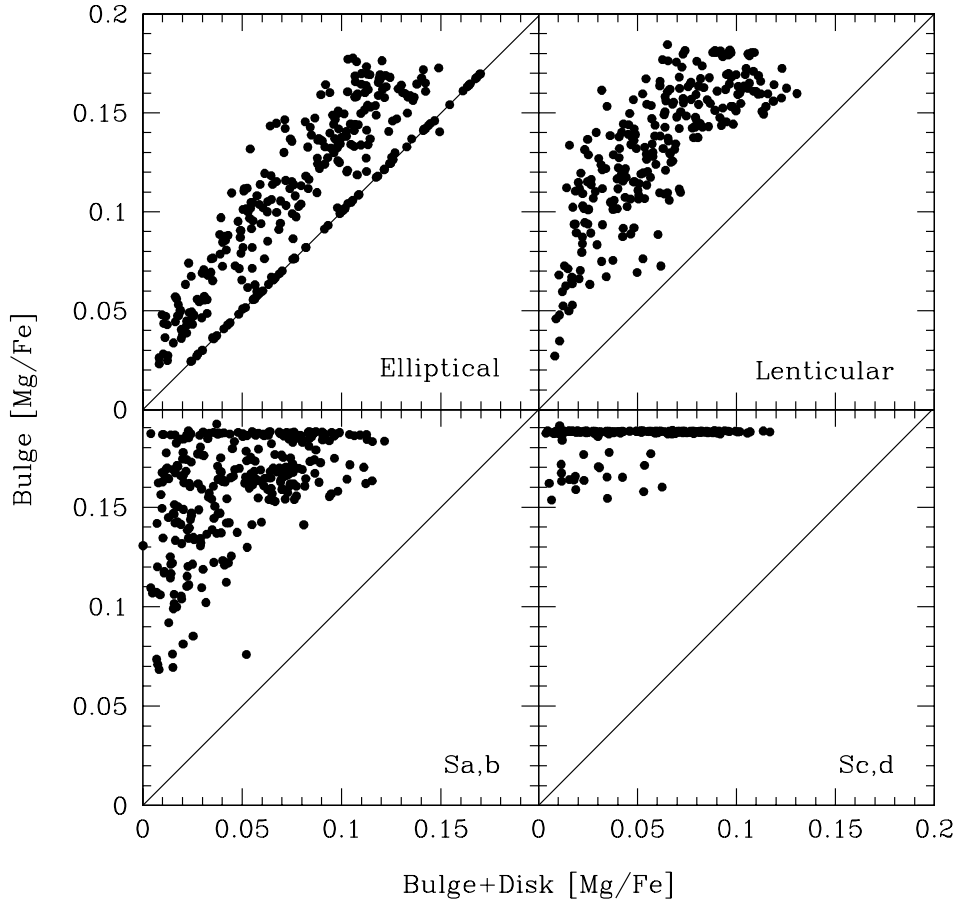


Figure 5.9: $[\text{Mg}/\text{Fe}]$ ratios in bulges of different galaxy types as a function of the global (bulge + disk) $[\text{Mg}/\text{Fe}]$ in the respective galaxies. Rich cluster environment.

In Fig. 5.9, the global value of Mg/Fe is plotted versus the Mg/Fe of the bulge component for different types of galaxies in a rich cluster. The value of Mg/Fe is always higher in the bulge than it is on average and this difference increases for late type galaxies. This result is interesting because the bulge component is expected to be more spatially concentrated, which implies a radial

gradient in Mg/Fe inside the galaxy. In elliptical galaxies, observations indicate that Mg/Fe is constant with radius inside the half-light radius (Worthey, Faber, & González 1992; Davies, Sadler, & Peletier 1993; Fisher, Franx, & Illingworth 1995; Mehlert et al. 2000).

5.2.5 Summary

It is shown that the consideration of individual star formation histories does not alter the main conclusion from the previous section: the current models of hierarchical galaxy formation do not reproduce the Mg/Fe ratios observed in elliptical galaxies. Moreover, the models predict a trend of decreasing Mg/Fe with increasing galaxy luminosity, which is the opposite of what is observed.

The models predict ellipticals in the field to be less α -enhanced than their counterparts in clusters. Furthermore, bulges turn out to exhibit higher Mg/Fe in hierarchical models, as they are the first spheroids to form. The bulge of our Galaxy, for instance, is predicted to be more α -element enhanced than the average elliptical galaxy.

5.3 Discussion

The main conclusion from the present analysis is that the star formation histories, predicted by current hierarchical galaxy formation models for elliptical galaxies, are too extended towards low redshift. Zepf (1997) argues that a burst-like star formation history in the framework of the classical monolithic collapse yields colors that are too red at intermediate redshift. Friaça & Terlevich (1998) developed a modification of the single collapse model by considering radial flows of gas within the galaxy, which leads to more extended star formation histories and to bluer colors (Jimenez et al. 1999). This formation scenario still produces super-solar Mg/Fe ratios, since at least 90 per cent of the stars are created in the first Gyr of the galaxy's evolution. Note that the star formation history from Kauffmann (1996) forms less than 30 per cent in the same time interval.

5.3.1 Universal or variable IMF?

It is shown that a flattening of the IMF during a major merger star burst could in principle reconcile the star formation histories of hierarchical galaxy formation with the observed α -enhancement. However, from a theoretical point of view it is still a controversial issue whether the assumption of a *systematically* variable IMF is sensible (Elmegreen 1997; Melnick & Selman 2000). Although the observational determinations of the IMF slope suffer from a large spread (Scalo 1998), they scatter around the Salpeter value (Elmegreen 1999). So far, there is no compelling evidence for a flattening of the IMF in star bursts with respect to the Salpeter value (Leitherer 1998). In particular, the star bursts of major mergers happen at intermediate redshift in high-metallicity environments, that highly resemble the local conditions for which the Salpeter IMF has been measured. In the single collapse scheme, instead, star bursts occur at high redshift, where the assumption of a different IMF seems more

sensible. It should also be emphasized that an increase of the lower mass cutoff (below $\sim 8 M_{\odot}$), which is often referred to as a ‘top-heavy IMF’, does not solve the α/Fe problem, since it only affects the metallicity yield, but *not* the Mg/Fe ratio.

5.3.2 Selective mass loss

Type Ia supernovae explode later than Type II, thus their ejection occurs at different dynamical stages of the merging history. A scenario in which preferentially Type Ia products (basically iron) are lost in galactic winds, makes it easier to accomplish enhanced Mg/Fe ratios with extended star formation timescales. The examination of this alternative, however, requires a more detailed analysis of the possible outflow and star formation processes during the merging history. On the other hand it is important to notice, that Mg -enhanced giant elliptical galaxies enrich — for Salpeter IMF — the intracluster medium (ICM) with Mg/Fe *underabundant* gas (see Chapter 7). A selective loss mechanism therefore further increases this ICM-galaxy asymmetry (Renzini et al. 1993) which is at odds with the observational evidence of \sim solar Mg/Fe ratios in the ICM (Mushotzky et al. 1996; Ishimaru & Arimoto 1997).

5.3.3 Cluster vs. Field

In a high density environment, the collapse of the density peaks on galaxy scale is boosted at high redshifts. In the low-density surroundings of the field (halos of $10^{13} M_{\odot}$), instead, the situation is entirely different. The Kauffmann (1996) model predicts that objects in the field are not destined to be ellipticals *or* spirals, but actually undergo continuous transformations between both types due to gas accretion (formation of a disk galaxy) or merging of similar sized spirals (formation of an elliptical). As a consequence, most of the objects we observe at present time as bright ellipticals in the field should have had a recent major merger in the past 1.5 Gyr. This leads to younger mean ages, but also to more extended star formation histories. It is shown here that later bursts yield lower Mg/Fe ratios, leading to the prediction that bright ellipticals in the field should be less α -enhanced than their counterparts in clusters. Thus, the *intrinsic* difference between cluster and field ellipticals, which manifests itself most prominent in the properties of *bright* elliptical galaxies, should be measurable in their α -element abundance patterns. Such a cluster-field dichotomy is not observationally confirmed, as the field galaxy samples of González (1993) and more recently of Beuing, Bender, & Mendes de Oliveira (2000) show the same degree of α -enhancement as the cluster galaxy samples. It is also interesting to note that Bernardi et al. (1998) find no significant difference in slope and zero-point of the $\text{Mg}-\sigma$ relation in field and cluster ellipticals.

5.3.4 Early star formation and late assembly?

It is important to emphasize that the properties of galaxies discussed here are the properties of their *stellar populations*. In particular in the framework of CDM hierarchical clustering, one has to distinguish between the epoch of the

formation of the object (e.g., a major merger forms an elliptical) and the epoch of the main star formation. As shown in Fig. 5.1, the final major merger and therefore the formation of an elliptical galaxy occurs in a redshift range where the larger fraction of stars have already formed. Still, star formation is too extended in the model ellipticals, so that the observed Mg/Fe ratios are not reproduced.

Remember that both α -enhancement and the color-magnitude relation constrain the formation ages of the *stellar populations*. Hence, an improvement of the hierarchical models does not necessarily need to concern the assembly of the galaxies, but should rather modify the link between dark matter halo evolution (the merger tree) and star formation. If structures indeed form hierarchically, then no significant star formation should be involved in the major mergers at low and intermediate redshifts.

The option of a late assembly of old stellar populations to a giant elliptical is attractive and can be tested through the redshift evolution of the K band luminosity function (Kauffmann & Charlot 1998b). These authors claim that the deficiency of bright objects at redshift $z \approx 1$ in the samples of Songaila et al. (1994) and Cowie et al. (1996) is better consistent with hierarchical clustering than with a model assuming pure luminosity evolution without merging. Certainly larger samples with better statistical significance are required. Indeed, analyzing the data of a large K band selected survey (Drory et al. 2000), N. Drory et al. (in preparation) find that the number of bright objects at $z = 1$ is neither consistent with pure luminosity evolution nor with the predictions of Kauffmann & Charlot (1998b). An argument against the late assembly of ellipticals, instead, comes from the velocity and density profiles of local elliptical galaxies indicating a high formation redshift ($z_F \approx 5$) not only for the stars but also for the dark matter halos (Gerhard et al. 2000).

Chapter 6

The Ages of Elliptical Galaxies

Almost 30 years ago it has been recognized that the modeling of the spectral energy distribution of ellipticals is affected by an ambiguity in age and metallicity (Tinsley 1972; Faber 1972; O’Connell 1976), which has turned out to be a general complication in population synthesis (Renzini 1986). However, considering Simple Stellar Populations (SSP) in the two-parameter space of Balmer and metallic lines, the age-metallicity degeneracy can be broken (González 1993; Worthey 1994). The major reason for the success of this strategy is that the Balmer line strengths of SSPs are predominantly age sensitive at metallicities above $\sim 1/3 Z_{\odot}$ that are supposed to be the only relevant for elliptical galaxies. Strong $H\beta$ lines are thus taken as an indication for young (intermediate-age) populations, the observed scatter is interpreted as a considerable spread in age (e.g., Faber et al. 1995).

An alternative path to obtain blue stars and hence strong Balmer lines is to consider old *metal-poor* populations. In collaboration with C. Maraston, we follow this approach and compute composite stellar populations that contain an old metal-poor subcomponent. The principal focus is to check if a combination of only old populations can reproduce strong $H\beta$ without invalidating further constraints for ellipticals like metallic indices, colors and spectral energy distributions. The content of this chapter is published in Maraston & Thomas (2000).

6.1 Simple stellar population models

We computed a new set of SSP models based on the population synthesis presented in Maraston (1998), in which the fuel consumption theorem (Renzini & Buzzoni 1986) is adopted to evaluate the energetics of the post main sequence phases. The new SSP models cover the metallicities $-2.25 < [\text{Fe}/\text{H}] < 0.5$ and ages $10^7 - 2 \cdot 10^{10}$ yr. The input stellar tracks are taken from Bono et al. (1997) and S. Cassisi (1999, private communication). These new models are discussed in detail in a future paper (C. Maraston, in preparation). The calibration of the model colors on globular clusters is presented in Maraston (Maraston 1998; Maraston 2000). The calibration of indices and spectral energy distributions of the SSP models that are relevant for the present study are shown in this

chapter.

6.1.1 Spectral line indices

Synthetic line indices for SSPs are computed using the fitting functions from Worthey et al. (1994). Fig. 6.1 shows $H\beta$, Fe5335, and Mgb as a function of $[Fe/H]$ for galactic globular clusters from various data sets (see the caption). Our SSP models of fixed age (15 Gyr) and various metallicities are plotted as solid lines. Dotted lines are the models from Worthey (1994) for $t = 17$ Gyr.

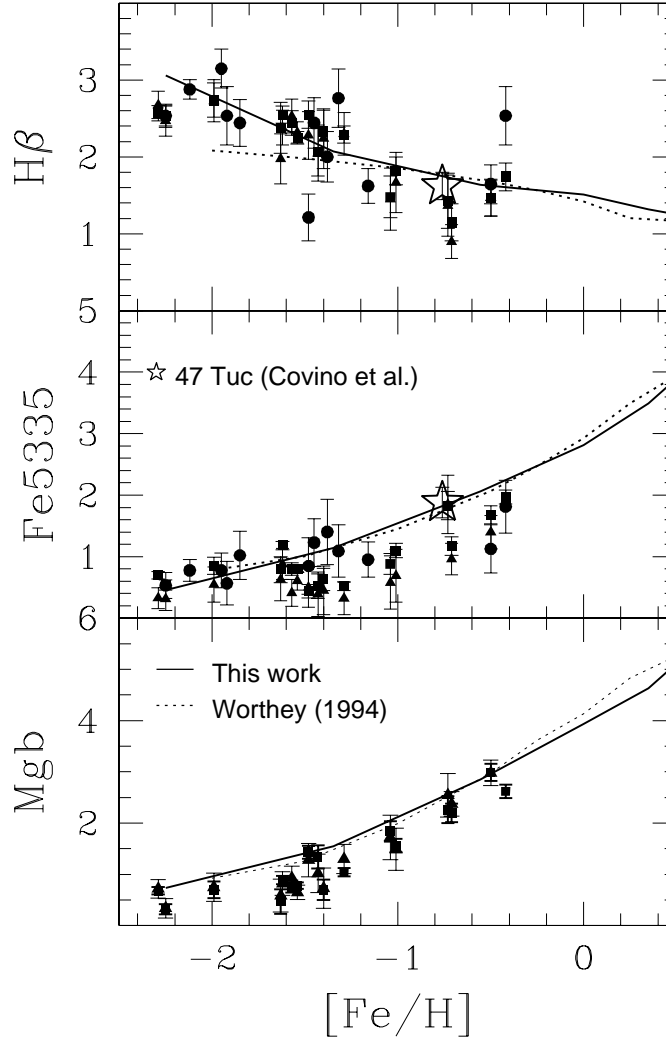


Figure 6.1: Calibration of the SSP models on galactic globular clusters. Data are from Burstein et al. 1984 (squares), Covino, Galletti, & Pasinetti 1995 (circles), and Trager 1998 (triangles). $[Fe/H]$ (Zinn & West (1984) scale) is taken from the Harris (1996) catalogue. Solid lines are our SSPs for age $t = 15$ Gyr. Worthey (1994) SSPs for $t = 17$ Gyr are shown as dotted lines.

As metal-poor stars ($[Fe/H] \lesssim -1.3$) spend their horizontal branch lifetimes

at temperatures $T_{\text{eff}} \gtrsim 5500$ K, $H\beta$ is steeply rising with decreasing $[\text{Fe}/\text{H}]$ (top panel in Fig. 6.1). This observed feature is the key for the present analysis and is well reproduced by our SSPs. The models from Worthey (1994), instead, predict a shallower trend, which implies that the very metal-poor globulars are younger than the more metal-rich ones. The synthetic Fe5335 indices are in good agreement with the Covino, Galletti, & Pasinetti (1995) data, while for $[\text{Fe}/\text{H}] \gtrsim -1.5$ Burstein et al. (1984) and Trager (1998) derive lower values. $\text{Mg } b$ indices seem slightly overestimated by the models at low metallicities.

Our synthetic metallic indices Fe5335, $\text{Mg } b$ and the Balmer line $H\beta$ for $[\text{Fe}/\text{H}] \gtrsim -1.5$ agree well with the models from Worthey (1994), because both sets of models are based on the same fitting functions (Worthey et al. 1994). The uncertainty introduced by the use of different fitting functions is discussed in Maraston, Greggio, & Thomas (2001). The low $H\beta$ values given by Worthey (1994) at very low metallicities are likely due to the assumption of too red horizontal branch morphologies in the models.

As discussed in Worthey et al. (1994), iron indices are favorable as metallicity indicators, because the analysis with Mg -indices is severely affected by α -enhancement. As at high metallicities the fitting functions of Fe5270 are significantly more uncertain (Maraston, Greggio, & Thomas 2001), in the following analysis we focus on $H\beta$ and Fe5335. We additionally consider the color $B-K$ as metallicity indicator which turns out to be in good agreement with Fe5335, while $\text{Mg } b$ systematically implies higher metallicities.

Combining $H\beta$ with Fe5335, for 47 Tuc we obtain a ‘spectroscopic age’ of 15 Gyr (Fig. 6.1) in agreement with the age derived from the color-magnitude diagram (14 ± 1 Gyr, Richer et al. 1996). This example shows that the $H\beta$ -Fe5335 plane is successful at breaking the age-metallicity degeneracy, when applied to simple systems like globular clusters. Note that the high resolution Balmer index $H\gamma_{\text{HR}}$, instead, leads to a ‘spectroscopic age’ in excess of 20 Gyr (Gibson et al. 1999).

6.1.2 Spectral energy distributions

The evolutionary synthesis code of Maraston (1998) is updated for the computation of the SSP spectral energy distributions (SEDs). The spectral library of Lejeune, Cuisinier, & Buser (1998) is adopted to describe the stellar spectra as functions of gravity, temperature and metallicity.

The tightest constraint on the amount and the metallicity of metal-poor stars in elliptical galaxies comes from the flux in the mid-UV (2000–4000 Å). In Fig. 6.2 the calibration of synthetic metal-poor SEDs on galactic globular cluster data in the wavelength range $\lambda = 1500\text{--}3300$ Å (van Albada, de Boer, & Dickens 1981) is presented. The model spectra are in excellent agreement with the data in the whole metallicity range. The increase of the flux shortward 3000 Å with decreasing metallicity is due to a hotter main sequence turnoff and a bluer horizontal branch. Note, however, that there are globulars of intermediate metallicity ($[\text{Fe}/\text{H}] \sim -1.5$) that show horizontal branches bluer than what is expected with the canonical mass-loss on the Red Giant Branch (van Albada, de Boer, & Dickens 1981). This case is shown in the bottom-left panel of Fig. 6.2

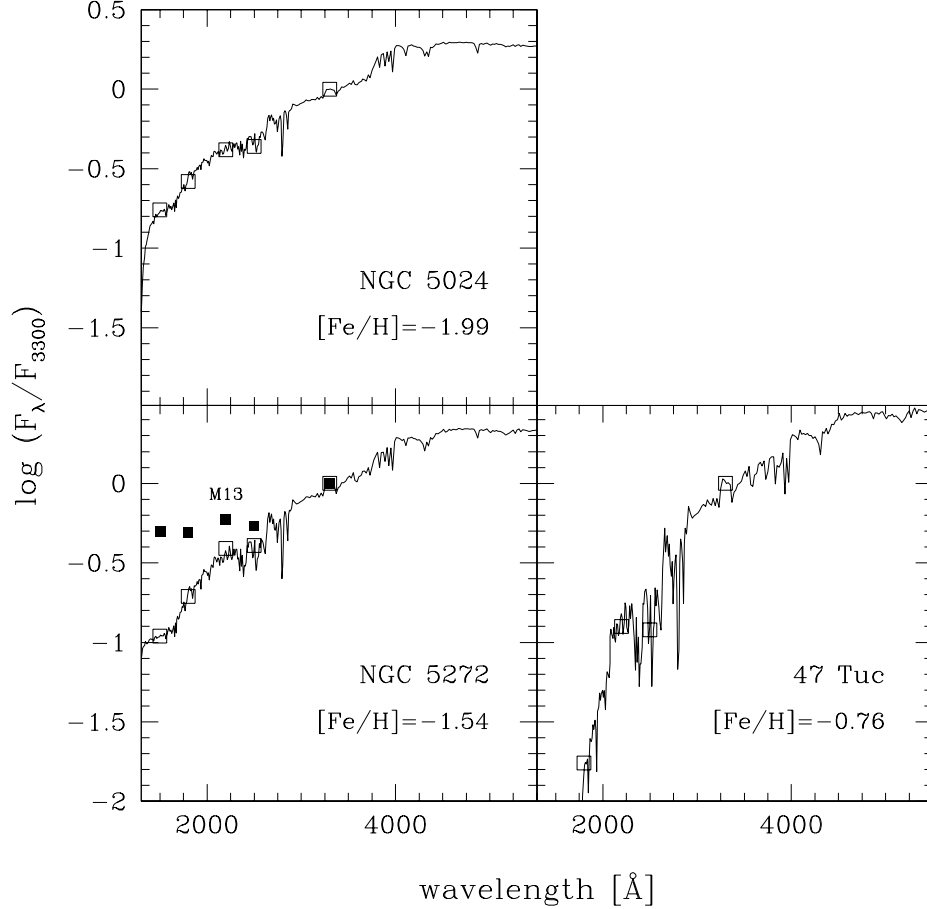


Figure 6.2: Calibration of the synthetic SEDs in the UV on galactic globular clusters. Data (squares) are taken from van Albada, de Boer, & Dickens (1981), $[\text{Fe}/\text{H}]$ (Zinn & West (1984) scale) is adopted from Harris (1996). The filled squares (bottom-left panel) show M13 that has an extreme blue horizontal branch morphology. The solid lines are our model SEDs ($t = 15$ Gyr) with metallicities as indicated in the panels.

for the globulars M13 (NGC 6205, filled squares) and NGC 5272, which have the same metallicity $[\text{Fe}/\text{H}] \sim -1.54$ but different horizontal branch morphologies. M13 contains extreme blue horizontal branch stars (‘blue tails’), and exhibits an excess of flux shortward $\sim 2000 \text{ \AA}$ (see Section 6.2.2).

As such blue tails are preferentially found in denser and more concentrated globulars, it is likely that the particular dynamical conditions in such ‘second parameter’ globular clusters lead to enhanced mass-loss and extremely hot horizontal branch stars (Fusi Pecci et al. 1993), which may not apply to the average stellar field population in galaxies. Since in early-type galaxies globular clusters contribute less than 0.6 per cent to the total V -light (Ashman & Zepf 1998), we adopt the canonical mass loss $\eta = 0.33$ for $[\text{Fe}/\text{H}] \sim -1.5$ calibrated on ‘normal’

globulars like NGC 5272 (Fusi Pecci & Renzini 1975).

6.2 Results

In the following we compare old (> 12 Gyr) composite stellar populations with data of elliptical galaxies. The models consist of two components: a major metal-rich population ($Z = Z_{\text{maj}}$) and a metal-poor subpopulation ($Z = Z_{\text{sub}}$).

6.2.1 Indices and colors

Fig. 6.3 displays $H\beta$ vs. Fe5335 (top panel) and $H\beta$ vs. $B-K$ (bottom panel) for composite models in which the ages of the major population and of the metal-poor subcomponent are fixed to 14 Gyr and 15 Gyr, respectively. The contribution from the low-metallicity population is 10 per cent by mass.

The grid in Fig. 6.3 shows models for various metallicities of the two components. Solid lines connect models with constant metallicity of the major component $Z_{\text{maj}} = 0.5, 1, 2, 3 Z_{\odot}$ (from left to right). The metallicity of the subcomponent is $Z_{\text{sub}} = 0.05$ (large open squares) and $Z_{\text{sub}} = 0.005 Z_{\odot}$ (large open circles). For comparison, simple stellar populations with metallicities $Z = Z_{\text{maj}}$ and $t = t_{\text{maj}}$ are shown as large open triangles. The dotted (horizontal) lines mark models of constant Z_{sub} .

The perturbation of metal-rich simple stellar populations with metal-poor stars leads to lower Fe5335 line strengths, bluer $B-K$ colors, and stronger Balmer lines. The models with $Z_{\text{sub}} = 0.005 Z_{\odot}$ reach $H\beta \sim 2 \text{ \AA}$. Observed line strengths (González 1993; Kuntschner & Davies 1998; Mehlert et al. 2000) and colors (Pahre 1998) of elliptical galaxies and lenticular galaxies are shown as small filled and small open symbols, respectively. The present set of composite models match the area that is covered by the majority of the galaxy data. Note that the objects exhibiting $H\beta > 2 \text{ \AA}$ are either classified as lenticular galaxies (small open symbols) or they are intermediate-mass *field* ellipticals (NGC 1700, NGC 3377, NGC 5831, NGC 6702, NGC 7454) or dwarf ellipticals (M32 (NGC 221), NGC 4489) from the González (1993) sample. All *luminous field ellipticals* and all *cluster ellipticals* (Coma, Fornax, and Virgo) in Fig. 6.3, instead, can be modeled with the old composite populations introduced above. It should be emphasized that the bulk of ellipticals scatter around $H\beta \sim 1.6 \text{ \AA}$, so that less than 10 per cent contribution from metal-poor stars is required in most cases. The observed range $H\beta \sim 1.3 - 2.0$ is then due to a spread in the metallicity and/or the weight of the metal-poor subcomponent. The analysis with simple stellar population models, instead, yields an *age*-spread of $\sim 7 - 15$ Gyr.

Another striking feature of Fig. 6.3 is that the positions of the galaxy data relative to each other are the same in the Fe5335 (top panel) and the $B-K$ (bottom panel) diagrams. Moreover, the locations of the model grids relative to the data points in the two panels are in good agreement, so that both the metallic index Fe5335 and the color $B-K$ consistently constrain the metallicity range for the major component to $1 - 3 Z_{\odot}$. This strongly reinforces the use of Fe5335 as metallicity indicator (see Section 6.1.2). In Fig. 6.4, the same data

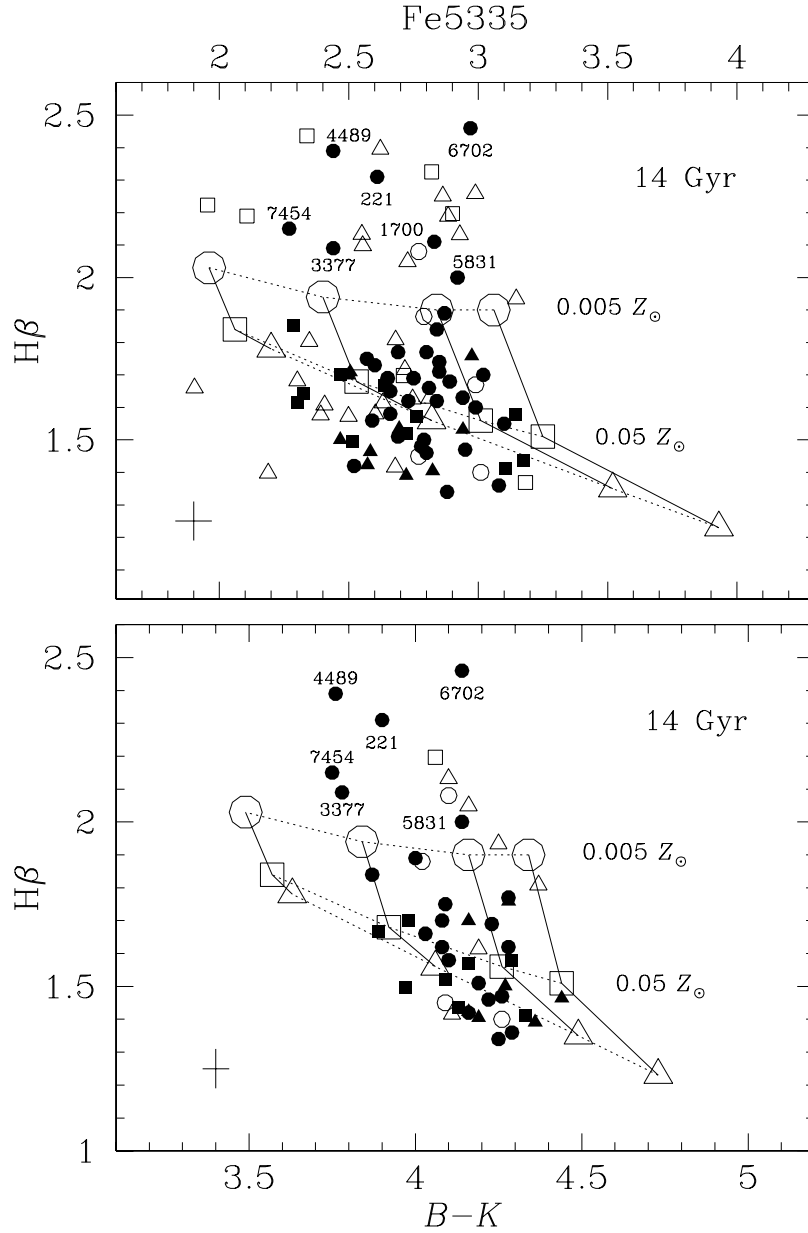


Figure 6.3: $H\beta$ vs. Fe5335 (top panel) and $B-K$ (bottom panel) for elliptical (small filled symbols) and lenticular (small open symbols) galaxies. Data are from González 1993 (circles, $R_e/8$ aperture, Virgo and field, labels indicate NGC numbers), Kuntschner & Davies 1998 (squares, Fornax), and Mehlert et al. 2000 (triangles, Coma). $B-K$ colors are taken from Pahre (1998). The error bars denote average 1σ errors. SSP models for $Z_{\text{SSP}} = 0.5, 1, 2, 3 Z_{\odot}$ are large open triangles, with Z_{SSP} increasing from left to right. Composite models for $Z_{\text{maj}} = Z_{\text{SSP}}$ and $Z_{\text{sub}} = 0.05, 0.005 Z_{\odot}$ are indicated by large open squares and large open circles. Solid and dotted lines denote fixed Z_{maj} and fixed Z_{sub} , respectively. The metal-poor subpopulation contributes 10 per cent by mass. The ages of the major component and the subcomponent are 14 Gyr and 15 Gyr, respectively.

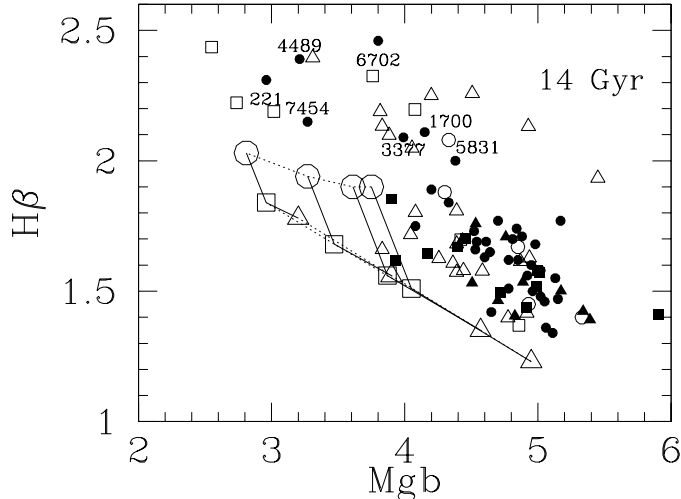


Figure 6.4: $H\beta$ vs. $Mg\,b$. Symbols and linestyles like in Fig. 6.3.

and the same model grid in the $H\beta$ - $Mg\,b$ plane are shown. As discussed above, Mg lines of ellipticals are generally stronger than any SSP model. This feature is attributed to an enhancement of Mg in luminous ellipticals. As a consequence the metallicities derived from the Mg -indices are substantially higher and provoke severe inconsistencies with observed colors (see also Saglia et al. 2000). As the latter are much less affected by abundance ratio anomalies, the $H\beta$ - $B-K$ plane represents the more reliable constraint on stellar population models.

Note that the $H\beta$ line index additionally suffers from uncertainties in the correction for contamination by emission (González 1993), which can lead to an underestimation of the observed $H\beta$ line strength. This effect may explain the low values $H\beta \lesssim 1.5$ Å that fall below the model grid in Fig. 6.3.

6.2.2 Constraints from the mid-UV

The fluxes radiated by metal-poor stellar populations are high in the mid-UV (2000–4000 Å), and decrease shortward 2000 Å (Fig. 6.2). The so-called UV-upturn below 2000 Å observed in elliptical galaxies (Burstein et al. 1988), instead, is most likely due to late evolutionary phases of old metal-rich populations (Dorman, O’Connell, & Rood 1995; Yi, Demarque, & Oemler 1998; Greggio & Renzini 1990; Greggio & Renzini 1999). The amount of metal-poor stars in elliptical galaxies is therefore tightly constrained by the flux in the mid-UV around 2500 Å.

A model based on the closed-box metallicity distribution is not compatible with the mid-UV flux of the elliptical galaxies NGC 4649 and NGC 1404 (Bresnan, Chiosi, & Fagotto 1994) and of the M31 bulge (Worthey, Dorman, & Jones 1996), which is referred to as the G-dwarf problem for ellipticals. On the other hand, Lotz, Ferguson, & Bohlin (2000) find that the spectra of ellipticals in the mid-UV even require the addition of a metal-poor component. In the following we investigate if the proportions of metal-poor stars required to explain the $H\beta$

line strengths are consistent with the fluxes observed in the mid-UV.

The objects with the strongest $H\beta$ (~ 1.65) that we obtain from cross correlating the samples of González (1993), Kuntschner & Davies (1998), and Mehlert et al. (2000) with the Burstein et al. (1988) sample ('quiescent objects') are M31 (NGC 224), NGC 4472, and NGC 3379. We additionally consider NGC 4649, which exhibits a low $H\beta = 1.40$. These objects cover a large range in $1500-V$ colors, NGC 4649 having the strongest UV-upturn. In the following we check if the composite models for these specific galaxies are in agreement with their SEDs. In order to constrain the flux from the metal-poor population in the mid-UV, it is necessary to model the UV-upturn. Following the description by Greggio & Renzini (1990), hot ($T \sim 25,000$ K) late evolutionary phases in the metal-rich components are included in the models, such that the observed UV rising branches are reproduced.

The main model parameters for each galaxy are listed in Table 6.1. Column (3) specifies the mass fractions (per cent) of the two components. Note that less than 10 per cent is required in all cases. The metallicities, ages, indices ($H\beta$, Fe5335, Mg b), and colors ($B-K$, $U-V$) of the two populations are given in Columns (4)–(10). The fuel F_{UV} (in M_{\odot}) in late evolutionary phases required to reproduce the observed UV-upturn is given in Column (11).

In Table 6.2 the relative contributions to $H\beta$ and to the total fluxes at the wavelengths 5550 (V -band), 3600 (U -band), 2500, and 1500 Å are presented. The weight of the metal-poor component increases with decreasing λ , with a maximum contribution in the mid-UV (~ 2500 Å) as the rising branch shortward 2000 Å is produced by the metal-rich component. It is important to emphasize that in the model proposed here, the Balmer line strengths and the UV upturn do not have a common origin: strong $H\beta$ is obtained with *metal-poor* (hot) horizontal branch stars, while blue $1500-V$ colors are due to extremely hot old *metal-rich* stars. The trend of decreasing $H\beta$ with increasing Mg₂ and decreasing $1500-V$ (Burstein et al. 1988) is therefore not affected.

In Table 6.3 the resulting indices and colors of the composed models are compared with the observed values. The indices $H\beta$, Fe5335 and the colors $B-K$, $U-V$ are in good agreement with observations.

The fits to the observed SEDs are shown in Fig. 6.5 as thick solid lines, the dotted lines are the SEDs of the metal-poor and the metal-rich components. The spectra in the UV (open symbols) are from Burstein et al. (1988) and L. Buson (1999, private communication), the spectro-photometry in the optical (thin solid lines) is from D. Hamilton (1999, private communication). In all cases, the observed spectra are well reproduced in the full wavelength range $\lambda = 1200-6000$ Å. Thus the amount of metal-poor stars required to reproduce the observed $H\beta$ (see Table 6.1) is consistent with the fluxes in the mid-UV, the model spectra perfectly match the minimum around 2500 Å. In the following, the individual galaxies are briefly discussed.

M31

As shown in Table 6.1, the observables of M31 (for the colors see NGC 4472) with $Z_{\text{sub}} = 0.005 Z_{\odot}$ contributing 3 per cent to the total mass of the population

TABLE 6.1
MODEL PARAMETERS

Galaxy (1)	Comp. (2)	Mass (%) (3)	$Z (Z_{\odot})$ (4)	t (Gyr) (5)	$H\beta$ (6)	Fe5335 (7)	Mg b (8)	$B-K$ (9)	$U-V$ (10)	$F_{UV} (M_{\odot})$ (11)
M31	major	97	1.750	12	1.51	3.20	4.38	4.34	1.73	0.003
	sub	3	0.005	15	3.09	0.53	0.78	2.64	0.53	–
N4472	major	94	2.000	12	1.48	3.32	4.54	4.42	1.81	0.003
	sub	6	0.030	15	2.33	1.02	1.38	2.91	0.72	–
N3379	major	99	1.000	14	1.56	2.82	3.90	4.06	1.59	0.002
	sub	1	0.005	15	3.09	0.53	0.78	2.64	0.53	–
N4649	major	90	1.550	15	1.38	3.21	4.41	4.36	1.73	0.020
	sub	10	0.300	15	1.69	2.08	2.87	3.53	1.15	–

TABLE 6.2
FLUX CONTRIBUTIONS

Galaxy	H β	5550Å	3600Å	2500Å	1500Å
M31	9	6	17	61	28
N4472	16	12	30	70	16
N3379	4	2	5	33	14
N4649	19	17	27	16	0

NOTE.—The Table gives the relative contributions from the subcomponent in per cent to H β (Column (2)) and to the flux at the wavelengths specified in Columns (3)–(6).

are reproduced, which corresponds to 6 per cent in V , 9 per cent at H β and 61 per cent at $\lambda = 2500$ Å. Wu et al. (1980), instead, claim that not more than 50 per cent contribution from a metal-poor component at $\lambda = 2500$ Å is compatible with the mid-UV flux of M31. The reason for this ostensible discrepancy is that the authors fix the metallicity of the metal-rich component to $Z_{\text{maj}} = 0.5 Z_{\odot}$, which is lower than the value adopted here by more than a factor of 3 (see Table 6.1). As the SED of a more metal-rich population has lower flux in the mid-UV, our composite model requires a larger contribution from the metal-poor component. Using exactly the same prescriptions as these authors, our models are consistent with their result. Due to the low metallicity of the metal-rich component, however, the model of Wu et al. (1980) fails in reproducing the other observational constraints of M31: it results in colors that are too blue ($B - K = 3.48$, $U - V = 1.21$), Fe indices that are too low ($\text{Fe}5335 = 2.01$), and Balmer line strengths that are too high ($\text{H}\beta = 2.07$).

NGC 4472

As the Virgo elliptical NGC 4472 has virtually the same properties as M31, it can be modeled with the same set of populations. The model given in the second line of Table 6.1 is an alternative option for both objects assuming a higher contribution from the metal-poor subcomponent and a higher metallicity of the major population. As a consequence, the contribution from the low-metallicity population increases to 70 per cent at 2500 Å and to 12 per cent in V . Wu et al. (1980) derive a lower contribution in V relative to 2500 Å (50 per cent at 2500 Å and 6 per cent in V), because the authors chose the globular cluster M13 (NGC 6205) as a representative of the metal-poor population. As discussed in Section 6.1.2, this particular globular cluster has an extreme blue horizontal branch morphology and exhibits very high fluxes in the mid-UV (see Fig. 6.2), which implies a lower V over 2500 Å flux ratio.

TABLE 6.3
RESULTS

Galaxy	H β		Fe5335		B-K		U-V	
	Model	Observed	Model	Observed	Model	Observed	Model	Observed
M31	1.65	1.67 ± 0.07	3.04	2.99 ± 0.06	4.26	—	1.61	—
N4472	1.62	1.62 ± 0.06	3.04	2.84 ± 0.08	4.28	4.28	1.59	1.57
N3379	1.62	1.62 ± 0.05	2.77	2.73 ± 0.04	4.05	4.08	1.55	1.52
N4649	1.44	1.40 ± 0.05	3.01	3.01 ± 0.05	4.24	4.26	1.61	1.61

NOTE.—Indices and colors of the models given in Table 6.1. Index data (1σ errors) are from González (1993), $B-K$ from Pahre (1998), and $U-V$ from Trager (1998).

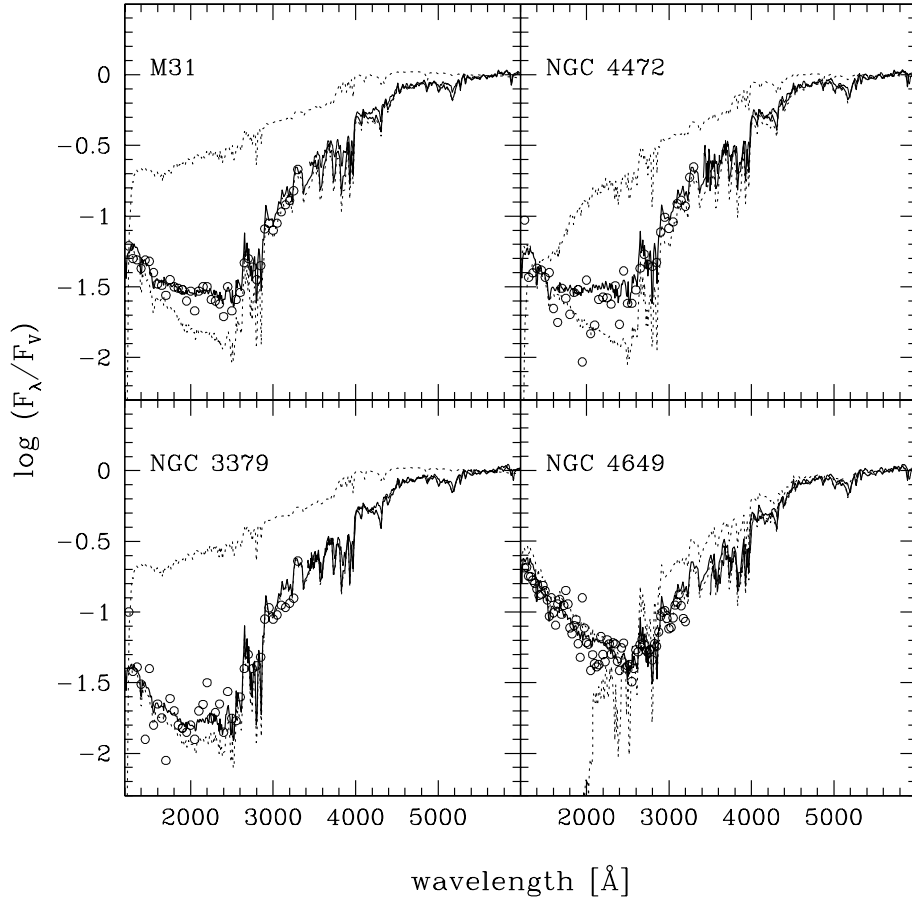


Figure 6.5: Spectral energy distributions as a function of wavelength. *IUE* data for $\lambda \leq 3300$ Å (circles) are from (Burstein et al. 1988) and L. Buson (1999, private communication); the spectro-photometry for $\lambda \geq 3440$ Å (thin solid lines) is from D. Hamilton (1999, private communication). The models from Table 6.1 are shown as thick solid lines, dotted lines are the SEDs of the metal-poor and the metal-rich components (100 per cent), respectively.

NGC 3379

NGC 3379 exhibits equally high $H\beta$, but bluer colors and lower metallic indices. The best fitting model thus has a lower $Z_{\text{maj}} = Z_{\odot}$ and requires only 1 per cent of $Z_{\text{sub}} = 0.005 Z_{\odot}$.

NGC 4649

NGC 4649 has the strongest UV upturn (bluest 1500–V), requiring a factor of ~ 10 more fuel at late evolutionary phases than the other cases (see Column (11) in Table 6.1). Given the low $H\beta$ line strength, the best fit is obtained with a

model containing only old metal-rich populations ($Z_{\text{sub}} = 0.3 Z_{\odot}$). This object strongly supports the view that the UV rising branch and $H\beta$ line strength are not produced by the same kind of stars.

6.2.3 Models for $H\beta > 2 \text{ \AA}$

The model grid in Fig. 6.3 extends to $H\beta \approx 2 \text{ \AA}$, while some low-mass and dwarf ellipticals exhibit stronger Balmer lines. In principle such high $H\beta$ can be obtained by increasing the weight of the low-metallicity component. For instance, the compact elliptical M32 (NGC 221) with $H\beta = 2.37 \pm 0.12$, $\text{Fe5335} = 2.54 \pm 0.20$ (Kormendy & Bender 1999) can be modeled by the 14 Gyr old two-component population with $Z_{\text{maj}} = 2 - 3 Z_{\odot}$ and 20 per cent of $Z_{\text{sub}} = 0.005 Z_{\odot}$. The SED of this model with such a large fraction of very metal-poor stars, however is not compatible with the fluxes observed in the mid-UV (see also Burstein et al. 1988; Rose & Deng 1999). On the other hand, from a deep *HST* color magnitude diagram, Grillmair et al. (1996) conclude that there is no evidence for an intermediate age population ($t \lesssim 2 \text{ Gyr}$). It is worth mentioning, however, that M32 is a peculiar object that does not have the properties of the average elliptical galaxy population.

Alternatively to the addition of metal-poor stars, metal-rich populations with blue horizontal branch morphologies could reproduce strong $H\beta$ without invoking young ages. Such hot horizontal branch stars are indeed observed in the metal-rich globular clusters NGC 6388 and NGC 6441 of the galactic bulge (Rich et al. 1997) and in M32 (Brown et al. 2000). A possible mechanism to produce these temperatures is enhanced mass loss along the RGB evolutionary phase. The investigation of this channel to obtain strong $H\beta$ in old metal-rich populations is the subject of future investigations.

6.3 Discussion

6.3.1 Metallicity distributions in ellipticals

The principle idea of this study is to enhance the Balmer line strengths of old metal-rich stellar populations with a small fraction of metal-poor stars. The real metallicity distribution of the stellar populations in elliptical galaxies is difficult to assess observationally, as the stars cannot be resolved. The *HST* color magnitude diagram of M32 (Grillmair et al. 1996) and the spectroscopy of K giants in the Bulge (Rich 1988) show that these spheroids contain a tail of low metallicity stars. The closest giant elliptical for which color magnitude diagrams are available is NGC 5128 (Harris, Harris, & Poole 1999). Analyzing deep *HST* images in the outer halo of NGC 5128, the authors find a differential metallicity distribution that is well reproduced by two closed-box-like chemical enrichment scenarios implying a large number of extremely metal-poor stars. In particular the differential shape of the distribution implies a formation picture in which a metal-poor and a metal-rich population are formed separately from each other.

This picture gets further support from a number of studies that discover bimodal color and metallicity distributions of globular clusters in at least half of the early-type galaxy population (Zepf & Ashman 1993; Gebhardt & Kissler-Patig 1999). Spectroscopic and photometric investigations indicate that both populations are old (Kissler-Patig et al. 1998; Cohen, Blakeslee, & Ryzhov 1998; Kissler-Patig, Forbes, & Minniti 1998; Kundu et al. 1999; Puzia et al. 1999). More specifically, Puzia et al. (1999) find that the two populations in NGC 4472 are old and coeval, with metallicities $\sim 0.05 Z_{\odot}$ and $\sim Z_{\odot}$, which has recently been confirmed spectroscopically (Beasley et al. 2000). In the framework of hierarchical structure formation galaxies are built by mergers of smaller objects (e.g., White & Rees 1978; White & Frenk 1991; Kauffmann, White, & Guiderdoni 1993). A merger of coeval systems without newly induced star formation would result in a coeval composite population. The accretion of a dwarf galaxy by a larger system (minor merger) qualitatively explains the existence of a metal-poor subpopulation.

There is an additional important effect that is independent of the assumed scheme of galaxy formation. As discussed by Greggio (1997), a sizable fraction of metal-poor stars from the outer parts of a galaxy contaminate the light coming from the center due to projection and orbital mixing (Ciotti, Stiavelli, & Braccetti 1995). The authors find that projection effects lower the actual central metallicity by roughly 10 per cent. The metal-poor components in the composite models of M31, NGC 4472 and NGC 3379 (Table 6.1) dilute the metallicities of the metal-rich populations by 3, 6, and 4 per cent, respectively. Projection effects alone thus may be sufficient to explain the amount of metal-poor stars considered in the present analysis.

6.3.2 Evidence against recent star formation

There are observational indications from the Fundamental Plane (Djorgovski & Davis 1987; Dressler et al. 1987; Bender, Burstein, & Faber 1992; Bender, Burstein, & Faber 1993; Renzini & Ciotti 1993) and the color-magnitude relation (Bender, Burstein, & Faber 1992) that limit the fraction of the young population to less than 10 per cent. As late star formation leads to low α/Fe ratios (see Chapters 4 and 5), the addition of a young population provokes severe inconsistencies with the high α/Fe ratios observed in elliptical galaxies. Also the redshift evolution of colors (Aragón Salamanca et al. 1993), of the Mg- σ relation (Bender, Ziegler, & Bruzual 1996), of the Kormendy relation (Ziegler et al. 1999), and of the color gradients in cluster ellipticals (Saglia et al. 2000) leave little space for a significant contribution from a young subcomponent. The addition of an old, metal-poor population as discussed in this chapter can reconcile these findings with strong Balmer lines.

Disturbed field ellipticals that have strong H β absorption (Schweizer et al. 1990) and blue optical colors (Schweizer & Seitzer 1992) do not show any signature of recent star formation activity in the infrared colors (Silva & Bothun 1998a; Silva & Bothun 1998b). As discussed by these authors, recent mergers may not have been accompanied by significant star formation, but metallicity effects are favored to explain the enhanced H β line strengths.

6.4 Summary

In this chapter it is shown that strong Balmer lines can be produced by composite populations that contain a small fraction of old *metal-poor* stars.

The key to this result is that at low metallicities and old ages our SSP models show a steep increase of $H\beta$ with decreasing metallicity, in accordance to what is observed in metal-poor globular clusters. Composite stellar population models are computed consisting of an underlying old metal-rich population and a small fraction of an old metal-poor subcomponent. Assuming a 10 per cent contribution from metal-poor stars, a grid of models in the $H\beta$ -Fe5335 and the $H\beta$ - $B-K$ planes is constructed reproducing $H\beta$ up to 2 \AA and covering most of the elliptical galaxy data. It should be emphasized that the same conclusion holds for all Balmer lines, e.g. $H\gamma$ and $H\delta$. More specifically, the data of all cluster and luminous field ellipticals can be explained by our models without invoking young ages. The scatter in Balmer line strengths is then caused by a spread in the metallicity and/or the weight of the metal-poor component. Most ellipticals can be modeled with less than 10 per cent of metal-poor stars as the data scatter about $H\beta \sim 1.6 \text{ \AA}$.

It is further shown that the spectral energy distributions of the composite models that reproduce the indices and colors of representative examples agree well with the observed spectra in the wavelength range 1200–6000 \AA . Our models are perfectly compatible with the observed minimum at 2500 \AA , that tightly constrains the possible amount of metal-poor stars.

We conclude that the age-metallicity degeneracy for complex systems like elliptical galaxies still remains to be solved. The perturbation with old *metal-poor* stars to obtain strong Balmer lines is alternative to the addition of a *young* metal-rich population (e.g., de Jong & Davies 1997; Kuntschner 2000; Longhetti et al. 2000). The key to discriminate between the two options lies in the evolution of Balmer lines with redshift. A young population of 2–5 Gyr should leave its fingerprints with a significant peak of Balmer line strengths at redshifts $z \sim 0.15\text{--}0.4$, depending on the cosmology, which has not been detected so far (Ziegler & Bender 1997). The model presented here, instead, predicts Balmer lines to become monotonically stronger with increasing redshift.

Chapter 7

Galaxy Clusters

Galaxy clusters are ideal laboratories to study the chemical enrichment processes on larger scales. In contrast to galaxies, clusters can be considered as closed box systems, so that all elements ejected from galaxies via galactic winds should be present in the intracluster medium (ICM). The analysis of element abundances and element ratios in the ICM therefore provides insight in the formation and evolution of galaxy clusters, and allows to check the consistency of models describing the chemical evolution of cluster galaxies.

The main observational constraints are the large amount of iron present in the ICM, implying very high so-called iron mass-to-light ratios (Ciotti et al. 1991; Renzini et al. 1993), and the roughly solar Mg/Fe ratios found by the *ASCA* satellite (Mushotzky et al. 1996; Ishimaru & Arimoto 1997). The principal focus of this chapter is to analyze the contributions from galaxies of different luminosities to the ICM enrichment adopting the cluster composite luminosity function recently determined by Trentham (1998). The content of this chapter is partly published in Thomas (1999b).

7.1 Observational diagnostics

Clusters of galaxies contain a huge amount of hot gas with temperatures $2.5 \lesssim kT \lesssim 5$ keV exhibiting continuum radiation in the soft X-ray. The presence of Fe emission lines in the X-ray spectrum further indicates that the hot intracluster gas does not have primordial element abundances but contains metals (Mitchell et al. 1976; Serlemitsos et al. 1977). L- and K-shell atomic physics are used in order to determine element abundances analyzing the equivalent widths of the emission lines. For the high temperatures of the ICM, the resulting iron abundance $Z_{\text{ICM}}^{\text{Fe}} \sim 0.3 Z_{\odot}^{\text{Fe}}$ is rather reliable, while the abundances of α -elements are still affected by uncertainties due to the weakness of these emission lines.

The 1/3-solar Fe abundance together with the large amount of gas between the galaxies in clusters implies the large iron mass-to-light ratios mentioned above. Indeed it turns out that there is as much iron between the galaxies as there is in their stellar populations (Renzini et al. 1993), and it is still a controversial issue which type of supernovae is the dominating source of the

intracluster Fe.

7.2 The luminosity function

In their comprehensive analysis of cluster properties, Arnaud et al. (1992) find that the total mass of iron ($M_{\text{Fe}}^{\text{ICM}}$) in the ICM is directly proportional to the luminosity of E/S0 cluster members. In particular there is no correlation with the spiral population. The logical conclusion is that ellipticals and lenticular galaxies dominate the chemical enrichment of the ICM.

On the other hand, there are several indications for additional ICM sources. At the very faint end, the galaxy luminosity function does not follow the simple Schechter (1976) shape, but steepens for objects fainter than $M_B \approx -14$ (e.g. Driver et al. 1994). Trentham (1994) even concludes that the entire ICM gas may originate from dwarf systems, which is in turn doubted by Gibson & Matteucci (1997). These authors, however, do not adopt a luminosity function covering the whole luminosity range but assume a certain contribution from dwarf galaxies that is consistent with extragalactic background measurements. Hence, the role of dwarf galaxies for the ICM enrichment is still a controversial issue. Moreover, intergalactic stars which are stripped from galaxies are theoretically predicted to contain 10–70 per cent of the cluster mass (Moore, Katz, & Lake 1998). Indeed, intergalactic planetary nebulae (Mendez et al. 1997) and RGB stars (Ferguson, Tanvir, & von Hippel 1998) have been found in the Virgo cluster. Finally, semi-analytic models of hierarchical galaxy formation predict that dwarf galaxies deliver up to 40 per cent of the ICM metals (Kauffmann & Charlot 1998a).

The aim of this study is to analyze the relative contributions from galaxies of different luminosities and masses to the ICM enrichment for a luminosity function covering the complete range of luminosities as derived by Trentham (1998) from composite cluster data. The data points by Trentham (1998) are shown in Fig. 7.1 as filled squares. The data can be fit by the following double-power law (Loveday 1997):

$$\phi(L) \sim (L/L^*)^\alpha \exp(-L/L^*) [1 + (L/L_t)^\beta] \quad (7.1)$$

The following parameters are chosen: $M_B^* = -20.3$, $M_t = -14.1$, $\alpha = -1.2$, $\beta = -0.7_{-0.2}^{+0.4}$. The luminosity function in clusters essentially consists of two populations: giant ellipticals and dwarf ellipticals (Binggeli, Sandage, & Tammann 1988; Trentham 1998). While the luminous objects typically follow a Gaussian distribution (e.g., Binggeli, Sandage, & Tammann 1988), the number of dwarf galaxies increases with decreasing luminosity, in agreement with other recent determinations (e.g., Zucca et al. 1997). At intermediate luminosities, there seems to be a conspiracy of the two luminosity functions such that the convolved luminosity function is flat around $-18 \lesssim M_B \lesssim -15$.

The histograms give the fractional contributions of the luminosity bins to the total number of galaxies (light-gray) and to the total B -luminosity (dark-gray). The steep slope $\alpha + \beta = -1.9$ at the very faint end results in a huge number of dwarf galaxies, so that dwarf ellipticals by far dominate the cluster population

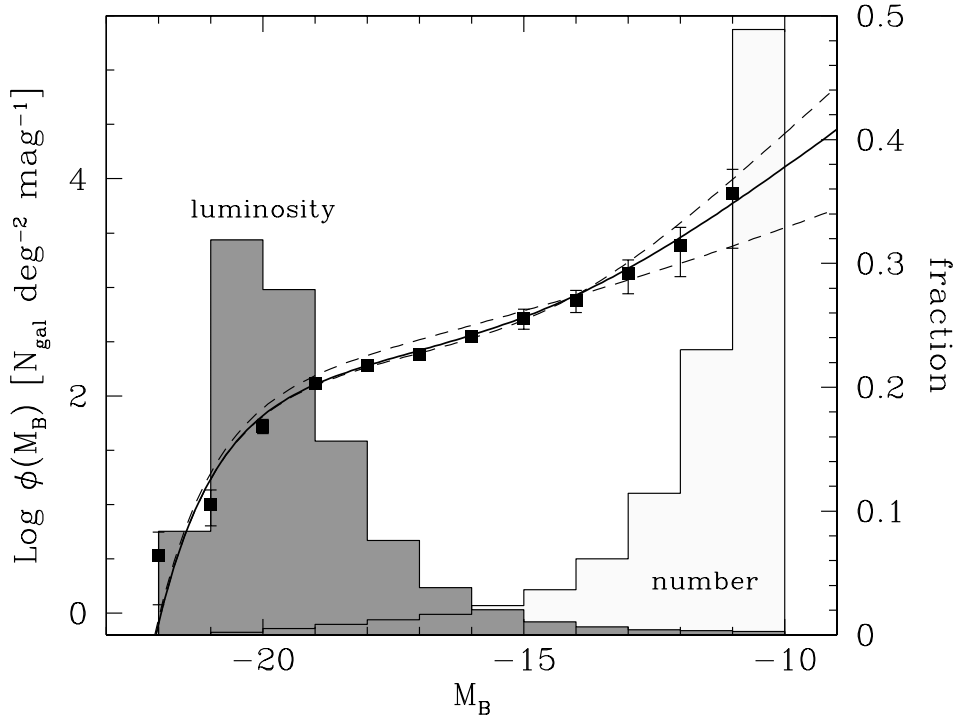


Figure 7.1: Luminosity function (left y-axis) from Trentham (1998) composite cluster data. The fit (solid line) yields the following values for the parameters of Equation 7.1: $M^* = -20.3$, $M_t = -14.1$, $\alpha = -1.2$, $\beta = -0.7$. The two long-dashed lines show the fit for $\beta = -0.3$ and $\beta = -0.9$, respectively. The fractional contributions (right y-axis) from the individual luminosity bins to total L_B and number of the galaxies are indicated by the dark-gray and light-gray histograms, respectively.

by number. The contribution of these objects to the total B -luminosity of a cluster, however, is negligible, as shown by the dark-gray histogram in Fig. 7.1. The cluster luminosity is clearly dominated by galaxies around L^* .

7.3 The model

7.3.1 Chemical evolution

The code of chemical evolution used for the present analysis is calibrated and tested on the abundance features in the solar neighborhood and in elliptical galaxies as described in Chapters 3 and 4. The slope above $1 M_\odot$ of the stellar initial mass function (IMF) is assumed universally Salpeter ($x = 1.35$). A flattening of the slope below $1 M_\odot$ with a turnover mass of $0.5 M_\odot$ is assumed following the recent determinations by Gould, Bahcall, & Flynn (1997). Type II supernova nucleosynthesis is taken from Thielemann, Nomoto, & Hashimoto (1996) and Nomoto et al. (1997).

7.3.2 Metallicity-luminosity relation

Before calculating the ejecta in galactic winds from the galaxy population in the cluster, the galactic chemical evolution for the various galaxy luminosities have to be modeled. For the cluster enrichment, it is crucial how much gas a galaxy of a given luminosity ejects. As the cluster population is dominated by gas-poor spheroidal systems (Trentham 1998), in the present simplified model I assume that the mass fraction $1 - f_{\text{trans}}$ of the galaxy that is not transformed into stars is ejected to the intergalactic space including the delayed stellar ejecta from low-mass stars and Type Ia supernovae. The latter assumption is based on hydro-dynamical models for gas flows in ellipticals by Ciotti et al. (1991), who find that the bulk of ellipticals are still in an outflow phase driven by Type Ia supernova heating. Hence, the mass ejected is

$$M_{\text{ej}} = (1 - f_{\text{trans}}) \cdot M_{\text{tot}} \quad (7.2)$$

The mass fraction f_{trans} that is transformed into stars determines the predicted mean metallicity $\langle Z \rangle$ of the stellar populations in the galaxy. The delayed enrichment of iron from Type Ia supernovae causes only a slight dependence of the metallicity on star formation timescales, that is negligible at first order. The driving parameter is f_{trans} as shown in Fig. 7.2, in which total metallicities $[Z/H]$ and iron abundances $[\text{Fe}/H]$ are plotted as functions of transformed gas fraction. The mean abundances in the stars are the thick lines, the abundances in the ISM 13 Gyr after beginning of star formation are the thin lines. The line-styles refer to the star formation timescales 1 Gyr (solid), 6 Gyr (dashed), and 11 Gyr (dotted).

The abundances in the ISM are always higher than the stellar average. Due to the delayed iron enrichment mentioned above, the mean metallicities in the stars increase by $\sim 2 \times 0.1$ dex when the star formation timescale is increased from 1 to 6 Gyr and from 6 to 11 Gyr. Note that the effect on the iron abundance is larger. For the same reasons, the mean $[Z/H]$ in the stars is larger than the mean $[\text{Fe}/H]$, with the opposite pattern in the ISM. The model with $\tau_{\text{SF}} = 1$ Gyr (solid lines) is the relevant one for the present study, as the α -enhanced abundance ratios of early-type galaxies constrain their formation timescales to be not significantly longer than 1 Gyr (Chapter 4). The Mg/Fe ratios as functions of f_{trans} are discussed in more detail in Section 7.3.3.

Taking the mean stellar $[Z/H]$ of the $\tau_{\text{SF}} = 1$ Gyr model, f_{trans} can be related to B -luminosity using the empirical correlation found by Zaritsky, Kennicutt, & Huchra (1994). The resulting M_B is given by the upper x-axis in Fig. 7.2. Finally, theoretical metallicity and age dependent stellar M/L_B ratios (Maraston 1998; Maraston 1999) are used to assign to every luminosity a total stellar mass ($f_{\text{trans}} \cdot M_{\text{tot}}$) determining the ejected mass as a function of M_B following Equation 7.2.

7.3.3 Galaxy-cluster asymmetry

In Fig. 7.3, Mg/Fe ratios are plotted as a function of f_{trans} in the same manner as Fig. 7.2. In contrast to the mean metallicity, the mean Mg/Fe in the stars is now

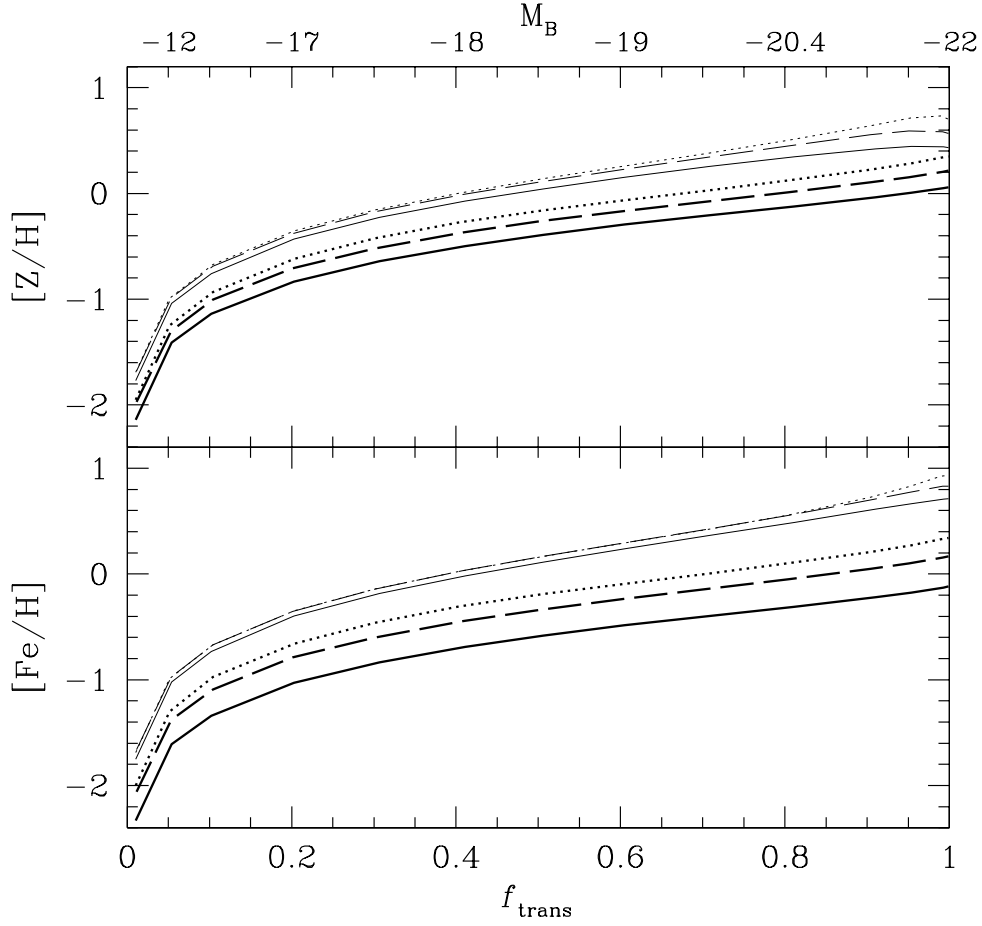


Figure 7.2: Metallicities (top panel) and iron abundances (bottom panel) as functions of transformed gas fractions. The thick lines give the mean abundance in the stellar populations of the galaxy. The abundances in the interstellar medium 13 Gyr after beginning of star formation are the thin lines. Cases for the star formation timescales $\tau_{\text{SF}} = 1$ Gyr (solid lines), $\tau_{\text{SF}} = 6$ Gyr (dashed lines), and $\tau_{\text{SF}} = 11$ Gyr (dotted lines) are plotted. In order to relate f_{trans} values to B -luminosity (upper x-axis) the mean stellar $[Z/H]$ ($\tau_{\text{SF}} = 1$ Gyr) is transformed to M_B using the empirical correlation found by Zaritsky, Kennicutt, & Huchra (1994).

very sensitive to the star formation timescale assumed. Only for $\tau_{\text{SF}} = 1$ Gyr the stars are significantly α -enhanced (thick solid line), which is the model adopted for the enrichment of the ICM. For the dwarf ellipticals the case is less clear, although they seem to exhibit solar or even sub-solar Mg/Fe as will be discussed in Chapter 8. For the purpose of the ICM enrichment, however, this uncertainty does not play a significant role, as for small f_{trans} the Mg/Fe in the ISM is only little sensitive to τ_{SF} (Fig. 7.3 and discussion below).

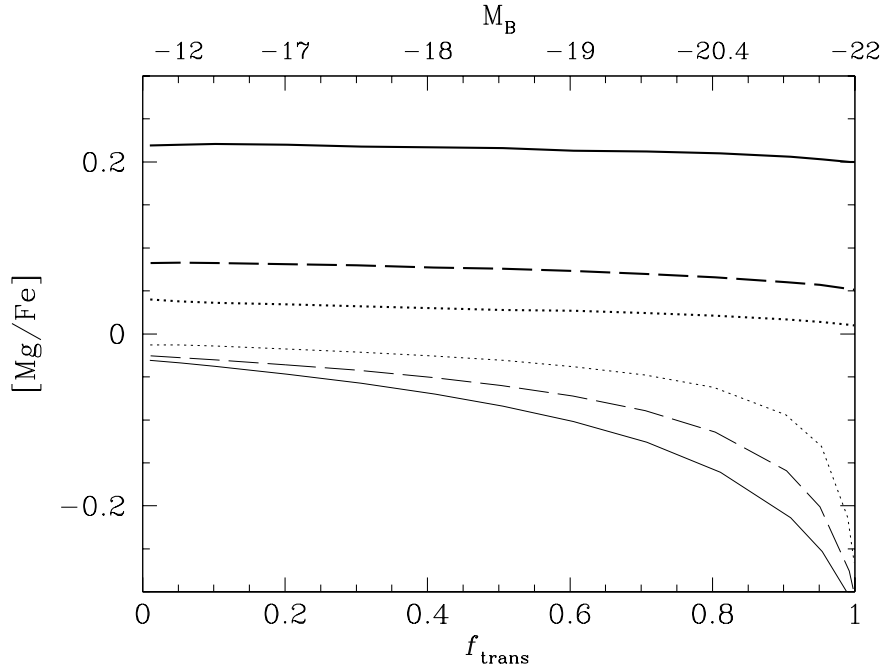


Figure 7.3: Abundance ratio Mg/Fe as a function of transformed gas fraction. The thick lines give the mean abundance ratio in the stellar populations of the galaxy. The Mg/Fe in the interstellar medium 13 Gyr after beginning of star formation are the thin lines. Cases for the star formation timescales $\tau_{\text{SF}} = 1$ Gyr (solid lines), $\tau_{\text{SF}} = 6$ Gyr (dashed lines), and $\tau_{\text{SF}} = 11$ Gyr (dotted lines) are plotted.

Fig. 7.3 shows a further important aspect: the so-called galaxy-cluster asymmetry already discussed by Renzini et al. (1993). While the stellar populations of an object have super-solar Mg/Fe (thick lines), the galactic wind including the Type Ia supernova products (mainly iron) is highly Mg/Fe underabundant (thin lines). This effect is strongest for the shortest star formation timescale (solid lines). Hence, if giant ellipticals would alone enrich the ICM, we would expect the ICM to have significantly sub-solar α/Fe ratios. This prediction, however, is in clear conflict with the solar abundance ratios recently derived from data of the *ASCA* satellite (Mushotzky et al. 1996; Ishimaru & Arimoto 1997). Mushotzky et al. (1996) even claim to have found super-solar Mg/Fe in the ICM, which would imply the main contribution to the ICM enrichment to come from Type II supernovae. In order to obtain super-solar Mg/Fe *and* the huge amount of iron found in the ICM, Loewenstein & Mushotzky (1996) and Gibson, Loewenstein, & Mushotzky (1997) had to assume a considerable flattening of the IMF assigning the main role of ICM enrichment (including Fe) to SNII. Ishimaru & Arimoto (1997), on the other hand, show that Mushotzky et al. (1996) derive a super-solar Mg/Fe, because they normalize to the *photospheric* solar Fe abundance given by Anders & Grevesse (1989), which is ~ 0.2 dex higher. Adopting the meteoritic values from Anders & Grevesse (1989) — as in most chemical evolution models —, instead, the apparent super-solar Mg/Fe is cor-

rected down to a solar value. This correction mainly impacts on the question, which type of supernovae provides the intracluster iron, as solar Mg/Fe ratios imply a significant contribution from Type Ia (Renzini 1997). Note, however, that the problem of the galaxy-cluster asymmetry is still present, if only massive ellipticals enrich the ICM. The argument that part of the iron from SNIa explosions is not ejected from the galaxy but remains bound to the galaxy in the interstellar medium is not promising, as the iron abundances measured in the ISM of ellipticals are much lower than expected (Arimoto et al. 1997).

Fig. 7.3 shows that there is yet another possible solution. The galaxy-cluster asymmetry is most prominent in luminous metal-rich ellipticals, while metal-poor dwarf ellipticals eject material with approximately solar Mg/Fe, independent of their star formation timescales. This feature has the following reason. As long as stars are forming, they enrich the ISM with SNII products (high Mg/Fe) plus SNIa products (mainly Fe) with a delay of $\sim 0.1 - 1$ Gyr. Once the star formation ceases, no more Mg is blown into the ISM, while the Fe abundance increases due to SNIa explosions. The net result is the decrease of the Mg/Fe in the ISM. In the most extreme case that all of the gas has been turned into stars (the most metal-rich massive ellipticals), the fingerprint of the previous Type II supernovae is wiped out, the highly Fe abundant delayed ejecta from the stellar populations dominate the abundance features of the galactic wind blown into the intracluster space. The less gas is processed to stars (in case of the dwarf galaxies), instead, the more SNII products are still present in the ejected ISM, and the galactic wind has considerable higher Mg/Fe. This trend is shown quantitatively in Fig. 7.3, in which the Mg/Fe in the ISM (thin lines) decreases with increasing f_{trans} . For the same reason, the Mg/Fe in the ISM is almost independent of the star formation timescale at small f_{trans} . It is easy to understand that the longer star formation takes place (dotted line), the higher is the Mg/Fe in the ISM for a given f_{trans} .

In the following section I will show that, with the model explained above, the contribution from intermediate-mass and dwarf ellipticals to the ICM enrichment is indeed high enough to circumvent the galaxy-cluster asymmetry and to predict Mg/Fe ratios that are consistent with the *ASCA* measurements.

7.4 Results

As mentioned above, the main constraint to the model is the total amount of iron found in the ICM, as this iron must have been synthesized in the stellar populations of the galaxies and ejected via galactic winds. The question if the iron comes predominantly from Type Ia or Type II supernovae, instead, is constrained by the abundance ratios Mg/Fe that will also be discussed in this section. For this purpose I consider the compilation of Arnaud et al. (1992) comprising cluster data with a large range of luminosities measured within 3 Mpc. As the sample does not include clusters at high redshift, evolutionary effects are not taken into account.

7.4.1 Total iron mass

Arnaud et al. (1992) found that the total mass of iron in the ICM is correlated with the cluster luminosity such that the more luminous clusters contain more iron (top panel in Fig. 7.4). The solid line shows the model predictions for the amount of iron ejected by the galaxy populations with the luminosity function of Fig. 7.1 ($\beta = -0.7$). The theoretical iron masses are in excellent agreement with the measurements. Hence, the iron mass-to-stellar mass ratio predicted to be $M_{\text{Fe}}/M_{\text{stars}} = 0.002$ perfectly matches the value that is found observationally ($2.05 \pm 0.45 \cdot 10^{-3}$) by Arnaud et al. (1992). This is an important result, as, e.g., Arnaud et al. (1992) and Gibson, Loewenstein, & Mushotzky (1997) claim that a flattening of the IMF is required in order to explain the observed $M_{\text{Fe}}/M_{\text{stars}}$. The present result shows that the universal Salpeter IMF is compatible with the iron mass observed in clusters, if the additional iron production from Type Ia supernovae is taken into account.

Only in case of Virgo — the loosest and least luminous cluster — the predicted iron *exceeds* the observational value. It is likely that due to the much lower potential well of this cluster, the assumption of a closed box may not be valid, so that the Virgo cluster may have lost some of the iron-rich intracluster material. Note also that the present model maximizes the iron ejected in galactic winds, due to the assumption that the galaxies eject all of their interstellar gas.

The dotted line indicates the results obtained assuming $\beta = -1.8$, which is the slope at the very faint end derived by Loveday (1997) for the *field* galaxy population. This slope is much steeper than the one found by Trentham (1998) for cluster galaxies, and gives more relative weight to dwarf galaxies. As with the field luminosity function less iron is produced, the intergalactic medium outside galaxy clusters is predicted to contain ≈ 30 per cent less iron per galaxy population than the ICM.

7.4.2 Total gas mass

The bottom panel in Fig. 7.4 shows the total mass of gas in the clusters as a function of cluster luminosity. Again, the observational data indicate a linear correlation, such that the gas mass increases with increasing luminosity. The predicted slope, however, is too shallow (solid line), so that the fraction of primordial gas in clusters increases with cluster richness from $\sim 1/2$ to $\sim 2/3$. Only the gas in the poorest cluster Virgo can be explained with galaxy ejecta alone. This result is in contradiction with Trentham (1994) who claims that all the intracluster gas can be produced in galactic winds if the steepening of the very faint end slope is taken into account. This discrepancy very likely comes from the fact that Trentham (1994) extrapolates the luminosity function to ‘galaxies’ with $M = 10^4 M_{\odot}$ which is even smaller than the typical mass of a globular cluster. In this way the amount of gas ejected by the galaxy populations is by far overestimated. The conclusion that a considerable fraction of the gas in rich clusters must be primordial is in agreement with other previous studies (e.g., Arnaud et al. 1992; Gibson & Matteucci 1997).

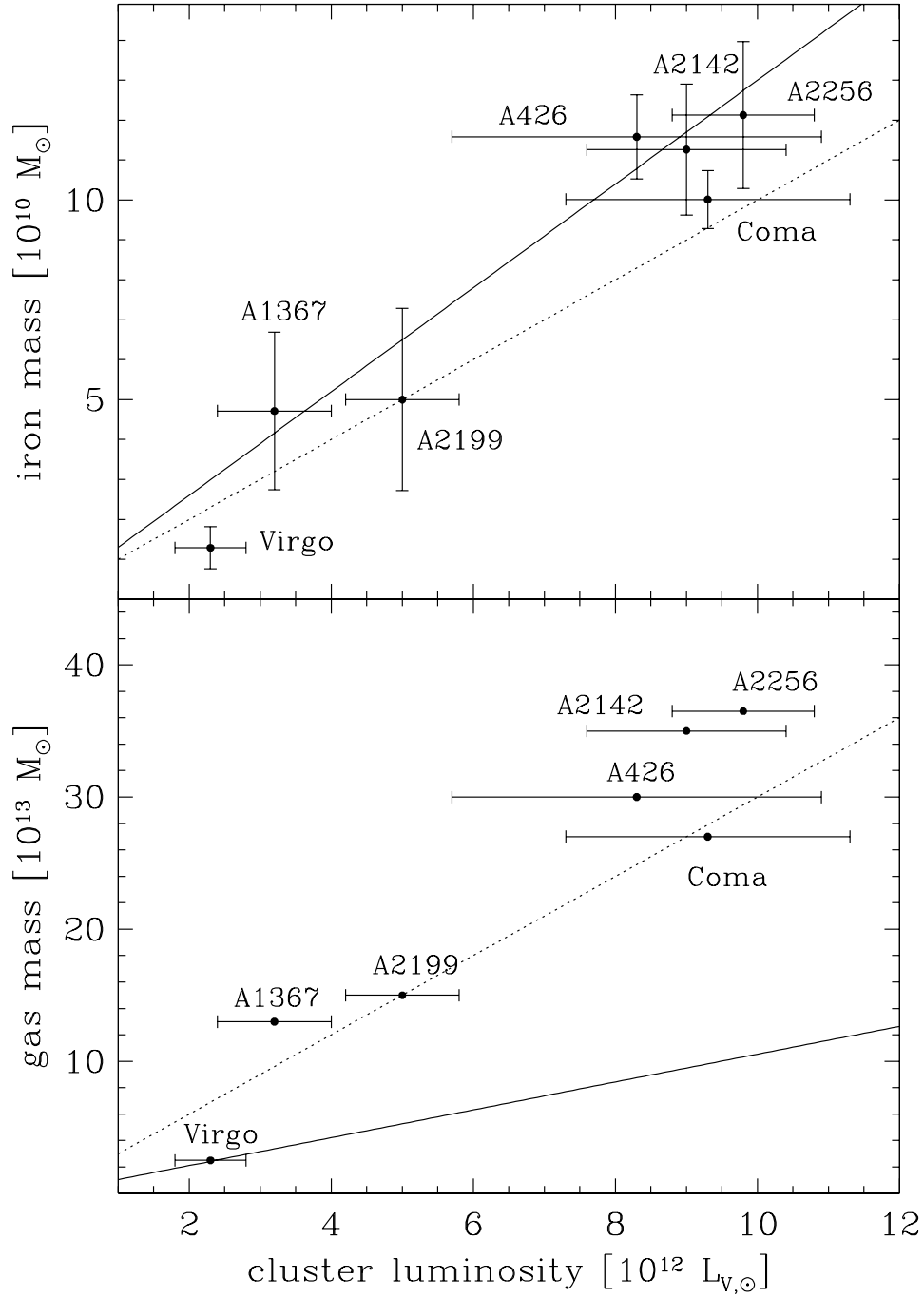


Figure 7.4: Cluster iron mass (top panel) and gas mass (bottom panel) as functions of cluster V -luminosity within 3 Mpc. The observational data points (filled circles) are from the compilation of Arnaud et al. (1992). The solid lines are the model predictions for the total amount of iron (top panel) and the total amount of gas (bottom panel) ejected from a galaxy population with the luminosity function of Fig. 7.1 ($\beta = -0.7$). The dotted line denotes the case $\beta = -1.8$ derived from *field* galaxy data by Loveday (1997).

The steeper slope $\beta = -1.8$ significantly increases the amount of gas ejected from the galaxy population, so that both the iron mass and the gas mass in Coma could stem from galactic enrichment. Note, however, that such a steep slope is not compatible with the composite cluster data of Trentham (1998).

It is also interesting to mention that the increase of the total intracluster gas mass with increasing luminosity is steeper than the increase of iron mass with the consequence that richer clusters have *lower* iron *abundances* in the ICM.

7.4.3 Abundance ratios

The Mg/Fe abundance ratio is crucial for determining the relative contributions to the iron enrichment of the ICM from the two different types of supernovae. As discussed in Section 7.3.3 there was some controversy on the original abundance determinations presented in Mushotzky et al. (1996). Normalizing the iron abundance to the meteoritic solar value (as also done in the present model), Gibson, Loewenstein, & Mushotzky (1997) revised the previous average [Mg/Fe] by ~ 0.2 dex down to [Mg/Fe] = -0.1 dex, thus even to a sub-solar value. The model presented here yields [Mg/Fe] = -0.12 in very good agreement with the *ASCA* measurements, implying that 63 per cent of the iron in the ICM stems from Type Ia supernovae. Due to the nearly solar Mg/Fe, this contribution from Type Ia is comparable to the situation in the solar vicinity (see Chapter 3).

Now, having calibrated the model on the iron mass and the Mg/Fe ratios in clusters, it is possible to investigate the fractional contributions from the various luminosity bins (Fig. 7.1) to the intracluster chemical enrichment.

7.4.4 Galaxy contributions

In Fig. 7.5 (see also Table 7.1) the black shaded histograms indicate the fractional contributions from the various luminosity bins to the enrichment of total mass (top panel), magnesium (middle panel), and iron (bottom panel) in the ICM. As discussed in Section 7.2, the main contribution to the cluster luminosity comes from galaxies with $M^* = -20.3$, in spite of the huge number of dwarf galaxies (Fig. 7.1). I recall here that the smaller the galaxy, the lower is the metallicity and therefore the larger is the expelled gas *fraction*. As a consequence, a considerable fraction of the total mass ejected from a galaxy population comes from the low-luminosity objects (top panel). The enrichment of metals, instead, is again more skewed towards luminous galaxies, because more massive galaxies are more metal-rich, i.e. they produce more metals per galaxy mass. The contributions to magnesium (middle panel) and iron (bottom panel) peak at luminosities ~ 1 mag lower than L^* . Note that the most luminous objects eject slightly more Fe than Mg, because the Mg/Fe ratio in the galactic wind decreases with increasing galaxy mass (Fig. 7.3).

A significant contribution to the metal-enrichment extends down to the brighter dwarf ellipticals with $M_B \approx -16$. Table 7.2 shows that $\sim 70-80$ per cent of the light and of the elements magnesium and iron comes from galaxies fainter than L^* . This result impacts on the galaxy-cluster asymmetry mentioned in Section 7.3.3. Owing to the dominant contribution from intermediate- and

TABLE 7.1
FRACTIONAL CONTRIBUTIONS

M_B^{up} (1)	M_B^{down} (2)	Number (3)	L_B (4)	Mass (5)	Ejected Mass (6)	Iron (7)	Magnesium (8)
-22	-21	0.0002	0.060	0.084	0.017	0.070	0.005
-21	-20	0.0020	0.258	0.319	0.102	0.298	0.263
-20	-19	0.0052	0.264	0.279	0.162	0.293	0.300
-19	-18	0.0085	0.177	0.156	0.156	0.173	0.192
-18	-17	0.0121	0.100	0.076	0.123	0.086	0.100
-17	-16	0.0167	0.055	0.038	0.084	0.035	0.041
-16	-15	0.0238	0.031	0.020	0.063	0.016	0.020
-15	-14	0.0364	0.019	0.011	0.061	0.012	0.015
-14	-13	0.0615	0.013	0.006	0.057	0.007	0.009
-13	-12	0.1144	0.009	0.004	0.058	0.005	0.006
-12	-11	0.2302	0.007	0.003	0.054	0.002	0.003
-11	-10	0.4489	0.006	0.003	0.062	0.002	0.002

NOTE.—Columns (1) and (2) are the boundaries of the luminosity bins. Columns (3)–(8) denote fractional contributions to the number of galaxies (3), total B -luminosity of the galaxy population (4), total mass of the galaxy population (5), total *ejected* mass in galactic winds (6), ejected iron (7), ejected magnesium (8).

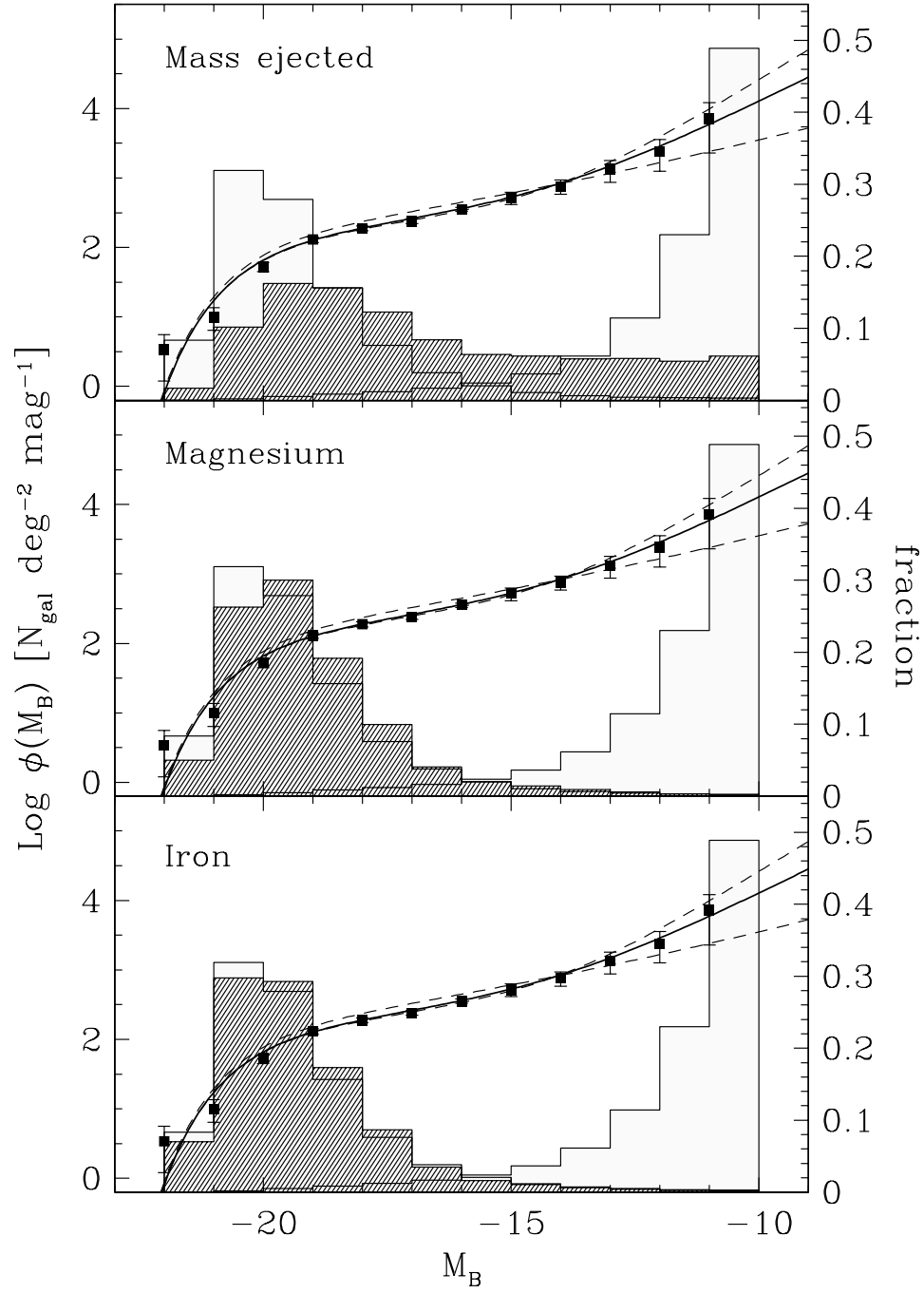


Figure 7.5: Same as Fig. 7.1. The contributions to the supply of total mass (top panel), magnesium (middle panel), and iron (bottom panel) in the intracluster medium are shown by the black shaded histograms.

TABLE 7.2
RELATIVE CONTRIBUTIONS

	Brighter L_*	Fainter L_*
B -luminosity	23	77
Mass	8	92
Magnesium	22	78
Iron	26	74

NOTE.—According to Fig. 7.1 the B -luminosity of L_* galaxies is $M_B^* = -20.3$ mag. The numbers denote percentages.

low-mass ellipticals, the resulting Mg/Fe in the ICM is higher than in the galactic winds of the most massive objects (see Fig. 7.3), and hence in agreement with observational measurements.

Note that in the present model the stellar populations of all galaxies are assumed to be α -enhanced, independent of their luminosities. However, there are indications that the stellar Mg/Fe in ellipticals decreases with decreasing galactic mass (Kuntschner 2000; Trager et al. 2000b). If galaxies with $-18 > M_B^* > -21$ are indeed less α -enhanced than assumed here, the predicted $[\text{Mg/Fe}] = -0.12$ increases as can be seen from Fig. 7.3. The impact from the exact Mg/Fe in dwarf galaxies, instead, is negligible as also discussed in Section 7.3.3.

The distribution of the total mass ejected from the galaxies to the ICM is much more skewed towards low-luminosity objects. The low metallicity of dwarf galaxies requires that these systems are much less efficient in processing gas into stars. As they are mainly gas-poor dwarf ellipticals, they expel a much larger fraction of their mass than giant ellipticals (Fig. 7.3).

7.5 Summary

For a given galaxy luminosity function observed in clusters, I analyze the fractional contributions to the ICM enrichment from galaxies of different luminosity bins. The luminosity function covers the whole relevant luminosity range from $M_B = -22$ to $M_B = -10$, which allows to investigate the significance of dwarf galaxies in a self consistent way. The galaxy evolution model is semi-empirical in the sense that the relation between metallicity and luminosity of the galaxies is taken from observational data.

Including the contribution from Type Ia supernovae to the enrichment of iron, the iron mass-to-light ratios measured in clusters of different luminosities can be reproduced without invoking a flattening of the IMF. SNIa are predicted to produce 63 per cent of the ICM iron, a proportion which is comparable to

the solar neighborhood chemistry. Hence, the ICM is not an archive of SNII nucleosynthesis alone. The total amount of gas in the more luminous clusters cannot be explained only with galaxy ejecta, the fraction of primordial gas must be $\sim 1/2-2/3$.

It turns out that galaxies fainter than L^* down to $M_B \approx -14$ provide an important contribution to the total light of the galaxy population and to the metals found in the ICM. Dwarf galaxies below this threshold, instead, deliver a significant fraction of the total gas mass that is ejected by the galaxy population. The inclusion of intermediate-mass and dwarf ellipticals in the model allows to produce the roughly solar Mg/Fe ratio in the ICM found in *ASCA* measurements.

Chapter 8

Dwarf Galaxies

The principal focus of this work is to understand, from a theoretical point of view, how chemical evolution and abundance ratios constrain galaxy formation models. As shown in the previous chapters, giant elliptical galaxies turn out to play a key role, because their very homogeneously old and α -element enhanced stellar populations cannot easily be accommodated with the current models of hierarchical galaxy formation.

The properties of dwarf galaxies are not yet used to constrain galaxy formation, because 1) such small masses are not resolved in the models and 2) our knowledge on the dwarf galaxy population is still rather poor. Although dwarf galaxies are the most abundant galaxies in the universe (see also Chapter 7) they are difficult to be studied observationally because of their low luminosities and low surface brightnesses. The dwarfs that are best studied are the members of the Local Group comprising both dwarf irregular and dwarf elliptical galaxies. The latter are interesting, as in the framework of hierarchical galaxy formation they may be the fossilized building blocks of giant galaxies.

In this chapter — complementary to the other purely theoretical chapters — I present observed spectra of dwarf early-type galaxies analyzing their stellar populations with respect to kinematical properties, ages, metallicities, and abundance ratios. This project is done in collaboration with R. Bender, L. Greggio, U. Hopp, and C. Maraston.

8.1 The dwarf galaxy population

8.1.1 Basic properties

Dwarf galaxies have masses $M \lesssim 10^9 M_\odot$ and blue luminosities $M_B \gtrsim -19$ (Binggeli 1994). The surface brightnesses are lower by ~ 6 magnitudes than the ones of classical galaxies. In particular dwarf ellipticals exhibit increasing surface brightness with increasing luminosity (Binggeli & Cameron 1991), which is the opposite trend found for giant ellipticals (Kormendy 1985). The radial surface brightness profiles can be fit with an exponential law for all kinds of dwarf galaxies including irregulars, Blue Compact Dwarfs, and ellipticals (Binggeli, Sandage, & Tarenghi 1984). Dwarf ellipticals are often nucleated having a steeper increase of surface brightness with decreasing radius in the

inner parts. The exponential fitting law does not imply disk components for all dwarfs. Because of the flattening distributions of dwarf ellipticals, these objects are likely to be spheroidals (Ichikawa 1989; Binggeli & Cameron 1991; Binggeli & Popescu 1995). Indeed, detailed kinematical studies of dwarf ellipticals show that these objects are not flattened because of rotation but anisotropic velocity distributions (Bender & Nieto 1990; Bender, Paquet, & Nieto 1991).

The morphology-density relation known for giant galaxies is even more pronounced for the dwarf galaxy population, such that dwarf ellipticals are always satellites, while dwarf irregulars are very homogeneously distributed (Binggeli, Tamman, & Sandage 1987). This dependence on environmental density implies that the luminosity functions are different for early and late types. In the Virgo cluster, the number of dwarf ellipticals steadily increases with decreasing luminosity (see also Chapter 7), while the luminosity function of dwarf irregulars and blue compact dwarfs levels off at faint magnitudes (Sandage, Binggeli, & Tamman 1985).

8.1.2 Open problems

As mentioned above, the different surface brightness-magnitude relations of giant and dwarf ellipticals suggest a clear structural dichotomy (Wirth & Gallagher 1984; Kormendy 1985; Binggeli & Cameron 1991). It is a controversial issue, whether giant and dwarf ellipticals belong to different populations, or whether they are the same class of objects. In the latter case, galaxies of intermediate luminosities would have the maximum surface brightnesses, connecting the faintest giant ellipticals and the brightest dwarfs. In order to answer this question it is necessary to additionally investigate if the stellar population properties like ages, metallicities and abundance ratios support or disfavor the existence of a dichotomy.

In the context of hierarchical galaxy formation, it is important to understand if today's dwarf galaxies are the candidates for being the remaining building blocks of giant galaxy formation as suggested by Silk (1986). In the present work, this issue shall be approached by exploring the properties of the stellar populations in dwarf ellipticals.

Besides the giants-dwarfs dichotomy it is still a controversial issue if early and late type dwarfs are the same objects at different evolutionary stages. In this picture dwarf irregulars would loose their gas either via ram pressure stripping (Einasto et al. 1974) or via star formation (Davies & Phillipps 1988), and would evolve into dwarf ellipticals. However, the higher surface brightnesses and metallicities in the dwarf ellipticals (Lin & Faber 1983; Binggeli 1986), the different flattening of the two galaxy types (Binggeli & Popescu 1995), and the fact that dwarf irregulars have no central nuclei highly disfavor these scenarios. The ages and abundance ratios of the dwarf ellipticals analyzed here will further help to support or to reject the early-late type dichotomy.

Additional open questions are the role of dwarf galaxies in the context of faint blue galaxy counts (Babul & Rees 1992) and the enrichment of the intra-cluster medium. The latter issue is addressed in detail in Chapter 7.

8.2 Observations

Because of the low surface brightnesses of dwarf galaxies, several hours of exposure times at 4m-class telescopes are typically required to obtain high-quality spectra of reasonable signal-to-noise. Hence, the achievement of a statistically large sample of dwarf galaxy spectra is a long-term program. The sample presented here comprises spectra of six dwarf early-type galaxies taken in three observing runs in October 1994 (Oct94), August 1995 (Aug95), and March 1998 (Mar98a, Mar98b referring to two different setups) with the TWIN spectrograph at the 3.5m telescope on Calar Alto. A long slit was placed along the major axis. The slit widths vary between 2.1–2.4 arcsec yielding a spectral resolution of 38–48 km/s at 5100 Å. This very high resolution resolves the velocity dispersions of dwarf galaxies, which allows for detailed kinematical studies. The observed wavelength range is 4500–5500 Å including the most widely used optical absorption lines $H\beta$, $Mg\ b$, Mg_2 , Fe5270, and Fe5335 as they are defined in the Lick system (see Section 8.3.2). With exposure times of 2–5 hours we obtained good signal-to-noise in the range 20–80 Å⁻¹ (Section 8.3.1).

For the kinematical studies and in order to calibrate the absorption line indices on the Lick system, spectra of Lick-standard stars (González 1993) of type A0II – K7III were taken in every run.

8.2.1 The sample

Names, coordinates, and photometric properties of the sample are summarized in Table 8.1. The sample selection is based on the catalogues of Vader & Chaboyer (1994) and Binggeli, Sandage, & Tamman (1985) (Virgo cluster galaxies). The first object observed in run Oct94 is a nucleated dwarf elliptical (dE,N) being a satellite of the AGN-elliptical NGC 1052, whose velocity relative to the Local Group is $v = 1539$ km/s (Vader & Chaboyer 1994). From run Aug95 we obtained spectra of two dwarf lenticulars (dS0) that are companions of NGC 7626, a giant elliptical member of the Pegasus cluster. The velocity of NGC 7626 relative to the Local Group is $v = 3625$ km/s (Vader & Chaboyer 1994). The objects classified as dS0 types are brighter variations of the bright dwarf elliptical (dE) types with a larger degree of flattening (Binggeli & Cameron 1991). Finally, in March 1998 we obtained spectra of three nucleated dEs taken from the Virgo cluster (redshift $c \cdot z = 1142 \pm 61$ km/s; Feder-spiel, Tammann, & Sandage 1998) catalogue of Binggeli, Sandage, & Tamman (1985). The sample thus spans a rather large range in magnitudes, including both bright and low-luminosity dEs and dS0s. Spectra of even fainter dwarfs are difficult to obtain with 4m-class telescopes mainly because of their very low surface brightnesses. Further observations are planned to enlarge the sample.

The redshifted spectra averaged within the respective effective radii (see Table 8.1) are shown in Fig. 8.1. The common absorption features can be identified by eye, the shaded boxes indicate the index passbands of the indices $H\beta$, Mg_2 , Fe5270, and Fe5335 as defined in Section 8.2.4. The exact heliocentric velocities are discussed in Section 8.3.1. The spectra show no significant emission line features. The apparent feature in the spectrum of NGC 7626#13 at

TABLE 8.1
DWARF GALAXY SAMPLE

Name (1)	Other Name (2)	R.A. (1950) (3)	Dec. (1950) (4)	Φ (5)	Type (6)	B_r (7)	M_B (8)	μ_{eff} (9)	r_e (10)	ϵ (11)	Source (12)	Run (13)
N7626#13	–	23 18 18	+07 51 42	–	dS02	17.21	–17.12	24.00	10.50	0.23	VC94	Aug95
N7626#15	–	23 18 35	+07 53 48	–	dS05	15.67	–18.70	21.06	6.00	0.45	VC94	Aug95
N1052#1	–	02 38 58	–08 20 24	–	dE2,N	16.01	–16.42	22.77	9.00	0.22	VC94	Oct94
NGC4322	VCC 608	12 20 30	+16 11 00	140	dE4,N	14.94	–16.73	22.92	15.85	0.21	BC93	Mar98a
IC3381	VCC 1087	12 25 44	+12 03 54	100	dE3,N	14.31	–17.36	22.54	17.78	0.09	BC93	Mar98b
IC3437	VCC 1308	12 28 14	+11 37 00	73	dE6,N	15.64	–16.03	22.35	8.71	0.21	BC93	Mar98b

NOTE.—Column (5): position angle in degrees measured from north to east. Column (7,8): blue apparent and absolute magnitudes. Column (9): mean surface brightness [$\text{mag}/\text{arcsec}^2$] within the effective radius. Column (10): effective radius in arcsec. Column (11): ellipticities $\epsilon = 1 - b/a$. Column (12): literature sources Binggeli & Cameron (1993) and Vader & Chaboyer (1994). Column (13): run for the spectroscopy presented here.

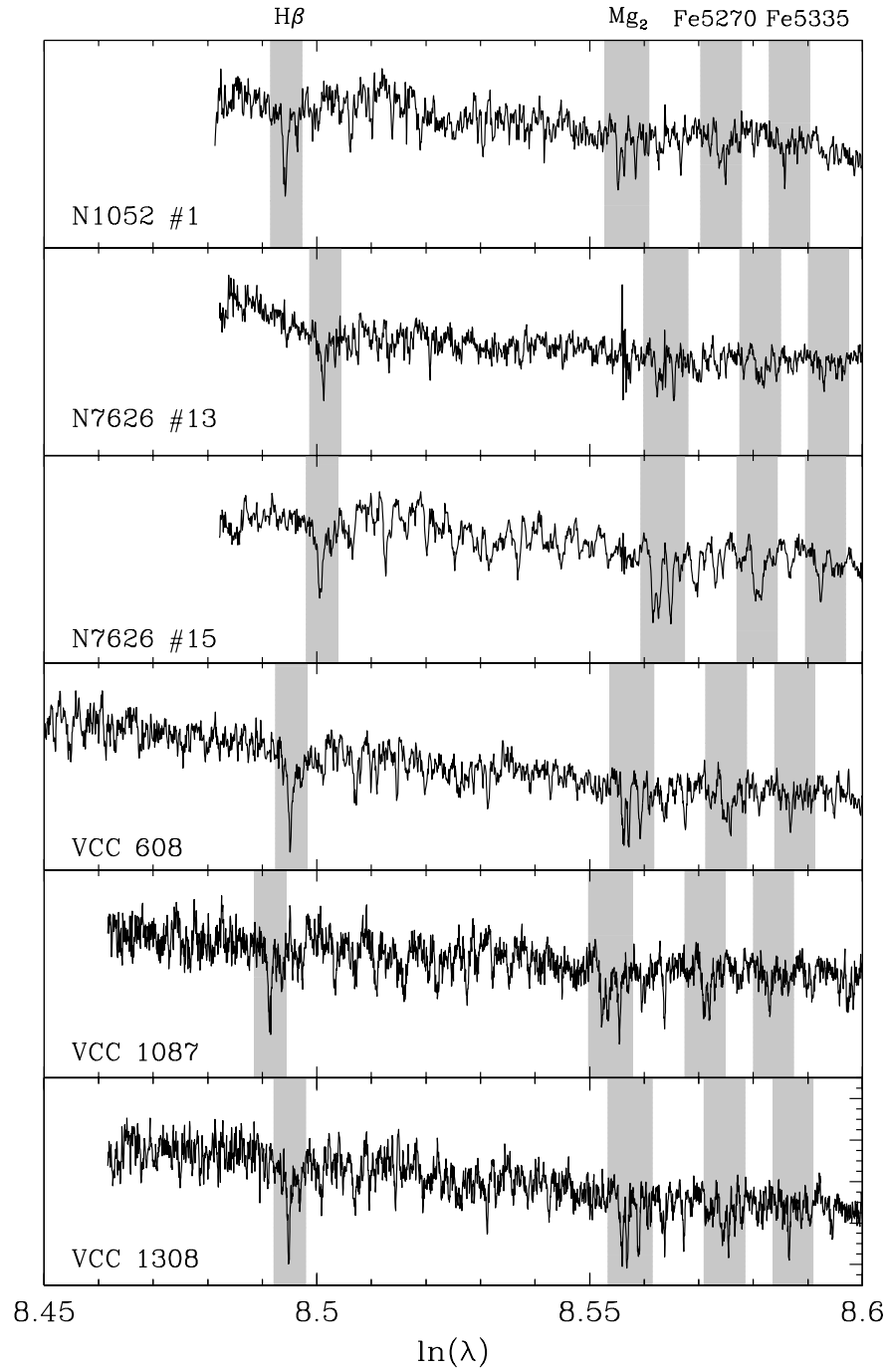


Figure 8.1: Redshifted spectra of the dwarf galaxy sample. The gray boxes indicate the passbands of the absorption line features measured. For the index definitions see Table 8.2, p. 121.

$\ln(\lambda) = 8.556$ is an artifact of the data reduction and has no impact on the data analysis. The spectra are not flux calibrated.

8.2.2 Data reduction

The two-dimensional spectra were reduced in the standard manner:

1. Bias subtraction
2. Flatfielding
3. Removal of cosmics on the galaxy frames
4. Wavelength calibration with FeNe and HeAr lamps
5. Sky subtraction
6. Centering of spectrum in radial direction

8.2.3 Kinematics

In order to investigate the kinematical properties of the galaxies, the radial velocities and velocity dispersions are determined by measuring the line of sight velocity distributions (LOSVD). These kinematical parameters are extracted from the LOSVD following the Fourier-Correlation-Quotient (FCQ) method developed by Bender (1990b). The spectra are divided by their continuum shapes. The instrumental velocity dispersion is determined with the aid of standard stars, whose intrinsic broadening of absorption lines can be neglected.

Possible errors due to sky subtraction are minimized with the long slit, because the sky can be determined at the two ends where the contribution from galaxy light is negligible (see Saglia et al. 1993). Template mismatching and incorrect continuum removals do not significantly affect the determination of heliocentric velocities and therefore the rotation curves (Bender, Saglia, & Gerhard 1994). Also the derived velocity dispersion is only little altered by errors in the continuum removal, if the LOSVD is well described with a Gaussian profile (Bender, Saglia, & Gerhard 1994).

The statistical errors are derived by means of Monte Carlo simulations. In order to create artificial galaxies, noise patterns are added to template stellar spectra. These spectra are broadened for a set of different kinematic parameters, which are then re-determined using the FCQ method. In this way, real S/N ratios and statistical errors which are dominated by photon noise are obtained. These simulations are particularly important, because the velocity dispersions of the observed galaxies are close to the instrumental resolution. It has to be checked carefully, whether real σ values or only the instrumental resolution are determined.

Fig. 8.2 shows the results of S/N ratios, σ , and $d\sigma$ from the Monte Carlo simulations for the Mar98a setup. The ratios of the FCQ values over the results from the Monte Carlo simulations as a function of input signal-to-noise ratios and various input velocity dispersions are plotted. The top panel shows that

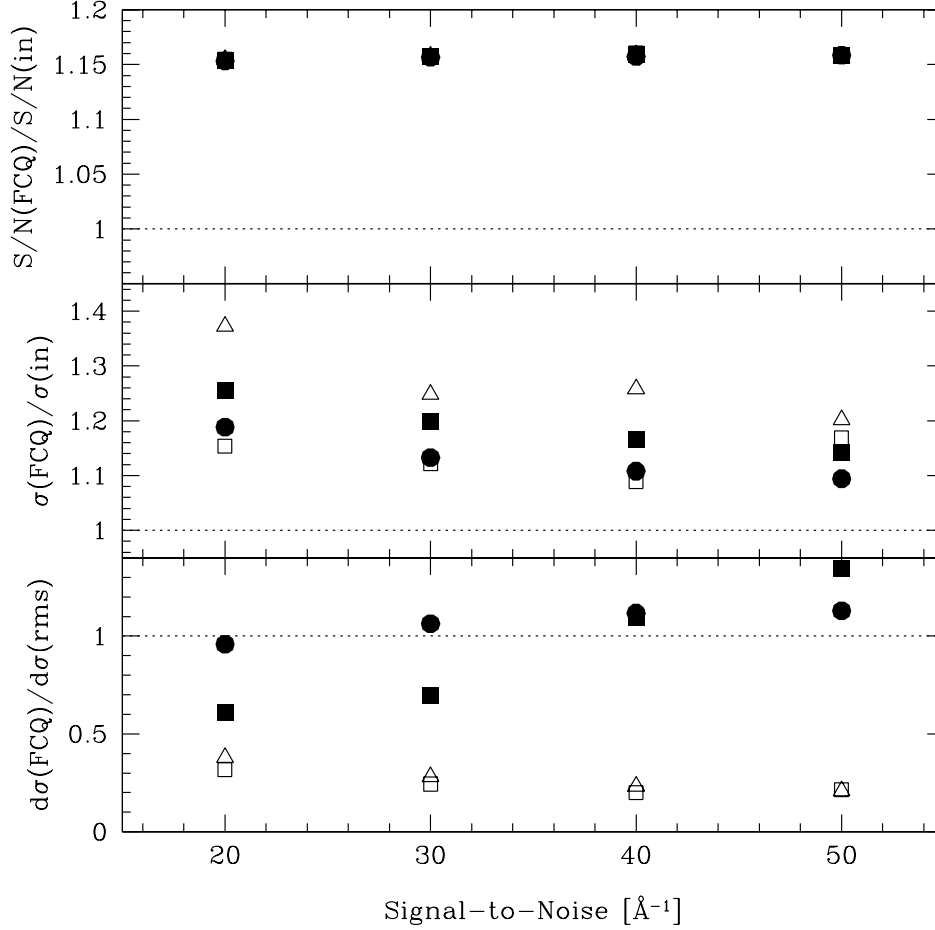


Figure 8.2: Ratios of FCQ values over the results from Monte Carlo simulations as a function of signal-to-noise ratio (per \AA) and various velocity dispersions for the Mar98a setup. *Top panel:* signal-to-noise. *Middle panel:* velocity dispersion σ . *Bottom panel:* error in σ . The symbols refer to different input σ with $\sigma = 50$ km/s (filled circles), $\sigma = 40$ km/s (filled squares), $\sigma = 30$ km/s (open squares), $\sigma = 20$ km/s (open triangles).

the FCQ procedure overestimates the real S/N by ~ 15 per cent, independent of the input σ and the input S/N. The σ seems to be overestimated by $\sim 5-40$ per cent, with larger deviations for lower input values of S/N and σ (middle panel). The bottom panel of Fig. 8.2 shows the error in σ given by the FCQ procedure over the real rms-scatter from the simulations. For $\sigma \gtrsim 50$ km/s, which is well above the limit of resolution, the FCQ-estimates are reliable, while they deviate by a factor of 2 for $\sigma = 40$ km/s and S/N= 20. At $\sigma \lesssim 30$ km/s, the discrepancies amount to a factor of 4 independent of the input S/N. This result is expected, as such low velocity dispersions (open symbols) cannot be resolved with the present setups. I conclude that $\sigma \approx 40$ km/s can be reliably

determined.

The Monte Carlo results for the other setups reveal similar trends, the discussion of which is not repeated here. For every setup separately, all the galaxy data are corrected for the features shown in Fig. 8.2.

8.2.4 Line indices

Definition of line indices

In order to allow for a universal analysis of galaxy spectra, Burstein et al. (1984) and Faber et al. (1985) defined a set of absorption line indices in the optical wavelength range, known as the Lick system. As described in Worthey et al. (1994), an index measured in Å is defined as an equivalent width EW

$$\text{EW} = \int_{\lambda_1}^{\lambda_2} \left(1 - \frac{F_{I\lambda}}{F_{C\lambda}} \right) d\lambda, \quad (8.1)$$

where $F_{I\lambda}$ and $F_{C\lambda}$ are the flux values of the line feature and of the local continuum as functions of the wavelength λ , respectively. The interval $[\lambda_1, \lambda_2]$ is the passband of the feature. $F_{C\lambda}$ is determined by interpolating the average fluxes of two pseudocontinua F_P red- and bluewards the line feature.

$$F_P = \int_{\lambda_1}^{\lambda_2} F_{\lambda} d\lambda / (\lambda_2 - \lambda_1) \quad (8.2)$$

Indices measured in magnitudes are defined by the following equation.

$$\text{Mag} = -2.5 \log \left(\frac{1}{\lambda_2 - \lambda_1} \int_{\lambda_1}^{\lambda_2} \frac{F_{I\lambda}}{F_{C\lambda}} d\lambda \right) \quad (8.3)$$

The value of an index is therefore a direct measure of the strength of a spectral feature. In Table 8.2 the definitions of the Lick indices (González 1993) that are used for the present analysis are listed.

The errors are — as the kinematical parameters — dominated by photon noise. A potential systematic error can be caused by filling of the absorption feature with emission lines, which mostly affects the $\text{H}\beta$ index. González (1993) corrects this depletion of the index value by estimating the expected $\text{H}\beta$ emission by means of the O[III] emission line at $\lambda = 5007$ Å. Because of the lack of emission lines in the spectra of the present sample (Fig. 8.1), the effect of possible emission can be assumed to be negligible.

Calibration to the Lick system

In order to obtain index measurements consistent with the Lick system, the resolution has to be artificially decreased to the instrumental resolution of the Lick spectrograph, which is $\sigma_{\text{Lick}} = 220$ km/s (Correction 1). In principle, one has to additionally correct for the broadening of the lines due to the velocity dispersion σ of the galaxy (Correction 2). The dependence of the equivalent width of an absorption feature on σ is determined by artificially broadening the spectra of the standard stars, which then yields the correction function.

TABLE 8.2
INDEX DEFINITIONS

Name	Index Bandpass [Å]	Pseudocontinua [Å]	
H β	4847.875–4876.625	4827.875–4847.875	4876.625–4891.625
Mg ₂	5154.125–5196.625	4895.125–4957.625	5301.125–5366.125
Mg <i>b</i>	5160.125–5192.625	5142.625–5161.375	5191.375–5206.375
Fe5270	5245.650–5285.650	5233.150–5248.150	5285.650–5318.150
Fe5335	5312.125–5352.125	5304.625–5315.875	5353.375–5363.375

NOTE.—Absorption indices defined by González (1993). The wavelengths are given in Å. The Mg₂ index is measured in magnitudes, H β , Mg *b*, and the iron indices are defined as equivalent widths (Å).

Correction 2 has been applied, although the effect is negligible in the case of dwarf galaxies having velocity dispersions well below the Lick resolution (see Section 8.3.1).

The most significant correction concerns the shape of the continuum (Correction 3), as the Lick standards are not flux calibrated. The shape of the continuum impacts on the index value particularly if the pseudocontinua are far from each other in terms of wavelength, which is the case for Mg₂ (Table 8.2). In order to correct for this effect, we took spectra of standard stars from the Lick library. The comparisons with the index values derived here (having applied Correction 1) with the ones given in González (1993) are shown in Fig. 8.3 (Oct94), Fig. 8.4 (Aug95), Fig. 8.5 (Mar98a), and Fig. 8.6 (Mar98b).

For all the four setups, the measurements of the indices H β , Mg *b*, Fe5270, and Fe5335 are in excellent agreement with the Lick standards. The pseudocontinua of these indices are close to the line, so that the shape of the continuum does not affect the index significantly. The Mg₂ index derived here, instead, is systematically lower by ~ 0.03 mag, depending on the setup, which is plausible because of the two very distant pseudocontinua in the Mg₂ index definition. The Mg₂ indices measured from the galaxy spectra are corrected for this effect for every setup separately by subtracting the shifts Δ given in Figs. 8.3 to 8.6.

8.3 Results

In this section I present the results from the spectral analysis of the galaxy sample in Table 8.1. In Section 8.3.1 the kinematical properties of the galaxies are shown. In Section 8.3.2, the Lick indices H β , Mg₂, Mg *b*, Fe5270, and Fe5335 derived from the spectra are discussed.

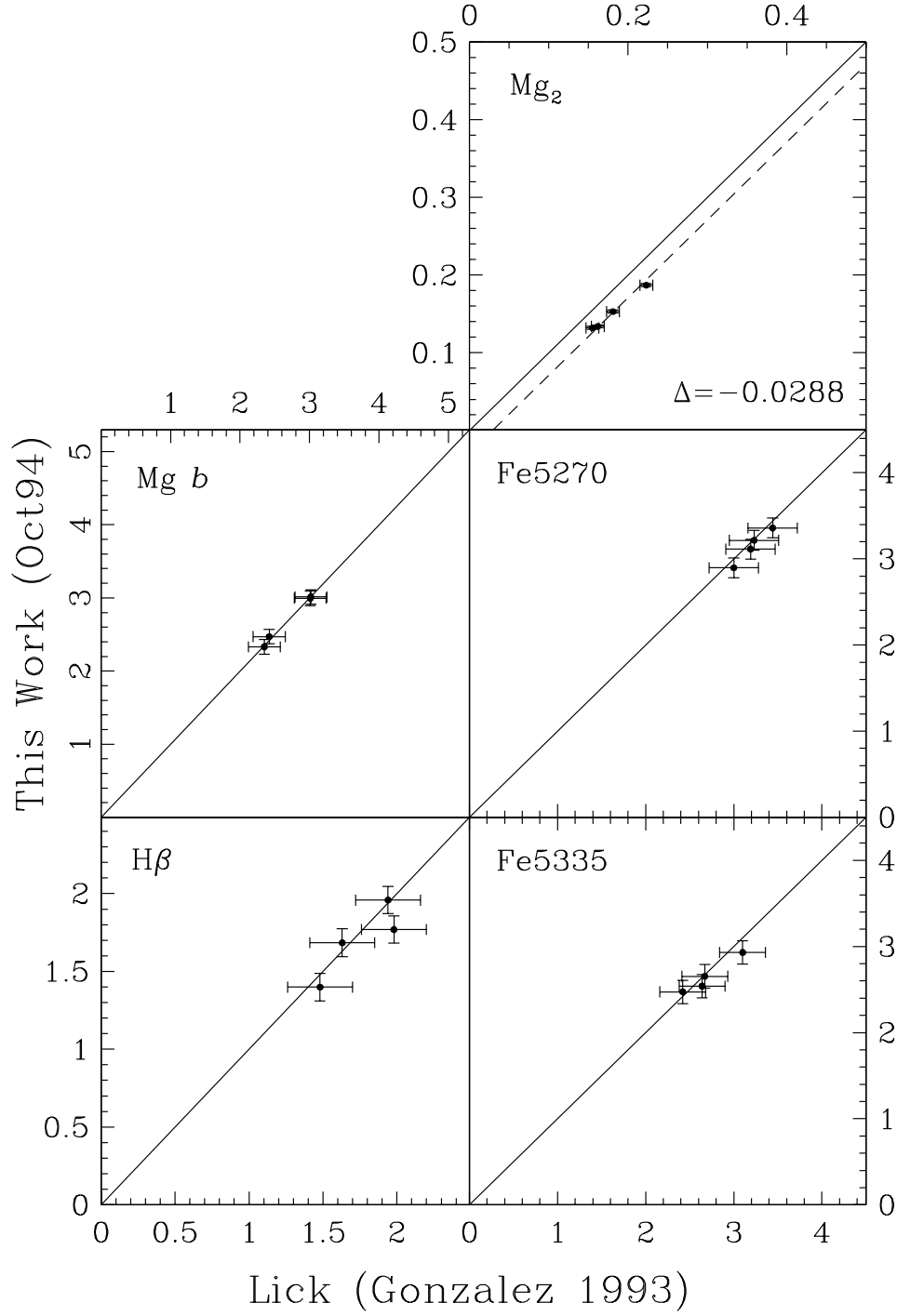


Figure 8.3: Calibration of the indices as defined in Table 8.2 on the Lick system for run Oct94. The index measurements of the present work (y-axis) are plotted as functions of the values given by González (1993). The constant shift in the Mg_2 index according to continuum shape is $\Delta \equiv \text{Mg}_2(\text{this work}) - \text{Mg}_2(\text{Lick}) = -0.0288$ mag.

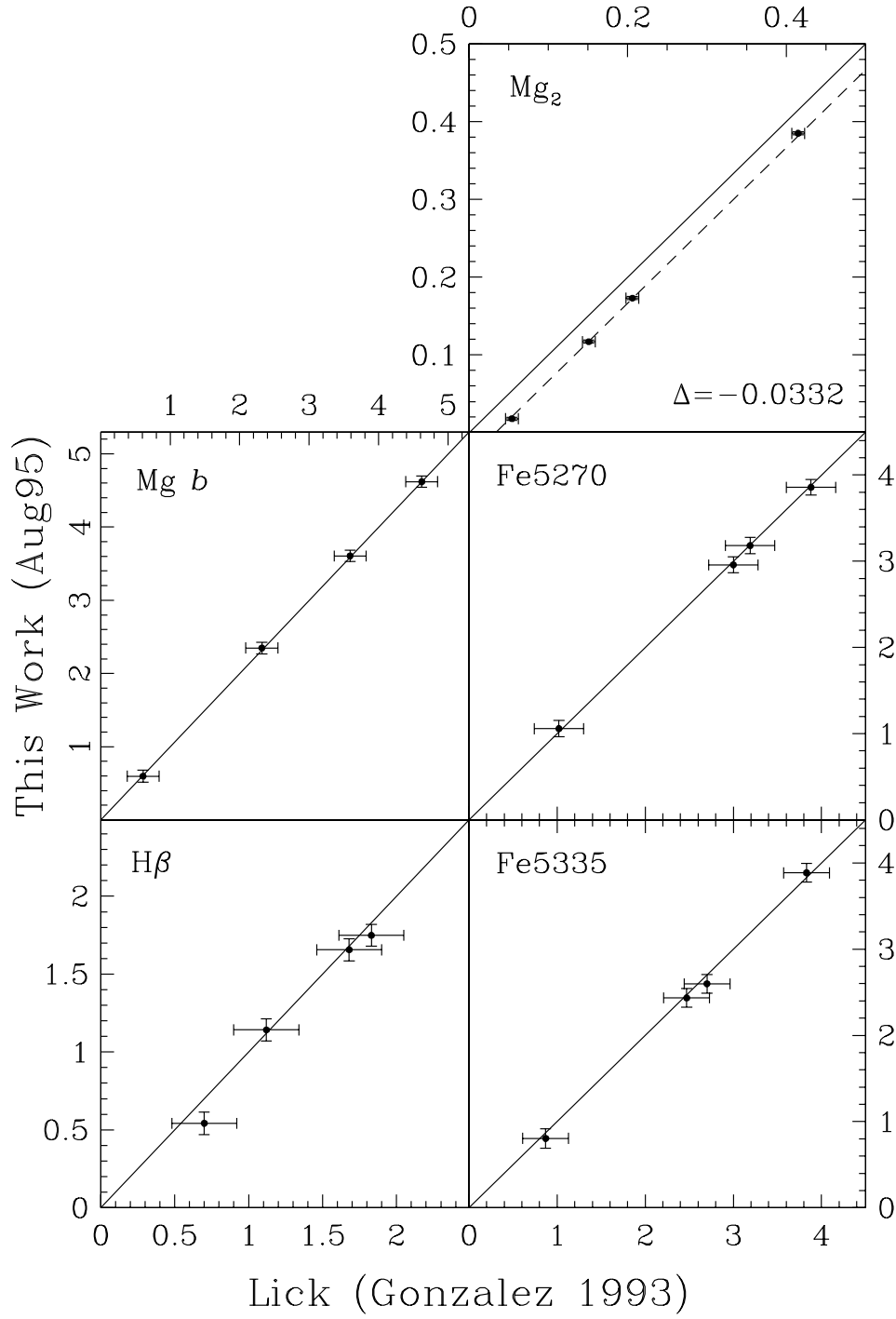


Figure 8.4: Calibration of the indices as defined in Table 8.2 on the Lick system for run Aug95. The index measurements of the present work (y-axis) are plotted as functions of the values given by González (1993). The constant shift in the Mg₂ index according to continuum shape is $\Delta \equiv \text{Mg}_2(\text{this work}) - \text{Mg}_2(\text{Lick}) = -0.0333$ mag.

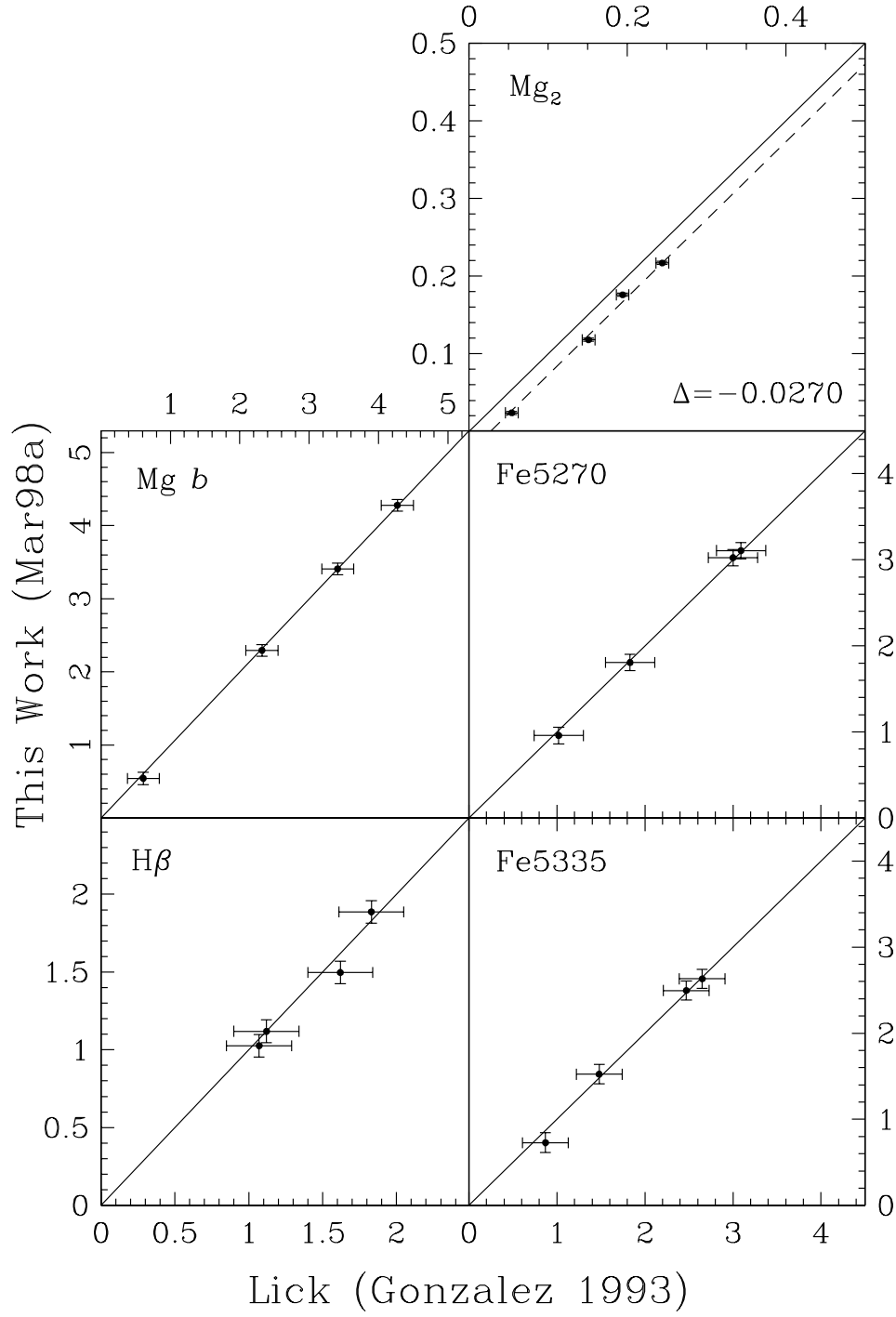


Figure 8.5: Calibration of the indices as defined in Table 8.2 on the Lick system for run Mar98a. The index measurements of the present work (y-axis) are plotted as functions of the values given by González (1993). The constant shift in the Mg_2 index according to continuum shape is $\Delta \equiv \text{Mg}_2(\text{this work}) - \text{Mg}_2(\text{Lick}) = -0.0270$ mag.

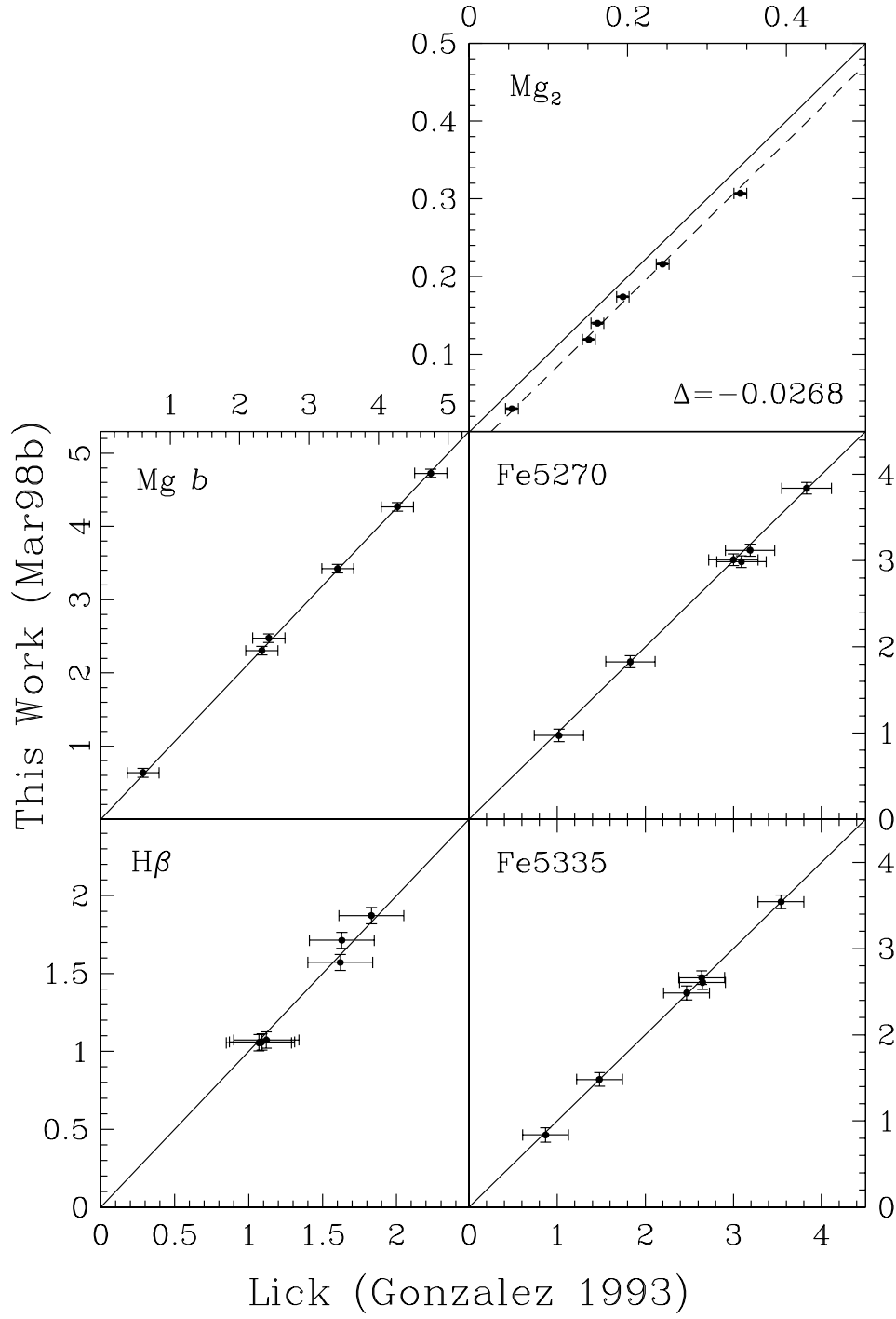


Figure 8.6: Calibration of the indices as defined in Table 8.2 on the Lick system for run Mar98b. The index measurements of the present work (y-axis) are plotted as functions of the values given by González (1993). The constant shift in the Mg_2 index according to continuum shape is $\Delta \equiv Mg_2(\text{this work}) - Mg_2(\text{Lick}) = -0.0268$ mag.

8.3.1 Kinematics

Figs. 8.7, 8.8, and 8.9 display the derived signal-to-noise ratios S/N (top panels), velocity dispersions σ (middle panels), and rotational velocities v_{rot} (bottom panels) as functions of radius r out to the effective radius r_e (vertical dotted lines) for the galaxy sample. The horizontal dotted lines in the middle panels are the mean velocity dispersions $\bar{\sigma}$ within r_e , determined by averaging the values $\sigma(r)$. The shaded regions denote the range of v_{rot} for which the ellipticity of the object (see Table 8.1) is not rotationally supported, but produced by anisotropic velocity distributions. These upper limits of v_{rot} are determined as follows.

Kormendy (1982) found that the rotational velocity v_{rot} of a rotationally flattened body with ellipticity ϵ and a mean velocity dispersion $\bar{\sigma}$ is

$$v_{\text{rot}} = \sqrt{\epsilon/(1-\epsilon)} \cdot \bar{\sigma} . \quad (8.4)$$

The anisotropy parameter $(v/\sigma)^*$ defined by Binney (1978) is then given by the following equation (Bender & Nieto 1990).

$$(v/\sigma)^* = \frac{v_{\text{rot}}/\bar{\sigma}}{\sqrt{\epsilon/(1-\epsilon)}} . \quad (8.5)$$

If $(v/\sigma)^* \gtrsim 1$ the object can be assumed flattened by rotation. In the following, objects are considered to be flattened by anisotropic velocity distributions if $(v/\sigma)^* \lesssim 0.7$ (Bender, Burstein, & Faber 1992). The shaded regions in Figs. 8.7, 8.8, and 8.9 indicate the resulting v_{rot} if $(v/\sigma)^* \leq 0.7$ with $\bar{\sigma}$ given by the horizontal dotted line in the middle panel.

NGC 7626#13

The results for NGC 7626#13 are shown in the upper diagram of Fig. 8.7. Owing to the very low surface brightness of this object ($\mu_{\text{eff}} = 24$, Table 8.1), the S/N is reasonable only at the center of the galaxy. Around r_e the $S/N \approx 10$ is already too low for accurate kinematical studies. The velocity dispersion is constant within $r_e/2$, with a mean $\bar{\sigma} = 39 \pm 3$ km/s. The galaxy — ellipticity $\epsilon = 0.23$ — is slowly rotating with $v_{\text{rot}} = 16 \pm 5$ km/s (measured at $r_e/2$), leading to $(v/\sigma)^* = 0.75 \pm 0.24$. Hence, the ellipticity of NGC 7626#13 is supported partly by rotation, partly by anisotropic velocity distributions. The derived heliocentric velocity is $v_{\odot} = 3690 \pm 9$ km/s.

NGC 7626#15

The results for NGC 7626#15 are shown in the lower diagram of Fig. 8.7. The quality of the data is much higher than for NGC 7626#13, mainly because of the higher surface brightness $\mu_{\text{eff}} = 22.77$. The profile in σ has the shape known from giant ellipticals: $\sigma_0 = 88.5 \pm 2$ km/s is maximal in the center, $\bar{\sigma} = 82 \pm 2$ km/s. Also the rotation curve is nicely resolved with $v_{\text{rot}} = 45 \pm 5$ km/s measured at r_e . However, as the ellipticity of this object (classified as a dS05) is rather high ($\epsilon = 0.45$), the rotation does suffice to explain the flattening, $(v/\sigma)^* = 0.6 \pm 0.07$. The rotation curve lies within the shaded

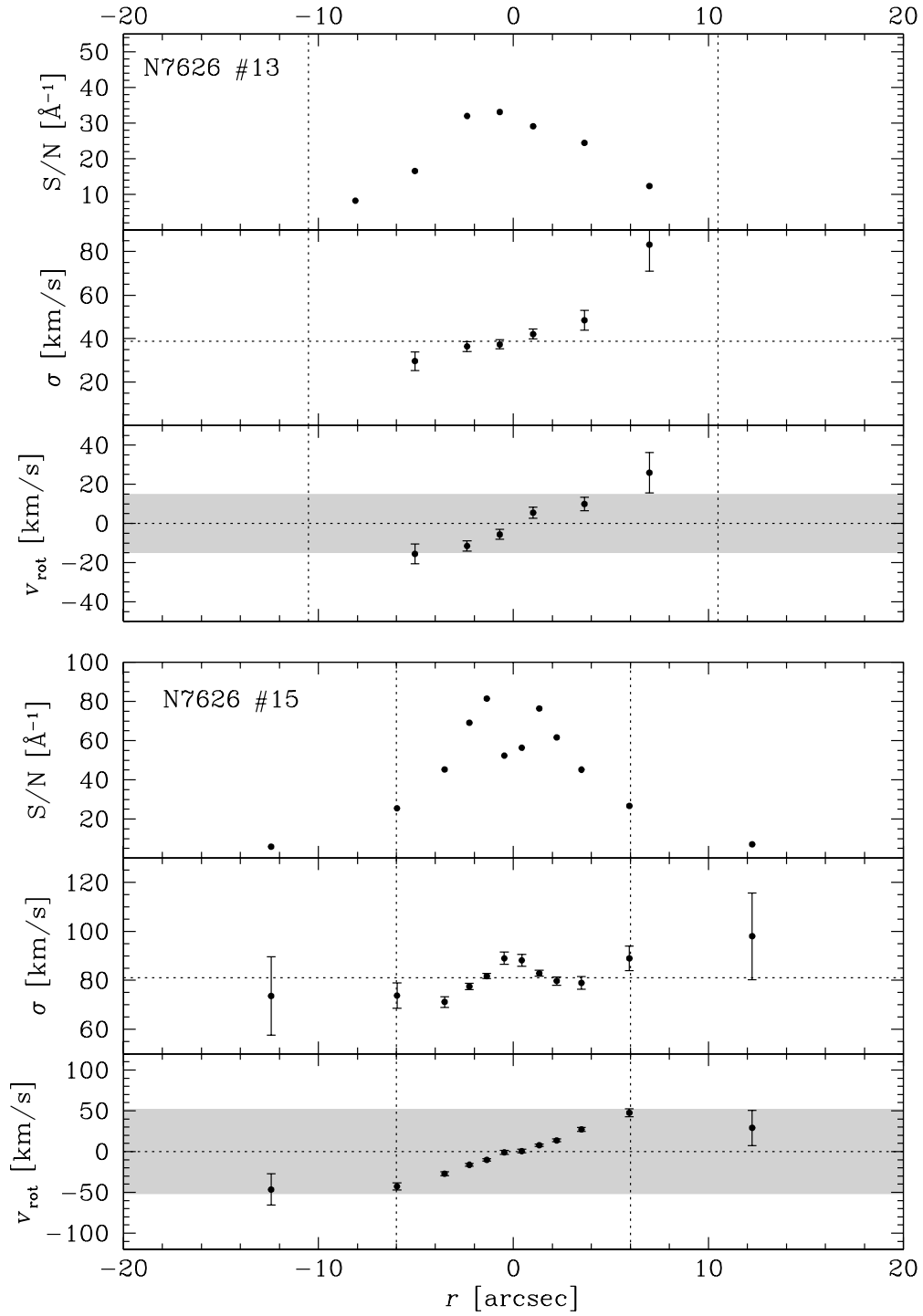


Figure 8.7: Signal-to-noise (top panel), velocity dispersions (middle panel), and rotational velocities (bottom panel) as functions of radius for NGC 7626#13 and NGC 7626#15. The vertical dotted lines mark the respective effective radii r_e . The shaded region gives the range of v_{rot} for which $(v/\sigma)^* \leq 0.7$ (see text).

area, implying that NGC 7626#15 is anisotropic. The heliocentric velocity is $v_{\odot} = 3519 \pm 2$ km/s.

NGC 1052#1

The results for NGC 1052#1 are shown in the upper diagram of Fig. 8.8. The object has flat kinematical profiles within r_e , $\sigma = 42 \pm 2$ km/s is constant, and no significant rotation could be determined, $v_{\text{rot}} < 10$ km/s, $(v/\sigma)^* < 0.4$. The derived heliocentric velocity is $v_{\odot} = 1541 \pm 2$ km/s.

The Virgo cluster dwarfs

VCC 608 The results for VCC 608 are shown in the lower diagram of Fig. 8.8. The values of σ out to r_e are well determined with $20 \lesssim S/N \lesssim 60$. $\sigma_0 \approx \bar{\sigma} = 35 \pm 2$ km/s is constant within the effective radius, no significant rotation is found, $v_{\text{rot}} < 6$ km/s, $(v/\sigma)^* < 0.3$. The heliocentric velocity $v_{\odot} = 1820 \pm 2$ km/s is consistent with the value from the Binggeli, Sandage, & Tamman (1985) catalogue ($v_{\odot} = 1803$).

VCC 1087 The results for VCC 1087 are shown in the upper diagram of Fig. 8.9. Again, $\sigma \approx 47 \pm 2$ km/s and $v_{\text{rot}} < 3$ km/s are constant within r_e , $(v/\sigma)^* < 0.2$. VCC 1087 is the largest dwarf ellipticals in the present sample, with the highest total luminosity, and the largest r_e , and has also the highest velocity dispersion. The heliocentric velocity ($v_{\odot} = 663 \pm 2$ km/s) is consistent with the Binggeli, Sandage, & Tamman (1985) value $v_{\odot} = 645$ km/s.

VCC 1308 Finally, the results for VCC 1308 are shown in the lower diagram of Fig. 8.9. Like in the previous cases, the kinematic profiles are flat within the effective radius. $\bar{\sigma} = 35 \pm 2$ km/s, $v_{\text{rot}} < 4$ km/s, $(v/\sigma)^* < 0.2$. The heliocentric velocity $v_{\odot} = 1732 \pm 2$ km/s is consistent with the Binggeli, Sandage, & Tamman (1985) value $v_{\odot} = 1721$ km/s.

The kinematical properties discussed above are summarized in Table 8.3 (p. 131). Being at the limit of resolution, it is very hard to draw firm conclusions on the kinematical profiles of the studied galaxy sample. In general it is found that the velocity dispersions of all the dwarf ellipticals are low, $35 \lesssim \sigma \lesssim 47$ km/s. No significant rotation was detected, implying that their ellipticities are produced by anisotropic velocity distributions. Also the dwarf lenticulars NGC 7626#13 and NGC 7626#15, although slowly rotating, are not fully rotationally flattened.

8.3.2 Line indices

In this section I present the line indices Mg₂, Mg *b*, Fe5250, Fe5335, and H β measured within $r_e/2$. The index values as functions of radius are in general rather constant out to r_e , however with a large scatter. I therefore do not discuss the gradients here and focus on the mean indices within $r_e/2$ given in Table 8.4.

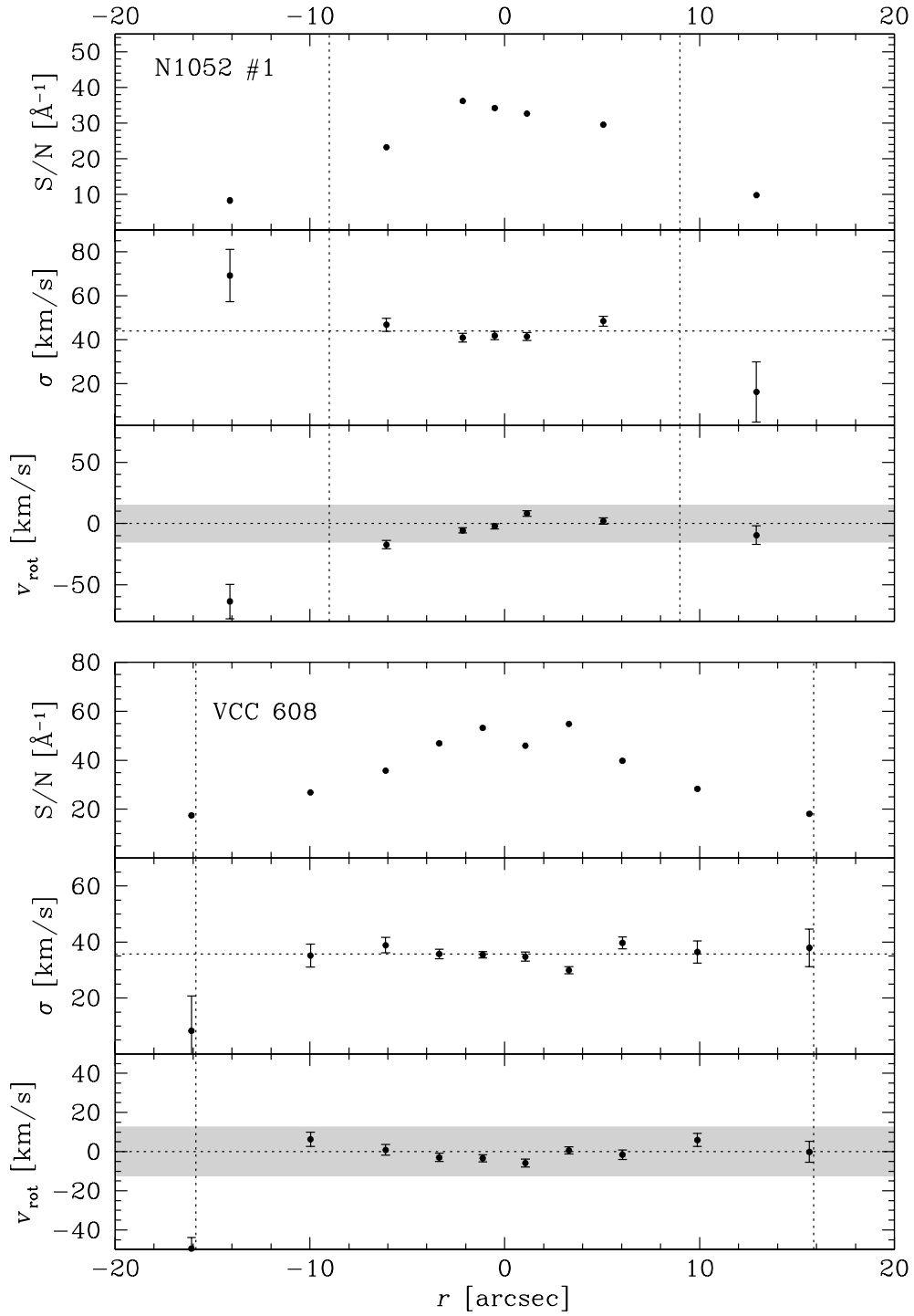


Figure 8.8: Signal-to-noise (top panel), velocity dispersions (middle panel), and rotational velocities (bottom panel) as functions of radius for NGC 1052#1 and VCC 608. The vertical dotted lines mark the respective effective radii r_e . The shaded region gives the range of v_{rot} for which $(v/\sigma)^* \leq 0.7$ (see text).

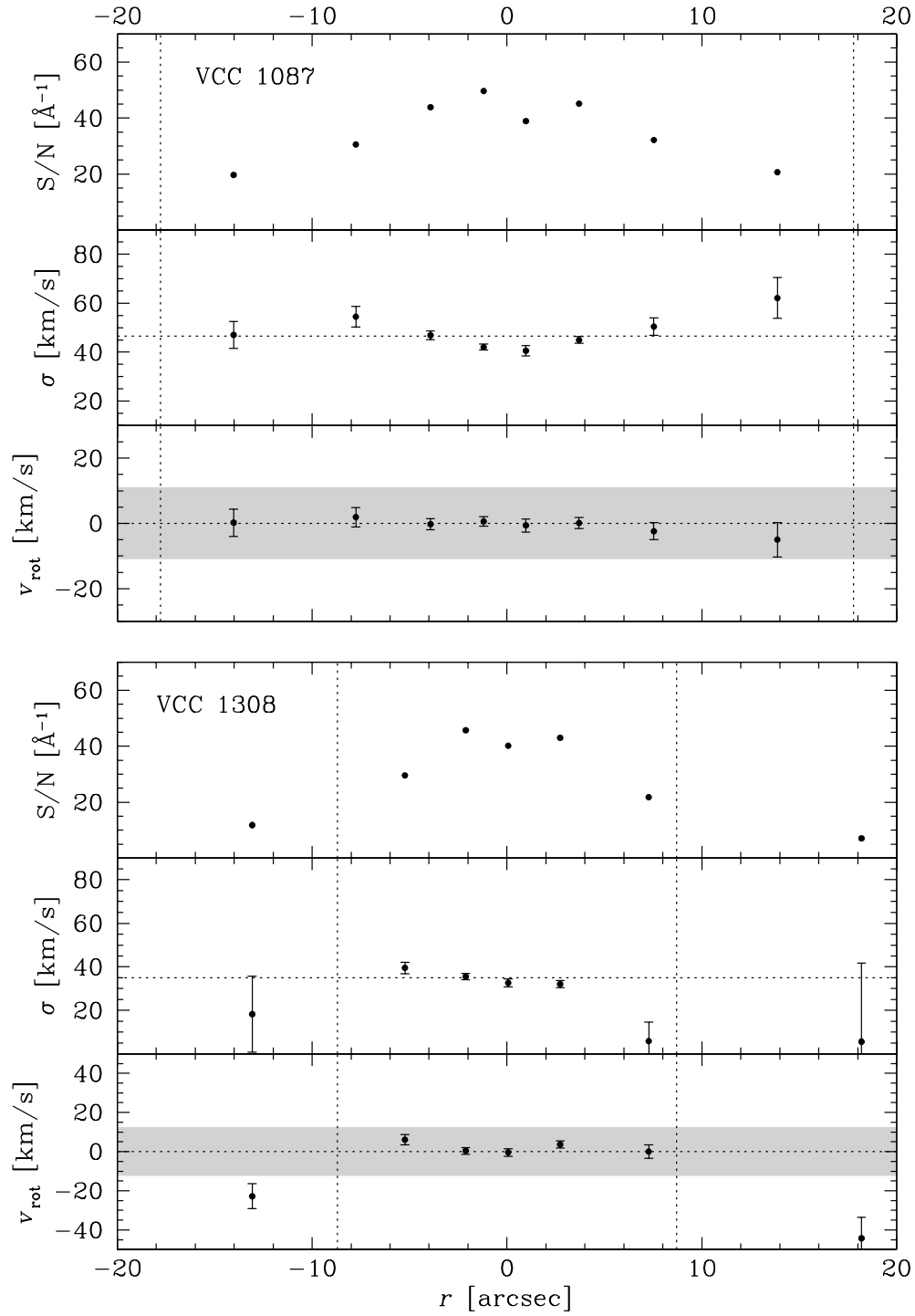


Figure 8.9: Signal-to-noise (top panel), velocity dispersions (middle panel), and rotational velocities (bottom panel) as functions of radius for VCC 1087 and VCC 1308. The vertical dotted lines mark the respective effective radii r_e . The shaded region gives the range of v_{rot} for which $(v/\sigma)^* \leq 0.7$ (see text).

TABLE 8.3
KINEMATICAL RESULTS

Object	$\bar{\sigma}$ [km/s]	σ_0 [km/s]	v_{rot} [km/s]	$(v/\sigma)^*$	v_{\odot} [km/s]
N7626#13	39 ± 3	39 ± 3	16 ± 5	0.75 ± 0.24	3690 ± 9
N7626#15	82 ± 2	89 ± 2	45 ± 5	0.60 ± 0.07	3519 ± 2
N1052#1	42 ± 2	44 ± 2	< 10	< 0.4	1541 ± 2
VCC 608	35 ± 2	35 ± 2	< 6	< 0.3	1820 ± 2
VCC 1087	47 ± 2	40 ± 2	< 3	< 0.2	663 ± 2
VCC 1308	35 ± 2	34 ± 2	< 4	< 0.2	1732 ± 2

NOTE.—For the two dS0 NGC 7626#13 and NGC 7626#15, rotation v_{rot} could be detected. Due to the lack of profiles in the velocity dispersions, then mean $\bar{\sigma}$ and the central σ_0 are mostly identical, except in NGC 7626#15. The quantity v_{\odot} is the heliocentric velocity.

The Mg- σ relation

In Fig. 8.10, the Mg_2 index is plotted as a function of velocity dispersion. The filled squares are the dwarf galaxies of the present work, the open triangles are bright dwarf ellipticals from Bender, Burstein, & Faber (1993). The dotted line is the fit

$$\text{Mg}_2 = 0.2 \cdot \log \sigma - 0.166 \quad (8.6)$$

derived by Bender, Burstein, & Faber (1993) for their complete galaxy sample including giant ellipticals. The dwarfs analyzed here follow the overall relation between Mg_2 and σ , deviating from the fit by at most -0.055 mag at a given σ (in the case of the dwarf lenticular galaxy NGC 7626#15). This deviation is comparable to the scatter shown by the Bender, Burstein, & Faber (1993) data. Note that the dS0 NGC 7626#15 and the dE VCC 1087, that differ significantly in σ , do not only have the same Mg_2 but are also similar with respect to the other line indices given in Table 8.4. This implies that both galaxies have, in spite of their discrepant velocity dispersions, the same mean ages and metallicities (see following section).

Ages and metallicities

Deriving ages and metallicities of stellar populations is affected by the well-known age-metallicity degeneracy, because both increasing the age or increasing the metallicity results in a reddening of stellar evolutionary tracks (see Chapter 6 and references therein). The degeneracy can be broken by coupling the primarily age sensitive Balmer indices (e.g., $\text{H}\beta$) with metallic indices

TABLE 8.4
LINE INDICES WITHIN $r_e/2$

object	σ [km/s]	M_{Fe2} [mag]	$M_{\text{Fe}b}$ [Å]	Fe5270 [Å]	Fe5335 [Å]	$\text{H}\beta$ [Å]
N7626#13	39 ± 3	0.113 ± 0.004	1.54 ± 0.16	1.75 ± 0.19	1.69 ± 0.22	2.11 ± 0.14
N7626#15	81 ± 2	0.163 ± 0.001	2.93 ± 0.04	2.60 ± 0.05	1.74 ± 0.06	1.93 ± 0.03
N1052#1	44 ± 2	0.116 ± 0.003	1.32 ± 0.11	1.99 ± 0.13	1.44 ± 0.15	2.24 ± 0.10
VCC 608	36 ± 2	0.122 ± 0.001	1.59 ± 0.06	2.27 ± 0.07	1.76 ± 0.08	2.72 ± 0.05
VCC 1087	47 ± 2	0.165 ± 0.001	2.78 ± 0.04	2.53 ± 0.05	1.86 ± 0.06	1.95 ± 0.04
VCC 1308	35 ± 2	0.130 ± 0.001	2.11 ± 0.04	2.13 ± 0.05	1.75 ± 0.06	2.41 ± 0.04

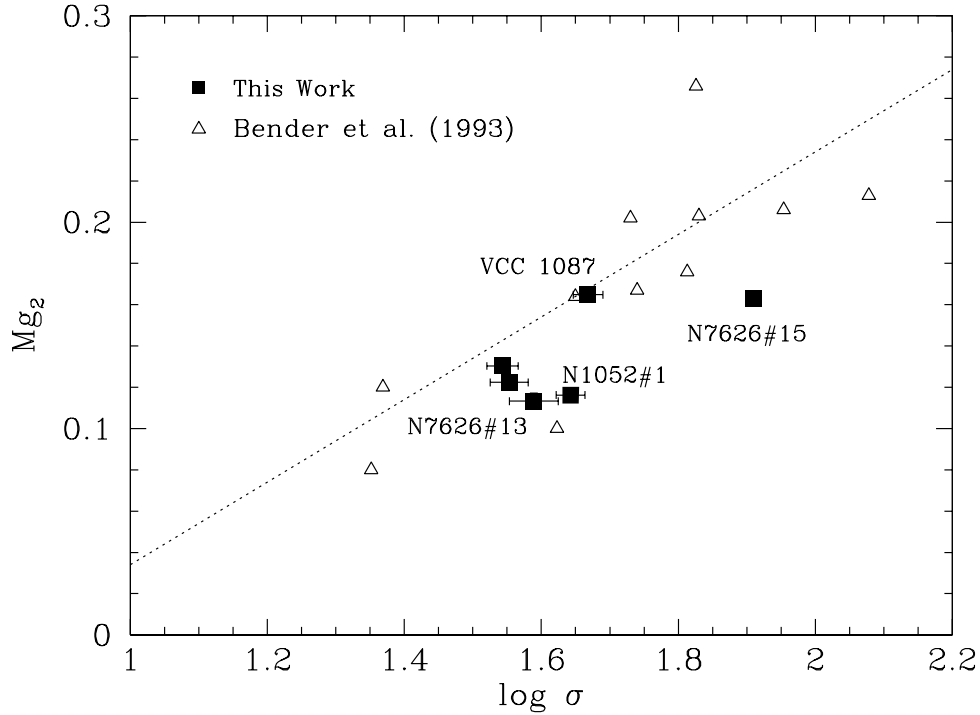


Figure 8.10: Mg_2 index as a function of velocity dispersion. The present sample (Table 8.4) are the filled squares. The open triangles are Local Group ‘bright dwarf ellipticals’ from Bender, Burstein, & Faber (1993). The dotted line is the fit $Mg_2 = 0.2 \cdot \log \sigma - 0.166$ derived by Bender, Burstein, & Faber (1993) for their complete galaxy sample including giant ellipticals. The errors in Mg_2 are smaller than the sizes of the symbols.

(e.g., Mg_2 , Mgb , $\langle Fe \rangle$) (González 1993; Worthey 1994). In Chapter 6 it is discussed, however, that at low metallicities also the Balmer indices are sensitive to metallicity as shown in the globular cluster data, because metal-poor horizontal branch stars significantly contribute to the $H\beta$ -line strength. In Chapter 6 it is shown that, considering a simple mixture of a major old metal-rich population and a minor *old* metal-poor subcomponent, giant ellipticals with $H\beta \lesssim 2 \text{ \AA}$ are consistent with being as old as 14 Gyr (see Chapter 6). The impact on the mean ages derived for the present dwarf galaxy sample will be discussed later.

In Fig. 8.11, $H\beta$ is plotted as a function of Mg_2 (top panel) and $\langle Fe \rangle = (Fe5270 + Fe5335)/2$ (bottom panel). The filled squares represent the six dwarf galaxies of the present work, the open squares are the dwarf galaxy data from Gorgas et al. (1997). For comparison, the González (1993) sample (giant ellipticals) is plotted as filled circles. The triangles are globular clusters from the Milky Way and M31, taken from Covino, Galletti, & Pasinetti 1995 (open triangles) and Trager 1998 (filled triangles). Overlaid is a grid of Simple Stellar Population (SSP) models from Maraston, Greggio, & Thomas (2001) and C. Maraston (in preparation), being based on the evolutionary synthesis code described in Maraston (1998). The input stellar tracks are from Bono et al.

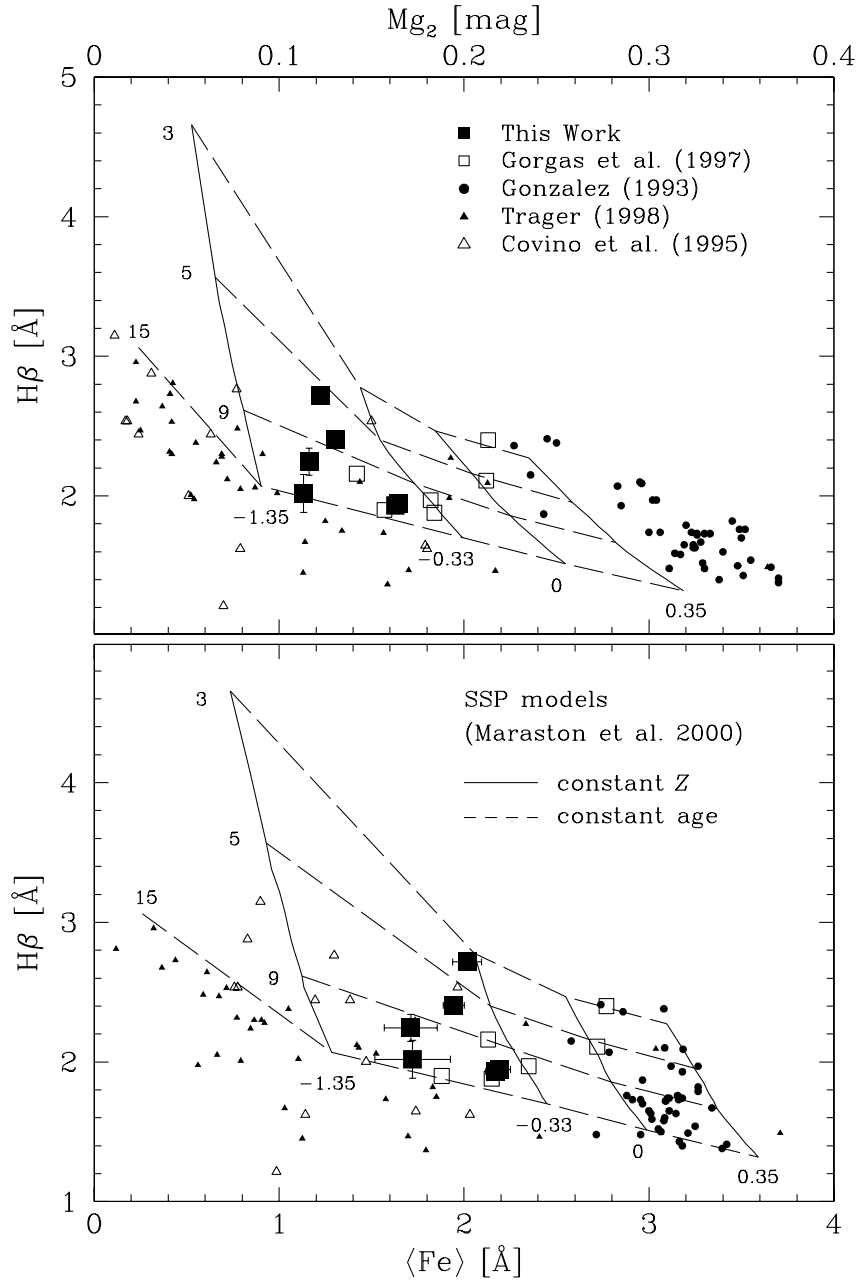


Figure 8.11: $H\beta$ as a function of Mg_2 (top panel) and $\langle Fe \rangle = (Fe5270 + Fe5335)/2$ (bottom panel). The filled squares are the index values of the present dwarf galaxy sample measured within $r_e/2$ (Table 8.4). The open squares are the dwarf galaxy data from Gorgas et al. (1997). Filled circles are giant ellipticals (González 1993), filled and open triangles globular clusters from Trager (1998) and Covino, Galletti, & Pasinetti (1995), respectively. The overlaid SSP models with ages $t = 3, 5, 9, 15$ Gyr and metallicities $[Z/H] = -1.35, -0.33, 0.0, 0.35$ are from Maraston, Greggio, & Thomas (2001). Solid and dashed lines (labeled) are lines of constant metallicity and age, respectively. The 15 Gyr model additionally includes the metallicity $[Z/H] = -2.25$.

(1997) and S. Cassisi (1999, private communication). The indices are computed adopting the fitting functions of Worthey et al. (1994), that give the index values as functions of the stellar parameters T_{eff} , g , Z . The labeled solid and dashed lines are lines of constant metallicities ($[Z/H] = -1.35, -0.33, 0.0, 0.35$) and constant ages ($t = 3, 5, 9, 15$ Gyr), respectively. The 15 Gyr model additionally includes the metallicity $[Z/H] = -2.25$.

The top panel of Fig. 8.11 shows the $H\beta$ versus Mg_2 . The very low Mg_2 indices of the dwarfs (squares) clearly separate them from the population of giant galaxies (circles). The Mg_2 indices of the dwarfs are compatible with the indices of the most metal-rich globular clusters (triangles). The dwarfs with the very high Mg_2 from the Gorgas et al. (1997) sample (open squares) are very bright dwarfs that are apparently transition types between dwarfs and giants. In the bottom panel of Fig. 8.11 $H\beta$ vs. $\langle Fe \rangle = (Fe5270 + Fe5335)/2$ is plotted. The striking difference with respect to the Mg_2 - $H\beta$ plane is that the discrepancy in the metallic index between giants and dwarfs becomes smaller, because the giants shift towards considerably lower, and the dwarfs towards slightly higher metallicities. As a consequence, the ages of the dwarfs are smaller and the metallicities are larger when determined with the $\langle Fe \rangle$ index. The figure also allows for the qualitative conclusion that the dwarf galaxies studied here are younger than the globular clusters of the Milky Way, because for a given metallic index the $H\beta$ indices of the dwarf ellipticals are higher.

TABLE 8.5
AGES AND METALLICITIES

Object	Mg_2		$\langle Fe \rangle$	
	t (Gyr)	$[Z/H]$	t (Gyr)	$[Z/H]$
N7626#13	14.7 ± 1.1	-1.12 ± 0.08	13.8 ± 1.9	-0.93 ± 0.13
N7626#15	13.2 ± 0.3	-0.61 ± 0.01	12.6 ± 0.4	-0.51 ± 0.02
N1052#1	11.5 ± 0.6	-1.02 ± 0.05	10.5 ± 1.0	-0.86 ± 0.08
VCC 608	6.2 ± 0.1	-0.76 ± 0.02	3.8 ± 0.2	-0.39 ± 0.02
VCC 1087	12.8 ± 0.3	-0.58 ± 0.01	12.2 ± 0.4	-0.48 ± 0.02
VCC 1308	8.4 ± 0.2	-0.77 ± 0.01	7.3 ± 0.2	-0.56 ± 0.02

NOTE.—Columns (2) and (3) give ages and metallicities, respectively, derived from the Mg_2 index. Columns (4) and (5) give ages and metallicities, respectively, derived from the $\langle Fe \rangle$ index.

Table 8.5 gives the mean ages t and metallicities $[Z/H]$ of the sample derived from Mg_2 (Columns (2) and (3)) and $\langle Fe \rangle$ (Columns (4) and (5)). The metallicities derived from Mg_2 scatter between $[Z/H] = -1.12$ and $[Z/H] = -0.58$, with the brightest objects VCC 1087 and NGC 7626#15 being most metal-rich. The $\langle Fe \rangle$ index yields metallicities $-0.93 \leq [Z/H] \leq -0.39$, higher by ~ 0.2 dex than those derived from the Mg_2 index.

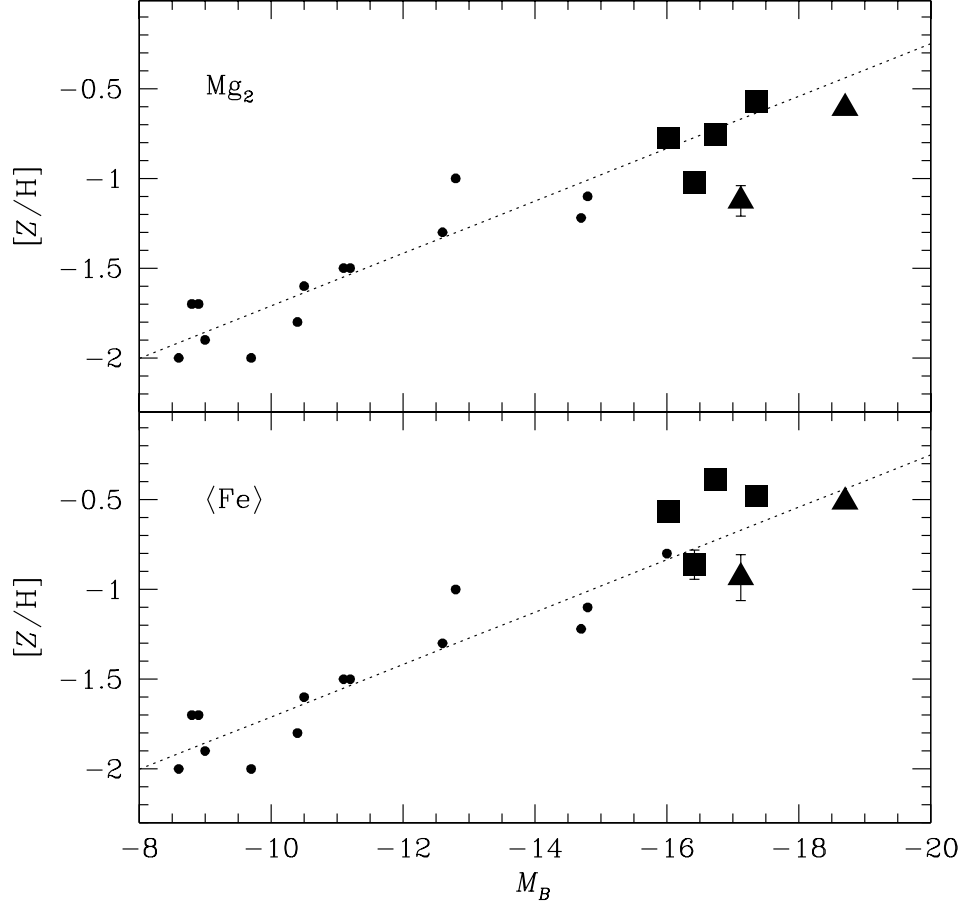


Figure 8.12: Metallicity $[Z/H]$ derived from Mg_2 (top panel) and $\langle Fe \rangle = (Fe5270 + Fe5335)/2$ (bottom panel) as functions of blue magnitude M_B . The filled squares and triangles are the dE and dS0 galaxies of this work, respectively. The small circles are Local Group dwarf ellipticals from the compilation of Mateo (1998). The dotted line is the fit to the Local Group objects alone.

In Fig. 8.12, the metallicity $[Z/H]$ is plotted as a function of the blue luminosity M_B . The Local Group dwarfs ellipticals from the compilation of Mateo (1998) are the small circles. The squares are the four dwarf ellipticals, the triangles the two dwarf lenticular galaxies of the present work. The top and bottom panels show the metallicities derived from the Mg_2 index and the $\langle Fe \rangle$ index, respectively. The dotted line is a linear fit to the Local Group data. Note that the metallicities of the dwarf ellipticals in the Local Group are derived from the color of the Red Giant Branch and from spectroscopy of individual stars and planetary nebulae (Mateo 1998, and references therein). As individual stars cannot be resolved outside the Local Group, the metallicities of the present objects, instead, are determined from the spectra of the integrated light by means

of population synthesis models.

The Local Group dwarf ellipticals exhibit a tight relation between $[Z/H]$ and M_B , in the sense that $[Z/H]$ increases with increasing blue luminosity. The metallicities derived from Mg_2 and $\langle Fe \rangle$ are both in good agreement with the extrapolation of the Local Group data to higher luminosities. From Fig. 8.12 it is difficult to decide which index is the better metallicity indicator. In case of the three Virgo dwarf ellipticals, the Mg_2 index seems favorable, as the $\langle Fe \rangle$ yields $[Z/H]$ values that are up to 0.3 dex above the relation. The two dwarf lenticulars and NGC 1052#1, instead, are better consistent with the Local Group data, if their metallicities are determined through $\langle Fe \rangle$.

The mean ages derived from the Mg_2 - $H\beta$ plane range from 6.2 to 14.7 Gyr, $\langle Fe \rangle$ leads to the younger ages $3.8 \leq t \leq 13.8$ Gyr. This rather large range in ages is consistent with the star formation histories of dwarf elliptical galaxies in the Local Group that are derived from color-magnitude diagrams (e.g., Grebel 1997; Mateo 1998). These studies further show that the bulk of stars in the Local Group dwarf ellipticals have ages $10 \leq t \leq 14$ Gyr with a small tail extending to $t \gtrsim 1$ Gyr. This truncation of star formation is in agreement with the V -light averaged ages of the present sample $t \gtrsim 4$ Gyr. Note that dwarf irregulars, instead, have fairly constant star formation rates including the past 1 Gyr (Greggio et al. 1993).

The Composite Stellar Population models presented in Chapter 6 yield $H\beta \approx 2$ for old populations with a 10 per cent contribution to the total mass of the population from very metal-poor stars. The rather high Balmer line strengths of the dwarf galaxies observed here ($1.9 \lesssim H\beta \lesssim 2.7 \text{ \AA}$) then require the metal-poor stars to contribute at least 20 per cent by mass, resulting in a very high flux in the mid-UV. Although spectra of dwarf spheroidals in that wavelength range are not available, such high fluxes in the mid-UV have not been confirmed for the compact elliptical M32 (see Chapter 6 and references therein). I conclude that the mean ages determined here on the basis of Simple Stellar Population models are real.

The present sample does not exhibit any relation between age and metallicity, hence does not confirm the interpretation by Gorgas et al. (1997) that younger dwarf ellipticals tend to be more metal-rich.

The α/Fe ratio

As discussed above, the two planes Mg_2 - $H\beta$ and $\langle Fe \rangle$ - $H\beta$ yield different ages and metallicities. In the most extreme case of VCC 608, the metallicity derived from $\langle Fe \rangle$ is higher by 0.37 dex than the one from Mg_2 , and the mean age decreases by 2.4 Gyr from 6.2 (derived from the Mg_2 index) to 3.8 Gyr (derived from the $\langle Fe \rangle$ index). Note that this pattern is the opposite of what is known for giant elliptical galaxies, whose metallicities are significantly larger when derived from the Mg_2 index. This effect is believed to be due to changes of the abundance ratios Mg (and the other α -elements) to Fe with respect to the solar Mg/Fe element ratio (see Section 1.2.2).

This effect can be better appreciated in Fig. 8.13, in which $\langle Fe \rangle$ is plotted as a function of Mg_2 . Giant ellipticals (circles) clearly exhibit stronger Mg_2 -

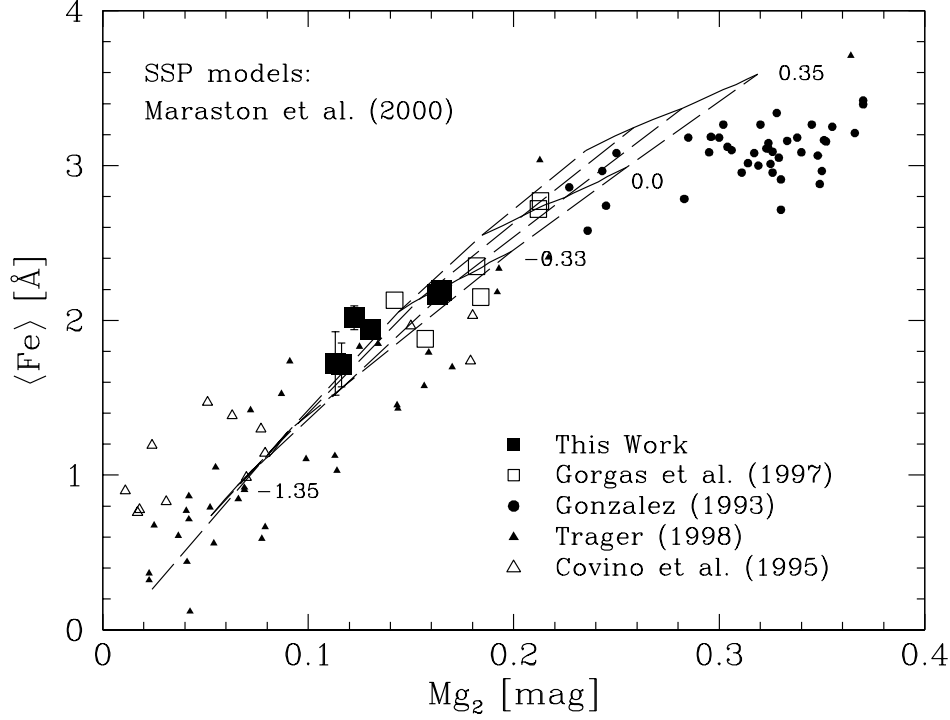


Figure 8.13: $\langle \text{Fe} \rangle = (\text{Fe}5270 + \text{Fe}5335)/2$ as function of Mg_2 . The SSP models are from Maraston, Greggio, & Thomas (2001). For more details see the caption of Fig. 8.11.

indices than predicted by the models with solar abundance ratios, while the dwarf ellipticals (squares) lie on the model grid or slightly above at stronger $\langle \text{Fe} \rangle$ values. If the α/Fe ratios reflected by the models do not significantly change as a function of metallicity, this result implies that dwarf ellipticals have lower α/Fe ratios than giant ellipticals (see also Gorgas et al. 1997). This qualitative conclusion gets support from comparing the dwarf galaxy indices with the data of Milky Way globular clusters (triangles), that are known to be α/Fe overabundant with $[\alpha/\text{Fe}] \approx 0.3$ dex (Pilachowski, Sneden, & Wallerstein 1983; Gratton, Quarta, & Ortolani 1986). Fig. 8.13 shows, that — for a given Mg_2 — most globular clusters (triangles) exhibit lower $\langle \text{Fe} \rangle$ -indices than the dwarf ellipticals (squares), implying that dwarf ellipticals have lower α/Fe than Galactic globular clusters.

Fig. 8.14 shows the difference $\Delta[Z/\text{H}]$ between the metallicities derived from Mg_2 and $\langle \text{Fe} \rangle$, as a function of age (averaged between the Mg_2 - and the $\langle \text{Fe} \rangle$ -ages). Except for the dwarf lenticular NGC 7626#13, $|\Delta[Z/\text{H}]|$ clearly increases with decreasing age, so that objects with younger *mean* ages have lower Mg/Fe ratios and therefore more extended star formation histories (see Section 1.2.1 and Chapter 4). The age scatter discussed above is therefore most likely the result of different star formation timescales. There is no hint for a dependence on environment, as the three objects of the Virgo cluster with ages 4–13 Gyr show the same variety in star formation histories found in Local Group dwarf

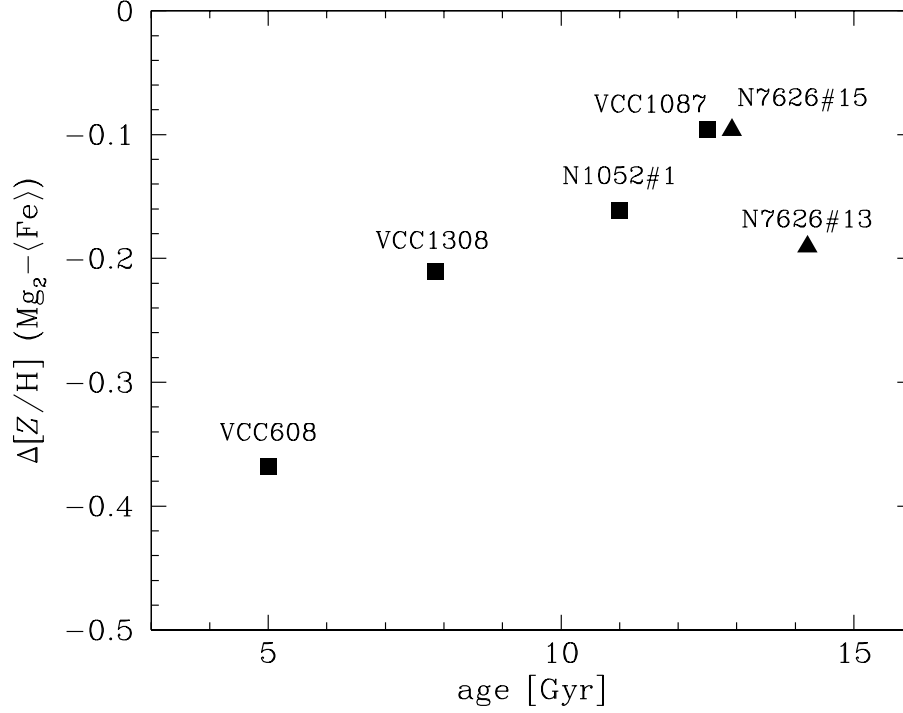


Figure 8.14: Difference of the two metallicities derived from Mg_2 and $\langle Fe \rangle$ as a function of age (averaged between Mg_2 - and the $\langle Fe \rangle$ -ages).

ellipticals.

For the derivation of absolute Mg/Fe values, it is usually assumed that the models, being based on the Worthey et al. (1994) fitting functions, reflect solar abundance ratios (e.g., Worthey, Faber, & González 1992; Greggio 1997; Trager et al. 2000a). If this is also true at metallicities $[Z/H] \lesssim -0.3$, as assumed by Gorgas et al. (1997), the present dwarf ellipticals have $[Mg/Fe] \lesssim 0$. It should be mentioned, however, that the fitting functions are essentially derived from disk stars, whose Mg/Fe ratios increase with decreasing metallicity from $[Mg/Fe] \approx 0$ at $[Fe/H] \approx 0$ to $[Mg/Fe] \approx 0.4$ at $[Fe/H] \approx -1$ (e.g., Fuhrmann 1998; see also Chapter 3). This issue and the impact on the derivation of Mg/Fe ratios in systems of different metallicities is the subject of future investigations.

8.4 Discussion

A major goal of this study is to investigate whether the early-type giant-dwarf dichotomy found in the structural properties like the surface brightness-magnitude relation (see Section 8.1.2) is also present in their stellar populations. Indeed, in Section 8.3.1 it is shown that all the six dwarf early-type galaxies exhibit anisotropic velocity distributions, reinforcing the earlier results from Bender & Nieto (1990) and Bender, Paquet, & Nieto (1991). Furthermore, as the importance of rotation increases with decreasing mass among the giant elliptical population, this finding strongly supports the existence of a giant-dwarf

dichotomy with respect to their kinematical properties. The properties of the stellar populations of the dwarf galaxy sample studied also point towards a clear separation between dwarfs and giants as discussed in Section 8.3.2. With metallicities similar to metal-rich globular clusters, dwarf ellipticals are significantly more metal-poor than giants, and have mean ages from 4 to 14 Gyr. This rather large spread in age within a small range of metallicities, and particularly the existence of very old dwarf ellipticals shows that dwarf galaxies are clearly not the simple extension or extrapolation of the giant family to lower masses. Note that in the González (1993) sample the least massive ellipticals tend to be the youngest (~ 5 Gyr). Finally, as also discussed in Gorgas et al. (1997), the low — possibly sub-solar — α/Fe ratios in the stellar populations of dwarf ellipticals clearly distinguish them from the α -enhanced giants.

Both the ages and the metallicities of the dwarf early-type galaxies studied here are higher than those of late-type dwarfs. Furthermore, also the anisotropic velocity distributions of the early-types point towards an early-type to late-type dichotomy. Hence, the conclusion of Binggeli (1994) that early-type dwarfs could not have formed out of late-type dwarfs is confirmed.

8.5 Summary

In this chapter I present high-resolution spectra of six dwarf early-type galaxies in the wavelength range 4500–5500 Å. The resolution of ~ 40 km/s allows to determine velocity dispersions and possible rotation curves. After the careful calibration on the Lick standard system, the indices $\text{H}\beta$, Mg_2 , $\text{Mg } b$, $\text{Fe}5270$, and $\text{Fe}5335$ are derived in order to study ages, metallicities, and Mg/Fe of the stellar populations.

Except for the dwarf lenticular galaxy NGC 7626#15 ($\sigma \approx 80$ km/s), the objects of the sample have low velocity dispersions $\sigma \approx 40$ km/s. None of the four dwarf ellipticals show significant rotation. The finding in previous kinematical studies (Bender & Nieto 1990; Bender, Paquet, & Nieto 1991), that dwarf elliptical galaxies have anisotropic velocity distributions, gets further support. The anisotropy parameter of the slightly rotating dS0s NGC 7626#15 ($v_{\text{rot}} \approx 45$ km/s) and NGC 7626#13 ($v_{\text{rot}} \approx 16$ km/s) is $(v/\sigma)^* = 0.6$ and $(v/\sigma)^* \approx 0.75$, implying that the ellipticities of these objects are not fully supported by rotation. The dwarf galaxy sample follows the Mg_2 - σ relation derived by Bender, Burstein, & Faber (1993). The mean ages, obtained by comparing the measured line indices with Simple Stellar Population models, range from 4 to 14 Gyr, in agreement with the star formation histories of Local Group dwarf ellipticals. The mean metallicities scatter between $[\text{Fe}/\text{H}] = -1.1$ and $[\text{Fe}/\text{H}] = -0.4$. The $\langle \text{Fe} \rangle$ -indices give systematically higher metallicities and lower ages, implying slightly sub-solar α/Fe ratios.

The kinematical properties, the ages, the metallicities, and the abundance ratios of the stellar populations in the present dwarf elliptical sample strongly support the view that dwarf galaxies form their own population and are clearly separated from the giant galaxies. This giant-dwarf dichotomy then implies that present-day dwarf ellipticals are not the fossilized building blocks of present-day

giant ellipticals.

Chapter 9

Outlook

Chemical evolution is a powerful tool for testing scenarios of galaxy formation and evolution. In this work it is shown that Type II supernova nucleosynthesis is still affected by uncertainties in stellar evolution and in the explosion mechanism. It would be very valuable for the future to further improve our knowledge on nucleosynthesis before and during the explosion particularly in massive stars, and to stabilize the reliability of the theoretical stellar yields. The nucleosynthesis in Type Ia supernovae, instead, is rather robust, while the model, the physical conditions for the explosion, and therefore the rate of Type Ia supernovae are essentially unknown, which impacts on the timescale of the delayed iron enrichment. These uncertainties in chemical evolution reinforce the need to calibrate the codes on data of the Milky Way. As this calibration suffers from the fact that the star formation history is not known, it is a challenge for the future to observationally derive the past star formation rate in the solar neighborhood. A further crucial parameter for the interpretation of abundance ratios is the IMF. It is very important to study the mechanism of star formation, with the aim at constraining the IMF — from both theoretical and observational side — in a way that is independent of chemical evolution.

Elliptical galaxies, that play an important role in the theory of galaxy formation, are still puzzling. Their kinematical properties show clear signatures of merging, while their stellar populations appear very homogeneous. Mergers seem to take place, but it is not clear when, and in how far processes like dissipation and star formation are involved. The results of this work show that an ‘elliptical galaxy’ cannot simply be formed through the merger of two spirals, even though numerical simulations show that we obtain an elliptically shaped object, and even though we can observe merging galaxies in the local universe. Current models of hierarchical structure formation are very promising, because they consider galaxy formation in a cosmological context and are based on very fundamental cosmological principles. But particularly the treatment of gas and star formation requires further improvements. The evolution of the stellar populations, that set the link to observables, is not yet well defined in hierarchical models, as they fail at reproducing — among other fundamental properties of the stellar populations in ellipticals — both the observed α -enhancement and the trend of increasing α/Fe with increasing galaxy mass. Hierarchical galaxy

formation implies clear differences between the cluster and the field galaxy populations. Detailed observational studies on the stellar populations in cluster and field galaxies, that are based on large and homogeneous data sets, will provide crucial tests for the model predictions.

Population synthesis models are the principal tool to derive ages, metallicities, and element abundances from galaxy spectra. Because observations are restricted to the diffuse light in ellipticals, only average properties by means of Simple Stellar Population models can be determined. However, with more complex models of composite populations it is hard to disentangle age and metallicity effects, as shown in this work. Globular clusters, instead, are in good approximation stellar populations of single age and metallicity, and are therefore much easier to interpret. With the new 8m-class telescopes it is now possible to take spectra of a large number of globular clusters in elliptical galaxies, which offers a promising way to gain better insight in the formation mechanisms of elliptical galaxies.

The derivation of metallicities, ages, and abundance ratios from spectral line indices crucially depends on both the fitting functions and the response functions, the latter giving the response of line indices to individual element abundance changes. There is the urgent need for a more comprehensive set of such response functions as calculated by Tripicco & Bell (1995), comprising a grid of different metallicities and ages.

As galaxy clusters can be described in good approximation as closed systems, they are ideal laboratories to consider the chemical evolution of a complete galaxy population in a self consistent way. With the new X-ray satellites, the quality of the data on element abundances in the intracluster medium will further improve, which opens the door to a better understanding of the chemical enrichment processes. From simulations of such processes, we can learn a great deal about both the evolution of galaxy clusters and the formation and evolution of galaxies in clusters.

Dwarf galaxies, i.e. their stellar population properties, are not considered in galaxy formation models so far. On the other hand, a large data base comprising ages, metallicities, and abundance ratios is still missing in the literature, as dwarf ellipticals outside the Local Group are very difficult to observe due to their low surface brightnesses. Once this lack will be filled, adding also the six objects presented in this work, dwarf ellipticals may become the new challenge for galaxy formation models.

Bibliography

- Anders, E., & Grevesse, N. 1989, *Geochim. Cosmochim. Acta*, 53, 197
- Aragón Salamanca, A., Ellis, R. S., Couch, W. J., & Carter, D. 1993, *MNRAS*, 262, 764
- Arimoto, N., Matsushita, K., Ishimaru, Y., Ohashi, T., & Renzini, A. 1997, *ApJ*, 477, 128
- Arimoto, N., & Yoshii, Y. 1987, *A&A*, 173, 23
- Arnaud, M., Rothenflug, R., Boulade, O., Vigroux, L., & Vangioni-Flam, E. 1992, *A&A*, 254, 49
- Arnett, W. D., Bahcall, J. N., Kirshner, R. P., & Woosley, S. E. 1989, *ARA&A*, 27, 629
- Arnett, W. D., & Thielemann, F.-K. 1985, *ApJ*, 295, 589
- Ashman, K. M., & Zepf, S. E. 1998, *Globular Cluster Systems* (Cambridge: Cambridge University Press)
- Babul, B., & Rees, M. J. 1992, *MNRAS*, 255, 346
- Barbuy, B. 1994, *ApJ*, 430, 218
- Barnes, J. E. 1988, *ApJ*, 331, 699
- Barnes, J. E., & Hernquist, L. 1996, *ApJ*, 471, 115
- Baron, E., Hauschildt, P. H., & Young, T. R. 1995, *Phys. Rep.*, 256, 23
- Baugh, C. M., Cole, S., & Frenk, C. S. 1996, *MNRAS*, 283, 1361
- Beasley, M. A., Sharples, R. M., Bridges, T. J., Hanes, D. A., Zepf, S. E., Ashman, K. M., & Geisler, D. 2000, *MNRAS*, in press, astro-ph/0007063
- Bender, R. 1990a, in *Dynamics and Interactions of Galaxies*, ed. R. Wielen (Heidelberg: Springer Verlag), 232
- Bender, R. 1990b, *A&A*, 229, 441
- Bender, R. 1996, in *New Light on Galaxy Evolution*, ed. R. Bender & R. L. Davies (Dordrecht: Kluwer Academic Publishers), 181

- Bender, R., Burstein, D., & Faber, S. M. 1992, *ApJ*, 399, 462
- Bender, R., Burstein, D., & Faber, S. M. 1993, *ApJ*, 411, 153
- Bender, R., & Nieto, J.-L. 1990, *A&A*, 239, 97
- Bender, R., Paquet, A., & Nieto, J.-L. 1991, *A&A*, 246, 349
- Bender, R., Saglia, R. P., & Gerhard, O. 1994, *MNRAS*, 269, 785
- Bender, R., & Surma, P. 1992, *A&A*, 258, 250
- Bender, R., Ziegler, B. L., & Bruzual, G. 1996, *ApJ*, 463, L51
- Bernardi, M., et al. 1998, *ApJ*, 508, 143
- Bessell, M. S., Sutherland, R. S., & Ruan, K. 1991, *ApJ*, 383, L71
- Beuing, J., Bender, R., & Mendes de Oliveira, C. 2000, *MNRAS*, submitted
- Binggeli, B. 1986, in *Star-Forming Dwarf Galaxies*, ed. D. Kunth et al. (Gif sur Yvettes: ASPÉditions Frontières), 53
- Binggeli, B. 1994, in *Dwarf Galaxies*, ed. G. Meylan & P. Prugniel (Garching b. München: ESO), 13
- Binggeli, B., & Cameron, L. M. 1991, *A&A*, 252, 27
- Binggeli, B., & Cameron, L. M. 1993, *A&AS*, 98, 297
- Binggeli, B., & Popescu, C. C. 1995, *A&A*, 298, 63
- Binggeli, B., Sandage, A., & Tamman, G. A. 1985, *AJ*, 90, 1681
- Binggeli, B., Sandage, A., & Tammann, G. A. 1988, *ARA&A*, 26, 509
- Binggeli, B., Sandage, A., & Tarenghi, M. 1984, *AJ*, 89, 61
- Binggeli, B., Tamman, G. A., & Sandage, A. 1987, *AJ*, 94, 251
- Binney, J. 1978, *MNRAS*, 183, 501
- Binney, J., & Tremaine, S. 1987, *Galactic Dynamics* (New York: Princeton University Press)
- Bond, J. R., Cole, S., Efstathiou, G., & Kaiser, N. 1991, *ApJ*, 379, 440
- Bono, G., Caputo, F., Cassisi, S., Castellani, V., & Marconi, M. 1997, *ApJ*, 489, 822
- Bothun, G. D. 1985, *AJ*, 90, 1982
- Bower, R. G., Lucey, J. R., & Ellis, R. S. 1992, *MNRAS*, 254, 589
- Bower, R. J. 1991, *MNRAS*, 248, 332

- Bressan, A., Chiosi, C., & Fagotto, F. 1994, *ApJS*, 94, 63
- Brown, T. M., Bowers, C. W., Kimble, R. A., Sweigart, A. V., & Ferguson, H. C. 2000, *ApJ*, 532, 308
- Burstein, D., Bertola, F., Buson, L. M., Faber, S. M., & Lauer, T. R. 1988, *ApJ*, 328, 440
- Burstein, D., Faber, S. M., Gaskell, C. M., & Krumm, N. 1984, *ApJ*, 287, 586
- Buzzoni, A. 1989, *ApJS*, 71, 817
- Buzzoni, A., Gariboldi, G., & Mantegazza, L. 1992, *AJ*, 103, 1814
- Buzzoni, A., Mantegazza, L., & Gariboldi, G. 1994, *AJ*, 107, 513
- Cameron, L. M. 1985, *A&A*, 146, 59
- Cappellaro, E. 1996, in *New Light on Galaxy Evolution*, ed. R. Bender & R. L. Davies, IAU Symposium 171 (Dordrecht: Kluwer Academic Publishers), 81
- Carlberg, R. G., Dawson, P. C., Hsu, T., & VandenBerg, D. A. 1985, *ApJ*, 294, 674
- Carollo, C. M., & Danziger, I. J. 1994, *MNRAS*, 270, 523
- Caughlan, G. R., & Fowler. 1988, *At. Data Nucl. Data Tables*, 40, 283
- Caughlan, G. R., Fowler, W. A., Harris, M. J., & Zimmermann, G. E. 1985, *At. Data Nucl. Data Tables*, 32, 197
- Charlot, S., & Bruzual, A. G. 1991, *ApJ*, 367, 126
- Chiappini, C., Matteucci, F., & Gratton, R. 1997, *ApJ*, 477, 765
- Chiosi, C., Bressan, A., Portinari, L., & Tantalo, R. 1998, *A&A*, 339, 355
- Ciotti, L., D'Ercole, A., Pellegrini, S., & Renzini, A. 1991, *ApJ*, 376, 380
- Ciotti, L., Stiavelli, M., & Braccisi, A. 1995, *MNRAS*, 276, 961
- Cohen, J. G., Blakeslee, J. P., & Ryzhov, A. 1998, *ApJ*, 496, 808
- Cole, S., Aragón-Salamanca, A., Frenk, C. S., Navarro, J., & Zepf, S. 1994, *MNRAS*, 271, 781
- Cole, S., Lacey, C. G., Baugh, C. M., & Frenk, C. S. 2000, *MNRAS*, in press, astro-ph/0007281
- Colless, M., Burstein, D., Davies, R. L., McMahan, R. K., Saglia, R. P., & Wegner, G. 1999, *MNRAS*, 303, 813
- Covino, S., Galletti, S., & Pasinetti, L. E. 1995, *A&A*, 303, 79
- Cowie, L. L., Songaila, A., Hu, E. M., & Cohen, J. G. 1996, *AJ*, 112, 839

- Davies, J. I., & Phillipps, S. 1988, *MNRAS*, 233, 553
- Davies, R. L. 1996, in *New Light on Galaxy Evolution*, ed. R. Bender & R. L. Davies, IAU Symposium 171 (Dordrecht: Kluwer Academic Publishers), 37
- Davies, R. L., Sadler, E. M., & Peletier, R. F. 1993, *MNRAS*, 262, 650
- de Jong, R. S., & Davies, R. L. 1997, *MNRAS*, 285, L1
- Djorgovski, S., & Davis, M. 1987, *ApJ*, 313, 59
- Dorman, B., O'Connell, R. W., & Rood, R. T. 1995, *ApJ*, 442, 105
- Dressler, A., Lynden-Bell, D., Burstein, D., Davies, R. L., Faber, S. M., Terlevich, R. J., & Wegner, G. 1987, *ApJ*, 313, 42
- Driver, S. P., Phillips, S., Davies, J. I., Morgan, I., & Disney, M. J. 1994, *Nature*, 268, 393
- Drory, N., Hopp, U., Bender, R., Feulner, G., Snigula, J., Mendes de Oliveira, C., & Hill, G. J. 2000, in *Clustering at high redshift*, astro-ph/9910268
- Edmunds, M. G. 1990, *MNRAS*, 246, 678
- Edmunds, M. G. 1992, in *Elements and the Cosmos*, ed. M. G. Edmunds & R. Terlevich (Cambridge: Cambridge University Press), 289
- Edvardsson, B., Andersen, J., Gustafsson, B., Lambert, D. L., Nissen, P. E., & Tomkin, J. 1993, *A&A*, 275, 101
- Eggen, O. J., Lynden-Bell, D., & Sandage, A. R. 1962, *ApJ*, 136, 748
- Einasto, J., Saar, E., Kaasik, A., & Chernin, A. D. 1974, *Nature*, 252, 111
- Elmegreen, B. G. 1997, *ApJ*, 486, 944
- Elmegreen, B. G. 1999, in *The Evolution of Galaxies on Cosmological Timescales*, ASP Conference Series (Kluwer)
- Faber, S. M. 1972, *A&A*, 20, 361
- Faber, S. M., Friel, E. D., Burstein, D., & Gaskell, D. M. 1985, *ApJS*, 57, 711
- Faber, S. M., Trager, S. C., González, J. J., & Worthey, G. 1995, in *Stellar Populations*, ed. P. C. Van der Kruit & G. Gilmore, IAU Symposium 164 (Dordrecht: Kluwer Academic Publishers), 249
- Faber, S. M., Worthey, G., & González, J. J. 1992, in *The stellar populations of galaxies*, ed. B. Barbuy & A. Renzini, IAU Symposium 149 (Dordrecht: Kluwer Academic Publishers), 255
- Farouki, R. T., & Shapiro, S. 1982, *ApJ*, 259, 103
- Federspiel, M., Tammann, G. A., & Sandage, A. 1998, *ApJ*, 495, 115

- Ferguson, H. C., Tanvir, N. R., & von Hippel, T. 1998, *Nature*, 391, 461
- Fisher, D., Franx, M., & Illingworth, G. 1995, *ApJ*, 448, 119
- Frenk, C. S. 1991, in *The Birth and Early Evolution of our Universe*, ed. J. S. Nilsson, B. Gustafsson, & B. S. Skagerstam, Nobel Symp. 79 (Singapore: World Scientific), 70
- Friça, A. C. S., & Terlevich, R. J. 1998, *MNRAS*, 298, 399
- Fuhrmann, K. 1998, *A&A*, 338, 161
- Fuhrmann, K. 2000, *A&A*, in press
- Fuhrmann, K., Axer, M., & Gehren, T. 1995, *A&A*, 301, 492
- Fusi Pecci, F., Ferraro, F. R., Bellazzini, M., Djorgovski, S., Piotto, G., & Buonanno, R. 1993, *AJ*, 105, 1145
- Fusi Pecci, F., & Renzini, A. 1975, *A&A*, 39, 413
- Gebhardt, K., & Kissler-Patig, M. 1999, *AJ*, 118, 1526
- Gerhard, O., Kronawitter, A., Saglia, R. P., & Bender, R. 2000, *AJ*, submitted
- Gerhard, O. E. 1983, *MNRAS*, 202, 1159
- Gibson, B. K., Loewenstein, M., & Mushotzky, R. F. 1997, *MNRAS*, 290, 623
- Gibson, B. K., Madgwick, D. S., Jones, L. A., Da Costa, G. S., & Norris, J. E. 1999, *AJ*, 118, 1268
- Gibson, B. K., & Matteucci, F. 1997, *MNRAS*, 291, L8
- Gilmore, G., & Wyse, R. 1998, *AJ*, 116, 748
- González, J. 1993, Phd thesis, University of California, Santa Cruz
- Gorgas, J., Efstathiou, G., & Aragón Salamaca, A. 1990, *MNRAS*, 245, 217
- Gorgas, J., Faber, S. M., Burstein, D., González, J. J., Courteau, S., & Prosser, C. 1993, *ApJS*, 86, 153
- Gorgas, J., Pedraz, S., Guzmán, G., Cardiel, N., & González, J. J. 1997, *ApJ*, 481, L19
- Goudfrooij, P., Gorgas, J., & Jablonka, P. 1999, *Ap&SS*, 269, 109
- Gould, A. 1990, *MNRAS*, 244, 25
- Gould, A., Bahcall, J. N., & Flynn, C. 1997, *ApJ*, 482, 913
- Gratton, R. G., & Ortolani, S. 1986, *A&A*, 169, 201
- Gratton, R. G., Quarta, M. L., & Ortolani, S. 1986, *A&A*, 169, 208

- Gratton, R. G., & Sneden, C. 1988, *A&A*, 204, 193
- Grebel, E. K. 1997, in *Reviews of Modern Astronomy*, Vol. 10, 29
- Greggio, L. 1996, in *The interplay between massive star formation, the ISM and galaxy evolution*, ed. D. Kunth, B. Guiderdoni, M. Heydari-Malayeri, & T. X. Thuan (Gif-sur-Yvette Cedex-France: Editions Frontieres), 89
- Greggio, L. 1997, *MNRAS*, 285, 151
- Greggio, L., Marconi, G., Tosi, M., & Focardi, P. 1993, *AJ*, 105, 894
- Greggio, L., & Renzini, A. 1983, *A&A*, 118, 217
- Greggio, L., & Renzini, A. 1990, *ApJ*, 364, 35
- Greggio, L., & Renzini, A. 1999, *Mem. Soc. Astron. Ital.*, 70, 691
- Grillmair, C. J., et al. 1996, *AJ*, 112, 1975
- Hansen, C. J., & Wheeler, J. C. 1969, *Ap. Space Sci.*, 36, 464
- Harris, G. L. H., Harris, W. E., & Poole, G. B. 1999, *AJ*, 117, 855
- Harris, W. E. 1996, *AJ*, 112, 1487
- Hensler, G., & Burkert, A. 1990, *Ap&SS*, 170, 231
- Hernquist, L. 1993, *ApJ*, 409, 548
- Hernquist, L., & Barnes, J. E. 1991, *Nature*, 354, 210
- Ibata, R. A., & Gilmore, G. F. 1995, *mnras*, 275, 605
- Ichikawa, S.-I. 1989, *AJ*, 97, 1600
- Ishimaru, Y., & Arimoto, N. 1997, *PASJ*, 49, 1
- Jimenez, R., Friça, A. C. S., Dunlop, J. S., Terlevich, R. J., Peacock, J. A., & Nolan, L. A. 1999, *MNRAS*, 305, 16
- Jørgensen, I., Franx, M., & Kjaergaard, P. 1995, *MNRAS*, 276, 1341
- Joseph, R. D., & Wright, G. S. 1985, *MNRAS*, 214, 87
- Kauffmann, G. 1996, *MNRAS*, 281, 487
- Kauffmann, G., & Charlot, S. 1998a, *MNRAS*, 294, 705
- Kauffmann, G., & Charlot, S. 1998b, *MNRAS*, 297, L23
- Kauffmann, G., Charlot, S., & White, S. D. M. 1996, *MNRAS*, 283, L117
- Kauffmann, G., & White, S. D. M. 1993, *MNRAS*, 261, 921
- Kauffmann, G., White, S. D. M., & Guiderdoni, B. 1993, *MNRAS*, 264, 201

- Kennicutt, R. C. 1989, *ApJ*, 344, 685
- Kissler-Patig, M., et al. 1998, *AJ*, 115, 105
- Kissler-Patig, M., Forbes, D. A., & Minniti, D. 1998, *MNRAS*, 298, 1123
- Kodama, T., & Arimoto, N. 1997, *A&A*, 320, 41
- Kormendy, J. 1982, in *Structure and Dynamics of Galaxies*, ed. L. Martinet & M. Mayor (Geneva: Geneva Observatory), 115
- Kormendy, J. 1985, *ApJ*, 295, 73
- Kormendy, J., & Bender, R. 1999, *ApJ*, 522, 772
- Kroupa, P., Tout, C. A., & Gilmore, G. 1993, *MNRAS*, 262, 545
- Kuijken, K., & Gilmore, G. 1989a, *MNRAS*, 239, 571
- Kuijken, K., & Gilmore, G. 1989b, *MNRAS*, 239, 605
- Kuijken, K., & Gilmore, G. 1989c, *MNRAS*, 239, 651
- Kuijken, K., & Gilmore, G. 1991, *ApJ*, 367, L9
- Kundu, A., Whitmore, B. C., Sparks, W. B., Macchetto, F. D., Zepf, S. E., & Ashman, K. M. 1999, *ApJ*, 513, 733
- Kuntschner, H. 1998, Phd thesis, University of Durham, Durham
- Kuntschner, H. 2000, *MNRAS*, 315, 184
- Kuntschner, H., & Davies, R. L. 1998, *MNRAS*, 295, L29
- Kurucz, R. L. 1979, *ApJS*, 40, 1
- Lacey, C. G., Guiderdoni, B., Rocca-Volmerange, B., & Silk, J. 1993, *ApJ*, 402, 15
- Lacey, C. G., & Silk, J. 1991, *ApJ*, 381, 14
- Larson, R. B. 1972, *Nature Phys. Sci.*, 236, 7
- Larson, R. B. 1974, *MNRAS*, 169, 229
- Larson, R. B. 1976, in *Galaxies*, ed. L. Martinet & M. Mayor, Sixth Advanced Course of the Swiss Society of Astronomy and Astrophysics (Sauverny: Geneva Observatory), 67
- Leitherer, C. 1998, in *The Stellar Initial Mass Function*, ed. G. Gilmore & D. Howell, Vol. 142 (San Francisco, CA: ASP), 61
- Lejeune, T., Cuisinier, F., & Buser, R. 1998, *A&AS*, 130, 65
- Lin, D. N. C., & Faber, S. M. 1983, *ApJ*, 266, L21

- Loewenstein, M., & Mushotzky, R. F. 1996, *ApJ*, 466, 695
- Longhetti, M., Bressan, A., Chiosi, C., & Rampazzo, R. 2000, *A&A*, 353, 917
- Lotz, J. M., Ferguson, H. C., & Bohlin, R. C. 2000, *ApJ*, 532, 830
- Loveday, J. 1997, *ApJ*, 489, 29
- Lynden-Bell, D. 1967, *MNRAS*, 136, 101
- Magain, P. 1989, *A&A*, 209, 211
- Malinie, G., Hartmann, D. H., Clayton, D. D., & Mathews, G. J. 1993, *ApJ*, 413, 633
- Maraston, C. 1998, *MNRAS*, 300, 872
- Maraston, C. 1999, in *Star Formation in Early-Type Galaxies*, ed. P. Carral & J. Cepa, Vol. 163 (ASP Conf. Ser.), 28
- Maraston, C. 2000, in *The chemical evolution of the Milky Way: stars versus clusters*, ed. F. Giovannelli & F. Matteucci
- Maraston, C., Greggio, L., & Thomas, D. 2001, *Ap&SS*, in press, astro/ph-9906088
- Maraston, C., Kissler-Patig, M., Brodie, J. P., Barmby, P., & Huchra, J. 2000, *A&A*, submitted
- Maraston, C., & Thomas, D. 2000, *ApJ*, 541, 126
- Mateo, M. L. 1998, *ARA&A*, 36, 435
- Matteucci, F. 1994, *A&A*, 288, 57
- Matteucci, F., & François, P. 1989, *MNRAS*, 239, 885
- Matteucci, F., & Greggio, L. 1986, *A&A*, 154, 279
- Matteucci, F., & Tornambè, A. 1987, *A&A*, 185, 51
- McWilliam, A., & Rich, R. M. 1994, *ApJS*, 91, 749
- Mehlert, D., Saglia, R. P., Bender, R., & Wegner, G. 1998, *A&A*, 332, 33
- Mehlert, D., Saglia, R. P., Bender, R., & Wegner, G. 2000, *A&AS*, 141, 449
- Melnick, J., & Mirabel, I. F. 1990, *A&A*, 231, L19
- Melnick, J., & Selman, F. 2000, in *The evolution of galaxies I. Observational clues*, ed. J. M. Vilchez, G. Stasinska, & E. Perez (Kluwer), in press
- Mendez, R. H., Guerrero, M. A., Freeman, K. C., Arnaboldi, M., Kudritzki, R. P., Hopp, U., Cappacioli, M., & Ford, H. 1997, *ApJ*, 491L, 23

- Meusinger, H., Reimann, H.-G., & Stecklum, B. 1991, *A&A*, 245, 57
- Mitchell, R. J., Culhane, J. L., Davison, P. J., & Ives, J. C. 1976, *MNRAS*, 175, 29P
- Moore, B., Katz, N., & Lake, G. 1998, *ApJ*, 457, 455
- Muller, R. A., Oort, J. H., & Raimond, E. 1963, *C.R. Acad. Sci. Paris.*, 257, 1661
- Mushotzky, R., Loewenstein, M., Arnaud, K. A., Tamura, T., Fukazawa, Y., Matsushita, K., Kikuchi, K., & Hatsukade, I. 1996, *ApJ*, 466, 686
- Negroponte, J., & White, S. D. M. 1983, *MNRAS*, 205, 1009
- Nissen, P. E., Gustafsson, B., Edvardsson, B., & Gilmore, G. 1994, *A&A*, 285, 440
- Nissen, P. E., & Schuster, W. J. 1997, *A&A*, 326, 751
- Nomoto, K. 1980a, in *Type I Supernovae*, ed. J. C. Wheeler (Austin: University of Texas), 164
- Nomoto, K. 1980b, *Space Sci. Rev.*, 27, 563
- Nomoto, K. 1981, in *Fundamental Problems in the Theory of Stellar Evolution*, ed. D. Sugimoto, D. Q. Lamb, & D. N. Schramm, *IAU Symposium 93* (Dordrecht: Reidel), 295
- Nomoto, K., Hashimoto, M., Tsujimoto, F.-K., Kishimoto, N., Kubo, Y., & Nakasato, N. 1997, *Nucl. Phys. A*, 616, 79c
- Nomoto, K., Iwamoto, K., & Suzuki, T. 1995, *Phys. Rep.*, 256, 173
- Nomoto, K., Thielemann, F.-K., & Yokoi, K. 1984, *ApJ*, 286, 644
- O'Connell, R. W. 1976, *ApJ*, 206, 370
- Oort, J. H. 1970, *A&A*, 7, 381
- Pagel, B. E. J. 1989, in *Evolutionary Phenomena in Galaxies*, ed. J. E. Beckman & B. E. J. Pagel (Cambridge: Cambridge University Press), 201
- Pagel, B. E. J. 1997, *Nucleosynthesis and Chemical Evolution of Galaxies* (First ed.) (Cambridge University Press)
- Pagel, B. E. J., & Patchett, B. E. 1975, *MNRAS*, 172, 13
- Pagel, B. E. J., & Tautvaisiene, G. 1995, *MNRAS*, 276, 505
- Pahre, M. A. 1998, Phd thesis, California Institute of Technology
- Peletier, R. 1989, Phd thesis, Rijksuniversiteit Groningen
- Pilachowski, C. A., Sneden, C., & Wallerstein, G. 1983, *ApJS*, 52, 241

- Portinari, L., Chiosi, C., & Bressan, A. 1998, *A&A*, 334, 505
- Press, W. H., & Schechter, P. G. 1974, *ApJ*, 187, 425
- Puzia, T. H., Kissler-Patig, M., Brodie, J. P., & Huchra, J. P. 1999, *AJ*, 118, 2734
- Rana, N. C. 1991, *ARA&A*, 29, 129
- Rana, N. C., & Basu, S. 1992, *A&A*, 265, 499
- Rebolo, R., Israelian, G., & García López, R. J. 1999, *apss*, 265, 165
- Renzini, A. 1986, in *Stellar Populations*, ed. C. A. Norman, A. Renzini, & M. Tosi (Cambridge: Cambridge University Press), 213
- Renzini, A. 1997, *ApJ*, 488, 35
- Renzini, A., & Buzzoni, A. 1986, in *Spectral evolution of galaxies*, ed. C. Chiosi & A. Renzini (Dordrecht: Reidel), 135
- Renzini, A., & Ciotti, L. 1993, *ApJ*, 416, L49
- Renzini, A., Ciotti, L., D'Ercole, A., & Pellegrini, S. 1993, *ApJ*, 419, 52
- Renzini, A., & Voli, M. 1981, *A&A*, 94, 175
- Rich, R. M. 1988, *AJ*, 95, 828
- Rich, R. M., et al. 1997, *ApJ*, 484, L25
- Richer, H. B., et al. 1996, *ApJ*, 463, 602
- Rose, J. A., & Deng, S. 1999, *AJ*, 117, 2213
- Saglia, R. P., et al. 1993, *ApJ*, 403, 567
- Saglia, R. P., Maraston, C., Greggio, L., Bender, R., & Ziegler, B. 2000, *A&A*, 360, 911
- Salpeter, E. E. 1955, *ApJ*, 121, 161
- Sandage, A., Binggeli, B., & Tamman, G. A. 1985, *AJ*, 90, 1759
- Sanders, d. B., Soifer, B. T., Elioas, J. H., Madore, B. F., Matthews, K., Neugebauer, G., & Scoville, N. Z. 1988, *ApJ*, 325, 74
- Scalo, J. M. 1986, *Fundam. Cosmic Phys.*, 11, 1
- Scalo, J. M. 1998, in *The Stellar Initial Mass Function*, ed. G. Gilmore & D. Howell, Vol. 142 (San Francisco, CA: ASP), 201
- Schaller, G., Schaerer, D., Meynet, G., & Maeder, A. 1992, *A&AS*, 96, 269
- Schechter, P. 1976, *ApJ*, 203, 297

- Schmidt, M. 1959, *ApJ*, 129, 243
- Schmidt, M. 1963, *ApJ*, 137, 758
- Schweizer, F., & Seitzer, P. 1992, *AJ*, 104, 1039
- Schweizer, F., Seitzer, P., Faber, S. M., Burstein, D., Dalle Ore, C. M., & González, J. J. 1990, *ApJ*, 364, L33
- Serlemitsos, et al. 1977, *ApJ*, 211, L63
- Silk, J. 1986, in *Star-Forming Dwarf Galaxies*, ed. D. Kunth et al. (Gif sur Yvettes: ASPÉditions Frontières), 465
- Silva, D. R., & Bothun, G. D. 1998a, *AJ*, 116, 85
- Silva, D. R., & Bothun, G. D. 1998b, *AJ*, 116, 2793
- Soifer, B. T., & et al. 1984, *ApJ*, 278, L71
- Somerville, R. S., & Primack, J. R. 1999, *MNRAS*, 310, 1087
- Sommer-Larsen, J. 1991, *MNRAS*, 249, 368
- Songaila, A., Cowie, L. L., Hu, E. M., & Gardner, J. P. 1994, *ApJS*, 94, 461
- Statler, T. S. 1989, *ApJ*, 344, 217
- Sugimoto, D., & Nomoto, K. 1980, *Space Sci. Rev.*, 25, 155
- Sutherland, R., & Dopita, M. 1993, *ApJS*, 88, 253
- Tammann, G. A. 1982, in *Supernovae: a Survey of Current Research*, ed. M. Rees & R. Stoneham, 371
- Tantalo, R., Chiosi, C., & Bressan, A. 1998, *A&A*, 333, 419
- Tantalo, R., Chiosi, C., Bressan, A., & Fagotto, F. 1996, *A&A*, 311, 361
- Thielemann, F.-K., Nomoto, K., & Hashimoto, M. 1996, *ApJ*, 460, 408
- Thomas, D. 1997, Diploma thesis, Ludwig-Maximilians-Universität, München
- Thomas, D. 1999a, *MNRAS*, 306, 655
- Thomas, D. 1999b, in *Chemical Evolution from Zero to High Redshift*, ed. J. R. Walsh & M. R. Rosa, *ESO Astrophysics Symposia* (Springer), 197
- Thomas, D. 2001, *Ap&SS*, in press
- Thomas, D., Greggio, L., & Bender, R. 1998, *MNRAS*, 296, 119
- Thomas, D., Greggio, L., & Bender, R. 1999, *MNRAS*, 302, 537
- Thomas, D., & Kauffmann, G. 1999, in *Spectrophotometric dating of stars and galaxies*, ed. I. Hubeny, S. Heap, & R. Cornett, Vol. 192 (*ASP Conf. Ser.*), 261

- Timmes, F. X., Woosley, S. E., & Weaver, T. A. 1995, *ApJS*, 98, 617
- Tinsley, B. M. 1972, *ApJ*, 178, 319
- Tinsley, B. M. 1980, *Fundam. Cosmic Phys.*, 5, 287
- Toomre, A., & Toomre, J. 1972, *ApJ*, 178, 623
- Tosi, M. 1988, *A&A*, 197, 47
- Trager, S. C. 1998, Phd thesis, University of California, Santa Cruz
- Trager, S. C., Dalcanton, J. J., & Weiner, B. J. 1999, in *When and How do Bulges Form and Evolve*, ed. C. M. Carollo & H. Ferguson, STScI workshop, astro-ph/9810376
- Trager, S. C., Faber, S. M., Worthey, G., & González, J. J. 2000a, *AJ*, 119, 164
- Trager, S. C., Faber, S. M., Worthey, G., & González, J. J. 2000b, *AJ*, 120, 165
- Trentham, N. 1994, *Nature*, 372, 157
- Trentham, N. 1998, *MNRAS*, 294, 193
- Tripicco, M. J., & Bell, R. A. 1995, *AJ*, 110, 3035
- Truran, J. W., & Cameron, A. G. W. 1971, *Ap&SS*, 14, 179
- Tsujimoto, T., Nomoto, K., Yoshii, Y., Hashimoto, M., Yanagida, S., & Thielemann, F.-K. 1995, *MNRAS*, 277, 945
- Tsujimoto, T., Shigeyama, T., & Yoshii, Y. 1999, *ApJ*, 519, L63
- Twarog, B. A. 1980, *ApJ*, 242, 242
- Vader, J. P., & Chaboyer, B. 1994, *AJ*, 108, 1209
- van Albada, T. S., de Boer, K. S., & Dickens, R. J. 1981, *MNRAS*, 195, 591
- van den Bergh, S. 1962, *AJ*, 62, 711
- van den Bergh, S., & Tammann, G. A. 1991, *ARA&A*, 29, 363
- VandenBerg, D. A. 1985, *ApJS*, 58, 711
- Vazdekis, A., Peletier, R. F., Beckmann, J. E., & Casuso, E. 1997, *ApJS*, 111, 203
- Wakker, B. P. 1991, *A&A*, 250, 499
- Wakker, B. P., & Schwarz, U. J. 1991, *A&A*, 250, 484
- Wakker, B. P., & van Woerden, H. 1991, *A&A*, 250, 509

- Weaver, T. A., & Woosley, S. E. 1980, in Texas Conference on Relativistic Astrophysics, ed. J. Ehlers (Ann. NY Acad. Sci.), 366
- Weaver, T. A., & Woosley, S. E. 1995, ApJS, in preparation
- Weiss, A., Peletier, R. F., & Matteucci, F. 1995, A&A, 296, 73
- Whelan, J., & Iben, I., Jr. 1973, ApJ, 186, 1007
- White, S. D. M., & Frenk, C. S. 1991, ApJ, 379, 52
- White, S. D. M., & Rees, M. J. 1978, MNRAS, 183, 341
- Wirth, A., & Gallagher, J. S. 1984, ApJ, 282, 85
- Woosley, S. E., & Weaver, T. A. 1995, ApJS, 101, 181
- Worthey, G. 1994, ApJS, 95, 107
- Worthey, G., Dorman, B., & Jones, L. A. 1996, AJ, 112, 948
- Worthey, G., Faber, S. M., & González, J. J. 1992, ApJ, 398, 69
- Worthey, G., Faber, S. M., González, J. J., & Burstein, D. 1994, ApJS, 94, 687
- Wu, C. C., Faber, S. M., Gallagher, J. S., Peck, M., & Tinsley, B. M. 1980, ApJ, 237, 290
- Wyse, R. F. G., & Gilmore, G. 1992, aj, 104, 144
- Yi, S., Demarque, P., & Oemler, A., Jr. 1998, ApJ, 492, 480
- Yoshii, Y., Tsujimoto, T., & Nomoto, K. 1996, ApJ, 462, 266
- Zaritsky, D., Kennicutt, R. C., Jr., & Huchra, J. P. 1994, ApJ, 420, 87
- Zepf, S. 1997, Nature, 300, 377
- Zepf, S. E., & Ashman, K. E. 1993, MNRAS, 264, 611
- Ziegler, B. L., & Bender, R. 1997, MNRAS, 291, 527
- Ziegler, B. L., Saglia, R. P., Bender, R., Belloni, P., Greggio, L., & Seitz, S. 1999, A&A, 346, 13
- Zinn, R., & West, M. J. 1984, ApJS, 55, 45
- Zucca, E., et al. 1997, A&A, 326, 477

Acknowledgments

Ralf Bender,
meinem Doktorvater, danke ich ganz herzlich für sein großes Engagement, mit dem er mich während meiner Zeit als Doktorand begleitet hat. Von ihm habe ich zweifellos (hoffentlich) viel gelernt. Durch seine extrem freundliche und freundschaftliche Art, die das sehr gute Arbeitsklima in der Gruppe deutlich prägt, haben die Promotion und die sehr interessante Arbeit viel viel Spaß gemacht. Ganz besonders schätze ich, dass er für die Studenten und Mitarbeiter immer Zeit und ein offenes Ohr findet.

Laura Greggio,
meiner Doktormutter bzw. Co-advisor danke ich ganz herzlich für den enormen Einsatz mit dem sie mich hier als Gastwissenschaftlerin betreut hat. In zahlreichen Diskussionen habe ich auch von ihr sehr viel lernen können.

Harald Lesch,
meinem Doktoronkel, danke ich ganz herzlich dafür, dass er sich bereit erklärt hat, diese Arbeit nicht nur zu lesen, sondern auch noch zu bewerten. Ganz besonders danke ich ihm aber für die vielen Kabaretteinlagen am Mittagstisch, die schon so manchen überarbeiteten Doktoranden ermuntert und wieder aufgerichtet haben.

Rolf Kudritzki,
meinem Doktorgroßvater, danke ich ganz herzlich, dass er diese äußerst freundliche und kollegiale Atmosphäre am Insitut geschaffen, und meinen Doktorvater ans Institut geholt hat.

Uli Hopp, Claudia Mendes de Oliveira, Roberto Saglia, Stella Seitz,
meinen Doktoronkels und -Tanten zweiten Grades, danke ich ganz herzlich für die tatkräftige Unterstützung in Form von wertvollen Tipps und vielen anregenden Diskussionen.

Paola Belloni, Jan Beuing, Dörte Mehlert, und Bodo Ziegler,
meinen großen Doktorgeschwistern, danke ich ganz herzlich für die offene Art, mit der sie mich als echten Münchner in ihrer Gruppe aufgenommen haben. Jede(r) einzelne hat auf ihre/seine Art ihren/seinen riesigen Teil dazu beigetragen, dass meine Promotionszeit und der Einstieg in die raue Welt der Wissenschaft unheimlich Spaß gemacht haben.

*Niv Drory, meinem Doktorbruder,
Claudia Maraston, Michael Matthias, meinen Doktorcousins,
und Christine Botzler, Georg Feulner, Jürgen Fliri, Armin Gabbasch, Claus
Gössel, Doris Merkl, Thomas Puzia, Arno Riffeser, Jan Snigula, meinen
kleinen Doktorgeschwistern,
danke ich für die vielen Diskussionen und gegenseitigen Hilfestellungen, die
gute Stimmung in der Gruppe, für die zahlreichen Espressi und vieles mehr.*

*Claudia Maraston,
meiner Doktorcousine, danke ich außerdem für das aufopferungsvolle
Korrekturlesen dieser Arbeit.*

Allen Mitarbeitern des Instituts danke ich ganz herzlich für alles.

*Meiner Familie und allen Freunden danke ich für ihre Unterstützung vor,
während und nach der Promotion.*

Lebenslauf

Persönliche Daten:

Name:	Daniel Georg THOMAS
Geburtsdatum:	14. Juli 1972
Geburtsort:	München, Deutschland

Ausbildung:

1997 – 2000:	Promotionsstudium der Astronomie an der Universitäts-Sternwarte München der Ludwig-Maximilians-Universität
1996 – 1997:	Diplomarbeit an der Universitäts-Sternwarte München
1991 – 1997:	Physikstudium an der Ludwig-Maximilians-Universität München
1982 – 1991:	Gymnasium in München
1978 – 1982:	Grundschule in München

